MINISTERUL EDUCAȚIEI NAȚIONALE

UNIVERSITATEA TEHNICĂ
DIN CLUJ-NAPOCA

Field: ELECTRICAL ENGINEERING

PhD THESIS

Multiphysics Design and Analysis of Synchronous Reluctance Machine

PhD Student:
Arkadiusz Grzegorz DZIECHCIARZ

PhD Supervisor:
Prof. Eng. Claudia Steluţa MARŢIŞ, PhD

Examination committee:
Chair: Prof. Eng. Călin Munteanu, PhD – Technical University of Cluj-Napoca
PhD Supervisor: Prof. Eng. Claudia Steluţa Marţiş, PhD - Technical University of Cluj-Napoca
Members:
- Prof. Eng. Nicolae Muntean, PhD - Politehnica University Timişoara
- Assoc. Prof. Eng. Leonard Livadaru, PhD - Gheorghe Asachi Technical University of Iaşi
- Prof. Eng. Lorand Szabo, PhD – Technical University of Cluj-Napoca
- Assoc. Prof. Eng. Maciej Sułowicz, PhD – Cracow University of Technology

– Cluj-Napoca –
2019

str. Memorandumului nr.28, 400114 Cluj-Napoca, România
tel. +40-264-401200, fax +40-264-592055, secretariat tel. +40+264-202209, fax +40-264-202280
http://www.utcluj.ro/

This work was supported by ADvanced Electric Powertrain Technology (ADEPT) project which is an EU funded Marie Curie ITN project, grant number 607361.

ACKNOWLEDGEMENT

I address my sincere thanks to my supervisor Prof. Claudia Steluța Marțiș, Professor at Technical University of Cluj-Napoca, who offered me the opportunity join the team at the university in frame of ITN Marie Curie ADEPT Project and who has been supporting me through the entire period of my work at the university. I am grateful for all the precious suggestions and advices which allowed me to accomplish my work.

I would like to thank Dr. Claudiu Alexandru Oprea for all the kindness and help which I received and a fruitful collaboration, during which I had a chance to significantly improve my skills.

My sincere thanks goes to Dr. Áron Attila Popp without whom accomplishing this thesis would not be possible.

I would also like to thank Eng. Radu Andrei Marțiș for help with laboratory tests, necessary to finish this work.

I would like to thank the evaluation committee for their time and effort to read my thesis and for precious suggestions in improving it.

My sincere gratitude goes to all members of Electrical Machines and Drives Department from Technical University of Cluj-Napoca for the amazing kindness and ambient they created, especially I would like to thank Eng. Sorin Iulian Cosman and Eng. Claudia Violeta Pop for all the kindness and help I received from them during my stay at the university.

I would like to thank Prof. Johan Gyselinck, Professor at Université Libre de Bruxelles who provided me with very helpful and constructive suggestions during my work.

My sincere thanks goes to my colleagues from Cracow University of Technology, from whom I learned a lot during the initial period of my scientific career. I would like to thank Dr. Maciej Sułowicz from Cracow University of Technology for all the help and support and precious advices which I was offered during my work. I also would like to thank Prof. Tadeusz Sobczyk and Prof. Konrad Weinreb for everything they taught me

about electric machines during my studies and at the beginning of my scientific career.

I would like to thank ITN ADEPT Project committee for giving me the opportunity to join the project and gain valuable experience. I also would like to thank all the researchers from ITN ADEPT Project for a wonderful collaboration.

Most of all, I would like to address my sincere gratitude to my family for their support and encouragement, especially to my wife for her support and patience, necessary for accomplishing this work.

I dedicate this work to my beloved wife and son.

Pracę tę dedykuję mojej żonie i synkowi.

TABLE OF CONTENT

1. ABREVIATIONS

ATV – acoustic transfer vector

CFD – computational fluid dynamics

EV – electric vehicle

FEM – finite element analysis

MEC – magnetic equivalent circuit

MMF – magnetomotive force

NVH – noise vibration and harshness

OASPL – overall sound pressure level

SRM – switched reluctance machine

SynRM – synchronous reluctance machine

TN – thermal network

WF – winding function

2. INTRODUCTION

Electric vehicles are of great interest nowadays. Climate change, air pollution and shortage of natural resources as well as increasing demand for mobility have led to consideration of alternative energy sources in everyday life applications. Transportation is a major field in which alternative energy sources can be used. Currently hybrid and plug-in hybrid vehicles are gaining more popularity. Due to constantly developed technology of battery manufacturing and wide variety of electric motor types, these vehicles have very good performance at significantly lowered fuel consumption. This technology is a major step in reducing greenhouse gases and limit consumption of fossil fuels [1]. It is also a temporary solution in switching to fully electric vehicles. It can be expected that the influence of electric mobility will grow in importance as it already has crossed a critical threshold [2]. The battery technology is still a bottleneck in electric vehicles development [3] however the technology is in constant development which leads to improve the battery performance [4]. Furthermore, in order to compensate for limitations coming from battery technology, rapid-charge stations for electric vehicles are developed [5]. While the technology of rapid-charge station is important for the charging process, a proper distribution of such stations is crucial for the transportation itself as this can significantly increase the range of electric vehicles. A research on optimal distribution of charging stations is presented in [6]. This shows how important electric mobility has become in these days and it can be expected that its importance will keep on increasing. For that reason, intensive research is being conducted on all aspects of electric mobility.

Nowadays there are several types of electric vehicles available in the market: pure electric vehicle (EV), hybrid electric vehicle (HEV), plug in electric vehicle (PHEV) and fuel cell vehicle (FCV) which uses hydrogen as a fuel to produce electricity to supply the electric motor. Each type of the electric vehicle has some advantages and some issues. Characteristics of the electric vehicles types is shown in Table 2.1.

The engineering process of EVs in general is essentially the integration of automobile and electrical engineering. The design process of modern electric vehicles should consider state-of-the-art technologies from

automotive, electrical, electronic and chemical engineering [7]. Energy management and energy sources development are key factors to enable electric vehicles to compete with internal combustion engine vehicles [7]. Propulsion system of hybrid electric vehicles consists of internal combustion engine (ICE) and an electric motor/generator. The configuration of an ICE and electric motor can be series or parallel [7]. In hybrid electric vehicles with series configuration, the output from internal combustion engine is initially converted to electric power using a generator. The converted electric power is either used to charge the battery or bypasses the battery and supplies electric motor which propels the wheels of the vehicle. In hybrid electric vehicle with parallel configuration, the electric motor and ICE are both coupled with the final wheels drive shaft. This configuration allows the power to be transferred to the drive by ICE alone, electric motor alone or in combined mode [7].

Some of the electric and hybrid vehicle models available in the market are described below.

Toyota Prius is the first mass produced hybrid electric vehicle in the world. This vehicle contains two permanent magnet motors – one originally used as a motor and the other one originally used as a generator. The battery is charged by the generator while coasting and with help of the motor while regenerative braking. During low vehicle's speed, the internal combustion engine is shut off [7]. The vehicle and its powertrain layout are presented in Fig. 2.1.

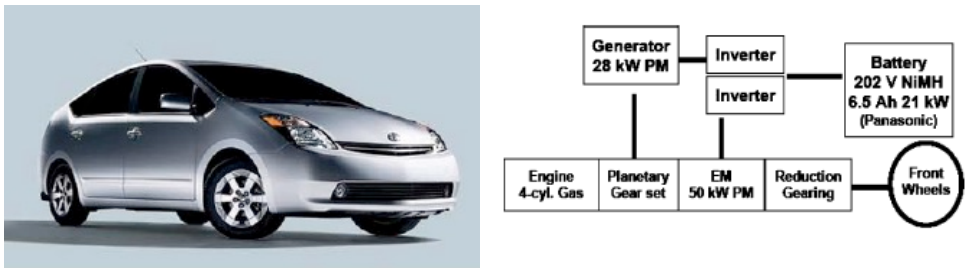

Fig. 2.1 Toyota Prius (left) and its powertrain scheme (right) [7]

TABLE 2.1 Characteristics of electric vehicles [7]

Types of EVs	Battery EVs	Hybrid EVs	Fuel Cell EVs
Propulsion	• Electric motor drives	• Electric motor drives • Internal combustion engines	• Electric motor drives
Energy system	• Battery • Ultracapacitor	• Battery • Ultracapacitor • ICE generating unit	• Fuel cells • Need battery / ultracapacitor to enhance power density for starting
Energy source & infrastructure	• Electric grid charging facilities	• Gasoline stations • Electric grid charging facilities (for Plug In Hybrid)	• Hydrogen • Hydrogen production and transportation infrastructure
Characteristics	• Zero emission • High energy efficiency • Independence on crude oils • Relatively short range • High initial cost • Commercially available	• Very low emission • Higher fuel economy as compared with ICE vehicles • Long driving range • Dependence on crude oil (for non-Plug In Hybrid) • Higher cost compared to ICE vehicles • Commercially available	• Zero emission or ultra-low emission • High energy efficiency • Independence on crude oil (if not using gasoline to produce hydrogen) • Satisfied driving range • High cost • Under development
Major issues	• Battery and battery management • Charging facilities • Cost	• Multiple energy sources control, optimization and management • Battery sizing and management	• Fuel cell cost, life cycle and reliability • Hydrogen infrastructure

Honda Civic has a different topology. In this vehicle the electric PM motor is placed between the internal combustion engine and the transmission. During high power demand, the PM motor provides assistance for the ICE engine while during low power demand. This vehicle offers 66% and 24% fuel efficiency improvement in the city or highway driving respectively [7].

Ford Escape is the first SUV hybrid in the world. This vehicle has a reduced sized engine and uses planetary gear for power splitting [7].

Saturn Vue has a power train equipped a 4 kW electric motor. The fuel economy reaches 20% however due to small size of the electric motor, the internal combustion engine cannot be shut off during driving at low speed [7].

Honda FCX is one of the fuel cell cars commercially available. This car is certified as a Zero-Emission Vehicle (ZEV). The vehicle is equipped with Honda developed and produced fuel cell stacks [7]. This vehicle is presented in Fig. 2.2.

Fig. 2.2 Honda FCX [7]

Tesla Roadster, Tesla Model S and Tesla Model X are all battery electric vehicles. Their powertrains basically contain lithium-ion battery of capacity depending on vehicle's version and induction motor. Depending on the model, the vehicle contains front, rear or front and rear electric traction motors [8].

Fig. 2.3 Tesla Model S – outside view (left) and interior (right) [7]

The induction machine and a model of its water jacket are presented in Fig. 2.4.

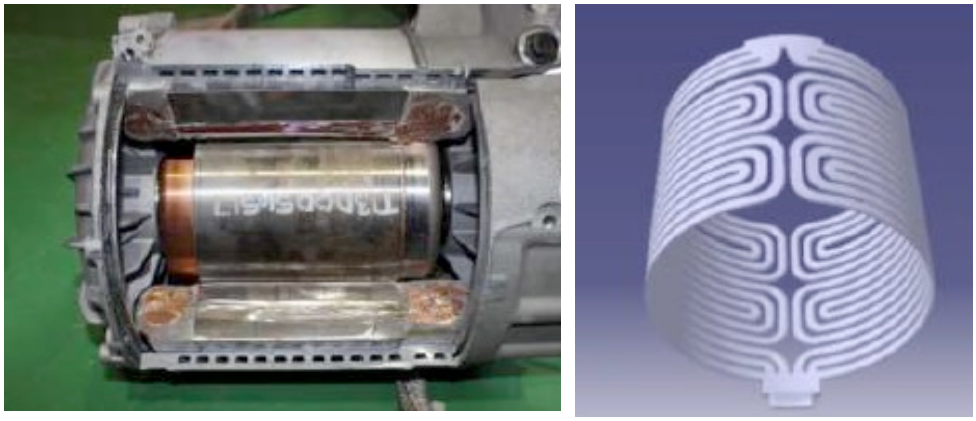

Fig. 2.4 Induction machine (left) and model of a water jacket (right) used in Tesla Model S [9]

Nissan Leaf is an electric vehicle with 80 kW interior permanent magnet motor with rare earths magnets. Geometry of the electric motor used in Nissan Leaf is presented in Fig. 2.5. The motor has two layers of magnets in the rotor and water jacket in the stator housing.

Fig. 2.5 Nissan Leaf [9]

The steel sheet of rotor core and stator housing are shown in Fig. 2.6.

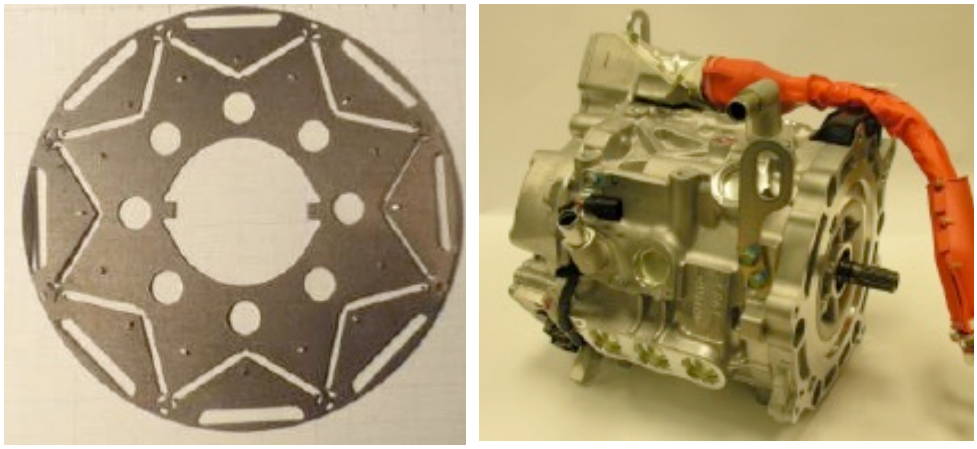

Fig. 2.6 Steel sheet of rotor core (left) and stator housing (right) [9]

BMW i3 with 125 kW NdFe-B internal permanent magnet motor and a new larger 33 kWh battery has a range of 115 miles. The vehicle is shown in Fig. 2.7.

Fig. 2.7 BMW i3

All the electric vehicles contain at least one electric motor in their powertrain. The motor plays a significant role in the performance of all the EVs, HEVs and FCVs. Typical requirements for an electric motor in a vehicle drive system are: high power and torque density, wide range of speed, high efficiency, robustness and reliability at a rational cost [7].

Electric motors which fit for EV, HEV and FCV applications are: PM synchronous or PM brushless motors, induction motors, switched reluctance motors, synchronous reluctance motors.

Induction motor is used for EVs, HEVs and FCVs due its simplicity, wide speed range and robustness. Induction motors are also well recognized in the literature and very popular. Thanks to field oriented control, the induction motor can behave like a DC machine [7], [10]. Field weakening can extend the speed range of the machine. Induction motor's efficiency is in general lower than that of a PM machine because of the inherent rotor losses.

Permanent magnet brushless DC motor is suitable for small electric vehicles which require maximum power of 60 kW. In this motor, the rotor has permanent magnets (most commonly NdFeB) and the stator is provided AC current. Since there is no winding in the rotor, there is no rotor copper loss which is an advantage compared to induction motors. This machine is also light, small, has good heat dissipation capability and high torque density. However, the constant power range is relatively short due to its restrained ability of field weakening. The EMF generated in stator windings at high speeds also affects generated torque [10].

Permanent magnet synchronous motor (PMSM) is the one of the most advanced. They can be operated at a wide range of speeds. These machines are suitable to be used in in-wheel applications since they provide high torque at low speeds. In order to provide high energy density, NdFeB permanent magnets are used. Due to the machine's construction, flux linkage in the air gap is of sinusoidal nature hence the motor is controlled by sinusoidal voltage supplies and vector control. The biggest disadvantage of this machine are iron losses at high rotational speeds which make the whole system unstable. Currently, the PMSMs are the most used motors in electric vehicles [10].

Switched reluctance motor (SRM) also called a doubly salient motor have simple and robust mechanical construction which makes them reliable at low cost. This motor can also operate at high speeds and its long constant power range and high power density make this machine suitable for EV applications. The downside of this motor is the generated noise, torque ripple, low efficiency and quite large size and weight especially compared to PM machines. Despite the simple construction of the machine, its control strategy is complicated due to slots and poles fringe effect and high saturation of pole tips. High cost of rare earth magnets results in increased interest in SRMs. Noise and torque ripple reduction are the main concerns of researchers working on switched reluctance machines [10].

Synchronous reluctance motor (SynRM) combines the advantages of permanent magnet and induction motors. The construction of this type of machine makes it robust, efficient and small without the drawbacks of PM machines. The control strategy of this motor is similar to that of a PM machine. The drawback of this type of motor is its quite low power factor. This can be compensated by using axially laminated rotor or by introducing permanent magnets into transversally laminated rotor of the machine. In the second case, the machine is called PM assisted synchronous reluctance motor. The idea of using permanent magnets in SynRM is to use fewer permanent magnets which results in lower flux linkage caused by permanent magnets compared to PM machines. The right amount of permanent magnets in the rotor increases the efficiency of the machine while keeping the back EMF in stator winding at negligible magnitude [10]. In general, machines which operate at synchronous speed have their rotor losses reduced almost to zero [11]. Iron losses in the rotor of a machine operating at synchronous speed

come from higher order harmonics which are smaller than the dominant base harmonic.

Synchronous reluctance machine is offered for industrial applications like pumps, compressors, mixers or fans. Synchronous reluctance machine has unprecedented reliability. The rotor runs cool which keeps machine's bearings' temperature low. This increases bearing system reliability. Performance of a SynRM is comparable to that of an induction machine and moreover, it is possible to get more output power from a SynRM of a smaller size than induction machine. This is illustrated in Fig. 2.8.

Fig. 2.8 Comparison of SynRM with induction motor of the same power [12]

Low voltage motors consume 28% of the world's electricity thus even a small efficiency gain in a low voltage motor results in large cost reduction [13]. Efficiency classes for electric motors are defined in IEC 60034-30-1 as follows:

- IE1 – Standard Efficiency
- IE2 – High Efficiency
- IE3 – Premium Efficiency
- IE4 – Super Premium Efficiency

In the market, electric motors of IE4 efficiency class are available and a new efficiency class called IE5 Ultra-Premium Efficiency Class is being under consideration [11].

Synchronous reluctance machine can achieve IE4 efficiency class while maintaining the frame size of an induction machine of lower (IE2) efficiency class as shown in Fig. 2.9.

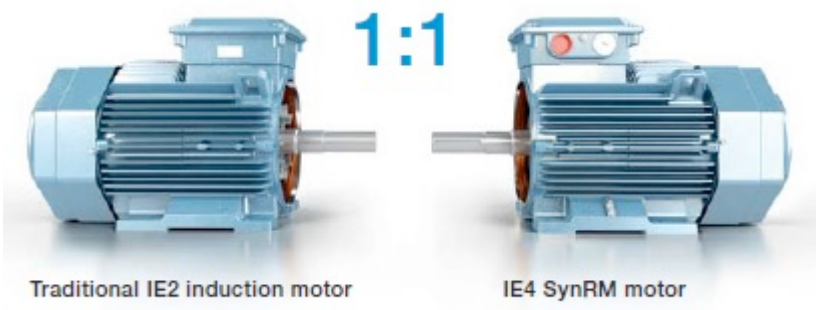

Fig. 2.9 Comparison of SynRM with induction machine by ABB - super premium efficiency from the same frame size [14], [12]

Synchronous reluctance motor manufactured by REEL is considered to be of IE5 efficiency class [15]. The machine and a 3D cross section model are presented in Fig. 2.10.

Fig. 2.10 REEL SynRM with dedicated drive (left) and SynRM model cross section (right) [15]

REEL SuPremE® synchronous reluctance motors do not use any rare earths magnetic materials or increased amount of copper. For this reason the total environmental footprint of manufacturing such a SynRM is 6 percent lower than that of permanent magnet synchronous motors [15]. The speed controlled REEL SuPremE® synchronous reluctance motor is able to save up to 10% of energy [15].

The synchronous reluctance motors manufactured by REEL were used in various industry applications such as centrifugal separator for a production line, aerator pump for wastewater treatment tanks or generation of electrical energy from hydropower where it works as a generator. In case of centrifugal separator and aerator pump, the synchronous reluctance motor was used as a replacement for an induction motor. This allowed to obtain higher reliability due to a more accurate speed regulation, less maintenance on the motor bearings thanks to low rotor temperature and energy savings due to reduction of electricity consumption [15].

As one can see, SynRM is becoming a serious competition for induction and permanent magnet machines. With a proper design in certain applications synchronous reluctance machines can provide good efficiency, robustness and good control properties at reasonable cost.

This thesis presents research results on synchronous reluctance machine modeling as this type of electric machine is a major candidate for electric propulsion in vehicles.

The thesis is divided into five chapters.

CHAPTER 2 contains the general description and characteristics of electric vehicles. It also presents various electric machines commonly used in electric vehicles and applications of synchronous reluctance machine in industry.

CHAPTER 3 is focused on multiphysics and sensitivity analysis of SynRM, with the main goal of identifying the most suitable topology for EV propulsion system. Electromagnetic analysis and the analysis of different parameters' influence (number of stator slots, number of rotor poles and barriers, shape of the rotor barriers, etc…) on the machine performances are carried out. An optimal shape of the flux barriers is proposed. Rotor with flux barriers of optimized shape is presented

together with mathematical formulas necessary to obtain optimized flux barriers' shape. A special attention is given to the results of structural analysis, especially for high speed operation. Rotor stiffness increasing methods are proposed. General principles on choosing the flux barriers' shape and rotor topology are derived. Based on these research works, a 27 stator slots – 4 rotor poles and four flux barriers with bridges and ribs is chosen for further more comprehensive analysis and development. This chapter shows three modeling approaches of the machine: using winding function, magnetic equivalent circuit and finite element method. Electromagnetic performance of a synchronous reluctance machine with such barriers is compared with other machines with more common rotor topologies. Modal and vibroacoustic analysis are performed in order to evaluate the level of noise and vibration. A study on the impact of rotor topology on NVH behavior of the machine is presented as well as the relation between torque ripple and noise generation is described.

CHAPTER 4 describes modeling and simulation of final topology of synchronous reluctance machine. Final topology and the parameters of the SynRM are presented. Using electromagnetic finite element analysis, parameters of the machine such as: nominal torque, rated current, torque ripple and inductances are estimated. The workflow of design and analysis of SynRM for EV application is shown and the final topology and the parameters of the SynRM are presented. Impact of rotor skewing on performance of the machine is investigated. Modeling of rotor skew is studied and two machine models are compared: 2D with multi slice and 3D. Machine's flux linkage is calculated and the impact of magnetic saturation on the flux linkage is described. Cross saturation effect is also investigated.Next, structural analysis of the rotor is performed. Both 2D and 3D rotor models are considered when performing the structural tests. Influence of radial magnetic forces acting on the rotor is also included in structural analysis of the rotor. Modal analysis of the machine is presented and NVH analysis results are shown. Typical normal modes of the stator and its natural frequencies are presented. Vibration of the stator is presented for the machine with skewed and non-skewed rotor. Analysis of power losses of the machine is shown. Iron loss distribution in stator and rotor of SynRM is studied. Thermal analysis of the machine is performed using two MotorCAD and JMAG software. Model of cooling jacket provided by MotorCAD is investigated at different water flow rates. Next thermal model of the

machine in JMAG is described. The results of thermal analysis from MotorCAD and JMAG software are compared.

CHAPTER 5 presents laboratory tests of synchronous reluctance machine. Description of the test bench is provided. Measurements carried out at no-load and load condition are presented. Analysis of switching frequency impact on noise of the machine is presented. Investigation of vibration and acoustic signal spectrum and measurement of machine orders and natural frequencies are presented. In load condition, analysis of load, speed and current angle impact on vibration and acoustic noise of the machine is performed. Major factor deciding about noise and vibration of the machine is described. Electromagnetic tests are performed in load condition for different values of load, speed and current angles. Influence of current angle on machine's voltage is investigated. Dependency between phase current, current angle and torque generated by the machine is shown. Next validation of machine's models is performed by comparing simulation results with the results obtained from measurements. Comparison of machine's calculated and measured flux linkage is shown. Measured torque vs. current angle and power factor vs. current angle curves are compared with the calculated ones. Calculated and measured natural frequencies of the structure are compared. Cooling system of the machine is validated by measuring the temperature of the winding.

CHAPTER 6 contains thesis summary and conclusion. Results obtained in each chapter are discussed. Future work and personal contribution of the author is also described.

3. Synchronous Reluctance Machines: Multiphysics Design and Analysis

3.1. Introduction

Reluctance machines have plenty of advantages such as low cost, simple construction without the need of external excitation source which reduces power losses in the rotor. Development of power electronics allowed reluctance machines to be used as drives in many industry applications. For this reason they are of great interest nowadays [16]. At present time, reluctance motors have four basic types: rotor with salient poles, rotor with circumferential segments, rotor with magnetic barriers and rotor consisting of magnetically anisotropy laminations [17]. Each of these types has its advantages and disadvantages like efficiency, power factor, cost etc. SynRM is another type of variable reluctance machines, whose stator is built from cylindrical structure. The stator of SynRM is identical to that of an induction motor with only the rotor having salient poles [18]. The rotor requires no cage or field winding which makes it potentially less expensive than permanent magnet motor or an induction motor [19]. The reluctance rotors major types are the simple salient pole, the transversally and axially laminated rotor [20]. Conventional SynRMs have simple rotor construction but unfortunately this lowers their performance due to a low ratio between the inductances on the direct and quadrature axes. The rotors of axially laminated topology have a higher value of saliency ratio and performance but eddy current losses are large. Also proper distribution of magnetic and non-magnetic materials can improve machine's performance [21]. In practice, transversally laminated rotor construction is the optimal choice for industrial manufacturing [22], [20]. Moreover, the transverse-laminated rotor structure is capable of being skewed, therefore allowing to decrease the torque ripple. The transverse-laminated rotor requires for the iron segments in the rotor to be joined with each other by thin iron ribs, which become magnetically saturated by the stator MMF. These ribs enhance cross saturation [23]. Another important issue in synchronous reluctance machines design is iron losses which at high speed can become the major cause of power dissipation. This is why many design techniques are used to minimize iron losses of SynRMs at high speeds [24]. The saliency can also be achieved with special flux barriers in the rotor [25], [16]. Rotor with internal flux barriers can achieve larger

effective saliency values. The optimization of rotor design which relies on optimization of two significant factors such as (L_d-L_q) called "motor torque index" and saliency ratio L_d/L_q is studied in [19]. To increase the L_d/L_q ratio, which increases torque produced by the machine and in general increases its performance, permanent magnets in the rotor are mounted [25]. The rotors of permanent magnet machines can be of two types: surface mounted and interior permanent magnets.

Design process of electrical machines requires a combination of multi-physical phenomena simulation including electromagnetism, mechanics, thermodynamics, structural dynamics, vibration, noise, and fatigue [26]. The functioning of the machine rises from the combination of electromagnetic and mechanical phenomena. Since reluctance machines are gaining popularity nowadays, their design process must be efficient and fast to cover the rising demand. Application in electric vehicles is very popular and the machine must be designed to cover different aspects and meet restrictive limitations. High power density, high efficiency and high torque at relatively low dimensions of the machine are crucial. Downsizing is very popular now and it allows saving space needed for electric drive in vehicles however it leads to heat dissipation problems. In this case, coupled analyses are often run to investigate thermal parameters of the machine or any other electric equipment. Such an analysis was performed in [27]. In order to estimate transformer's thermal parameters, the authors performed electromagnetic analysis and power loss calculation. This allowed them to obtain temperature distribution in a transformer. Obtaining temperature distribution of a linear motor with multiphysics analysis was described in [28]. Thermal analysis of electric machines is of big interest nowadays. Various methods and techniques are being in use and their combination gives a powerful tool in estimating temperature of an operating machine. In [29] the authors present an extended survey on evolution of thermal analysis of electric machines. Lumped parameter network thermal analysis, FEM based thermal analysis, and computational fluid dynamics are considered in their work. Additionally, an overview of the issues linked to the thermal parameters estimation is also investigated. Lumped parameters thermal network along with finite element method application in electric machines' analysis is described in [30]. Thermal network was also used along with structural analysis in optimization process of a switching machine [31] and [32]. Various methods for thermal design of a high-speed permanent magnet machine are

presented in [33]. The first implemented method combines computational fluid dynamics and heat-transfer equations with the geometry of the machine to be considered as 2D axi-symmetrix. This approach gives simultaneous solutions for the turbulent properties of the cooling fluid. The second method allows for estimating the temperature distribution in the machine with a 3D numerical heat-transfer. 3D finite element thermal analysis is presented in [34] where authors presented a 3D numerical analysis of the thermal behavior of a small permanent magnet DC motor. Coupled electromagnetic and thermal analysis was run to estimate the air-gap torque of an induction machine in [35]. Machine's cooling system is a very important issue which needs to be addressed when designing a machine. Since the overloading of the machine is limited by the maximum temperature in the electric motor, cooling system can increase the maximum power of the motor. Although a cooling jacket construction is of a great importance in lowering the motor's maximum temperature, there has not been as a lot of research in the thermal analysis of motors [36]. The author of [36] performed a three-dimensional steady state numerical method to examine the cooling jacket performance with water as the primary coolant of a three-phase induction motor. Multiphysics analysis of electric machines was investigated in [37] where the authors used separate lumped parameter models to analyze the electromagnetic and thermal behavior of the machine. The vibroacoustic and mechanical behavior was investigated with analytical approach. Structural and vibroacoustic behavior of the machine is another aspect of multiphysics design of electric motors. The SynRM is often forced to operate at very high rotational speeds. This causes high stress in the material which might damage the rotor. Moreover, high rotational speeds combined with magnetic field harmonics might cause the structure to vibrate at a resonance frequency. These phenomena should be minimized and for that reason the ability to predict vibroacoustic behavior of the machine is crucial during design process. For the machine's noise to be estimated, one needs to know the noise sources. In [38] the author presents magnetic vibration sources in induction motors and motor structure dynamic response. The vibration behavior of the machine caused by electromagnetic forces is simulated using finite element structural analysis. Relation between machine's geometry and generated noise was investigated in [39]. It was proved that the noise is caused by radial forces and there is hardly a relation between torque ripple and noise generated by the machine. Estimation of machine's noise using 2D

electromagnetic finite element model and boundary element method for sound pressure calculation was presented in [40]. The machine analyzed in [40] was used in an electric vehicle. Another multiphysics analysis of a machine for automotive application was shown in [41] where authors presented a complete approach to the noise generated by machine's stator.

3.2. SynRM General Issues

Depending on the application, machine's topology might vary. Machines with higher number of poles generate higher torque but may not be applied in high speed applications. Rotor constructions which give very good magnetic performance, might not have enough mechanical strength to withstand high mechanical loads [18].

Interest in SynRM for variable speed applications was very high in 1960s. Back in those days the machine was operated in open loop fashion where the inverter output voltage and the frequency were set independently of the rotor speed and position.

In that case the rotor of the machine could follow synchronously for low load torques and slew rates. This determined the machine to operate at low power factor and lower efficiency than a comparable induction machine since the achieved saliency ratio was very small. In 1960s, the rotor construction was made of a transversally placed lamination with some punching oriented so as to create a saliency effect as shown in Fig. 3.1. In [42] the author stated that the inferiority of the synchronous reluctance motor is due to its rotor's construction.

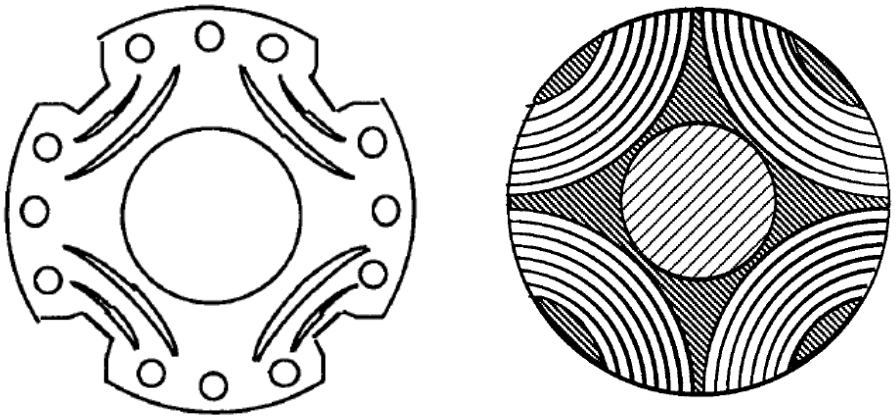

Fig. 3.1 Laminated Type Rotor Punching (left),
Axially Laminated Rotor Structure (right) [18]

Due to the need of structural integrity, the rotor needed the bridges which made this rotor capable of achieving the saliency ratio of two or three. Rotor with axially aligned magnetic laminations has also quite long history. In this rotor topology, the laminations are bent in such a way that they produce the minimum reluctance paths in direction of laminations and maximum reluctance paths in direction normal to laminations. Machine with this type of rotor can achieve much higher saliency ratio. This in turn significantly increased the efficiency and power factor of the machine. However, the manufacturing process of the rotor with axially placed laminations is more complicated and expensive thus transversally laminated rotor design is the best choice for industrial manufacturing [22].

Unlike the SRM, synchronous reluctance machine's stator is constructed from cylindrical structure just like the one of induction machine. This allows to significantly reduce the production costs since the stator of the SynRM can be manufactured on the same assembly line as that of the induction motor. Moreover, torque ripple and acoustic noise which are common problems in SRMs can be eliminated in synchronous reluctance machines. The rotor requires no cage or field winding which makes it potentially less expensive than permanent magnet machine. Moreover, lack of field winding reduces power losses in the rotor.

Design of transversally laminated rotor synchronous machine and optimization of this process has been intensively studied lately and in the literature one can find various papers which address this topic. Many

research studies were devoted to optimize the structure of SynRM with special attention put on rotor's construction as the stator is usually used from standard induction machine. The main parameters used in optimization algorithms are torque mean value and torque ripple. In [43] and [44] the authors optimize two different rotor's structures of SynRM. The topologies are compared by means of 2D finite element analysis. The authors focused on finding the relation between the amount of rotor's barriers and the amount of stator slots. The study proved that the number of flux barriers has a higher impact on electromagnetic behavior of the machine rather that the shape of flux barriers. According to the authors, four flux barriers seems to be the optimal choice for SynRM rotor topology. The geometry of the flux barriers in the rotor are based on general design recommendations. With a given amount of flux barriers, one can influence the performance of the machine by choosing flux barriers' position and shape. The issue of finding the best positions of flux barriers was addressed in [45]. The authors developed a simplified analytical model of SynRM with flux barriers. The assumptions made during developing of this model allowed to focus on the main cause of torque ripple. The authors investigate different flux barriers' shapes with various angular positions of flux barriers' ends. Each configuration experienced different torque ripple. By choosing different angular positions of flux barriers' ends, it was possible to reduce the torque higher harmonics. Although research on SynRM rotor's topology optimization is quite popular, the machine's performance depends not only on the topology of the rotor but on the relation between stator and rotor structure. This issue is addressed in [46] where the authors investigate the combination of the number of stator slots and rotor flux barriers in order to achieve the optimum design of a SynRM. The authors used multi-objective optimization algorithm and finite element analysis in order to maximize the torque and minimize the torque ripple. The comparative study performed by the authors involved eighteen different combinations of stator slots and flux barriers numbers. The authors proved that the optimal combination of slots and flux barriers numbers depends on the application and the torque ripple minimization does not necessarily involve lower power losses. Another study on finding the optimum SynRM's topology is presented in [47]. In this paper, the authors investigated two different rotor topologies and three stators with different slot numbers. The comparison was based on SynRM's torque mean value, torque ripple and saliency ratio. The rotor topologies had each four flux barriers per pole with different flux barriers' shapes.

It was proven that machine with fractional winding experiences the lowest torque ripple. Moreover, the torque ripple was lower for the machine with optimized flux barriers in the rotor. Minimization of torque ripple in SynRM is also investigated in [48]. The authors proposed a transversally laminated rotor with sinusoidal lamination shape in the axial direction. This allowed to cancel some torque harmonics produced by the slotting effect. Due to the non-uniform geometry of the rotor in the axial direction, a 3D finite element analysis was used. With the optimized flux barrier geometry, the authors were able to achieve the torque ripple lower than 10%. Another approach was proposed in [49] and [50] where the authors investigated a SynRM with six stator slots and non-overlapping fractional slot-concentrated winding. That topology of SynRM proved to be robust and low cost with high torque density and high efficiency. However, torque quality of the machine is affected by parasitic rotor saliencies and air-gap field harmonics. In [51] the authors compare two SynRM topologies with two different windings while keeping the same rotor topology. The investigated winding types were: full pitch distributed winding and integer slot concentrated winding. Using concentrated winding brings some challenges during design such as obtaining high winding factor and keeping space harmonics low. Performed analyses proved that machine with distributed winding has an overall higher efficiency and performance compared to the machine with concentrated winding. SynRM with concentrated winding tends to have a higher MMF harmonic content compared to the SynRM with distributed winding.

Since the rotor of a SynRM is crucial in achieving high torque and low torque ripple, many different rotor topologies are studied and compared. In [52] the authors compare SynRM topologies with two different rotors: transversally and axially laminated. Comparison is done using finite element analysis and the compared parameters are torque and torque ripple. Machine with axially laminated rotor can provide a very high saliency ratio compared to the one with transversally laminated rotor. However axially laminated rotor has some drawback from mechanical point of view. Moreover, in machine with transversally laminated rotor, the performance can be improved with a proper number of flux barriers, their shape and positions. SynRM with axially laminated rotor can generate a higher maximum torque that a machine with transversally laminated rotor. Torque ripple is also lower for the motor with axially laminated rotor. Design of a machine nowadays is often performed using

various optimization algorithms and methodologies. Three conventional methods of SynRM design process are described in [53]. The first investigated method is based on combination of finite element analysis with optimization algorithm. In this way one can obtain optimal design but at high computational cost. Another option is to use analytical methods which are faster than FEM but less accurate. The last method is to put constraints on parameters. By doing this, one refines the parameter relationship and lowers computational time due to reduced number of parameters. Another methodology of designing a synchronous reluctance machine's rotor using 2D numerical analysis is presented in [54]. The authors parameterize the rotor in function of certain design variables defining the arrangement of flux barriers. The methodology is based on systematically changing the design variables. The authors of [55] presented another approach of finding optimum design of a SynRM. In their work they used response surface methodology in order to determine the design parameters to reduce torque ripple.

Maximum generated torque and torque ripple are the main input parameters for optimization algorithms during machine design. Although the machines designed in this way with optimized rotor geometry present very good electromagnetic properties, from mechanical point of view the construction has many drawbacks. Rotor construction optimized to achieve the highest torque density usually has very thin bridges and no ribs in order to maximize the saliency ratio. That construction cannot operate at high rotational speeds due to very high stress in the weakest parts of the rotor such as bridges. For machines operating at very high rotational speeds, rotor diameter should be small in order to minimize the centrifugal force acting on rotor parts. There are of course some limitations in lowering the diameter of the rotor since the generated torque decreases. For high speed application, rotor's construction must be properly modified as shown in [56] where the authors modified the geometry of the rotor by introducing additional ribs in flux barriers. Similar approach was proposed in [57]. By introducing ribs in flux barriers of the rotor, one can decrease von Mises stress occurring in the rotor. Modification of rotor topology however resulted in decreased electromagnetic performance of the machine as the additional ribs in flux barriers decreased saliency ratio of the machine thus the generated torque was lower. Such a modification of rotor's geometry was necessary in order for the machine to be able to

operate at high speeds. Another approach of rotor's optimization for high speed application was investigated in [20]. The author proposed a different shape of flux barriers. This allowed the machine to operate at high rotational speeds.

As one can see, optimization of machine's geometry from electromagnetic performance point of view might result in obtaining a machine topology unable to operate at high rotational speeds. For the best electromagnetic performance, the bridges in the rotor should be very thin and there should be no ribs as they decrease the saliency ratio. This however is necessary for the rotor to be able to withstand high von Mises stress occurring during operating at high speeds. One can see that designing rotor's topology is a trade-off between electromagnetic performance of the machine and structural integrity of the rotor. A complete study on design aspects concerning magnetic and mechanical performance along with determining the maximum rotational speed and rotor robustness investigation is presented in [58].

3.2.1. Machine's Inductances

In SynRM, the torque generation is based on anisotropy of machine's magnetic circuit and depends on the $\frac{L_d}{L_q}$ ratio where L_d and L_q are the SynRM's inductances in direct and quadrature (d and q) axis respectively. It can be noticed that increasing L_d and decreasing L_q the ratio increases and making the torque generated by the machine higher. The anisotropy is achieved by introducing flux barriers in the rotor. By choosing the right amount of flux barriers, their shapes and distribution one can find optimal $\frac{L_d}{L_q}$ ratio. Inductances L_d and L_q have an impact on machine's power factor. Not only increasing their ratio is crucial but also making the difference $L_d - L_q$ large is essential in obtaining high torque density and high power factor [59]. The power factor of the machine is defined as [16]:

$$\cos\varphi = \frac{\xi - 1}{\sqrt{\xi^2 \frac{1}{\sin^2\gamma} + \frac{1}{\cos^2\gamma}}} \qquad (3.1.1)$$

in which $\xi = \frac{L_d}{L_q}$ is the saliency ratio and γ is the current angle.

The maximum power factor is of the form [16]:

$$\cos\varphi_{max} = \frac{\xi - 1}{\xi + 1} \tag{3.1.2}$$

The current angle γ is shown in SynRM phasor diagram in Fig. 3.2.

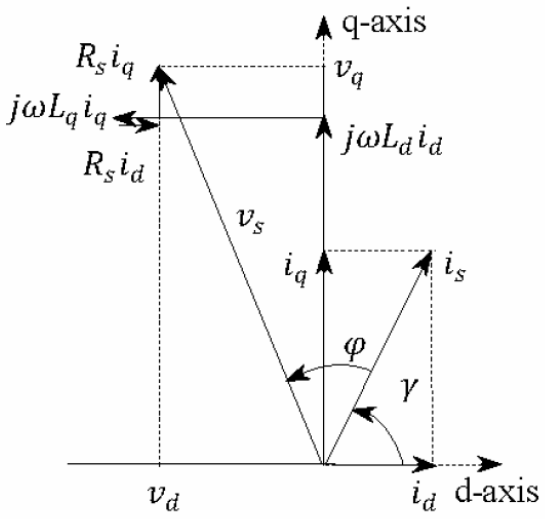

Fig. 3.2 SynRM phasor diagram [16]

Performance of a SynRM mainly relies on these two inductances which are affected by the rotor topology [60]. Moreover, the inductances of the SynRM with transversally laminated rotor vary with both d-q currents, due to common flux path in the rotor core. The position of the rotor with respect to the stator has also an impact on the SynRM inductances [60]. When creating simple models of synchronous machines it is common to assume that inductances L_d and L_q depend only on self-currents. This however is not true since the inductances depend on both currents I_d and I_q and this dependency is called cross-saturation. The inductances also decrease as the magnetic circuit of the machine saturates. The effect of magnetic saturation in SynRM was investigated in [60]. The authors proved that d-axis flux linkage varies linearly with I_d current for small

values of d-axis current. As the I_d current increases, flux linkage becomes saturated thus reducing L_d inductance. Moreover the variation of q-axis flux linkage has a significant influence on the SynRM performance [60]. Since the inductances have a great impact on machine's electromagnetic properties, a lot of effort is put to increase saliency ratio. In [61] the authors investigated the influence of different electrical steel grades on the performance of a synchronous reluctance machine. The L_d and L_q inductances are affected by the steel properties due to different permeabilities. Rotor's geometry has an impact on the d-q inductances as the flux barriers in the rotor affect the flux path between the stator and the rotor. The authors of [21] proved that the saliency ratio depends on the position or span of the flux barriers. Additionally, the axially laminated rotor might not be the optimum topology due to large number of flux guides. Improved performance can be obtained by proper distribution of flux barriers and flux paths. The authors of [62] investigated the impact of rotor shape on L_d and L_q inductances. Moreover, they proposed an open rib topology of the rotor so as to achieve a greater value of saliency ratio. The d-q axis inductances of the machine and thus the saliency ratio and power factor are heavily affected by stator's leakage inductance as shown in [63].

3.2.2. Flux Barriers

Various techniques of optimization of rotor topology with internal flux barriers have been investigated to increase machine's performance. Optimal shape of flux barriers should follow the shape of natural flux lines in solid rotor as shown in Fig. 3.3. Three types of flux barriers are shown in Fig. 3.4.

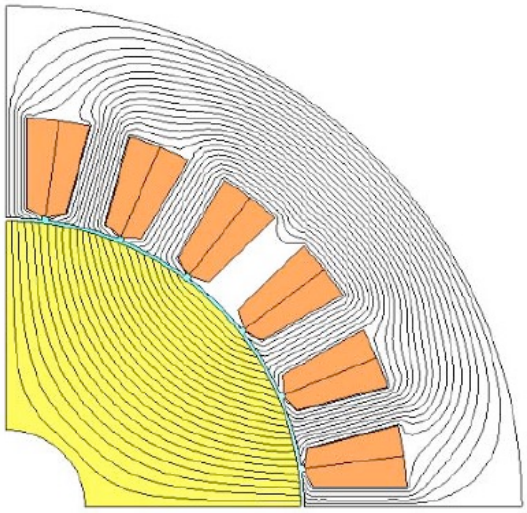

Fig. 3.3 Flux lines in the solid block rotor machine

Fig. 3.4 Three types of flux barriers: rectangular, round and based on Zhukovski's curves

Optimized shape of flux barrier can be obtained from conformal mapping using function defined as [64]:

$$g(z) = \left(z + \frac{w}{z}\right)^2 = z^2 + 2w + \frac{w^2}{z^2} \qquad (3.1.2)$$

which is derived from Zhukovski's function [64]:

$$f(z) = \frac{z + \frac{w}{z}}{2} \qquad (3.1.3)$$

In this equation, z is a complex number and w is a positive number [64]. Given that $z = x + iy$ where x and y are real numbers and $i^2 = -1$, imaginary part of function $g(z)$ is of the form:

$$Im\{g(z)\} = 2xy - \frac{2xyw^2}{x^2 + y^2} \qquad (3.1.4)$$

Desired curve is characterized by the equation:

$$2xy - \frac{2xyw^2}{x^2 + y^2} = v \qquad (3.1.5)$$

By varying the values of parameters w and v, it is possible to obtain the whole family of curves. Analytical solution of equation (3.1.5) is difficult since one has to deal with implicit function, however Zhukovski's curves can be defined with parametric equations.

$$\frac{y}{x} = tan(\alpha) \qquad (3.1.6)$$

$$x^2 + y^2 = r_d(\alpha, w, v) \qquad (3.1.7)$$

Taking into account equations (3.1.6) and (3.1.7) and applying them in equation (3.1.5), it is possible to obtain parametric equations of Zhukvski's curves as presented below.

$$\begin{cases} x = r_d(\alpha, w, v)\,\mathrm{COS}(\alpha) \\ y = r_d(\alpha, w, v)\,\mathrm{SIN}(\alpha) \end{cases} \qquad (3.1.8)$$

$$r_d(\alpha, w, v) = \sqrt{\frac{w^2 \sin(2\alpha) + v}{\sin(2\alpha)}} \qquad (3.1.9)$$

Equation (3.1.9) defines "radius" of varying length which depends on the angle α and two parameters of the curve w and v as shown in Fig. 3.5. Using this equation, one can create optimized geometry of flux barriers shown in Fig. 3.4.

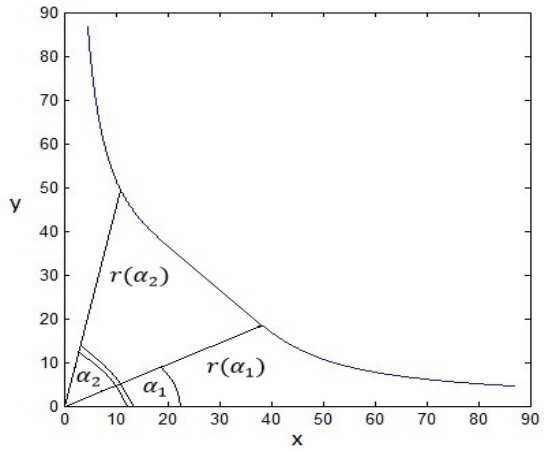

Fig. 3.5 Example curve with two various "radii" for different angles α

Example of rotor topologies presented above belong to four pole synchronous reluctance machines. SynRM however can have any number of poles. For rotor topologies with higher number of poles, rectangular flux barriers are very easily obtained. The shape of round barriers changes to elliptic. However, to obtain the shape of flux barriers constructed from Zhukovski's curves in case of greater number of poles, one needs to introduce a modification into equation (3.1.9). In general, for machine with p pole pairs, the equation (3.1.9) is of the form:

$$r_d(\alpha, w, v) = \sqrt{\frac{w^2 \sin(p\alpha) + v}{\sin(p\alpha)}} \qquad (3.1.10)$$

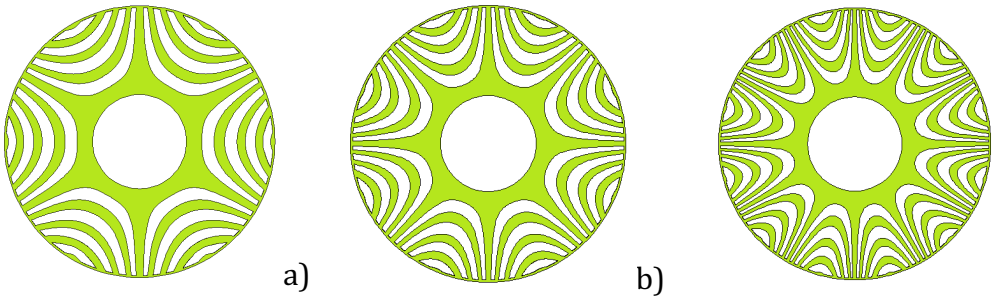

Fig. 3.6 Example rotors with Zhukovski's flux barriers: a) 6 poles, b) 8 poles, c) 12 poles

Example rotor topologies with higher number of poles are presented in Fig. 3.6.
The optimized flux barriers provide a better air-gap magnetic field distribution compared to other flux barriers shapes as shown in [64].

3.3. Electromagnetic Analysis of SynRM

In order to calculate machine's electromagnetic parameters, it is compulsory to create a proper magnetic model of the machine. Finite element (FE) method is the most popular and the most powerful tool in electric machines analysis. This method however requires specialized software and quite high computational power depending on the accuracy of the model. It is also time consuming. During the process of machine design, it is convenient to have a simplified machine model which allows to quickly estimate the parameters of the machine. Linear models of electric machines based on winding function are very popular and have been widely used. Their advantage is that no specialized FEM software is needed. However, in winding function (WF) method, the presence of iron core is neglected and only air gap magnetic field is taken into account. Despite this simplifying assumption, WF method has been popular in analysis of induction motor and synchronous machine with wound rotor. Especially monoharmonic models based on base harmonic are very helpful in estimating machine's performance. Polyharmonic models use

Fourier series to approximate air gap magnetic field. These models have been very useful in diagnostics since they allow predicting current harmonics typical for certain type of fault i.e. broken bar in cage induction motor or rotor eccentricity. Since WF model does not include the iron, the saturation is not taken into account. This might be a problem when analyzing a highly saturated machine. Taking into account the magnetic field in iron is therefore necessary. Using magnetic equivalent circuit (MEC) method, allows for including saturation of the machine. Power losses in iron and magnets can be simply estimated using magnetic equivalent circuit as shown in [65]. Since FE analysis requires a significant amount of time, at the beginning of design process, reduced order models of the machines are very helpful. Such a model was investigated in [66]. It was proven that simplified model can provide acceptable accuracy during design and performance evaluation process. Reluctance network proves to be convenient and relatively easy method of electric machines performance analysis. MEC method can be also used in magnetic circuits with eddy currents [67]. Magnetic reluctance calculation methods for various parts of the machine are described in the literature. In [68], the mathematical formulas for reluctances calculation of basic shape elements are presented.

3.3.1. FEM Modeling

Accurate machine's model can be built using Finite Element Method (FEM). Since the software computational power nowadays is very high, the complexity of created models can be also increased. FEM model of the machine is based on Maxwell's equations which yield magnetic and electric fields behavior.

Majority of magnetic field problems can be solved using 2D models. Two dimensional models are popular when analyzing electric machines since the most important phenomena can be taken into account at a significant reduction of computational time.

Solving large FEM equations can involve various developed methods such as Gaussian elimination, triangular factorization or the in-complete Cholesky-conjugate gradient (ICCG) algorithm. ICCG algorithm is fast and requires small storage resources. When dealing with non-linear problems, Newton-Raphson method is often used [69]. In 2D analysis the

end-effects are neglected and the vector potential contains only axial component. The magnetic field is present in planes normal to the machine's axis. For magnetostatic model with no eddy currents induced, the magnetic field can be calculated by solving [69]:

$$\frac{\partial}{\partial x}\left(\frac{1}{\mu}\frac{\partial A}{\partial x}\right)+\frac{\partial}{\partial y}\left(\frac{1}{\mu}\frac{\partial A}{\partial y}\right)=-J \qquad (3.2.1)$$

In the equation above, A is magnetic vector potential, μ is magnetic permeability and J is current density. When eddy currents are considered, the equation (3.2.1) is of the form:

$$\frac{\partial}{\partial x}\left(\frac{1}{\mu}\frac{\partial A}{\partial x}\right)+\frac{\partial}{\partial y}\left(\frac{1}{\mu}\frac{\partial A}{\partial y}\right)=-J+\sigma\frac{\partial A}{\partial t} \qquad (3.2.2)$$

where σ is the material conductivity. The relation between magnetic vector potential and magnetic flux density vector is shown below:

$$\vec{B}=curl(\vec{A}) \qquad (3.2.3)$$

When preparing a simulation, a lot of work lies in constructing the finite element mesh. There are various mesh generation algorithms which can be found in the literature [70]. The effectiveness of a mesh generation method depends on the geometry of the analyzed structure. Fine mesh with large number of elements can precisely model complicated geometry but this significantly increases computational time. One needs to find a compromise between calculation accuracy and computational time. Figure below presents a geometry of one pole of synchronous reluctance machine with optimized flux barriers and bridges in the rotor. Such a complex structure of the rotor results in large number of finite elements in order for the geometry to be modeled.

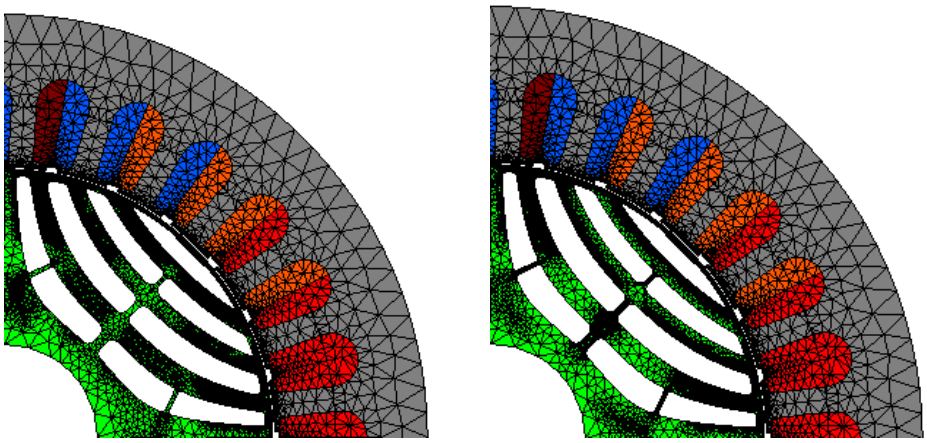

Fig. 3.7 Mesh of a SynRM: fine mesh (left) and reduced rotor mesh (right)

In Fig. 3.7. one can see a comparison of mesh used for the analysis of a SynRM. Since the geometry of the rotor of analyzed SynRM structure is quite complex, the mesh generated in this region is fine with a large number of small elements. Rotor flux barriers were drawn with a lot of points in order to obtain good accuracy and smooth edges. This however resulted in generating a lot of finite elements in order to model such accurate curves. When the number of points constituting the curves was reduced, the number of finite elements in rotor's mesh decreased. This allowed to accelerate the computations. Reducing the accuracy of the geometry results in faster computational by the accuracy of the results might decrease. For this reason, the simplification of the geometry and reduction of finite elements of the mesh must be done with care.

In this work, the simulation of the final topology of the machine is done using finite element method. The obtained results are shown in the following chapters.

3.3.2. Winding Function Method

SynRM has similar construction to typical synchronous motors (with permanent magnets or field winding in the rotor). Sinusoidal winding distributed in stator slots is supplied from a three phase voltage source.

Electric machines modeling based on WF leads to far reaching assumptions such as:

- Flux crosses the air gap radially (axial flux is negligible);
- Saturation is neglected;
- Eddy current, friction and windage losses are neglected;
- The magnetic permeance of the magnetic material is infinite.

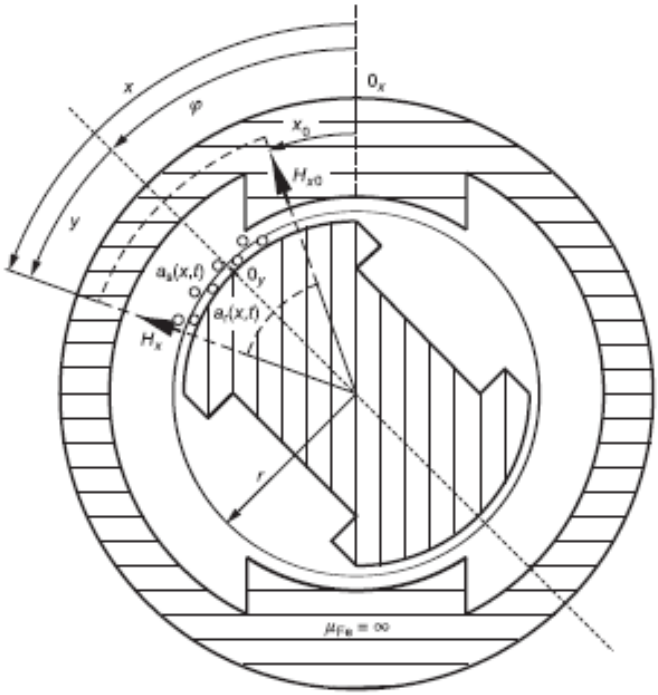

Fig. 3.8 Illustration of salient pole stator and rotor and integration path [71]

Since the permeance of the iron core is considered to be infinite, the analysis of the electric machine is narrowed to analysis of the air gap

magnetic field and more precisely, only its radial component. Using Ampere's law for the contour shown in Fig. 3.8 leads to:

$$\int_{x} \overrightarrow{Hdl} - \int_{x_0} \overrightarrow{Hdl} = \int_{x_0}^{x} [a_s(x,t) - a_r(x+\varphi,t)]dx \tag{3.2.4}$$

In equation 3.2.4 functions $a_s(x,t)$ and $a_r(x+\varphi,t)$ (for stator and rotor respectively) are defined as:

$$a_s(x,t) = w_s(x)i_s(t)$$

$$a_r(x-\varphi,t) = w_r(x-\varphi)i_r(t) \tag{3.2.5}$$

where $w(x)$ is the turns function and represents the number of turns of the winding enclosed by path of integration. Turns carrying current into the page are considered positive and those carrying current out of the page are considered negative as presented in Fig. 3.9.

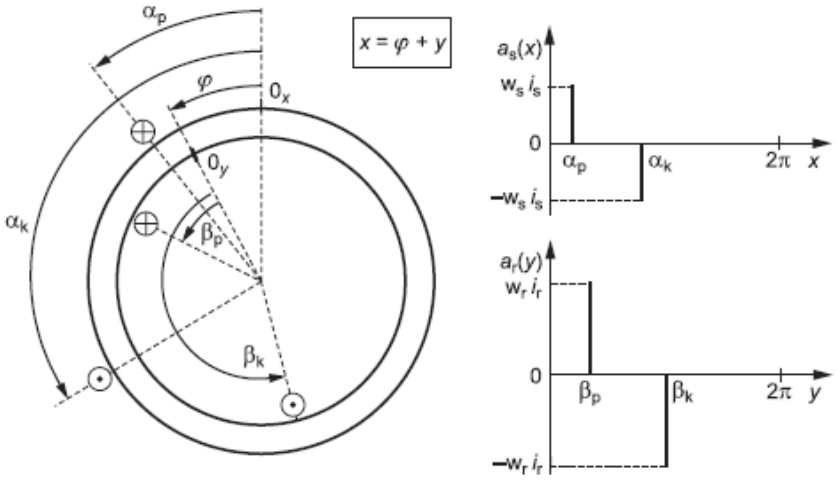

Fig. 3.9 Illustration of turns function [71]

The left part of equation (3.2.4) is equal to the average value of magnetic field strength in the air gap along the radius multiplied by air gap length. The function of air gap length denoted as $\delta(x,\varphi)$ depends on two variables: angular position x related to stator coordinates and rotation angle φ of the rotor. Equation (3.2.4) can be written as:

$$H(x,\varphi,t)\delta(x,\varphi) - H(x_0,\varphi,t)\delta(x_0,\varphi) = \theta_t(x,\varphi,t) - \theta_t(x_0,\varphi,t) \tag{3.2.6}$$

where function θ_t is defined as:

$$\theta(x,t) \stackrel{\text{def}}{=} \int a(x,t)dx \tag{3.2.7}$$

and satisfies the condition:

$$\int_{x}^{x+2\pi} \theta(x,t)dx \equiv 0 \tag{3.2.8}$$

Magnetic field strength in the air gap for a specified angular position is defined as:

$$\begin{aligned} H(x,\varphi,t) = \frac{1}{\delta(x,\varphi)}\big(&\theta_t(x,\varphi,t) - \theta_t(x_0,\varphi,t) \\ &+ H(x_0,\varphi,t)\delta(x_0,\varphi)\big) \end{aligned} \tag{3.2.9}$$

Air gap magnetic flux density can be calculated from:

$$B(x,\varphi,t) = \mu_0 H(x,\varphi,t) \tag{3.2.10}$$

$$\oint_S \vec{B}d\vec{S} = 0 \tag{3.2.11}$$

Considering equations (3.2.9), (3.2.10) and Gauss' law for magnetism defined by equation (3.2.11), the air gap magnetic flux density is defined as:

$$B(x,\varphi,t) = \mu_0 \lambda(x,\varphi)\left(\theta_t(x,\varphi,t) - \frac{\int_x^{x+2\pi} \lambda(x,\varphi)\theta_t(x,\varphi,t)dx}{\int_x^{x+2\pi} \lambda(x,\varphi)dx}\right) \quad (3.2.12)$$

In equation above $\lambda(x,\varphi)$ is called the permeance function and it is equal to reciprocal of air gap length function$\delta(x,\varphi)$. When in equation (3.2.12) the term $\int_x^{x+2\pi} \lambda(x,\varphi)\theta_t(x,\varphi,t)dx$ equals zero (which is true for rotating machines due to symmetrical construction) then the air gap magnetic flux density can be simply calculated from $B(x,\varphi,t) = \mu_0\lambda(x,\varphi)\theta_t(x,\varphi,t)$. The permeance function is constant for machines with uniform air gap (when neglecting stator slots). However, for salient pole synchronous machines, the air gap length changes along rotor's circumference. The smallest air gap is over rotor's pole (d axis) and the largest is between rotor poles (q axis). The air gap permeance is thus a quite complicated function and cannot be described analytically hence it is approximated by Fourier series [72].

$$\lambda(x) = \frac{\lambda_0}{2} + \sum_n \lambda_{2n} \cos(2nx) \quad (3.2.13)$$

The permeance function of the air gap in a synchronous machine with salient poles for a specified rotor angular position φ is given by equation (3.2.13). The Fourier series has only even spatial harmonics [72]. Limiting the series to only two terms allows to obtain quite accurate distribution of the magnetic flux density in the air gap.

$$\lambda(x) \approx \frac{\lambda_0}{2} + \lambda_2 \cos(2x) \quad (3.2.14)$$

The inductances of the machine can be obtained from the winding flux linkage. Flux linkage between n^{th} and k^{th} elementary coil of the winding can be calculated using equation below.

$$\Psi_{n,k} = rl \sum_{m=1}^{M} w_m \int_{\alpha_{s,m}}^{\alpha_{e,m}} B_k(x, \varphi, t) dx \tag{3.2.15}$$

Using equations (3.2.12) (3.2.14) and (3.2.15), simplified equations of a three phase salient pole synchronous machine with field winding in the rotor can be obtained.

$$\begin{bmatrix} u_a(t) \\ u_b(t) \\ u_c(t) \\ u_f(t) \end{bmatrix} = \begin{bmatrix} R_a & 0 & 0 & 0 \\ 0 & R_b & 0 & 0 \\ 0 & 0 & R_C & 0 \\ 0 & 0 & 0 & R_f \end{bmatrix} \begin{bmatrix} i_a(t) \\ i_b(t) \\ i_c(t) \\ i_f(t) \end{bmatrix} + \frac{d}{dt} \begin{bmatrix} L(\varphi) & M(\varphi) & M(\varphi) & M_{sf}(\varphi) \\ M(\varphi) & L(\varphi) & M(\varphi) & M_{sf}(\varphi) \\ M(\varphi) & M(\varphi) & L(\varphi) & M_{sf}(\varphi) \\ M_{sf}(\varphi) & M_{sf}(\varphi) & M_{sf}(\varphi) & L_f \end{bmatrix} \begin{bmatrix} i_a(t) \\ i_b(t) \\ i_c(t) \\ i_f(t) \end{bmatrix} \tag{3.2.16}$$

Applying Park transformation to the equations of the machine the simplified d-q model of the synchronous machine can be obtained. The Park transformation matrix is defined below.

$$T_{Park} = \sqrt{\frac{2}{3}} \begin{bmatrix} \frac{1}{\sqrt{2}} & \frac{1}{\sqrt{2}} & \frac{1}{\sqrt{2}} \\ \cos(p\varphi) & \cos\left(p\varphi - \frac{2\pi}{3}\right) & \cos\left(p\varphi - \frac{4\pi}{3}\right) \\ -\sin(p\varphi) & -\sin\left(p\varphi - \frac{2\pi}{3}\right) & -\sin\left(p\varphi - \frac{4\pi}{3}\right) \end{bmatrix} \tag{3.2.17}$$

Simplified equations of synchronous machine in d-q coordinates allow to analyze the machine as two separate equivalent circuits with constant parameters. These equations are given as:

$$\begin{bmatrix} u_0(t) \\ u_d(t) \\ u_q(t) \\ u_f(t) \end{bmatrix} = \begin{bmatrix} R_0 & 0 & 0 & 0 \\ 0 & R_d & 0 & 0 \\ 0 & 0 & R_q & 0 \\ 0 & 0 & 0 & R_f \end{bmatrix} \begin{bmatrix} i_0(t) \\ i_d(t) \\ i_q(t) \\ i_f(t) \end{bmatrix} + \begin{bmatrix} L_{\sigma s} & 0 & 0 & 0 \\ 0 & L_d & 0 & \sqrt{\frac{3}{2}}M \\ 0 & 0 & L_q & 0 \\ 0 & \sqrt{\frac{3}{2}}M & 0 & L_f \end{bmatrix} \frac{d}{dt} \begin{bmatrix} i_0(t) \\ i_d(t) \\ i_q(t) \\ i_f(t) \end{bmatrix} + \frac{d\varphi_e}{dt} \begin{bmatrix} 0 & 0 & 0 & 0 \\ 0 & 0 & -L_q & 0 \\ 0 & L_d & 0 & \sqrt{\frac{3}{2}}M \\ 0 & 0 & 0 & 0 \end{bmatrix} \begin{bmatrix} i_0(t) \\ i_d(t) \\ i_q(t) \\ i_f(t) \end{bmatrix} \quad (3.2.18)$$

Electromagnetic torque generated by the machine results as:

$$T_e = \frac{3}{2} p(\Psi_d i_q - \Psi_q i_d) \quad (3.2.19)$$

This model is often used in control systems since it takes into account only the basic phenomena occurring in the machine. Due to its simplicity it is possible to apply those equations in real time control systems. However, depending on the machine and its operation regime, the model with constant parameters might not be enough, especially when the machine operates at high saturation. In this case it is possible to increase the complexity of the model in order to include more phenomena. The inductances in d and q axes can be functions of phase current or rotor position. Magnetic circuit saturation can be taken into account by using various coefficients available in the literature. The inductances can be also calculated using other methods such as magnetic equivalent circuit or finite element method. This process will be described in the following chapters.

Calculation of d and q axis flux linkages and air gap magnetic field of synchronous reluctance machine can be done analytically. Magnetomotive force generated by stator winding can be calculated using winding function. Air gap permeance function of SynRM with flux barriers however cannot be described by Fourier series from equation (3.2.13) since this Fourier series approximates well air gap permeance function of a classical salient pole synchronous machine. In synchronous reluctance machine with flux barriers in the rotor, the air gap is uniform however the flux barriers which introduce the saliency of the magnetic circuit, affect the path of magnetic flux lines. As it is shown in the next chapters, the flux lines almost completely avoid flux barriers when the MMF is applied in d axis and cross the flux barriers perpendicularly when stator MMF is applied in q axis. For any stator magnetomotive force applied between d and q axis, the flux lines cross the flux barriers at various angles. This makes the analytical description of air gap permeance very troublesome. Following the assumptions when using winding function, magnetic field in the iron is neglected and only the magnetic field in the air gap is considered. For the synchronous reluctance machine, only the magnetic field in the air gap and in the flux barriers is taken into account. When calculating the air gap field distribution for q axis MMF, it is assumed that the flux lines are orthogonal to the geometrical lines of the flux barriers. For d axis MMF, the flux is assumed to flow through flux paths in the rotor and is parallel to flux barriers. Considering very high permeability of the iron, only magnetic voltage drops in the air gap and flux barriers is considered. In this manner, the air gap profile for d axis MMF shown in Fig. 3.10. was calculated. As one can see in Fig. 3.11. analytical solution fairly approximates air gap magnetic field of the machine. This is caused by simplified representation of the air gap profile. The rotor has bridges between flux paths which cause the magnetic flux to flow smoothly into flux paths. Since the presence of the bridges is not taken into account in the d axis air gap profile the magnetic field calculated analytically experiences some step changes along the rotor's circumference.

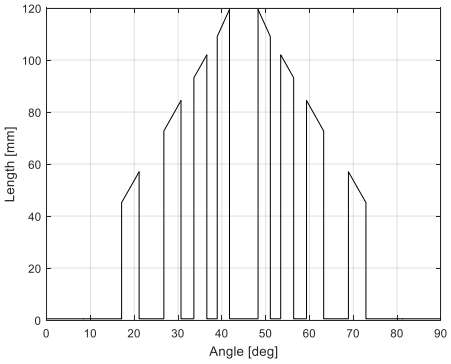

Fig. 3.10 Air gap profile - d axis MMF

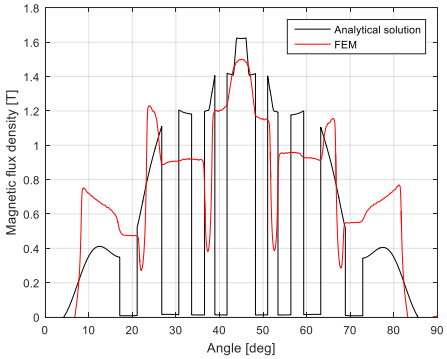

Fig. 3.11 Magnetic field in the air gap - d axis MMF

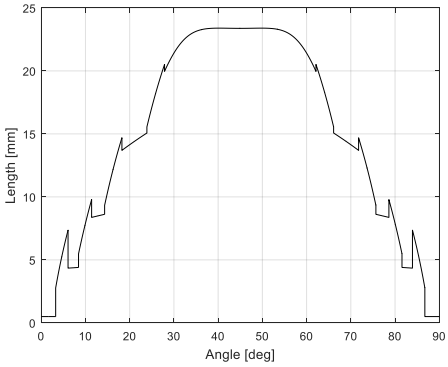

Fig. 3.12 Air gap profile - q axis MMF

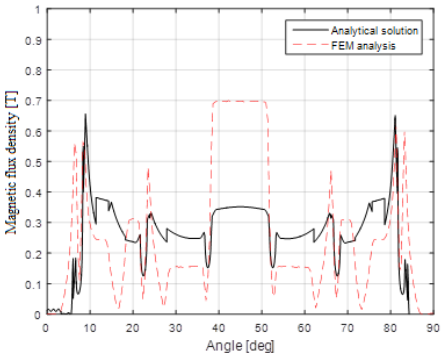

Fig. 3.13 Magnetic field in the air gap - q axis MMF

The air gap profile shown in Fig. 3.12. is valid only when the maximum of stator magnetomotive force is located right above rotor's q axis. Any rotation of the rotor causes the flux lines to change their paths and cross the air gap and flux barriers at various angles which makes it very complicated to describe the air gap field distribution analytically.

The application of the presented method is limited since it only lets to obtain constant inductances of the machine. In order to include saturation of the iron core or rotor position impact on the inductances, other methods should be used. Fig. 3.13. shows that winding function for modeling of synchronous reluctance machine with flux barriers in the rotor provides quite poor accuracy. Flux fringing is hard to model with winding function.

3.3.3. Magnetic Equivalent Circuit

Magnetic equivalent circuit (MEC) can be treated as finite element method of reduced order [73]. Its advantage comparing to winding function method is that magnetic field in the iron core of the machine is taken into account. This allows performing a simplified analysis of saturated machine. This method is convenient for simple geometries. In order to calculate the field in electrical machines of more complicated geometry, the machine is divided into regions where magnetic field density is assumed to be constant, each of them to be treated as a simple reluctance. Magnetic flux density along the machine's axial direction is assumed to be constant. Reluctance of each element has to be calculated depending on the direction of magnetic flux. In Table 3.1 several typical shapes are presented with their reluctances calculated for radial flux direction (flux crosses the air gap) and tangential flux direction (flux flows along the air gap). The geometry of the machine can be approximated using shapes given below.

TABLE 3.1 Reluctances of typical shapes [68]

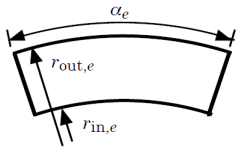	$R_{mr} = \frac{1}{\mu l_e \alpha_e} \ln\left(\frac{r_{out,e}}{r_{in,e}}\right)$ $R_{mt} = \frac{\alpha_e}{\mu l_e \ln\left(\frac{r_{out,e}}{r_{in,e}}\right)}$
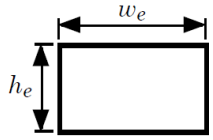	$R_{mr} = \frac{h_e}{\mu l_e w_e}$ $R_{mt} = \frac{w_e}{\mu l_e h_e}$
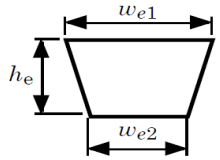	$R_{mr} = \frac{h_e}{\mu l_e (w_{e2} - w_{e1})} \ln\left(\frac{w_{e2}}{w_{e1}}\right)$ $R_{mt} = \frac{(w_{e2} - w_{e1})}{\mu l_e h_e \ln\left(\frac{w_{e2}}{w_{e1}}\right)}$

Although the air gap of SynRM is smooth (when neglecting stator slots), flux barriers in the rotor change the reluctance of the magnetic circuit and hence modify the path for magnetic flux that links the stator and rotor. That causes some difficulties in modeling of SynRM using MEC. Flux lines follow a complicated path when crossing the air gap which decreases the MEC model accuracy. Moreover, the machine behaves differently when the MMF is applied in d or q axis, respectively. For this reason, two separate MEC models of the machine were developed as shown in Fig. 3.14, considering only one pole of the machine due to machine's symmetry.

In equations shown in Table 3.1, μ is magnetic permeability and l_e is the machine's axial length. Reluctances of the flux tubes are calculated assuming that the magnetic flux passes through them in radial and tangential direction.

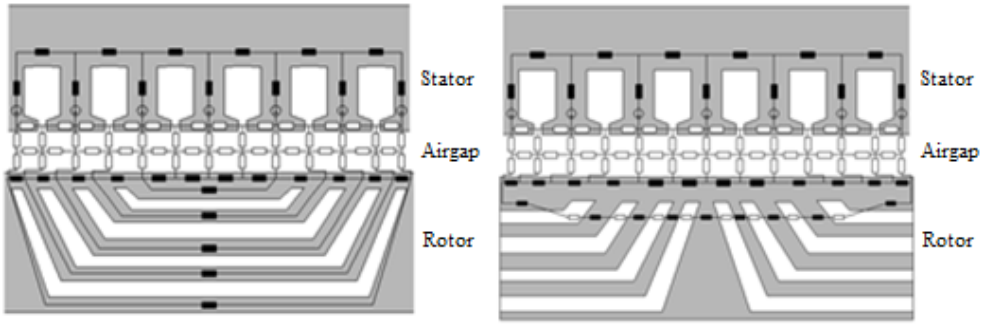

Fig. 3.14 Reluctance network of the machine for d (left) and q axis (right) [74], [75]

Reluctance network of the rotor was developed based on the flux paths in the rotor for d and q axis magnetomotive force (MMF), respectively, as shown in Fig. 3.14. The blocks in black color represent iron nonlinear reluctances while the white blocks represent air reluctances. As one can see in Fig. 3.15, when d axis MMF is applied, the flux flows along the flux paths in the rotor and there is hardly some flux crossing the flux barriers. For this reason, flux barriers can be neglected in MEC model for MMF applied in d axis. In case of MMF applied in q axis, the flux crosses the flux barriers hence reluctance of flux barriers has to be taken into account when creating MEC model.

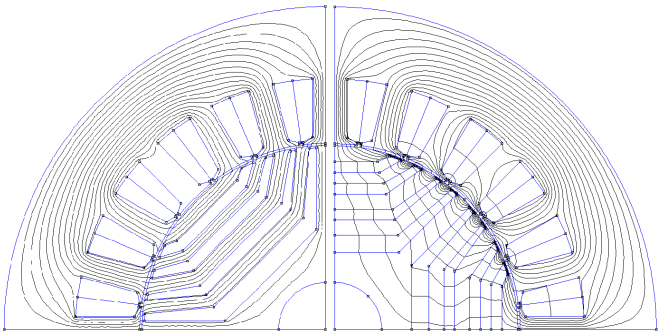

Fig. 3.15 Flux in the rotor for d axis MMF (left) and q axis MMF (right)

As it can be noticed in Fig. 3.14, the reluctance network for the stator remains unchanged; the only change is made in the rotor. The air gap was modeled as a connection of radially and tangentially placed reluctance tubes. This approach was described in [68] and it allows for modeling of air gap field distribution without using finite element method as presented in [76]. For the clearance of Fig. 3.14, only several air gap reluctance tubes were shown. In the derived model, the air gap consisted of 29 sections. The number of sections in the air gap is directly related to the alignment of stator slots and rotor's flux barriers.

When calculating reluctances of stator and rotor with rectangular or round flux barriers, it is enough to use equations shown in Table 3.1. However, for the rotor of SynRM with flux barriers of optimized shape based on Zhukovski's function, calculation of the reluctances becomes more complicated. It is necessary to begin with magnetic reluctance definition:

$$R_M = \oint \frac{dl}{\mu S} \qquad (3.2.20)$$

The shape of the flux barriers can be retrieved by using parametric equations. This leads to a quite complicated implicit functions when calculating the reluctance defined above.

In order to calculate the magnetic reluctance, it is necessary to know the length and the cross section of the flux barrier. Due to flux barrier's geometry, the length and the cross section will vary with respect to the

angle. These parameters can be obtained using numerical calculations. The length of the flux barrier (and also flux path) can be retrieved by using the formula below:

$$l = \int_{\alpha_1}^{\alpha_2} \sqrt{\left(\frac{dx(\alpha)}{d\alpha}\right)^2 + \left(\frac{dy(\alpha)}{d\alpha}\right)^2}\, d\alpha \qquad (3.2.21)$$

The cross section of the flux barrier can be calculated if the orthogonal curves to Zhukovski's curves are found. This will allow to find the height of the flux barrier by calculating the length of the orthogonal curve described by equation (3.2.22) between intersection points with Zhukovski's curves described by equation (3.1.5).

The variation of flux barrier cross section with respect to the angle α is presented in Fig. 3.18. When the length and cross section functions are known, the element's reluctance can be calculated using the integral (3.2.20). Since function (3.1.2) is of a complex type, family of the desired orthogonal curves can be obtained by taking the real part of the function $g(z)$, which is of the form:

$$2\mathrm{w} + \mathrm{x}^2 - \mathrm{y}^2 + \frac{(\mathrm{x}^2 - \mathrm{y}^2)\mathrm{w}^2}{(\mathrm{x}^2 + \mathrm{y}^2)^2} = \mathrm{u} \qquad (3.2.22)$$

Applying equations (3.1.6) and (3.1.7) to equation (3.2.22) the parametric equations (3.1.8) of the orthogonal curves can be obtained, where the "radius" is of the form:

$$r_q(\alpha, w, u) = \sqrt{\frac{u - 2w + \sqrt{(2w-u)^2 - 4w^2(\cos(2\alpha))^2}}{2\cos(2\alpha)}} \qquad (3.2.23)$$

The q index indicates that the orthogonal lines go across the flux barriers in q axis direction.

Reluctance calculation requires some mathematical operations to be performed, since the functions of length and cross section area defined previously, depend on different variables. It is inevitable to perform transformations so the integrand of one variable could be obtained. In this case, the integrand depends on the angle α as shown below.

$$R_M = \oint \frac{dl}{\mu S} = \oint \frac{\frac{dl(\alpha)}{d\alpha} d\alpha}{\mu S(\alpha)} \tag{3.2.24}$$

The meaning of angle α is shown in Fig. 3.16 below. Part of the flux barrier marked in red is shown with more details in Fig. 3.17.

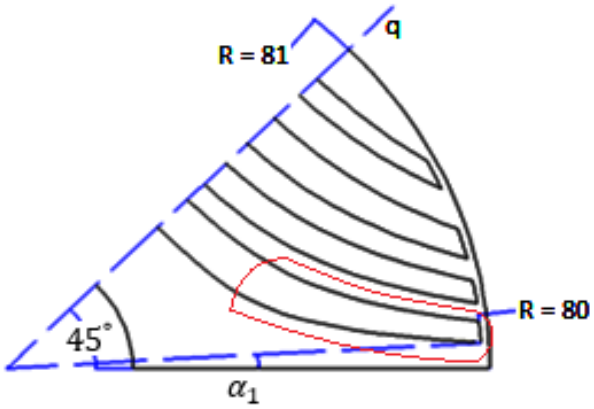

Fig. 3.16 Half of rotor's pole [74]

The angle α is measured along one pole of the machine. For a machine which has four poles, the value of the angle covers the range from 0° to 90°. However, because of the rotor's symmetry it is sufficient to consider only a half of rotor's pole which means the angle α is between 0° and 45°.

When calculating the height of the flux barrier, the element was split into two parts shown in Fig. 3.17. The second part consists of a part of a circle and Zhukovski's curve. It can be assumed that in the second element (marked in yellow), the flux lines are also perpendicular to the orthogonal curves defined by equation (3.2.22). In this part of the flux

barrier, it is necessary to find the intersection point of orthogonal curve with the circle of radius R.

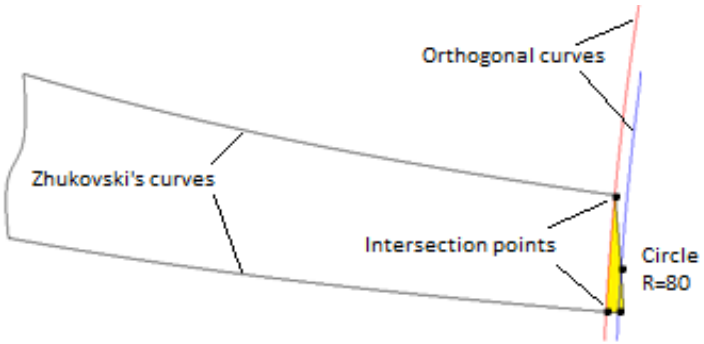

Fig. 3.17 Two parts of flux barrier [74]

The length of the curve is computed using parametric equations (3.1.8) between two angles α_1 and α_2. The value of angle α_2 is constant and equals $\alpha_2 = 45^{\circ}$ and the value of α_1 varies according to the equation:

$$\alpha_1 = \frac{1}{2}\sin^{-1}\left(\frac{v}{R^2 - w^2}\right) \qquad (3.2.25)$$

Taking into account equations (3.2.21) and (3.2.25), the curve length along the flux barrier, depends on the parameter v. The values of the curve length for parameter v between 700 and 1200 are shown in Fig. 3.18.

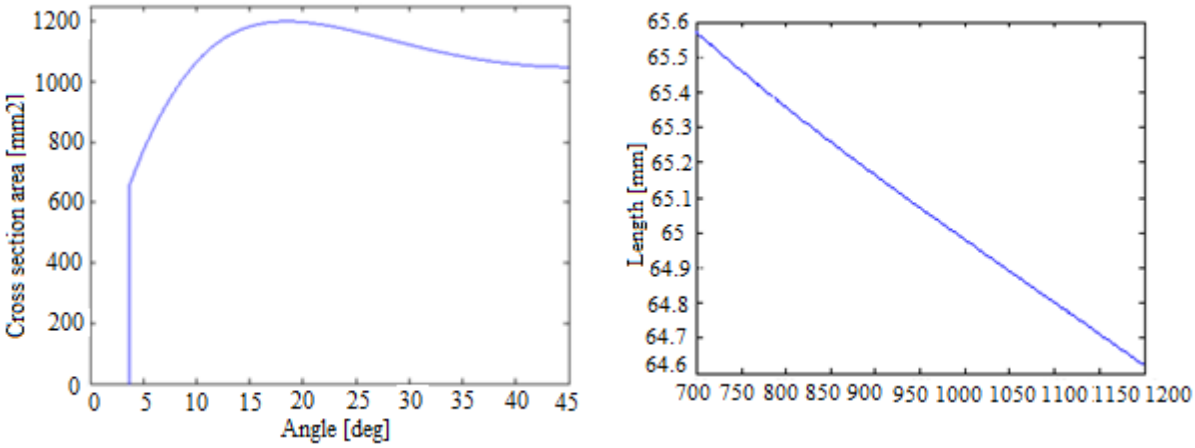

Fig. 3.18 Cross section of flux barrier as a function of angle α (left) and length of flux barrier as a function of parameter v (right)

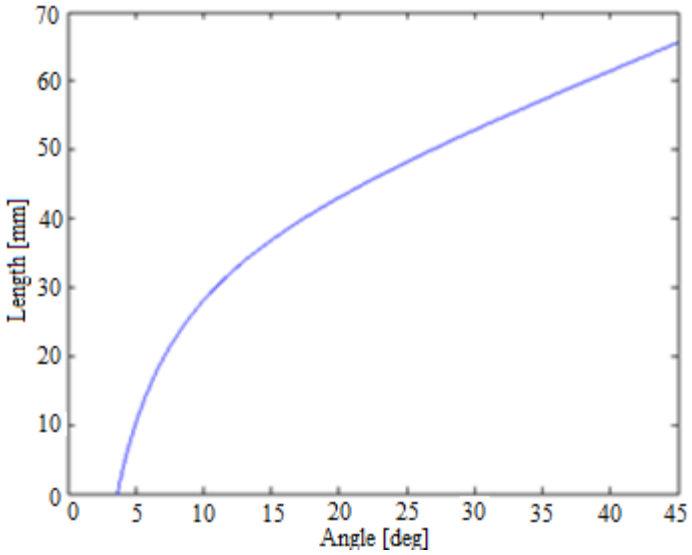

Fig. 3.19 The length of flux barrier as a function of α for parameter v=700

In order to calculate the integral from equation (3.2.24), it is necessary to obtain the length of flux barrier as a function of angle α and its derivative with respect to this angle. The flux barrier length function of angle α for parameter $v = 700$ is presented in Fig. 3.19. The derivative of the flux barrier length function with respect to the angle α is presented in Fig. 3.20.

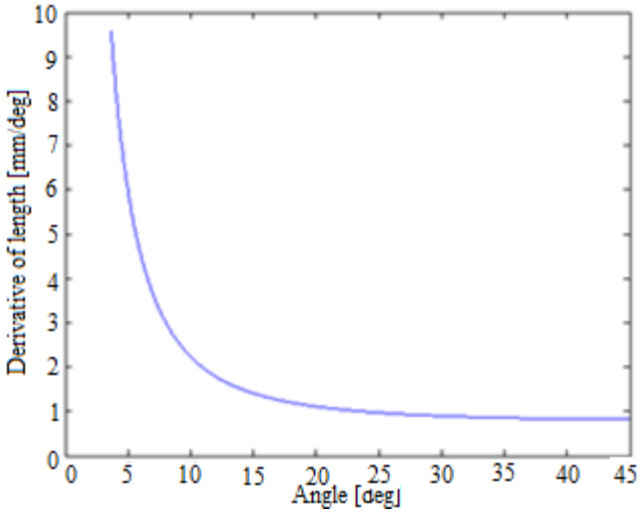

Fig. 3.20 Derivative of flux barrier length function with respect to angle α for parameter v = 700

When the necessary functions are defined, the reluctance of the rotor's flux path can be computed using equation (3.2.24). The reluctance was computed in MATLAB® since finding analytical solution of integral (3.2.24) is quite complicated.

The MMF sources in the reluctance network of MEC model are placed in stator's slots [77]. The MMF of each stator tooth depends on the ampere-turns of all slots [78]. For this reason, certain constraints have to be put on the MMF sources.

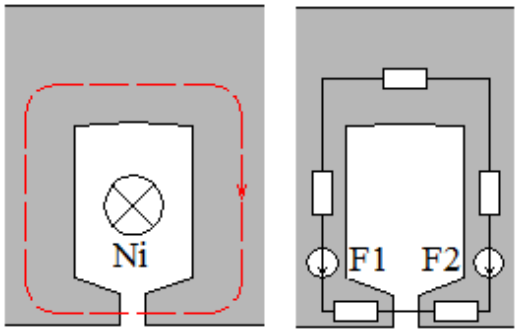

Fig. 3.21 Magnetic flux around and equivalent MMF sources [74]

Applying Ampere's current law:

$$\oint \vec{\mathrm{H}} \circ \overrightarrow{dl} = \mathrm{Ni} \qquad (3.2.26)$$

the current carrying conductors can be represented as magnetic potential sources. In equation (3.2.26) N is the number of turns in one slot and i is current flowing through the winding. Fig. 3.21 presents a current carrying conductor in stator slot and its representation in reluctance network of MEC model. The MMF amplitudes of sources in Fig. 3.21 are constrained by:

$$F_2 - F_1 = Ni \qquad (3.2.27)$$

In general, the constraint presented above is put on all stator slots and teeth. The last constraint for magnitudes of MMF sources is derived from Gauss's law:

$$\oint \vec{\mathrm{B}} \circ \overrightarrow{\mathrm{ds}} = 0 \qquad (3.2.28)$$

which requires the sum of all MMF sources over one pole of the machine to be equal to zero since magnetic monopoles do not exist. This constraint of MMF sources magnitudes can expressed as:

$$\sum_n F_n = 0 \qquad (3.2.29)$$

MEC model was built using nodal method [79]. Because the model contains nonlinear elements, a set of nonlinear algebraic equations needs to be solved. To achieve this, Newton-Raphson method was used [80]. The algorithm is shown below.

$$x^{(k+1)} = x^{(k)} - \left[J\left(x^{(k)}\right)\right]^{-1} f\left(x^{(k)}\right) \qquad (3.2.30)$$

In the equation above, $J\left(x^{(k)}\right)$ is Jacobi matrix which has to be computed in each iteration. Since the permeances are not in the form of explicit functions of nodal potentials, approximate method of Jacobian calculation must be used as described in [77].

Nodal equations are given in the form:

$$\Lambda * u = \Phi \tag{3.2.31}$$

In this equation Λ is the permeance matrix, u is the nodal potential vector and Φ is the magnetic flux vector. For the purpose of Newton-Raphson method application, equation (2.2.31) has to be written in the following form:

$$f(u) = \Lambda * u - \Phi \tag{3.2.32}$$

In this method, Jacobian has to be computed in each iteration. Derivative of function $f(u)$ with respect to nodal potential u is given by:

$$\frac{\partial f(u)}{\partial u} = u\frac{\partial \Lambda}{\partial u} + \Lambda - \frac{\partial \Phi}{\partial u} \tag{3.2.33}$$

In general, derivative of a magnetic permeance function with respect to nodal potential can be defined as [77]:

$$\frac{\partial \Lambda_m}{\partial u} = \frac{\partial \Lambda_m}{\partial \mu_r}\frac{\partial \mu_r}{\partial B}\frac{\partial B}{\partial \phi}\frac{\partial \phi}{\partial u} \tag{3.2.34}$$

Since:

$$\Lambda_m = \frac{1}{R_m} = \frac{1}{\frac{1}{\mu_r \mu_o}\oint \frac{\mathrm{dl}}{\mathrm{S}}} = \frac{\mu_r \mu_o}{\oint \frac{\mathrm{dl}}{\mathrm{S}}} \tag{3.2.35}$$

The derivative of magnetic permeance function with respect to relative magnetic permeability in equation (3.2.34) is defined as:

$$\frac{\partial \Lambda_m}{\partial \mu_r} = \frac{\mu_o}{\oint \frac{\mathrm{dl}}{\mathrm{S}}} = \frac{\Lambda_m}{\mu_r} \tag{3.2.36}$$

The second term in equation (3.2.34) is obtained from magnetizing curve (Fig. 3.22).

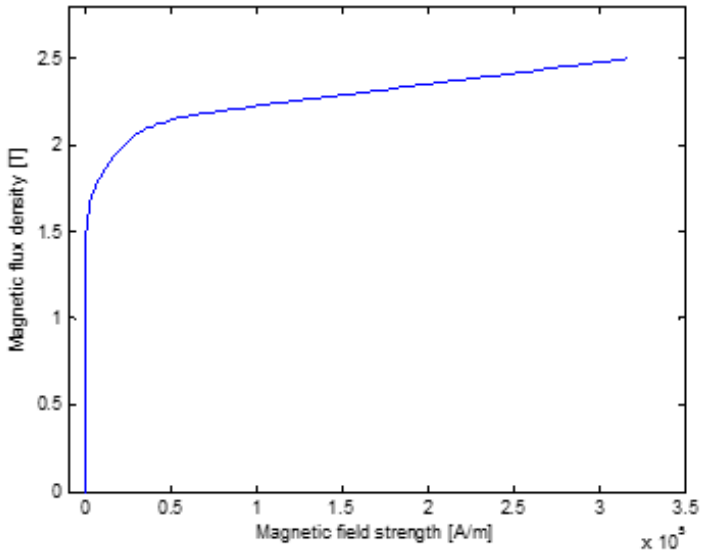

Fig. 3.22 Magnetizing curve of the considered steel sheet

Given the B-H curve, the relative magnetic permeability of the material can be calculated. Fig. 3.23. shows the steel sheet relative magnetic permeability.

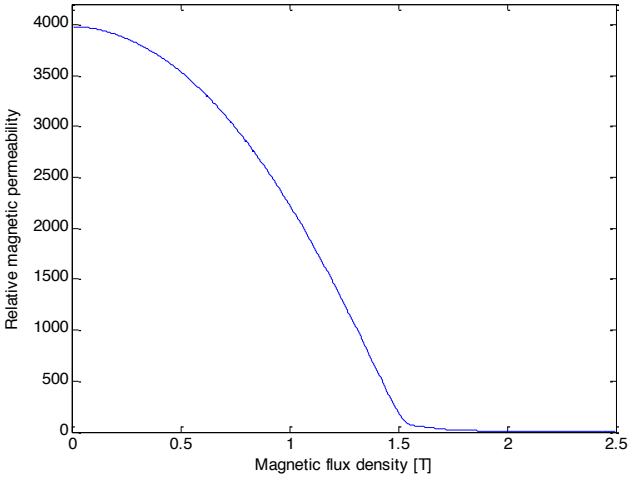

Fig. 3.23 Magnetic permeability

Calculating the second term of equation (3.2.34), requires computing the derivative of the material magnetic permeability funciton with respect to the magnetic flux density. This derivative is shown in Fig. 3.24.

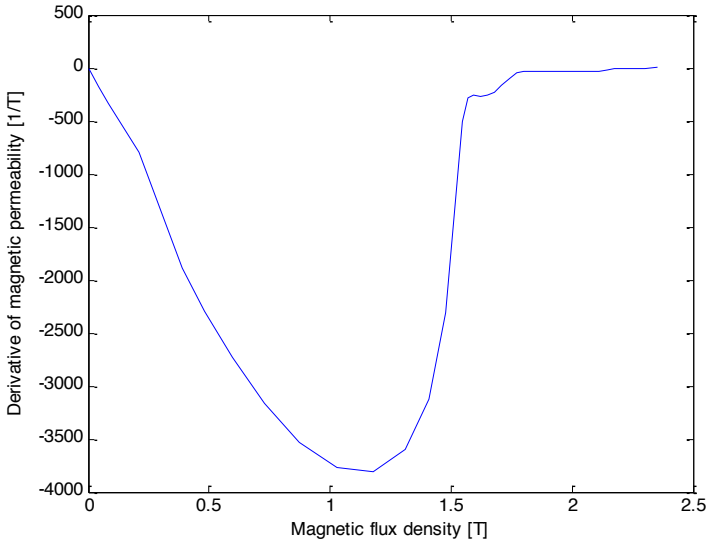

Fig. 3.24 Derivative of magnetic permeability

Third term in equation (3.2.34) equals:

$$\frac{\partial B}{\partial \phi} = \frac{1}{S} \tag{3.2.37}$$

where S is the cross section area of flux tube. The last term of equation (3.2.34) which is a derivative of magnetic flux with respect to nodal potential can be calculated as:

$$\phi_{12} = \Lambda_{m12}(u_1 - u_2) \tag{3.2.38}$$

where u_1 and u_2 are nodal potentials of two consecutive nodes, Λ_{m12} is the permeance between these nodes and ϕ_{12} is the magnetic flux flowing through permeance Λ_{m12}, the derivative of the flux with respect to specified nodal potential can be written as:

$$\frac{\partial \phi_{12}}{\partial u_1} = \frac{\partial \Lambda_{m12}}{\partial u_1}(u_1 - u_2) + \Lambda_{m12} \tag{3.2.39}$$

Putting equations (3.2.36), (3.2.37) and (3.2.38) to equation (3.2.34), the derivative of magnetic permeance with respect to specified nodal potential will be obtained:

$$\frac{\partial \Lambda_{m12}}{\partial u_1} = \frac{\alpha\beta\gamma\Lambda_{m12}}{1 - \alpha\beta\gamma(u_1 - u_2)} \qquad (3.2.40)$$

with $\alpha = \frac{\partial \Lambda_m}{\partial \mu_r}$, $\beta = \frac{\partial \mu_r}{\partial B}$ and $\gamma = \frac{\partial B}{\partial \phi}$. All the elements of Jacobian matrix at each iteration are computed in this manner.

The nonlinear equations of MEC reluctance network were solved in MATLAB®. The results were then compared with results obtained from FEM model simulated in FEMM 4.2. Fig. 3.25 and Fig. 3.26 present the air gap field for d and q axis MMF obtained from MEC and FEM analysis. Geometry data of analyzed machine is contained in Table 3.2.

TABLE 3.2 Main dimensions of analyzed machine

Number of slots	24	
Rotor radius	85.5 mm	
Shaft radius	22 mm	
Bridge thickness	1 mm	
Air gap length	1 mm	
Axial length	180 mm	
First flux barrier	w = 25	
	v1 = 400	v2 = 1000
Second flux barrier	w = 25	
	v1 = 1700	v2 = 2400
Third flux barrier	w = 25	
	v1 = 3300	v2 = 4000
Fourth flux barrier	w = 25	
	v1 = 4800	v1 = 5500

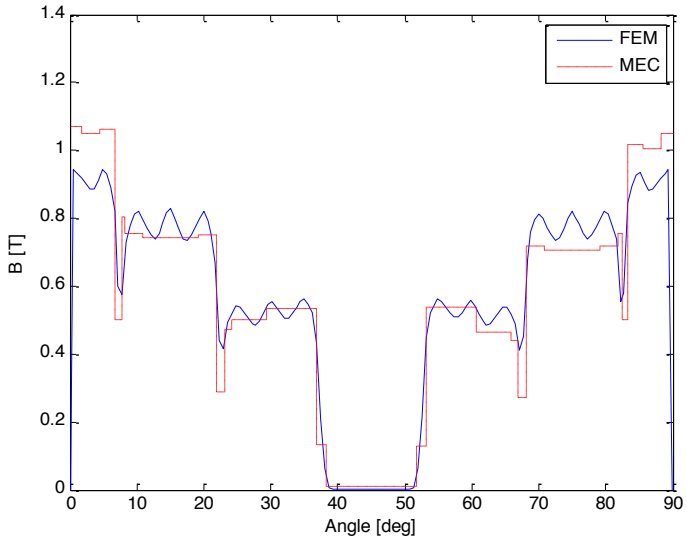

Fig. 3.25 Distribution of air gap magnetic field for d axis MMF [74], [75]

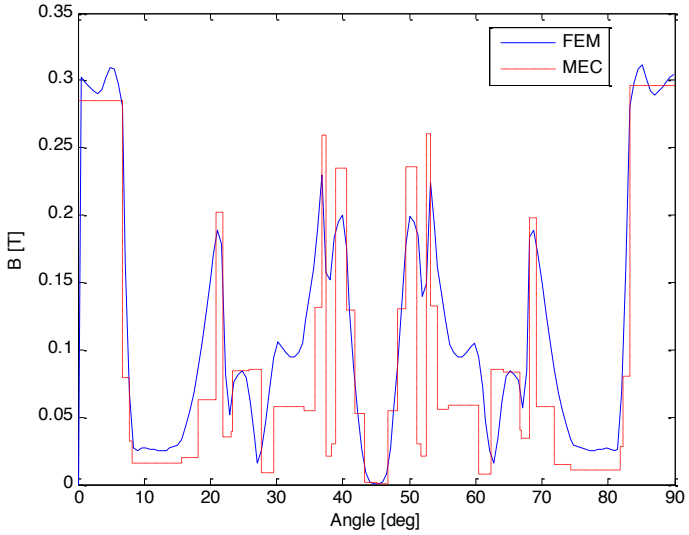

Fig. 3.26 Distribution of air gap magnetic field for q axis MMF [74], [75]

The results obtained from MEC and FEM analyzes are similar. In case of q axis model, the number of air gap divisions is increased so more precise air gap field distribution could be obtained. During design process, it is

necessary to predict machine's performance, thus estimating machine's L_d and L_q inductances and saliency ratio defined as L_d/L_q is crucial [81]. Calculation of the machine's flux linkages and saliency ratio was performed using MEC and FEM model. Comparison of the results is presented in Fig. 3.27.

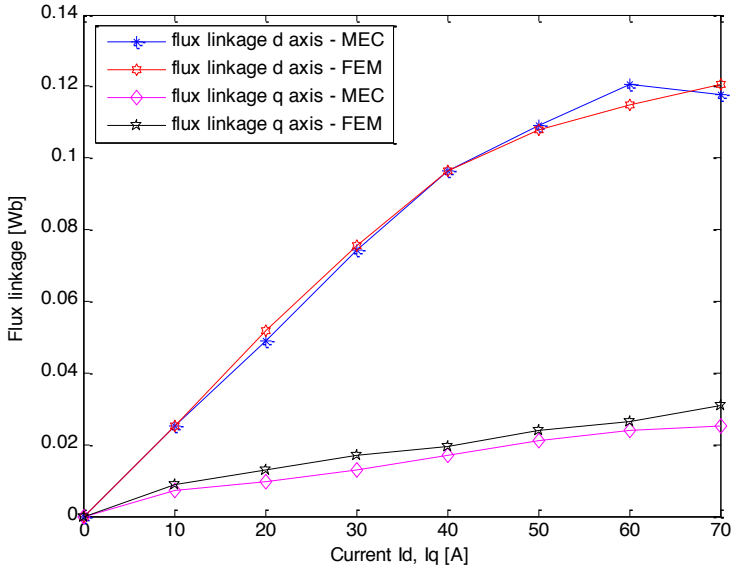

Fig. 3.27 Machine's flux linkage in d and q axis [74], [75]

Inductances L_d and L_q of the machine can be computed as derivative of flux linkage function with respect to current I_d and I_q.

$$L_d = \frac{d\Psi_d}{dI_d} \approx \frac{\Delta\Psi_d}{\Delta I_d} \qquad (3.2.41)$$

$$L_q = \frac{d\Psi_q}{dI_q} \approx \frac{\Delta\Psi_q}{\Delta I_q} \qquad (3.2.42)$$

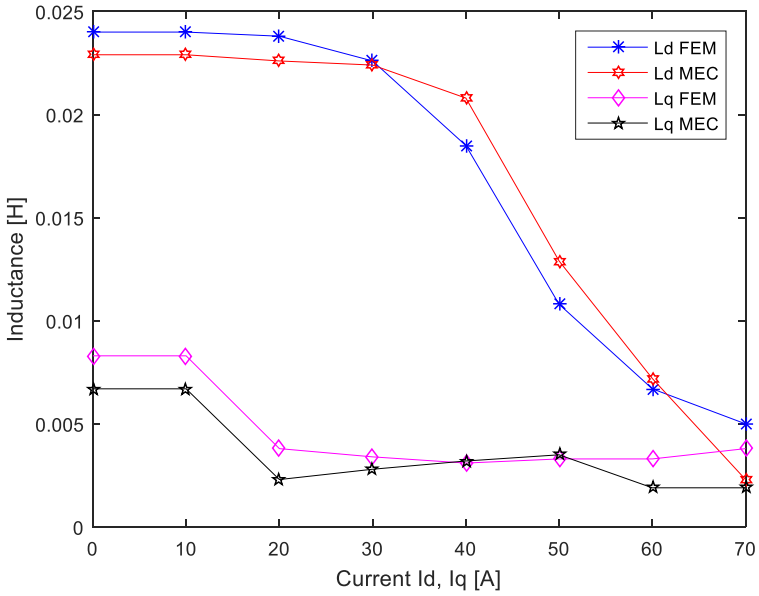

Fig. 3.28 Inductances the machine in d and q axis [74]

In Fig. 3.27 it can be seen that flux linkage obtained from MEC and FEM analysis is similar. Flux linkage in q axis is close to linear because of the flux barriers in the path of magnetic flux. In d axis saturation occurs. because the magnetic flux avoids the flux barriers, almost the entire flux path consists of nonlinear reluctances. Machine's inductances in d and q axis are presented in Fig. 3.28. Results obtained from MEC model and FEM model coincide with each other. This proves that MEC model provides acceptable accuracy in inductance calculation of SynRM when cross saturation is neglected.

Figures below show results of FEM analysis of the modeled SynRM. The models were adjusted to perform analysis for stator MMF in d and q axis.

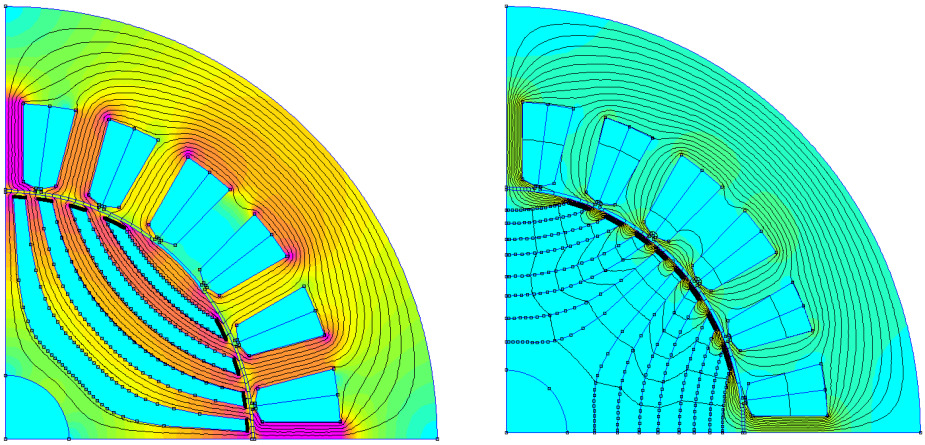

Fig. 3.29 Magnetic flux density distribution for d (left) and q (right) axis MMF

MEC method can provide satisfying accuracy in inductance calculation. This method however is based on lumped parameters which in some cases might be difficult to calculate. For flux barriers built on Zhukovski's curves, calculation of rotor's reluctance network was quite problematic and it was performed only for two rotor positions as the flux paths are too complicated to be described using analytical equations. Using two separate MEC models does not let to include cross saturation when calculating machine's flux linkage and inductances. For MEC analysis, SynRM with 24 stator slots was used. This significantly simplifies the analysis since only one pole of the machine needs to be modeled. The final topology however has 27 stator slots which means that there is no geometrical symmetry and the entire structure has to be analyzed. Moreover, results of electromagnetic analysis are further processed and used in thermal and vibroacoustic analyses. These analyses require accurate power loss and magnetic radial forces distribution. This cannot be obtained with MEC analysis hence FEM analysis is necessary. Analysis of the final SynRM topology includes cross saturation analysis and rotor skewing modeling for which the finite element method is much better than MEC analysis.

This part presented simplified methods of SynRM electromagnetic analysis. Machine models used for these analyses have 24 stator slots in order to provide geometrical symmetry which simplifies the models.

3.3.4. SynRM Design Parameter Sensitivity

Since the object of interest is a machine for high speed applications, only machines with four poles will be considered in this work. The anisotropy of the magnetic circuit is delivered by the rotor construction but the overall performance of the machine depends on the stator and rotor interaction. Different number of stator slots and winding configurations affect machine's parameters such as generated torque, torque ripple or supply voltage.

In general the number of slots of an electrical machine's stator is defined based on the rated power and the main geometrical dimensions; in case of the SynRMs presented in this work the performance of the machines is investigated for 3 different stator topologies: 24, 30 and 36 slots. For each case the outer and inner diameter of the laminations, are kept unchanged, along with the slot opening, width and depth. The three resulting topologies are presented in Fig. 3.30 [47].

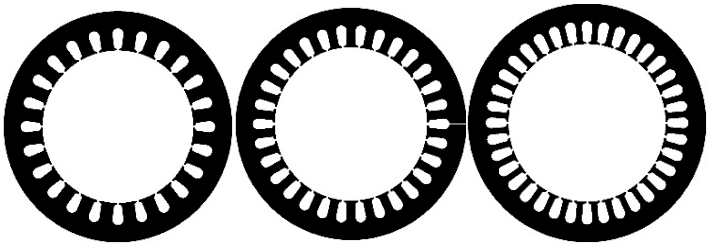

24 slots 30 slots 36 slots

Fig. 3.30 SynRM stator topologies [47]

Various winding topologies were considered for each case and the most appropriate was used in the comparative study: full-pitch winding for the 24 slot structure, fractional pitch for the 30 slots structure and short-pitch winding for the 36 slots stator. Because the number of slots/pole/phase varies, different number of turns per coil was considered, so that the total number of turns per phase is similar for the three stators. Fractional slot concentrated windings were studied for this type of machine [9]. For each stator, two rotor topologies were studied. First rotor topology was the rotor with round flux barriers and the second topology was the rotor with optimized flux barriers whose shape is based on Zhukovski's curves.

In order to compare the performances of the different topologies electromagnetic simulations were carried out in JMAG Designer, which is

a FEM based commercial software. Fig. 3.31 shows the magnetic flux lines and the distribution of the magnetic flux density in analyzed structures in case when rotor's d axis is aligned with the axis of stator magnetic field. The left column presents the conventional rotor SynRMs with round barriers and the motor with "Zhukovski" shaped barriers are shown on the right. It can noticed that the initial rotor position is different for the two barrier shapes because of the different methods used for creating the model: the "Zhukovski" barrier rotor has the d-axis drew on the symmetry of the model, while for the initial rotor there is a 45^0 between the d-axis and the symmetry line.

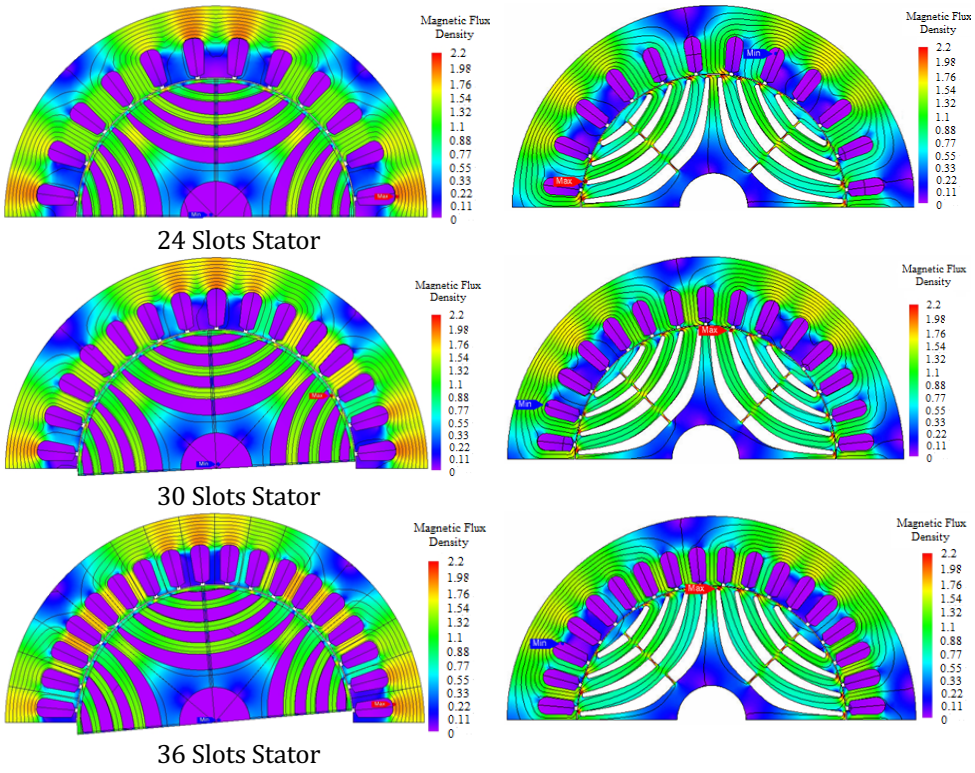

Fig. 3.31 Magnetic flux density and flux lines [47]

The air gap magnetic flux field obtained for these rotor positions are presented in Fig. 3.32: the radial component is plotted along the entire air gap circumferential length when stator d axis magnetomotive force was applied. It was computed to show how rotor topology influences magnetic flux density distribution in the air gap in no load state. For 24 slot stator and the rotor with "Zhukovski" based flux barriers, the air gap field is closer to the ideal (sinusoidal) shape but the average value remains

similar for both types of rotor. For the 30 and 36 slots structures the differences are caused by the different distance between the flux barriers, causing the stator teeth to be aligned with the rotor flux paths in a different manner.

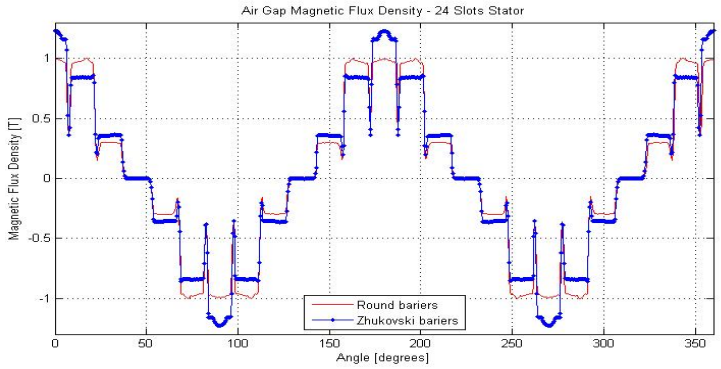

24 slot stator

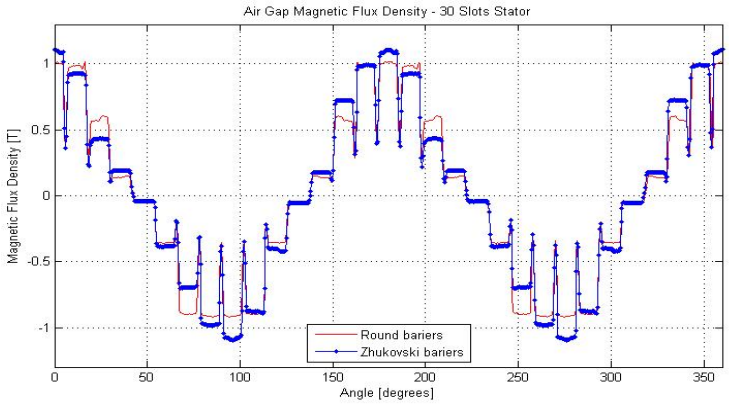

30 slot stator

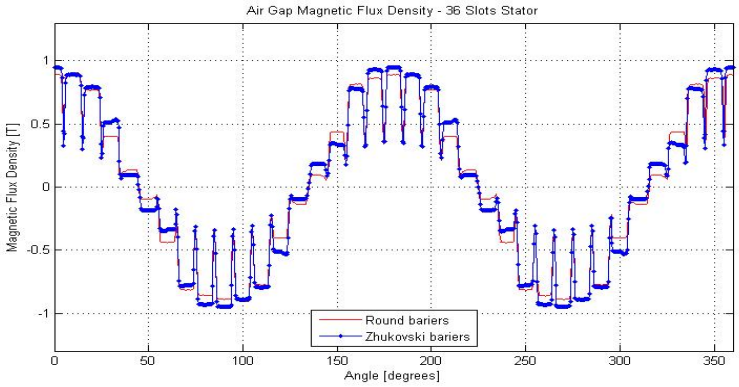

36 slot stator

Fig. 3.32 Distribution of magnetic flux density in the air gap [47]

Fig. 3.33 presents instantaneous torque waveforms of all machine topologies. The waveform shown in the top of the figure is the torque generated at peak power while the bottom waveform is the torque generated at continuous power. Red continuous line represents the torque waveform of machine with Zhukovski's type flux barriers in the rotor and black dotted line represents torque waveform of machine with round rotor barriers. One can see relevant difference in torque ripple for each case between those two rotor types.

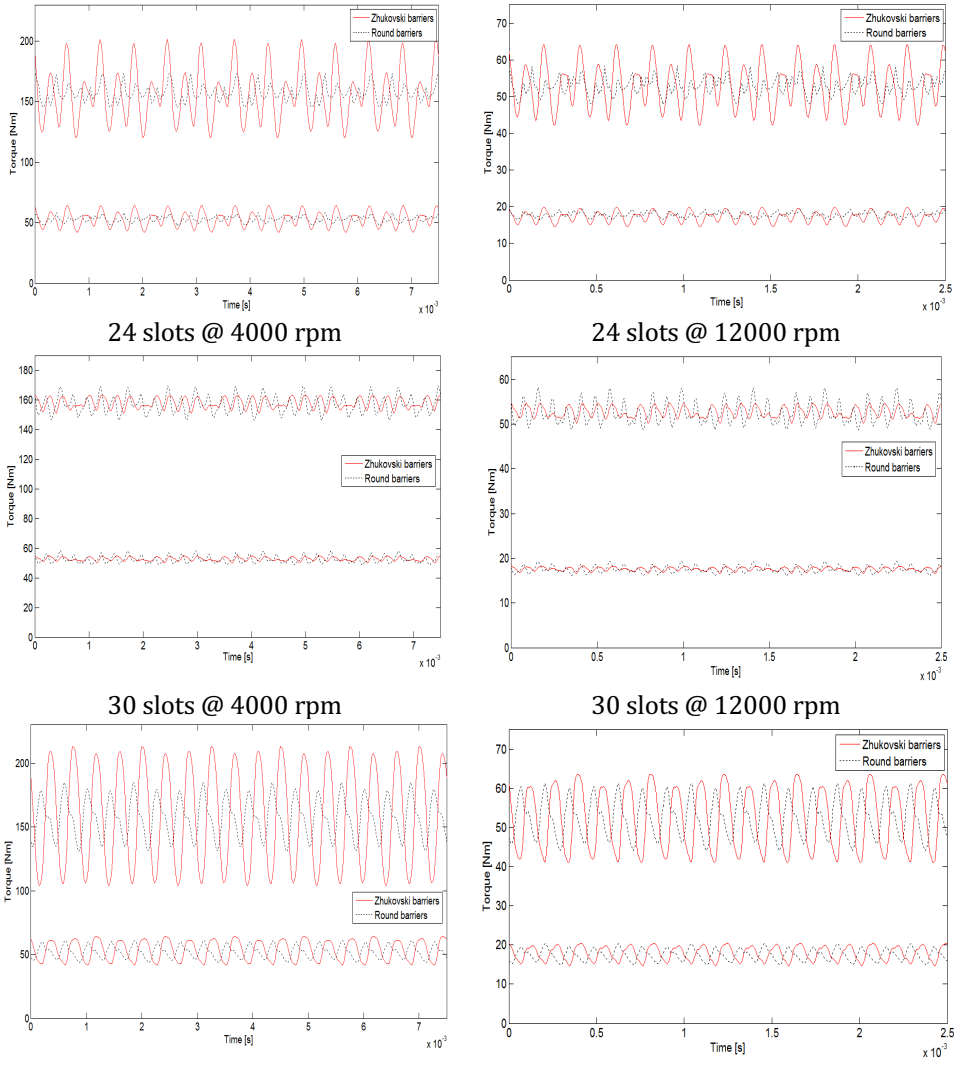

24 slots @ 4000 rpm

24 slots @ 12000 rpm

30 slots @ 4000 rpm

30 slots @ 12000 rpm

36 slots @ 4000 rpm

36 slots @ 12000 rpm

Fig. 3.33 Instantaneous torque waveforms of all machine topologies [47]

The exact information on percentage torque ripple and torque mean values is given in Table 3.3.

TABLE 3.3 Torque and torque ripple information for each topology [47]

Case				**Results**		
Stator	***Speed [rpm]***	***Operating Point***	***Rotor***	***Current [A]***	***Average Torque [Nm]***	***Torque ripple [%]***
24 slots	4000	Cont.	Round.	42.5	52.8	19.57
			Zhuk.	39	52.9	41.12
		Peak	Round.	113	157.08	17.67
			Zhuk.	106	157.17	51.56
	12000	Cont.	Round.	21.6	17.8	15.54
			Zhuk.	18	17.3	30.71
		Peak	Round.	42.5	52.8	19.57
			Zhuk.	39	53.1	41.41
30 slots	4000	Cont.	Round.	46.2	52.36	18.07
			Zhuk.	43	52.69	8.77
		Peak	Round.	123	156.69	14.85
			Zhuk.	118	157.77	7.75
	12000	Cont.	Round.	24	17.47	18.28
			Zhuk.	20	17.58	9.54
		Peak	Round.	46.2	52.39	18.01
			Zhuk.	43	52.68	8.78
36 slots	4000	Cont.	Round.	47.5	52.23	33.14
			Zhuk.	49	53.09	41.54
		Peak	Round.	130.1	157.32	34.13
			Zhuk.	134	158.66	68.66
	12000	Cont.	Round.	24.2	17.48	30.93
			Zhuk.	23	17.87	32.08
		Peak	Round.	47.7	52.51	33.14
			Zhuk.	48.5	52.47	43.15

The magnetic flux density in the air gap is shown for all the structures, showing that when using the new barrier shape the variation is closer to the ideal sinusoidal form. Since the SynRM torque is depending on the ratio between the direct and quadrature inductances the variation of coil magnetic flux was studied, considering a constant current through one of the phases, so the maximum and the minimum inductances, corresponding to the d and q axes, respectively, could be determined. The results showed that the new rotor geometry has higher saliency at mid-

range currents, while for high currents the ratio is almost equal because of the saturation of the magnetic circuit.

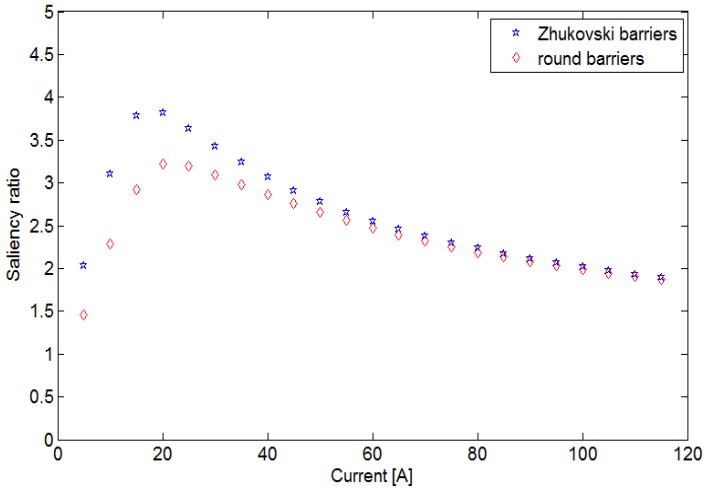

Fig. 3.34 Saliency ratio comparison - 24 slot [47]

Figures 3.34 to 3.36 show the comparison of saliency ratios of examined machine topologies. One can see that machine with optimized flux barriers in the rotor achieves higher saliency ratios for all stator topologies. The figures show that the saliency ratio changes with phase current. The highest values of saliency ratios occur around 20A phase current. The higher phase current the lower the saliency ration due to saturation of magnetic circuit.

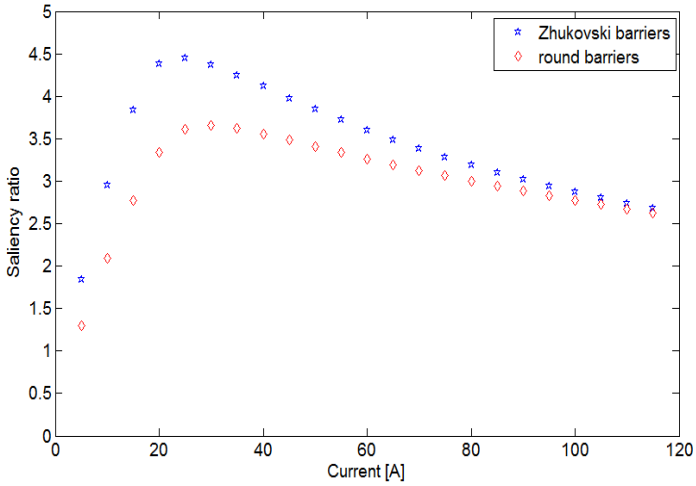

Fig. 3.35 Saliency ratio comparison - 30 slot stator [47]

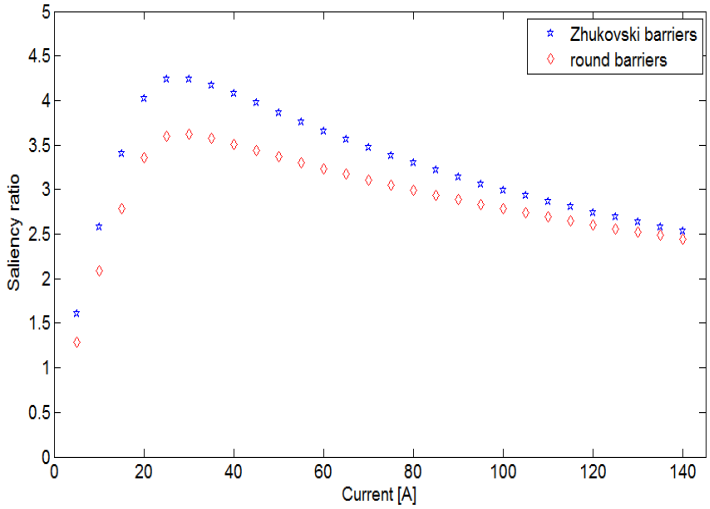

Fig. 3.36 Saliency ratio comparison - 36 slot stator [47]

The torque mean value and torque ripple ratio were determined for the 4 typical operating points, proving that for the 24 and 30 slots structures a lower current is required when using the “Zhukovski” curves based barriers shapes to get the same torque than in the case of the round shaped barriers; for the 36 slots structure the conventional rotor seems to be more efficient than the new variant. For 24 and 36 slot stators the

torque ripples are higher when using the new barrier shapes, so further analysis on the location of the barriers must be performed. Promising results are obtained for 30 slot stator that exhibits lower torque ripple values compared to the other stator topologies. When using the "Zhukovski" shaped barriers the ripple is further reduced to half the value calculated for the conventional structure.

3.4. Structural and Vibroacoustic Analysis

Failure refers to a number of different mechanisms that can occur. It could mean permanent distortion, yield or fracture of the component. It could also mean that the component has compromised functionality. The failure mechanisms used in this work is considered to be yield or fracture of the component. In order to determine which failure theory to use, for static failure theories, it is really critical to correctly classify the material as a brittle material or a ductile material. Failure theories for static loading are presented in Table 3.4.

For ductile materials, it is very clear where the plastic deformation begins. The yield point on the stress strain curve is clearly noted. Brittle materials however do not have a clear yield point so it is hard to determine where the beginning of plastic deformation is.

TABLE 3.4 Failure theories

Loading	Behavior	Strength	Theory
Static	Ductile $\varepsilon \geq 0.05$	$S_{yt} = S_{yc}$	Maximum Shear Stress
			Von Mises Theory
		$S_{yt} \neq S_{yc}$	Ductile Coulomb Mohr Theory
	Brittle $\varepsilon \leq 0.05$	$S_{yt} \neq S_{yc}$	Brittle Coulomb Mohr Theory
			Modified Mohr

In Table 3.4 S_{yt} and S_{yc} are tensile and compressive yield stresses respectively and ε is strain. Yield stress is the value of stress which causes permanent deformation of the material. The concept of yield stress is presented in stress-strain diagram below. Yield stress is marked with letter C. Normal stress and strain are defined by equations (3.3.1) and (3.3.2):

$$\sigma = \frac{F}{A} \tag{3.3.1}$$

In equation (3.3.1) F is the force acting on a surface and A is the cross section area perpendicular to the force vector.

$$\varepsilon = \frac{l - l_0}{l_0} \tag{3.3.2}$$

Strain is defined as the ratio of total deformation to the initial dimension of the body. In equation (3.3.2) l_0 is the initial length of the body and l is the length of the body after deformation.

For materials whose yield strength in tension is equal to or close to yield strength in compression, the Maximum Shear Stress Theory and von Mises Theory can be applied. If the yield strength in tension is vastly different than the yield strength in compression, Ductile Coulomb Mohr Theory should be used. Brittle materials typically are much stronger in compression than they are in tension, so the tension and compressions strengths are almost never the same. In that case Brittle Coulomb Mohr Theory or Modified Mohr Theory can be used.

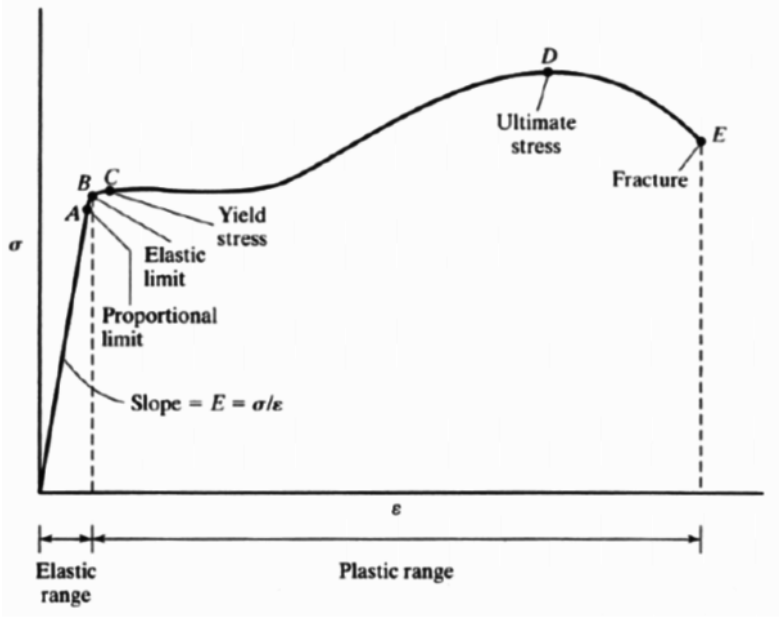

Fig. 3.37 Stress strain curve [82]

When determining the failure of a structure one has to choose a proper failure theory depending on the type of loading and the mechanical properties of the material. In the tests presented in this work, von Mises Theory was used.

In order to apply Maximum Distortion Energy Theory also known as von Mises Theory when determining the failure of the structure one has to agree for the following assumptions:

- Homogenous structure
- Isotropic material
- Linear elastic material
- Static loading
- Ductile material
- $S_{yt} = S_{yc}$

Maximum distortion energy theory has its basis in strain energy which is essentially the energy stored by the system undergoing deformation. In developing the distortion energy theory, the postulate was made that the total strain energy can be divided into two parts: the energy associated solely with change in volume termed dilatation energy and the energy associated solely with change in shape termed distortion energy [83].

Dilatation energy can be associated to hydrostatic component of the loading applied to the material and distortion energy can be associated to distortion component of the loading. Materials can withstand high levels of hydrostatic loading but have limited capacity for distortion energy.

Fig. 3.38. shows the idea of tri-axial stress state. Hydrostatic component of stress which is responsible for volume change and distortional component which is responsible for the change of shape contribute together to total stress of the material.

Failure criteria in von Mises theory states that the failure takes place when the component strain energy per unit volume is greater than or equal to a distortion energy per unit volume at yield of a tensile test specimen of the same material as the component. To compare the energies von Mises equation is used.

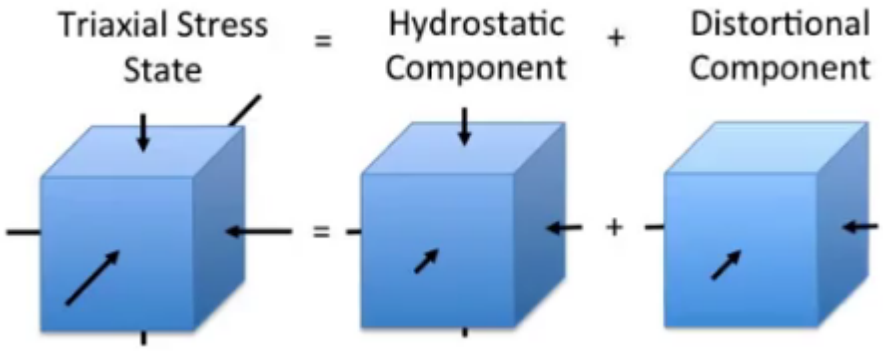

Fig. 3.38 Tri-axial stress state

$$\sigma' = \frac{1}{\sqrt{2}}\sqrt{(\sigma_x - \sigma_y)^2 + (\sigma_y - \sigma_z)^2 + (\sigma_z - \sigma_x)^2 + 6(\tau_{xy}^2 + \tau_{yz}^2 + \tau_{zx}^2)} \quad (3.3.3)$$

In equation above σ' is effective stress, σ_x, σ_y, σ_z are normal stresses in x, y and z axes and τ_{xy}, τ_{yz}, τ_{zx} are shear stresses in XY, YZ and ZX planes. The failure occurs when $\sigma' \geq S_y$.

During design process, for a given stator topology, one wants to find a topology of the rotor which provides the highest value of saliency ratio. The goal is to maximize the permeance of the rotor in d axis and to minimize the permeance in q axis. This is obtained by a proper design and distribution of flux barriers in the rotor. However, rotor topology which provides the best electromagnetic performance might not be suitable for high speed applications. In high speed machines, the rotor has to withstand huge stress in its parts due to centrifugal forces. In [20] the author investigated structural performance of the rotor at medium rotational speeds. Study on mechanical robustness of the rotor at high rotational speeds lead the author to obtain a unique robust rotor with dovetail design flux barriers.

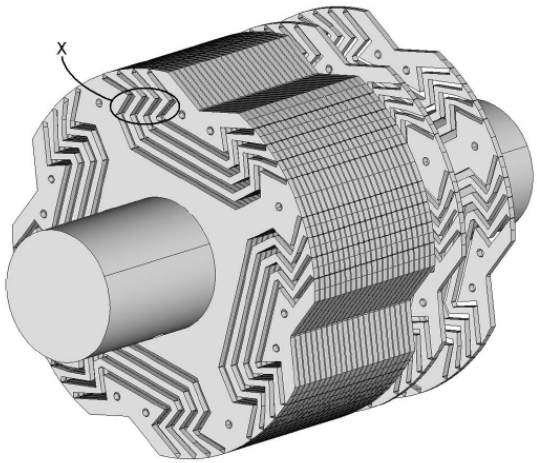

Fig. 3.39 Construction of rotor with modified flux barriers [20]

The rotor in the machine presented in this work uses optimized flux barriers constructed using Zhukovski's function. In order to make the rotor construction more robust and capable of operating at high speeds, additional parts called ribs, have to be introduced to the topology as shown in Fig. 3.40.

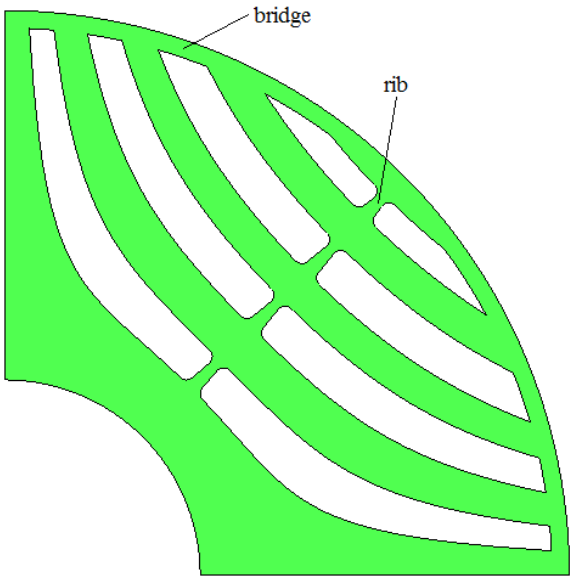

Fig. 3.40 One pole of rotor with ribs in flux barriers

Introducing ribs in flux barriers reduces performance of the machine. Inductance in q axis increases because the ribs provide additional path for the flux in q axis. This causes the saliency ratio to drop and as a result, the torque decreases. For that reason, the ribs should be placed only in crucial places in the rotor, and should be as thin as possible. Thicker ribs make the rotor capable of operating at high speeds but the performance significantly drops, this is why for a given maximum speed and safety factor, optimal size and configuration of the ribs should be found. At high speeds, the diameter of the rotor should be small, in order to reduce centrifugal forces, but sometimes due to space limitations it is not possible to have a long machine. In that case, using additional ribs in rotor topology seems to be unavoidable. Structural analysis of the rotor was performed for this 12000 rpm since it is the maximum speed of the rotor.

Structural static analysis of rotor with three flux barriers and a cutout was performed in JMAG. The presence of the cutout caused the centrifugal force to decrease as the radius in q axis is smaller. Several modifications of this rotor topology were tested starting from the one without any ribs. In all tests, von Mises stress distribution was checked. Mechanical properties of steel sheet used in simulations are presented in Table 3.5.

TABLE 3.5 Mechanical properties of steel sheet

Parameter	Value
Density	7850 kg/m3
Young's Modulus	200000 MPa
Poisson's Ratio	0.266

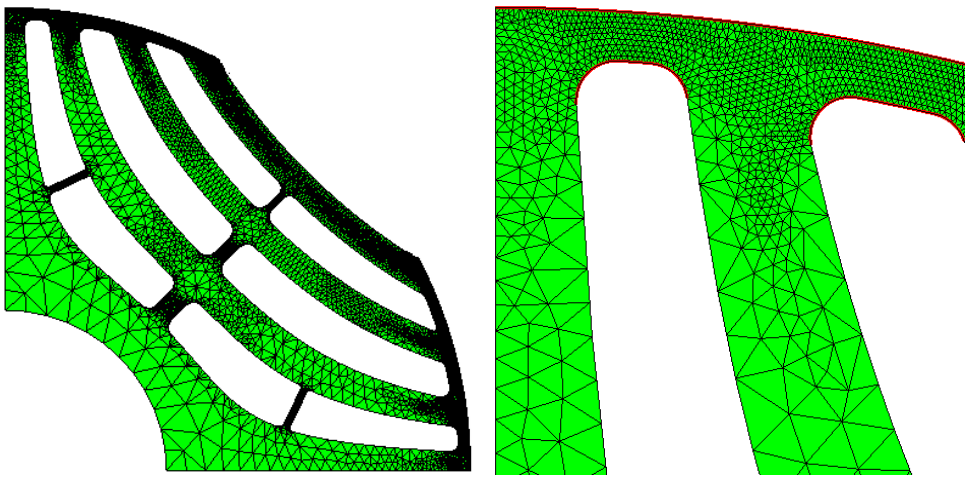

Fig. 3.41 Structural mesh of the rotor

Fig. 3.41. shows the mesh used to perform structural analysis of the rotor. Fine mesh around any corners and sharp edges is necessary in order to obtain reliable values of von Mises stress in those areas. This results in increased computational time but it is inevitable.

Results of structural analysis of the rotors are shown below. The initial topology was the rotor containing flux barriers without ribs since this topology provides the best electromagnetic behavior of the machine. At maximum rotational speed, von Mises stress was too high though hence ribs placement was necessary. In order to keep good magnetic performance of the machine, the ribs in the rotor should be as thin as possible but wide enough to withstand high centrifugal forces. Placing ribs in each flux barrier significantly lowered the maximum von Mises stress in the rotor. For more safety, additional ribs in the first flux barrier (closest to the shaft) were added.

In case of rotor with four flux barriers, the flux barrier which is the closest to the air-gap does not have a rib since von Mises stress is very low in that area.

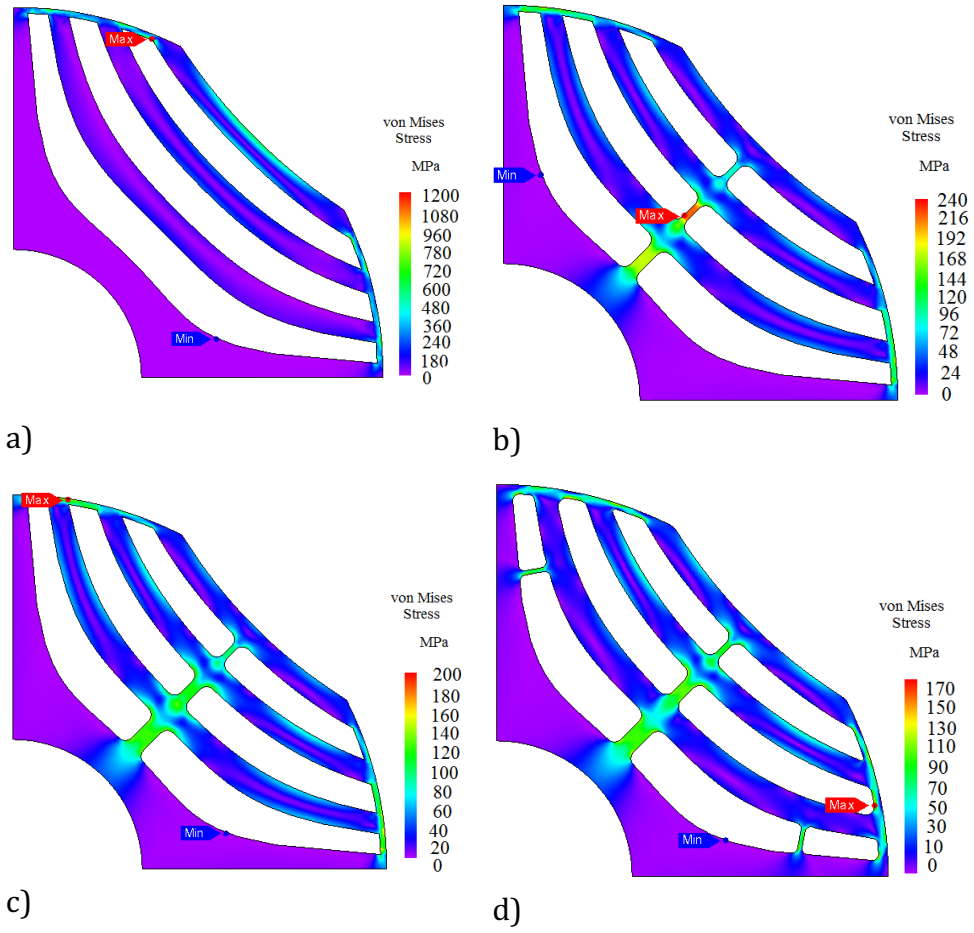

Fig. 3.42 Simulation results - distribution of von Mises stress: a) rotor with no ribs, b) rotor with three ribs, c) rotor with three ribs of higher thickness, d) rotor with five ribs

The critical value of von Mises stress of the material used in simulation is 250 MPa so the aim of the design was to achieve such a topology in which the maximum stress is lower than 250 MPa. Due to safety issues, a certain value of safety factor has to be obtained. Safety factor is defined

as: $\frac{\sigma_c}{\sigma_{max}}$ where σ_c is the critical value of stress (at which the material brakes) and σ_{max} is the maximum stress occurring in the material due to internal forces. Maximum values of von Mises stress of rotor topologies shown in Fig. 3.42 for rotational speeds from 600 rpm to 12000 rpm with 600 rpm step are presented in Fig. 3.43.

The highest von Mises stress occurs in the rotor without any ribs. Since all the flux paths in the rotor are attached to each other by the rotor bridges, they are the parts of the rotor where the highest von Mises stress occurs. The ribs located in flux barriers take a part of the mechanical load from the bridges and thus significantly limit the maximum value of von Mises stress occurring in the rotor. Geometry data of four rotor topologies together with maximum stress occurring in the rotor are presented in Table 3.6.

One can observe that the highest stress occurs in rotor's bridge. Red color means that the stress achieves or exceeds the maximum allowed stress of 250 MPa.

One can see that maximum von Mises stress achieves the highest values in rotor without ribs which makes this topology unable to work at very high speeds. Safety factor for all rotor topologies is presented in Fig. 3.44. Since the safety factor achieves very high values at low speeds, Fig. 3.44 shows the values of safety factor starting from 3000 rpm. When safety factor equals 1, the maximum von Mises stress achieves the value of critical stress which results in damaging of the construction. Rotor without ribs can withstand rotational speeds up to 5400 rpm. In Fig. 3.44, safety factor for rotor without ribs at 5400 rpm is 1.05 which means that the construction is very close to brake. In practice, such low safety factor is not allowed which makes the maximum speed of the rotor even lower.

TABLE 3.6 Geometry parameters of four rotor topologies and maximum stress in the rotor

Rotor type	**Part name**	**Width**	**Maximum stress at 12000 rpm**
Rotor without ribs	First bridge	1 mm	1175 MPa
	Second bridge	1 mm	
	Third bride	1 mm	
Rotor with three ribs - Fig. 3.42b	First bridge	1 mm	224 MPa
	Second bridge	1 mm	
	Third bridge	1 mm	
	First rib	2 mm	
	Second rib	1 mm	
	Third rib	1 mm	
Rotor with three ribs - Fig. 3.42c	First bridge	1 mm	199 MPa
	Second bridge	1 mm	
	Third bridge	1 mm	
	First rib	3 mm	
	Second rib	2 mm	
	Third rib	1 mm	
Rotor with five ribs - Fig. 3.42d	First bridge	1.5 mm	168 MPa
	Second bridge	1.2 mm	
	Third bridge	1 mm	
	First rib (middle)	3 mm	
	Side ribs (first flux barrier)	0.7 mm	
	Second rib	2 mm	
	Third rib	1 mm	

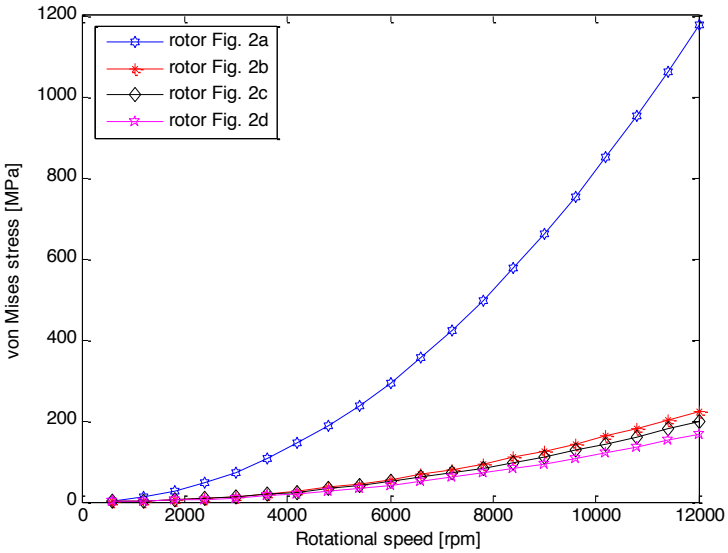

Fig. 3.43 Simulation results - distribution of von Mises stress

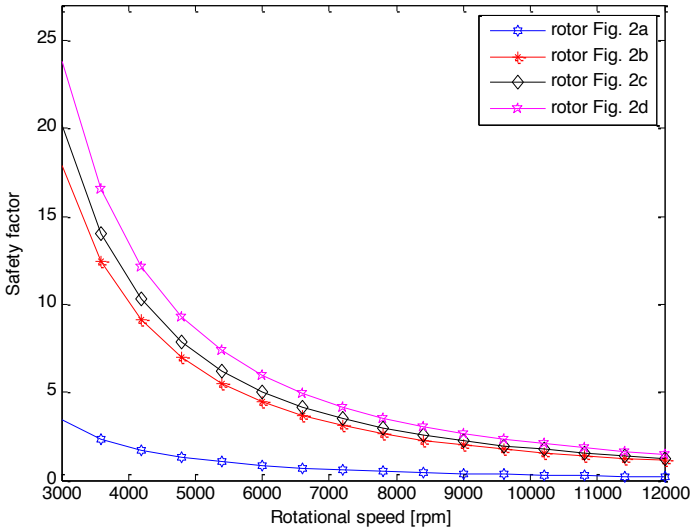

Fig. 3.44 Safety factor

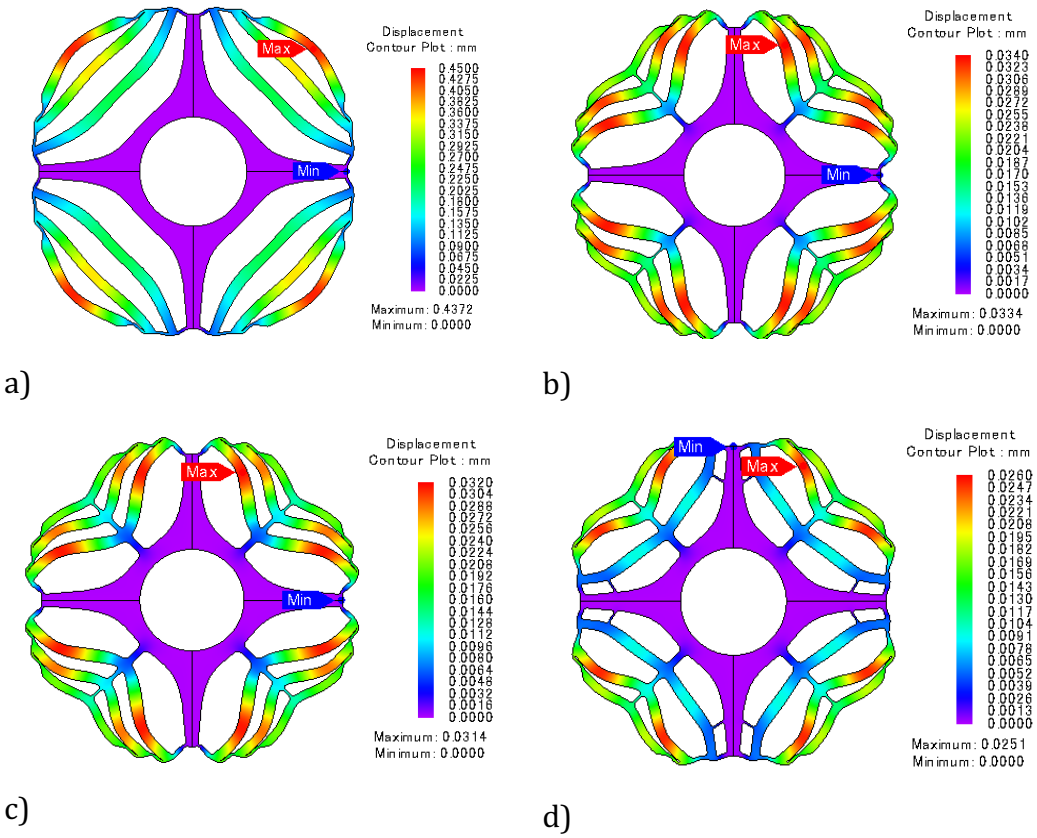

Fig. 3.45 Rotor's deformation and displacement

Fig. 3.45 shows deformation of the rotor and displacement of rotor's parts at 12000 rpm due to centrifugal force. The highest displacement occurs in rotor without ribs. The maximum value of displacement is 0.4372 mm. Rotors with ribs (Fig. 3.45 b and c) have maximum displacements equal to 0.0334 mm and 0.0314 mm respectively. Fourth topology of rotor has maximum displacement equal to 0.0251 mm.

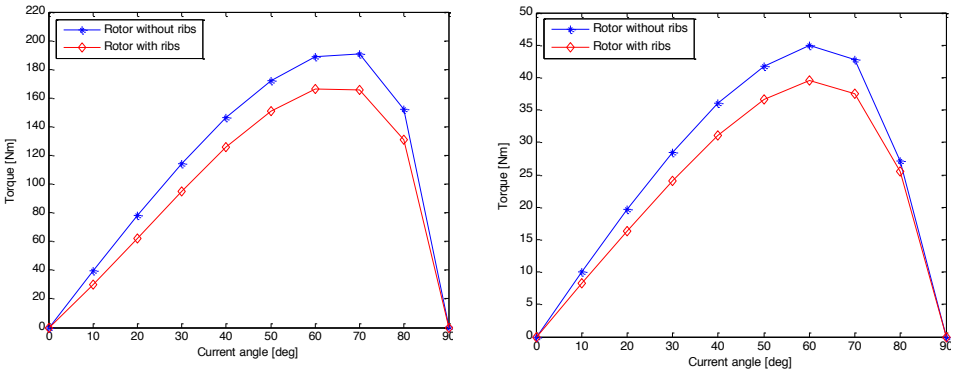

Fig. 3.46 Torque comparison at 4500 rpm (left) and 12000 rpm (right)

Ribs in flux barriers of the rotor, affect electromagnetic properties of the machine. In order to see the influence of the ribs, two magnetic transient simulations were performed for peak power - at 4500 rpm and at 12000 rpm. Torque comparison is shown in Fig. 3.46 for 4500 rpm and 12000 rpm respectively. Two rotor topologies were considered when performing electromagnetic simulations - rotor without ribs and rotor with ribs shown in Fig. 3.42 d) since this topology provides the highest safety factor. One can see that introducing the ribs decreases the torque. Maximum torque at 4500 rpm for rotor without ribs is 190.4 Nm and for rotor with ribs maximum torque is 166.2 Nm. When operating at 12000 rpm, maximum torque for rotor without ribs is 44.95 Nm and for rotor with ribs maximum torque is 39.52 Nm.

Noise and vibration is another important aspect in electric machines. Basic sources of machine's noise are [84]:

- Electromagnetic source
- Mechanical source
- Aerodynamic source

Sound is a wave in flexible environment. Sound waves can be divided by frequency:

- Infrasound - up to 20Hz
- Low frequency - 20Hz to 40Hz
- RF - 8kHz to 16kHz
- Ultrasound - 20kHz over

The frequency range of audible sound for human ear is from 20Hz to 20kHz. Noise and vibration of electrical machines is a well documented issue in the literature [85]. The noise from electromagnetic source is the main nosie component of electric machines. Machines nowadays are supplied from power converters which improves their speed and torque control capabilities. The converters use pulse width modulation method which apart from the motor driving fundamental component also generate high frequency components [85]. These components are present in stator currents and magnetic flux. The variable magnetic field passing through each phase creates forces on stator poles. The stator deformations are one of the main sources of vibration and noise in the SynRM [40], [86], [87]. Acoustic noise is caused by the pressure fluctuation imposed by the deformations of the motor's outer surface which cause the surrounding air to move. Only the laminated stator core has been taken into account in this study. Therefore, the impact of the housing with the cooling jacket, end windings and the end caps is neglected. Forces created by each phase which act on stator pole are related to magnetic field distribution in the machine. The magnetic field distribution in turn depends on the magnetic circuit of the machine. It is possible that machine with desired electromagnetic parameters can at the same time have very high vibration and noise which might not be acceptable for electric drive application. This is why to obtain required parameters of the machine, coupled electromagnetic-vibroacoustic multi-physics design approach should also be used. The equation of motion of a generic multiple-degree-of-freedom structural system in the time-domain is described as:

$$[M]\{\ddot{x}(t)\} + [C]\{\dot{x}(t)\} + [K]\{x(t)\} = \{F(t)\} \tag{3.3.4}$$

where $[M]$, $[C]$ and $[K]$ are respectively the global mass, damping and stiffness matrices $x(t)$ is a displacement at a given degree of freedom and $F(t)$ is the excitation force. The unforced and undamped equation of motion transformed to Laplace domain is of the form:

$$([K] - \omega^2[M])X(\omega) = 0 \tag{3.3.5}$$

The solution of this equation in Laplace domain results in eigenvectors Φ_n and eigenvalues being resonance frequencies ω_n. An approximate forced response of equation (3.3.6) for lightly damped structures can be computed using the formula below:

$$X(\omega) = \sum_{n=1}^{N} \frac{\Phi_n^T F(\omega) \Phi_n}{(\omega_n^2 - \omega^2 + i2\xi_n \omega \omega_n)} \tag{3.3.6}$$

Forced response of a continuous structure such as machine's stator can be found by means of modal analysis. The idea of modal analysis is based on simplification of the solution of a multi-degree freedom system.

Analytical approach of modal analysis is well known for basic structures such as plates, beams or rings. The equation of motion for vibrating thin ring is defined as [88]:

$$\frac{EI}{R^4}\left(\frac{\partial^2 u_\theta}{\partial \theta^2} - \frac{\partial^3 u_3}{\partial \theta^3}\right) + \frac{Ehg}{R^2}\left(\frac{\partial^2 u_\theta}{\partial \theta^2} + \frac{\partial u_3}{\partial \theta}\right) + q_\theta = \rho g h \frac{\partial^2 u_\theta}{\partial t^2} \tag{3.3.7}$$

$$\frac{EI}{R^4}\left(\frac{\partial^3 u_\theta}{\partial \theta^3} - \frac{\partial^4 u_3}{\partial \theta^4}\right) - \frac{Ehg}{R^2}\left(\frac{\partial u_\theta}{\partial \theta} + u_3\right) + q_3 = \rho g h \frac{\partial^2 u_3}{\partial t^2} \tag{3.3.8}$$

where E is Young's Modulus, ρ is mass density, g is the size of the ring along z axis, h is ring thickness and I is the moment of inertia of the rectangular cross section:

$$I = \frac{gh^3}{12} \tag{3.3.9}$$

Geometry of the ring is shown in Fig. 3.48.

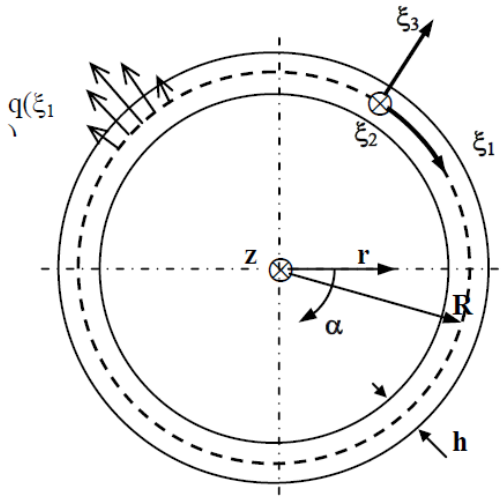

Fig. 3.47 Geometry of the ring [88]

Modeling of stator lamination vibration using equations defined above is usually done by increasing the ring density which represents the presence of the teeth and winding. This approach unfortunately brings error for low orders [88]. The author presented another method of analytical modeling of stator lamination vibration. Modeling the behavior of stator teeth is based on assumption that they follow the local yoke displacement in form of the rigid body motion and they only change the inertia of the ring. During vibration of the stator, bending is the dominant type of deformation. This means that displacement radial component along neutral surface achieves positive and negative values. At the same time the neutral plane remains stress free [88]. The increase of angular inertia of continuous ring caused by the discrete set of teeth can be done in few steps. At the beginning the real shape of a single tooth should be reduced to a rectangle as shown in Fig. 3.48 [88]. The inertial term related to displacements have to be increased by the ratio k_p due to the presence of the stator teeth.

$$k_p = 1 + \frac{Q b_z h_z}{2\pi R h} \tag{3.3.10}$$

In equation (3.3.10), Q is the number of stator teeth, h_z and b_z are shown in Fig. 3.48. and R and h are shown in Fig. 3.47. The moment of inertia of

the cuboid substituting the stator tooth, against z_n axis (Fig. 3.48) is of the form:

$$J_{zn} = \rho I_{z0}\left[1 + \left(\frac{b_z}{h_z}\right)^2 + 3\left(1 + \frac{h}{h_z}\right)^2\right] b_z \tag{3.3.11}$$

Since the ring equation requires continuous properties, the inertia of the tooth must be spread along slot pitch measured on neutral layer. It can be added to the yoke moment of inertia. This can be done by multiplying the value of I (eq. 3.3.9) by a factor equal to:

$$k_I = 1 + \left(\frac{h_z}{h}\right)^3\left[1 + \left(\frac{b_z}{h_z}\right)^2 + 3\left(1 + \frac{h}{h_z}\right)^2\right]\frac{Q b_z}{2\pi R} \tag{3.3.12}$$

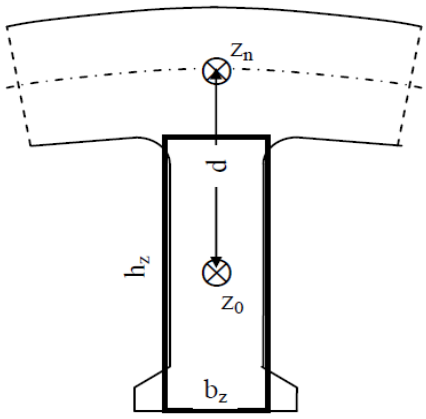

Fig. 3.48 Simplified geometry of lamination tooth [88]

Analytical methods of modes calculation provide fast and quite accurate estimation of natural frequencies of a structure. However, their accuracy may vary depending on the structure's mode order. To predict stator's natural frequencies more precisely, finite element method should be used. Moreover, calculation of normal modes is the first step of NVH analysis of the stator. The structure of the stator is continuously excited by magnetic forces. During the numerical analysis, only the radial component of magnetic forces is considered since this component is responsible for structure's deformation. NVH analysis was performed in

VirtualLAB® which is a dedicated software for acoustic and vibration analysis. Radial magnetic forces were calculated in JMAG and exported to *.unv* file. Since the structural mesh and electromagnetic mesh were different, the radial forces had to be mapped from electromagnetic mesh to structural mesh using dedicated algorithm in VirtualLAB®. In order to obtain good frequency resolution, signal of magnetic radial forces was multiplied using digital signal processing tool in VirtualLAB®. Sampling time was adjusted to the rotational speed so at high speeds obtained signals are accurate enough.

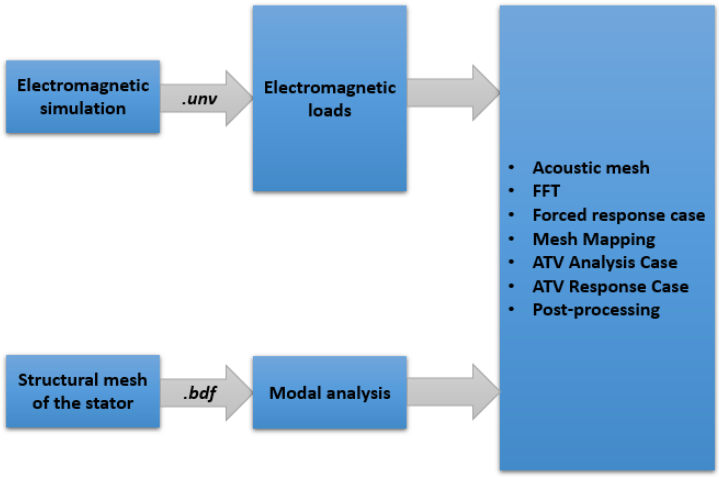

Fig. 3.49 Workflow diagram of NVH analysis

Fig. 3.49. presents the workflow of NVH analysis of electric machines. Magnetic radial forces obtained from electromagnetic simulation are transferred as *.unv* files to analysis in VirtualLAB®. The geometry of analyzed structure must be created and properly meshed. Next, modal analysis of the structure needs to be performed. After creating acoustic mesh and performing forces mapping, electromagnetic and structural analysis results can be combined together and acoustic behavior of the machine can be simulated. This is done by using ATV analysis. All the steps will be described in the following sections.

Stator as a continuous structure has an infinite number of freedom and thus the infinite number of resonance frequencies. In numerical simulations only the relevant ones are considered. Using modal decomposition, it is possible to simplify the solution of a multi-degree

freedom system by substituting in with a set of single degree freedom systems. The basis of this simplification are eigenvectors. After modal decomposition, the equations are completely decoupled.

3.5. Topology of the Machine and NVH Behavior

As shown in previous chapters, magnetic field in the machine depends on its magnetic circuit. Number of stator slots and rotor flux barriers affect electromagnetic performance of the machine. Depending on the topology of the machine, air gap magnetic field might contain various spatial harmonics [64]. Spatial and time harmonics of magnetic field interacting with each other generate high frequency components of torque and magnetic forces. This clearly indicates that machines topology should affect the generated noise. This case was investigated by performing numerical simulations for different SynRM topologies.

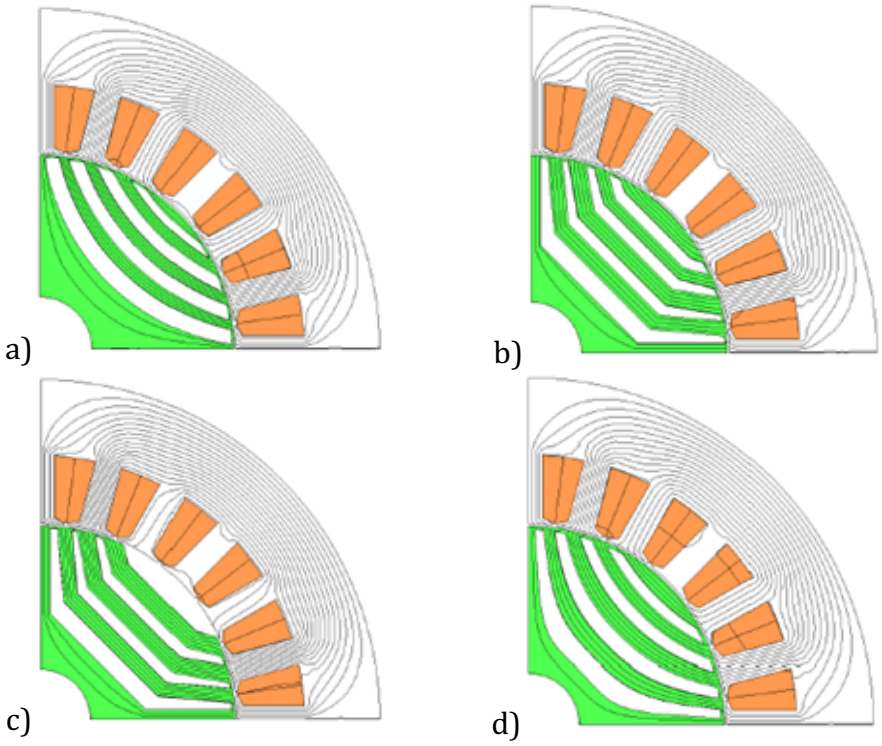

Fig. 3.50 One pole of the 1st (a), 2nd (b) 3rd (c) and 4th (d) rotor topologies with flux lines

To investigate how the noise of the machine is related to its construction, some theoretical studies were performed. Synchronous reluctance machine with four different rotor topologies was designed and simulated to check the influence of machines construction on noise generation. These topologies are presented in Fig. 3.50. First rotor has four round flux barriers and the flux barriers of the second rotor are rectangular. Third rotor has three flux barriers and a cut-off. The last rotor topology has four optimized flux barriers. Torque ripple varied with each rotor and speed. Optimized flux barriers provided the lowest value of torque ripple but even that value was quite high. Torque ripple values for each topology occurring at certain speed are presented in Table 3.7.

TABLE 3.7 Torque ripple comparison [39]

Speed [rpm]	**Torque Ripple [%]**			
	Rotor 1	**Rotor 2**	**Rotor 3**	**Rotor 4**
1600	32.9	34.8	37.6	18.7
2000	32.4	34.8	37.2	18.6
2400	33.9	34.5	36.9	18.8
2800	33.3	32.6	36.3	18.1
3200	35.3	28.5	39.6	21.0
3600	33.4	34.1	36.9	18.6
4000	34.8	39.0	39.1	20.8
4400	31.5	30.2	34.9	16.8
4800	32.5	34.2	36.8	19.0

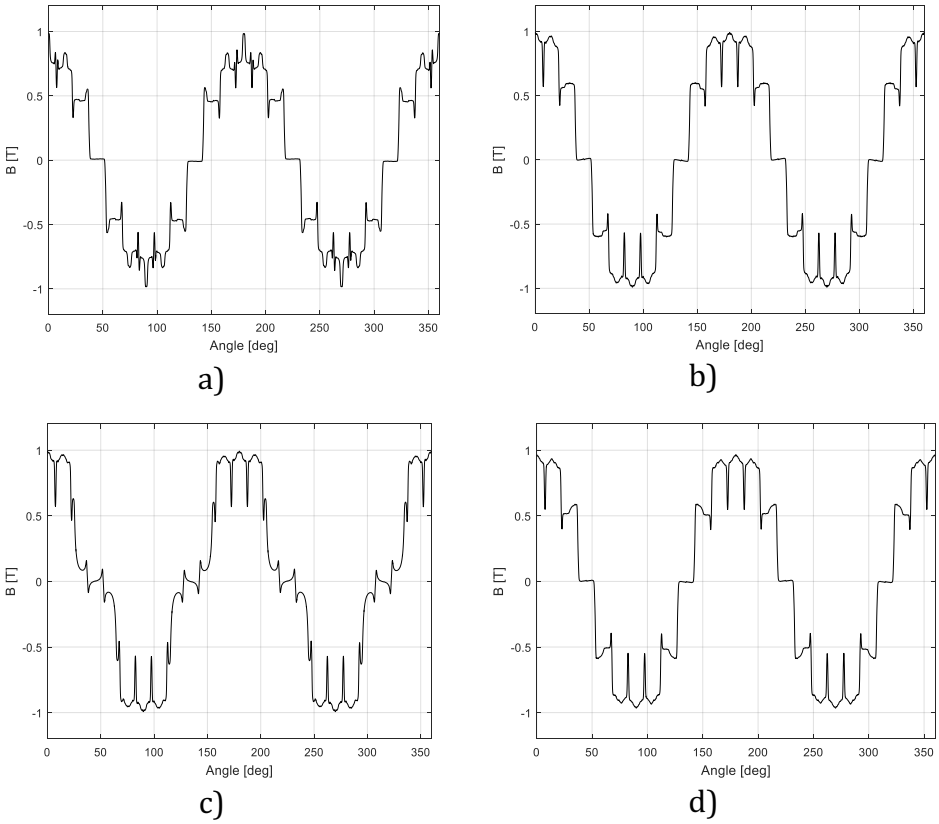

Fig. 3.51 Magnetic field distribution in the air gap for d axis stator MMF: a) first topology, b) second topology, c) third topology and d) fourth topology

Fig. 3.51. shows the magnetic field distribution in the air-gap. The air-gap field was calculated for d axis stator MMF to show how rotor's topology affects the permeance of the machine's magnetic circuit. It can be observed that air-gap field is similar for second and fourth topology (Fig. 3.51b and Fig. 3.51d respectively).

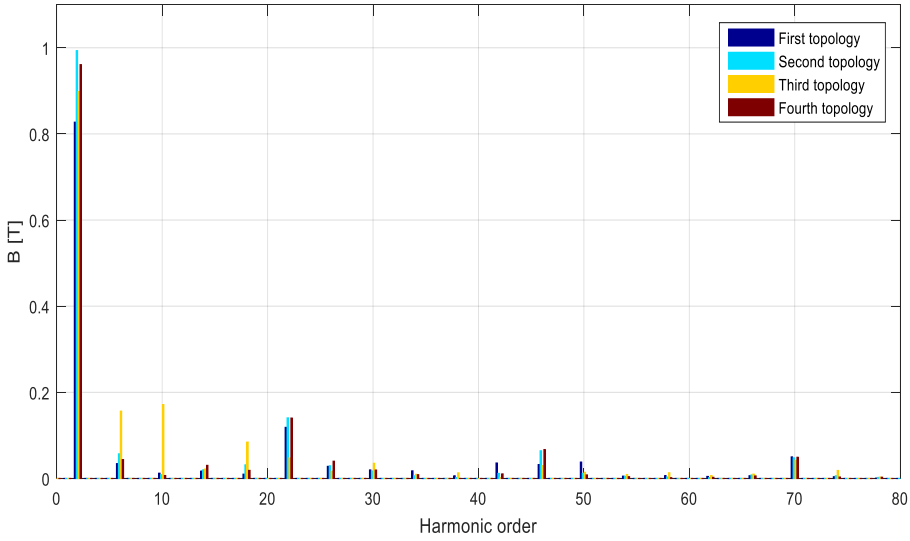

Fig. 3.52 Spatial harmonics of air-gap magnetic field [39]

Spatial harmonics of air-gap field are presented in Fig. 3.52. Third topology has the highest amplitudes of spatial harmonics from 5^{th} to 20^{th} order.

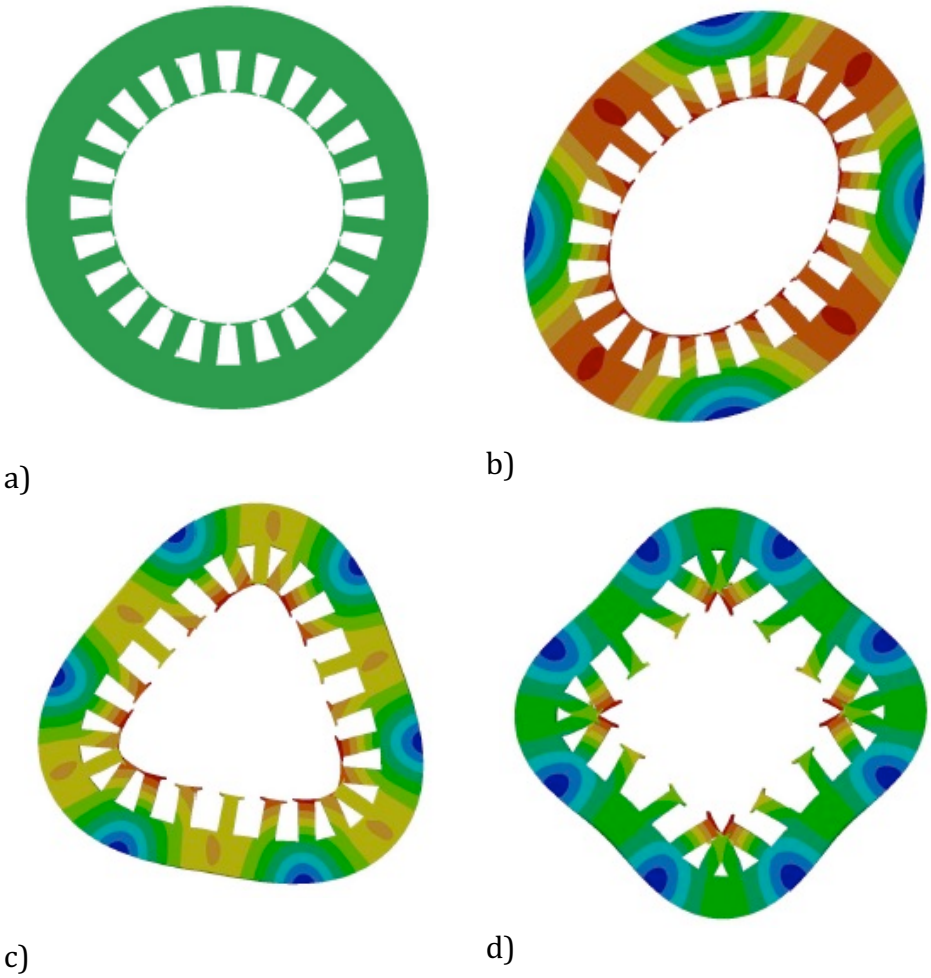

Fig. 3.53 Structural mesh a), ovalization mode 974 Hz b), triangular mode 2531Hz c) and square mode 4324 Hz d) of the stator [39]

Acoustic response of the machine can be found by solving equation (3.3.5) in order to collect natural modes of the stator. Three main normal modes together with undeformed stator's structure are shown in Fig. 3.53. Each normal mode has its own natural frequency. The normal modes of the stator together with their natural frequencies were found by means of the finite element analysis performed in Virtual.Lab®.

Numerical analyses performed for each SynRM topology assume the steel constituting the stator core to follow an isotropic behavior with the following mechanical parameters: Young's modulus of $1.85 * 10^{11}\ \frac{N}{m^2}$,

Poisson coefficient of 0.287 and mass density of 7650 $\frac{kg}{m^3}$. Therefore, the shifts of natural frequencies that can be noticed while assuming isotropy instead of orthotropy [89] or transversally-anisotropy [90], are not taken into account. Additionally, the windings and the stacking factor are not taken into consideration. As mentioned in [91], these assumptions might lead to a non-negligible shift of eigenfrequencies. However, in the purpose of comparison of rotor topologies, this analysis becomes relevant.

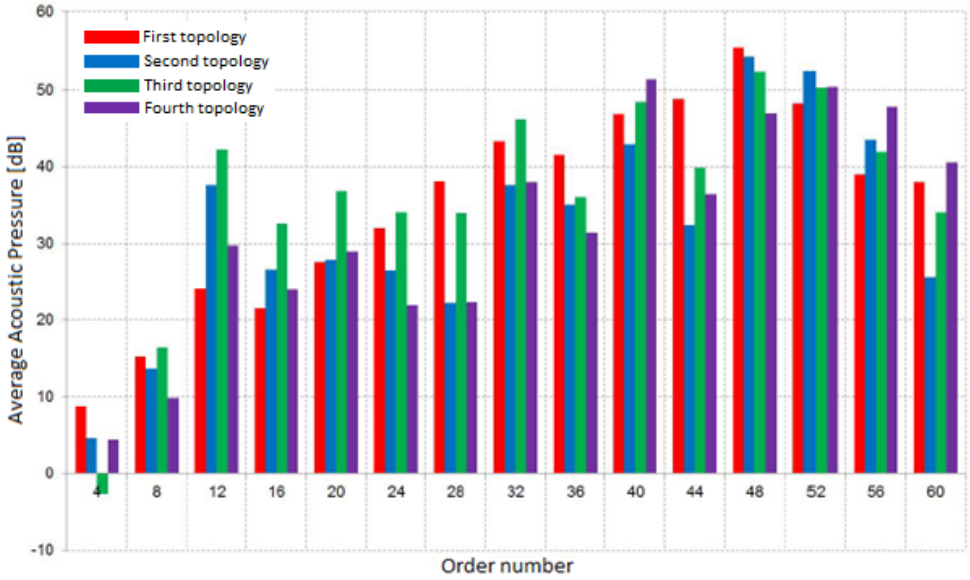

Fig. 3.54 Acoustic pressure for each harmonic order [39]

Fig. 3.54 shows acoustic pressure for each harmonic order of all topologies. One can see that the acoustic pressure values vary depend on the harmonic order and it is hard to select one topology which generates the highest acoustic pressure.

Once the equation (3.3.5) is solved, the structural response can be computed through equation (3.3.6). Acoustic pressure at a chosen sink (i.e. a microphone) can be obtained by computing acoustic transfer vector (ATV) response case. ATV is defined as [92]:

$$\begin{bmatrix} p_1 \\ p_2 \\ \vdots \\ p_i \\ \vdots \\ p_m \end{bmatrix} = \begin{bmatrix} \Omega_{1,1} & \Omega_{1,2} & \cdots & \Omega_{1,j} & \cdots & \Omega_{1,n} \\ \Omega_{2,1} & \Omega_{2,2} & \cdots & \Omega_{2,j} & \cdots & \Omega_{2,n} \\ \vdots & \vdots & \ddots & \vdots & \ddots & \vdots \\ \Omega_{i,1} & \Omega_{i,2} & \cdots & \Omega_{i,j} & \cdots & \Omega_{i,n} \\ \vdots & \vdots & \ddots & \vdots & \ddots & \vdots \\ \Omega_{m,1} & \Omega_{m,2} & \cdots & \Omega_{m,j} & \cdots & \Omega_{m,n} \end{bmatrix} \begin{bmatrix} v_1 \\ v_2 \\ \vdots \\ v_j \\ \vdots \\ v_n \end{bmatrix} \quad (3.3.13)$$

ATV is defined as the transfer function between the normal nodal velocity and the acoustic pressure at field points. The sound power was computed at a microphone located one meter away from the stator. In equation (3.3.13) p_i is the acoustic pressure at field point i and v_i is the actual normal velocity at node j, m is the number of field points and n is the number of nodes in boundary elements. The acoustic pressure at field point i due to unit normal velocity at node j is represented by $\Omega_{i,j}$. It is worth mentioning that all the variables in equation (3.3.13) are frequency dependent. Moreover, the variables are complex. For a given frequency and given geometry, the ATV matrix is constant and does not depend on loading condition.

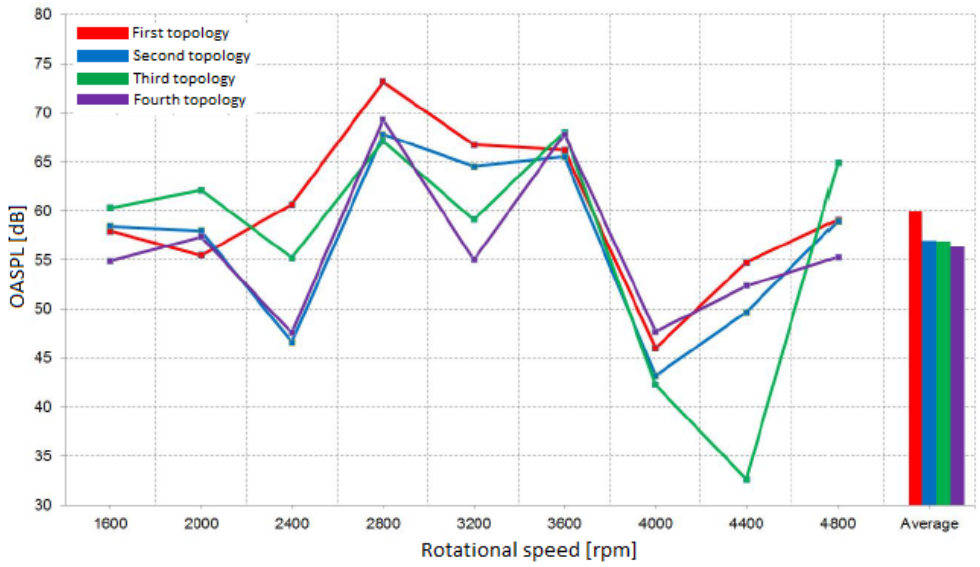

Fig. 3.55 OASPL [39]

The overall sound pressure level (OASPL) for each topology at selected rotational speeds shown in Fig. 3.55. is not impacted by the torque ripple. As one can see, it is hard to find any correlation between the torque ripple and the OASPL value. The OASPL is define as [39]:

$$OASPL_N = 10 \log 10 \left(\int_{f_{min}}^{f_{max}} S_N(f) df \right) \tag{3.3.14}$$

Presented results show that noise generated by the machine barely depends on the machine's torque ripple. The torque is produced by the tangential component of the magnetic force hence torque ripple is associated with variations of this component. However, the sound generated by the stator structure due to is deformation is caused by the radial component of the magnetic force. This means that when optimizing the machine design for acoustic behavior or choosing a control strategy, one should minimize the radial forces acting on the stator in order to decrease the noise generated by the machine.

3.6. Thermal Analysis

In the field of electric machine design, lots of effort is put to improve machine's efficiency. There is a high pressure on the research and development of highly efficient, robust and cheaper machines. Along with these demands, nowadays there is also an issue of motor downsizing due to increasing interest in electric vehicles.

Machines of high power at reduced size are exposed to higher current densities which cause serious problems with heat dissipation. This aspect draws the attention of design engineers, who have to include thermal design part along with electromagnetic design of the machine.

The temperature is the main factor determining how much electrical load the machine can withstand and how long the machine can operate at peak power. Excessive heat generated in the machine can lead to accelerated fatigue of insulation, cause mechanical stresses in the structure which can result in mechanical failure or change of geometry. High temperature also decreases machine's performance. Winding resistance rises with temperature and permanent magnet machines

generate less torque due to demagnetization of the magnets. In the past when computers did not have such a computational power as nowadays, motor sizing was traditionally made using D^2L, D^3L and D^xL sizing equations. This method did not include thermal analysis of the machine. It was done by the designer who used appropriate current density values obtained from past experience to prevent overheating [29]. At that time, only simple thermal networks based on lumped parameters were available for thermal analysis. This was a serious limitation in optimization and downsizing of the machine. When computer analysis was introduced to machine design, the complexity of thermal networks significantly increased.

3.6.1. Power Losses in Electrical Machines

The losses in electric machine can be divided into resistive losses, iron losses in stator and rotor's magnetic circuit and additional mechanical losses.

A. Resistive losses

Resistive losses also known as Joule losses occur when an electric current passes through a conductor of a specified resistance. They are proportional to the product of the resistance R and square of the current I. For a winding of m phases, the losses have to be multiplied by the number of phases.

$$P = mRI^2 \tag{3.4.1}$$

Resistive losses change with temperature since the resistance changes with temperature. For most of the metals, the resistance rises linearly with temperature.

$$R_T = R_0(1 + \alpha\Delta T) \tag{3.4.2}$$

where R_T is the resistance at temperature T, R_0 is resistance at reference temperature, α is resistance temperature coefficient and ΔT is temperature change. The power loss in the winding is the major source

of heat. The common approach of thermal analysis of electric machines relies on the assumption of equivalent winding DC power loss for a single point. However this approach is only valid for machines where ac power loss is negligible. Proximity and skin effects contribute to AC winding power loss [93]. Winding power loss at AC operation can be described by simplified expression which includes three main components:

$$P_{AC}(I,f,T) = P_{DC}(I,T) + P_{AC\,effE}(I,f,T) + P_{AC\,effR}(f,T) \tag{3.4.3}$$

Where P_{DC} is the DC winding power loss, $P_{AC\,effE}$ is the power loss related to AC effects resulting from the winding excitation and $P_{AC\,effR}$ is the winding power loss component caused by rotation of the rotor assembly. The winding loss component related to rotation of the rotor is assumed to be independent of the winding excitation. The DC and AC power loss components vary with temperature in different manners. The AC component of power loss varies with temperature in quite complex manner which can be approximated by:

$$P_{AC|T} = P_{DC|T_0}\big(1+\alpha(T-T_0)\big) + P_{DC|T_0}\frac{\left(\frac{R_{AC}}{R_{DC}}\right)|_{T_0} - 1}{\big(1+\alpha(T-T_0)\big)^{\beta}} \tag{3.4.4}$$

where $\frac{R_{AC}}{R_{DC}}$ is the equivalent AC to DC resistance ratio and β is the AC loss component temperature coefficient derived from curve fitting of (3.4.4).

B. Iron losses

Iron loss can be of two types: hysteresis and eddy current loss. When some part of magnetic circuit is magnetized by external magnetic field, the molecules are aligned in the same direction. When the external magnetic field is reversed, the alignment of the molecules takes the opposite direction. The internal friction of the molecular magnets counteract the reversal of magnetism which results in magnetic hysteresis. In order to overcome this internal friction also known as residual magnetism, some part of the magnetizing force has to be used. This work, done by the magnetizing force generates heat; this waste of energy in the form of heat is called the hysteresis loss. Alternating

magnetic flux induces voltages in iron core which causes eddy currents to flow in the core. These currents oppose changes of the flux and moreover they prevent the magnetic flux from penetrating the object. In order to eliminate the eddy currents, stator and rotor cores of the machine are made of thin steel sheet laminations. The magnitude of core power loss is strongly influenced by the machine topology and the machine's operating cycle. The most common method of core loss computing during design and analysis of an electric machine is based on the Steinmez and Bertotti approaches. These methods nowadays are usually implemented within FEA software packages [93].

The hysteresis and eddy current losses can be computed separately, but the manufacturers of steel sheets usually combine the data about the losses. The power losses of steel sheets are given per mass unit at a specified maximum value of magnetic flux density and frequency. To obtain iron losses of an electric machine, the magnetic circuit is divided into a certain number of sections where the magnetic flux has approximately constant value. The losses of each section of the machine can be calculated from:

$$P_{Fe,n} = P_{10}\left(\frac{B_n}{1T}\right)^2 m_{Fe,n} \text{ or } P_{Fe,n} = P_{15}\left(\frac{B_n}{1.5T}\right)^2 m_{Fe,n} \qquad (3.4.5)$$

where $m_{Fe,n}$ is mass of nth section of the machine.

The total iron losses of a machine are calculated as sum of power losses of all sections of the machine. The problem is that the iron loss data is valid only for sinusoidal flux variations. In electric machines however, magnetic flux variations are never purely sinusoidal. In this case the losses can be estimated using empirical correction coefficients $k_{Fe,n}$ [94].

$$\begin{aligned} P_{Fe,n} &= \sum_{n=1}^{N} k_{Fe,n} P_{10}\left(\frac{B_n}{1T}\right)^2 m_{Fe,n} \text{ or } P_{Fe,n} \\ &= \sum_{n=1}^{N} k_{Fe,n} P_{15}\left(\frac{B_n}{1.5T}\right)^2 m_{Fe,n} \end{aligned} \qquad (3.4.6)$$

Various power loss coefficients associated to computational technique and core loss mechanisms are derived from the specific power loss data provided by the manufacturer of the material. In most cases the coefficients refer to hysteresis loss, Joule's (eddy current) loss and excess

loss. In the literature it has been reported that manufacture process of laminated core packs has a significant impact on the core losses. It also has been proven that elevated laminated core material temperature has a moderate influence on the power losses.

C. Mechanical losses

Mechanical losses components are usually neglected or are subjected to some base assumptions and approximations considering their contribution to overall power losses of the machine. An insight into the mechanical losses is usually based on hardware tests. Mechanical losses from machine's bearings are usually obtained empirically. The most commonly used bearings in electric machines are roll bearings. A common approach of power loss estimation is to use bearing loss data provided by the manufacturer. Another mechanical loss component is windage/drag losses. This type of power losses is linked to the aerodynamic effects related to rotor's rotation. These aerodynamic effects are hard to analyze. The latest research in this field is limited to some selected aspects such as machines with forced air or liquid cooling of the rotor or high speed applications. In general, the research shows that mechanical losses might have a significant effect on the overall machine's power losses. Windage power loss can be estimated using existing analytical approximations which rely on gained experience and empirical tests. Example analytical formula applicable for the windage loss calculation of a smooth cylinder rotating within a concentric cylinder is presented below:

$$P_{windage} = \pi C_d \rho R^4 \omega^3 L \tag{3.4.7}$$

where C_d is the skin friction coefficient, ρ is the air density, R is the rotor radius, ω is the angular speed and L is the active length of the stator-rotor assembly. Such simplified formulas are limited to specific machine topologies and operating conditions. In order to obtain more widely applicable approach, it is necessary to use computational fluid dynamics modeling techniques. Synchronous reluctance machine analyzed in this work contains smooth cylindrical rotor and concentric stator. In this case with stator slotting neglected, equation (3.4.7) can be applied in windage loss calculations. Although the rotor has flux barriers, laboratory tests

proved that there is no air flowing along the rotor through the flux barriers [95].

3.6.2. Heat Transfer

A. Conduction

If a temperature gradient exists in a body, the heat is transferred for the high temperature to the low temperature region. This type of energy transfer is called conduction and it is a transmission of energy between molecules in a medium. This process can be described by:

$$Q = G(T_i - T_j) \tag{3.4.8}$$

where Q is power flow, G is thermal conductance and T_i and T_j are temperatures of two adjacent nodes. There exist two mechanisms of heat transfer by conduction. In the first mechanism the heat can be transferred by molecular interaction in which the molecules with higher energy release energy for neighboring molecules at a lower energy via lattice vibration. This kind of conduction is possible between solids, liquids and gases. The second mechanism of conduction is the heat transfer between free electrons. This type of conduction is typical for liquids and pure metals in particular [94]. The thermal conductivity of solids is directly linked to the number of free electrons hence pure metals are the best heat conductors. The heat flow transferred by conduction is given by Fourier's law:

$$\Phi_{th} = -\lambda S \nabla T \tag{3.4.9}$$

where: Φ_{th} is the heat flow rate, λ is the thermal conductivity, S is the heat transfer area and ∇T is the temperature gradient. Materials with high electrical conductivity are in general also good thermal conductors. The insulators on the other hand are poor thermal conductors [94].

B. Convection

This type of heat transfer occurs in fluids and gases. Since the molecules have more freedom to move around the heat transfer is improved by the transportation of the molecules themselves. Convection is defined as the

heat transfer between a region of higher temperature and a region of cooler temperature that takes place as a consequence of motion of the cooling fluid relative to high temperature surface which at the molecular level, means that the warmer molecules displace the cooler fluid molecules [94]. To simplify the computation process, some dimensionless parameters have been generated. When calculating heat transfer from solid surfaces to the coolant, the most important parameters are the Nusselt number Nu, the Reynolds number Re and the Prandtl number Pr. Convection heat transfer coefficient α can be expressed with the dimensionless Nusselt Number as:

$$Nu = \frac{\alpha L}{\lambda} \tag{3.4.10}$$

where L is the characteristic surface length and λ is the thermal conductivity of the coolant. The Nusselt number describes the effectiveness of convection heat transfer compared to conduction heat transfer [94]. Reynolds number describes the ratio between inertia and viscous forces and is given by:

$$Re = \frac{vL}{\upsilon} \tag{3.4.11}$$

where: v is the speed of the coolant on the surface, L is the characteristic length of the surface and υ is the kinematic viscosity of the coolant. The third dimensionless number is the Prandtl number, which describes the relation between momentum and thermal diffusivity. The Prandtl number is given by:

$$Pr = \frac{c_p \mu}{\lambda} \tag{3.4.12}$$

where: c_p is the specific heat capacity, μ is the dynamic viscosity and λ is the thermal conductivity of the coolant. The convection heat transfer always takes place in the direction of a lower temperature. Convection can be of two types: forced and natural. In forced convection, external instruments such as pumps or blowers assist the flow of coolant. Natural convection occurs due to density variations caused by temperature differences. The density of a heated coolant changes which creates some currents in the coolant.

C. Radiation

The mechanism of radiation is based on emitted photons carrying energy. The level of radiation of a body depends on the emissivity of the

body, the surface area and strongly on the temperature. Heat radiation is electromagnetic radiation whose wavelength lies between 0.1 to 100 μm. This wavelength range includes visible light, infrared and ultraviolet. The radiation does not require a medium for heat exchange.

The energy transfer can be described by:

$$Q = G\left(T_i^4 - T_j^4\right) \tag{3.4.13}$$

When radiation meets an object, part of it is absorbed into the object, some of it is reflected back from the surface of the object and some of it might be transmitted through the object. This situation is illustrated in Fig. 3.56.

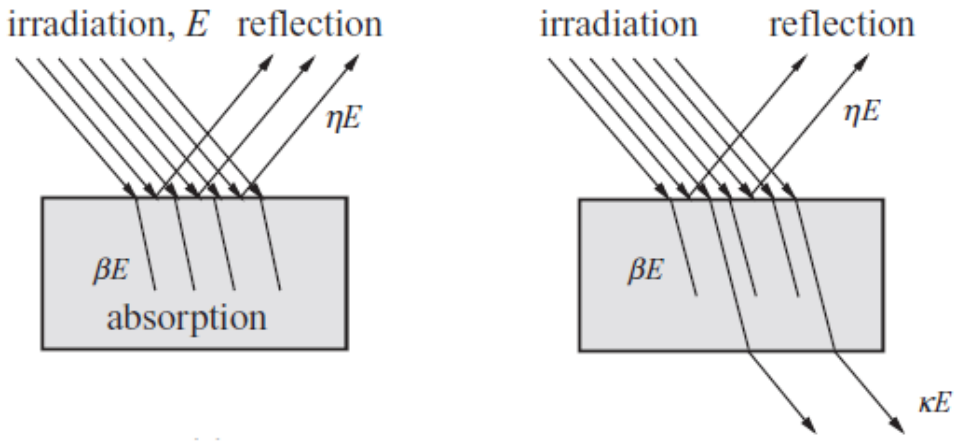

Fig. 3.56 Radiation: reflective surface (left) and semi-transparent surface (right) [94]

The rate of absorption of the radiation energy by the surface is called absorptivity β, the rate of reflection of energy is called reflectivity η and the rate of energy transmission is called transmissivity κ. The sum of these coefficients equals one.

$$\beta + \eta + \kappa = 1 \tag{3.4.14}$$

Air principally does not absorb or emit radiation hence the radiation from electrical machine to its surroundings and inside the machine can be assumed to occur only between two surfaces.

In electric machines the convection and radiation heat transfer mechanisms will contribute to the air gap and frame thermal resistances. The effects of radiation can be neglected in electric machines since it is rather small.

3.6.3. Thermal Analysis Methods

When dealing with thermal aspects of electric machines, heat flow calculation and temperature estimation can be done using thermal network (TN) based on lumped parameters, finite element method (FEM) or computational fluid dynamics (CFD).

Thermal model based on lumped parameters has been used for a long time for estimation of the temperatures in electric machines [96]. When performing the thermal analysis using lumped parameter model, the electrical machine is geometrically divided into lumped components. Each of the components has a certain thermal capacity and heat generation. The interconnections to neighboring components through are realized by linear mesh of thermal impedances. The lumped parameters are developed from the geometry of the machine and the thermal properties of the materials used in the design. The thermal circuit in steady-state condition consists of thermal resistances and heat sources connected between the nodes. For transient analysis, the heat thermal capacitances are introduced to take into account the time behavior of the internal energy. Heat transfer in electrical machines is a combination of conduction within solid and laminated components, and convection from surfaces which are in contact with air or other cooling fluids [96]. Lumped parameter TN is widely used and is constantly modified and improve. In [97] the lumped parameter thermal model was used to calculate temperature rise in permanent magnet synchronous machine. The authors took into account conductive heat transfer in slots and teeth, stator and rotor yokes, end-windings and permanent magnets. Convective heat transfer in air-gap, housing, end-plates, end-windings, inside and outside of the machine was also considered. In that study the main heat sources were considered Joule and iron losses.

In order to run a TN model of the machine, it is necessary to define thermal resistances of machine's parts. Thermal resistance of an object is calculated with respect to direction of heat flow. If an object is homogenous, its thermal resistance can be calculated as:

$$R = \frac{L}{\lambda A} \tag{3.4.15}$$

where L is length of an object in direction of heat flow, λ is thermal conductivity and A is cross sectional area. Some parts of an electric machine can be modeled as cylindrical shapes.

Approximating machine's parts with cylinders might sometimes not provide a good accuracy. To calculate a thermal resistance of an object whose shape is not homogenous, one can use the equation in integral form shown below:

$$R = \int_0^L \frac{dL_{path}}{\lambda A(L_{path})} \tag{3.4.16}$$

Example of a thermal network is presented in Fig. 3.57.

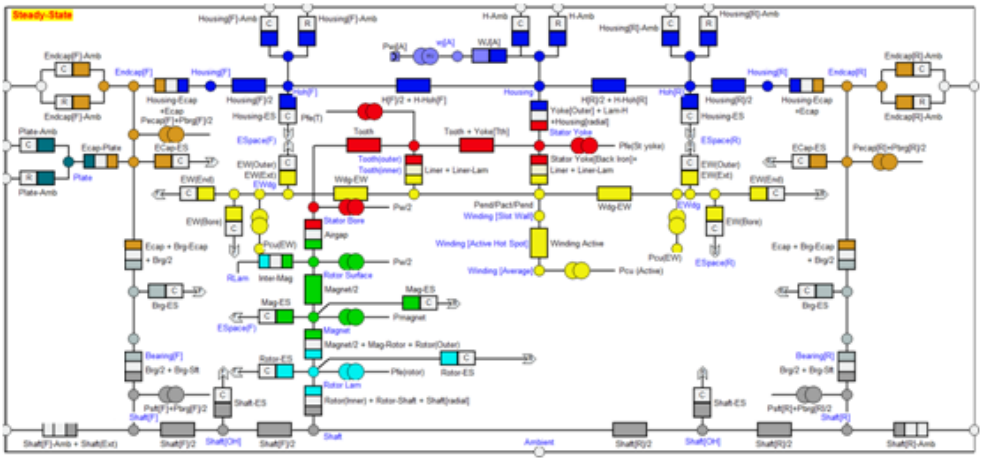

Fig. 3.57 Thermal network in MotorCAD

FEM-based models are more accurate than lumped parameter models and can provide high resolution of the temperature field but only if the heat conductivity and the specific heat is known accurately over the whole domain [98]. The lumped parameter model is the opposite to high

resolution FEM-based model. For a correct temperature estimation, the parameters used in the model have to be identified experimentally which is not useful during design process. For this reason, the authors introduced correction parameters for heat transfer coefficients or winding resistances. These correction parameters can be used during design process to predict machine's temperature rise. TN model is also used to calculate machine's temperature rise when operating with dynamic workloads [99]. The lumped parameter model provided quite accurate results in temperature prediction. The limitation of this model is the resolution of the discrete heat source network. When analyzing heat flow in complex regions such as around end windings or non-uniform air-gap, CFD becomes very helpful [29]. Heat in electric machines is generated by the electromagnetic losses and the mechanical friction during rotor's rotation. Computational Fluid Dynamics (CFD) can be used to predict and analyze the thermal performance of an electrical machine where high speed rotation is coupled with small flow gaps as was presented in [100]. The model developed by the authors captures the complex Taylor vortex flow very well and provides detailed insight of the flow and heat transfer inside the machine's air-gap. Moreover, the model predicts the heat transfer coefficient with overall good accuracy. A modification of CFD method is presented in [101] where the authors performed a combined computational fluid dynamics and network approach. In this approach, the analysis is first performed using lumped parameter thermal network. Next CFD calculations are performed to estimate thermal resistances which are used as input to the thermal networks. The network is solved using iterative procedure. A complete CFD model of a synchronous generator was investigated in [102]. The authors investigated thermal management and air flow around major components of the machine. Additionally, power and torque consumption by the fan was calculated. Computational fluid dynamics method does not need to be applied to simulate the thermal behavior of the entire machine. In [103] the authors used CFD to model the coolant flow in cooling channels and on the outer surface of end winding bodies. The results of CFD simulation are next used as input to the analytical models describing the convective heat transfer to the coolant.

3.7. Conclusions and Contributions

This chapter presented different methods of electromagnetic, structural & vibroacoustic and thermal modeling of SynRM. Results obtained from previous analyses were used as a database when designing the final structure of the machine.

For electromagnetic analysis it was shown that the simplest model based on winding function requires very far-reaching assumptions and its application is very limited. Saturation of the iron core plays a significant role in reluctance machines analysis thus neglecting the magnetic field in the iron leads to reduced accuracy of the results. Magnetic equivalent circuit allows to take into account the magnetic field in the iron during calculations hence the results obtained from this method are more accurate than in case of winding function. MEC can be treated as an extension of winding function modeling. Its major disadvantage is the difficulty of modeling complicated geometry. In case of SynRM, magnetic equivalent circuit proved to be useful when cross saturation was neglected. This simplification allowed to analyze the machine by building two separate models of the machine. Including the cross saturation by means of MEC could be troublesome since the paths of magnetic flux are too complicated to be approximated by lumped parameters. The most accurate method of electric machines analysis is finite element method. Using this method, it is possible to analyze all kinds of topologies. There are no limits when it comes to geometry of analyzed object. This method however depending on the analyzed object might be time consuming and it requires a dedicated software. Several different topologies of SynRM were tested. It was proven that some types of flux barriers provide better electromagnetic properties of the machine. Performed analyses proved that configuration of stator slots and rotor flux barriers has a strong influence on generated torque and torque ripple. In general, machines with fractional winding experienced lower torque ripple than machines with integer winding. Moreover, machines with flux barriers based on Zhukovski's curves in most cases experienced the lowest torque ripple and could produce higher torque. Skewing the rotor of the machine (that will be presented in Chapter 3) could allow to obtain lower values of torque ripple.

In case of optimized shape of flux barriers, the curves that were used to create the barriers can be described using parametric equations. This

simplifies the process of creating the flux barriers as the curves can be generated in MATLAB and then exported to a *.dxf* file. It was proven that a SynRM with optimized flux barriers in the rotor in general has better electromagnetic properties. When building MEC model of the machine, one needs to calculate reluctances of flux tubes in the rotor. When the flux barriers in the rotor are based on Zhukovski's curves, calculation of rotor reluctances becomes problematic and numerical methods of integration must be used. Algorithm of calculating the reluctances of flux tubes in the rotor for optimized flux barriers was presented.

Structural analysis was performed for the rotor as this part of the machine has to withstand high centrifugal forces when operating at high rotational speeds. Rotor without additional ribs in the flux barriers provides very good electromagnetic properties of the machine but its structural behavior does not allow the machine to operate at high speed. Mechanical stress that occurs during machine's operation achieves the highest values in the bridges as these parts connect the flux paths and are responsible for maintaining the structural integrity of the rotor. It is necessary to introduce the ribs in the flux barriers for the machine to operate at high speeds. Moreover, there should be no sharp edges in the construction of flux barriers since the mechanical stress concentration is the highest at discontinuities. In case of operating at very high speeds such as 12000 rpm it was proven that additional ribs in the first flux barrier are necessary. The cutout in the rotor increases torque ripple and windage losses.

Influence of rotor's topology on the noise generated by the machine was also investigated. Numerical analyses were performed for a SynRM with four different rotor topologies while keeping the stator topology unchanged. The NVH analysis of the machine was performed using modal analysis. Depending on the rotor topology, the machine experienced different level of torque ripple. The lowest torque ripple was for the machine whose rotor had optimized flux barriers. However, the noise generated by the machine did not depend directly on machine's torque ripple. It was shown that there is hardly a relation between the noise and torque ripple. Torque ripple depends on the tangential component of the electromagnetic force whereas the noise of the machine origins from stator deformation which in turn depends on the radial component of the electromagnetic force.

Thermal analysis is the final stage of the design process. The aim of the thermal analysis is to confirm that the machine can operate at certain loads without any damage due to high temperature. Thermal analysis also allows to design a cooling system which in turn allows to downsize the machine. Thermal analysis of the final topology of SynRM will be presented in Chapter 4.

The machine models and the obtained results presented in this chapter were published in various papers. The results of performed analyses of SynRM make a general knowledge base on modeling of synchronous reluctance machine.

Personal contribution of the author is:

- Investigation on optimized flux barriers in the rotor
- Application of parametric equations in design process of flux barriers in the rotor
- Analysis of the influence of rotor topology on electromagnetic and NVH behavior of SynRM
- Structural analysis of the rotor construction for high speed applications
- Analysis of the influence of additional ribs in the rotor on electromagnetic properties of the machine
- Application of winding function and magnetic equivalent circuit method in analysis of air gap magnetic field of SynRM
- Description of reluctance calculation process of the rotor with optimized flux barriers

4. SynRM for EV Propulsion Systems

In EVs the electric machine is the main component of the propulsion system. Based on the requirements of the propulsion system, EVs can have various numbers and locations of electric motors. The advance of power electronics and control systems allowed different motor types to be used in EVs [10]. A brushed DC motor can provide maximum torque at low rotational speed but its disadvantages are low efficiency, bulky structure and the presence of the brushes which impacts the robustness of the machine. For these reasons this type of machine is not used anymore in EVs [10]. Permanent magnet brushless DC motor (BLDC) tends to be more efficient than induction motors since there are no windings in the rotor and thus nor copper loss. Moreover, this motor is also lighter, smaller and heat dissipation is good as it is mainly generated in the stator. However, the range of constant power is quite short and the torque drops as the speed increases due to generated back EMF. The use of permanent magnets also increases the cost of this machine [10]. Permanent magnet synchronous motor (PMSM) is capable of being operated at a range of speeds without the need of any gear system. A configuration with outer rotor is also possible and can be used as an in-wheel motor. Switched reluctance motor (SRM) have a robust and simple mechanical construction, low cost, wide constant power range and high power density. Low efficiency, noise, torque ripple ang larger size compared to PM machines are its disadvantages. Despite a simple construction its control strategy is not simple [10]. Synchronous reluctance motor (SynRM) combines the advantages of both PM and induction motors. This type of machine is robust, fault tolerant, efficient and small like a PM motor. The drawback of this motor might be a low power factor. However recent research shows that a proper design of the rotor which provides a high saliency ratio, significantly increases machine's power factor. This can be achieved by using axially laminated rotor structures or transversally laminated rotor with properly designed flux barriers' topology. Also control systems can help this machine to be competitive in EV application.

Chapter 4 presents the whole process of defining the requirements, design and analysis of a SynRM for EV propulsion systems. The SynRM under study was designed and analyzed based on the requirements generated in the European FP7 project ARMEVA (http://www.armeva-project.eu/). After a brief market research, the

target for the technology developed in ARMEVA was defined, and the required vehicle level characteristics were determined. These characteristics served as input for simulation models to define the electric motor specifications. The simulations were performed using well-defined driving profiles (a combination of official profiles and custom drive cycles and real data logged from an operational fleet of electric vehicles) and specific load cases. Based on these requirements and on the previous chapter results, a topology for the SynRM was chosen and analyzed.

4.1. Motor Requirements and High Level Specifications

The type of the vehicle to develop a propulsion electrical machine for was chosen after a brief market analysis. It corresponds to a B-segment vehicle produced by an Asian OEM. It is equipped with an electric powertrain, but also optionally equipped with a range extender unit. Two powertrain architectures were proposed: single and two speed transmission. The first one is a widely used solution for electric vehicles, with electric motor connected to the wheels by means of a transmission with a fixed gear ratio. The second solution, developed by the coordinator of ARMEVA project (Punch PowerTrain NV) leads to a higher efficiency and a downsizing of the electric motor due to the ratio spread offered by the two gears. The vehicle parameters are shown in Table 4.1.

TABLE 4.1 Target vehicle characteristics

Vehicle characteristics	
Total vehicle mass	1454 kg
Mass distribution	50 %
Tire width	195 mm
Tire height	50 mm
Wheel rim diameter	16 in
Aerodynamic and rolling parameters	
Air penetration coefficient (Cx)	0.32
Vehicle active area for aerodynamic drag	1.95

Moreover, the characteristics of the battery pack to be installed were defined, as presented in Table 4.2.

TABLE 4.2 Battery pack characteristics

Battery pack		
	Unit	**Value**
Maximum charge / discharge power	W	130000
Nominal capacity	Ah	60
Element nominal capacity	Ah	60
Number of elements in series in one branch	-	108
Number of branches in parallel	-	1
Battery total energy	kWh	23.6
Open circuit voltage	V	394
Ohmic resistance (one cell)	Ohm	0.001

The requirements for the EV performance are presented in Table 4.3.

TABLE 4.3 EV performances requirements

0-50 km/h acceleration	< 3.8 s
0-100 km/h acceleration	< 9 s
0-130 km/h acceleration	< 20 s
80-120 km/h acceleration	< 9 s
Top speed	145 km/h
Top speed at 12% hill	100 km/h

Geometrical constraints were imposed, based on existing motors as used by Punch Powertrain in similar power rated PHEV and EV applications. Global dimensions are limited to:

- Diameter (excluding cooling in- and outlets and cable connections): 240.0 mm
- Length (excluding shaft end): 257.7 mm

The EV operating modes were then analyzed. A model of the EV was developed using LMS Imagine Amesim. Based on a realistic motor efficiency map and on real driving cycles implemented in the model, the operation points and the overall efficiency on all driving cycles were extracted.

Electric machine's requirements were determined according to the vehicle parameters. In order to specify the required power and torque of the electric machine, one needs to know the required acceleration of the vehicle along with the vehicle's gross weight and motion resistance forces of the vehicle. The total motion resistance force (or the road load) of a vehicle is the sum of particular resistance forces as given below [104]:

$$F_w = F_{ro} + F_{sf} + F_{ad} + F_{cr} \tag{4.1.1}$$

The rolling resistance is given by the formula [104]:

$$F_{ro} = \gamma m g \cos(\alpha) \tag{4.1.2}$$

where:

γ – tire rolling resistance coefficient
m – mass of the vehicle
g – gravitational acceleration constant
α – grade angle

This resistance results from tire flattening at the road contact surface. Viscous or Stokes friction force is defined as [104]:

$$F_{sf} = k_A V \tag{4.1.3}$$

where:

k_A – Stokes coefficient
V – vehicle speed

Aerodynamic drag is the air viscous resistance which acts upon the vehicle and is given by the formula [104]:

$$F_{ad} = \frac{1}{2}\xi C_w A_f (V + V_0)^2 \tag{4.1.4}$$

where:

ξ – density of the air
C_w – aerodynamic drag coefficient
A_f –frontal area of the vehicle
V_0 – head-wind velocity

With road load given, it is possible to calculate the power P_v required to drive an EV [104].

$$P_v = VF_w \tag{4.1.5}$$

With the reduction gear, the relations between load torque and angular speed of the wheel and the motor are given by [104]:

$$\omega_{Wheel} = \frac{\omega_m}{i} \tag{4.1.6}$$

$$T_L = \frac{T_{LWheel}}{i} \tag{4.1.7}$$

where:

ω_{Wheel} – mechanical speed of the wheel
ω_m – electric motor mechanical speed
T_L – load torque
T_{LWheel} – load torque on the wheel
i – transmission ratio

Table 4.4 shows the required power and torque of the electric motor. The parameters were obtained during simulation of different scenarios. One can see that meeting the requirements for the EV in 0 to 50 km/h test, the maximum power of the electric motor is required to be 60 kW. However, this power is not sufficient to meet the requirements in 10 to 100 km/h test. In this case the required maximum power is higher.

TABLE 4.4 Maximum torque and power for the EV electric motor

	Motor maximum torque (Nm)	**Motor maximum power (kW)**
Gradeability	1680	
0 to 50 km/h	1760	60
80 to 120 km/h		64
0 to 100 km/h	<= 1760	87
0 to 130 km/h	<= 1760	<= 87
Top speed at 12%	<= 1760	<= 87

In case of maximum speed of the motor, this parameter is not an output of any simulation test. The requirement for the rotational speed is that it should not exceed 20000 rpm.

Finally, for a configuration using gear box (with a gear ratio of 9.4) the requirements for the EV electrical machine design are given in Table 4.5.

TABLE 4.5 Electrical machine requirements

Rated power	30 kW
Rated speed	4500 rpm
Maximum power	87 kW
Maximum speed	12000 rpm
DC bus voltage	600V
Torque ripple content	2-4%

4.2. Multiphysics Design and Analysis of SynRM for EV Propulsion Systems

Diagram presented in Fig. 4.1 shows the main workflow during design and analysis of the final structure of SynRM for EV propulsion. General dimensions were set based on available space and mounting method. With dimensions specified, it was possible to design stator and rotor based on required torque and supply voltage. Initial design was put to simulation tests in order to find the best topology in terms of electromagnetic torque, power factor and efficiency. Machine's parameters such as inductances, nominal current and torque were obtained from electromagnetic analysis. These parameters were used to build mathematical model of the machine used in control systems. Electromagnetic analysis provided a topology of the machine which had to be validated from the structural point of view in order to provide the required robustness and integrity of the structure. NVH analysis of the stator allowed to find natural frequencies of stator's structure and to estimate the noise level generated by the machine. In order to make sure that the machine can operate at nominal and maximum load, thermal analysis was necessary. This allowed to estimate temperature rise of the machine and design a suitable cooling system.

As previous studies showed, machine with fractional winding has the lowest torque ripple. The final topology of SynRM, as resulted from the preliminary design, has 27 stator slots and rotor with four flux barriers of optimized shape based on Zhukovski's curves. Geometry of the machine is presented in Fig. 4.2. Flux barriers in the rotor have additional ribs which allow the machine to operate at high speed. These ribs affect electromagnetic performance of the machine. The study on ribs placement in the rotor and their influence on the properties of the machine was described in Chapter 3. The final topology of the machine is shown in Fig. 4.2. Main dimensions of the machine are contained in Table 4.6.

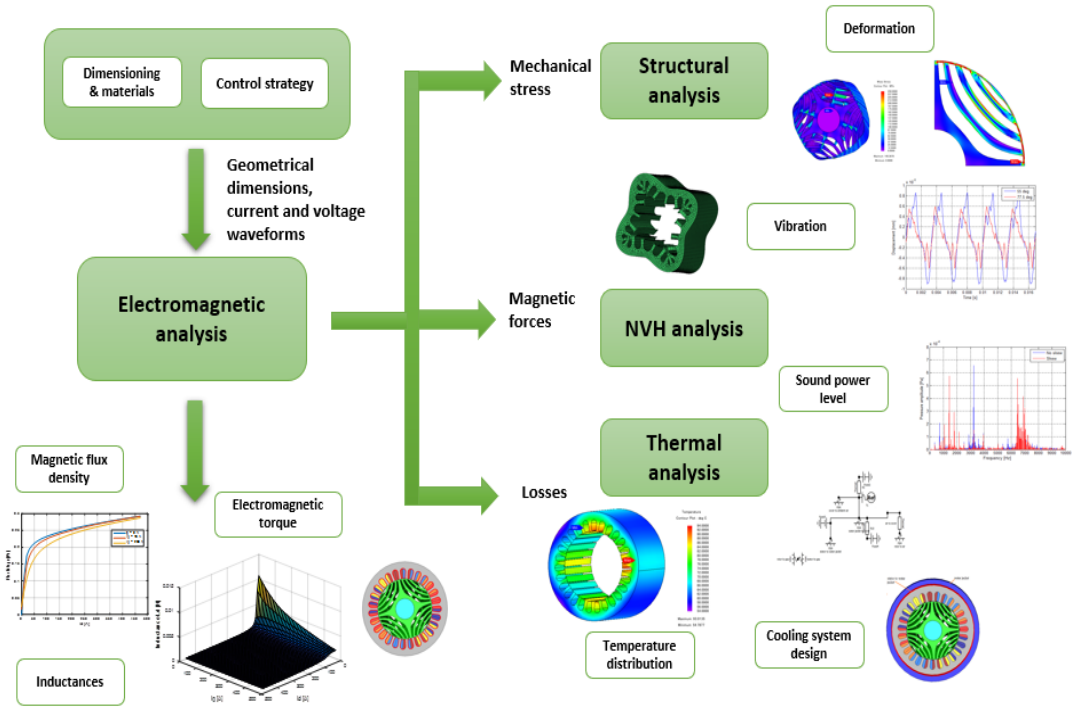

Fig. 4.1 Design and analysis process of a SynRM

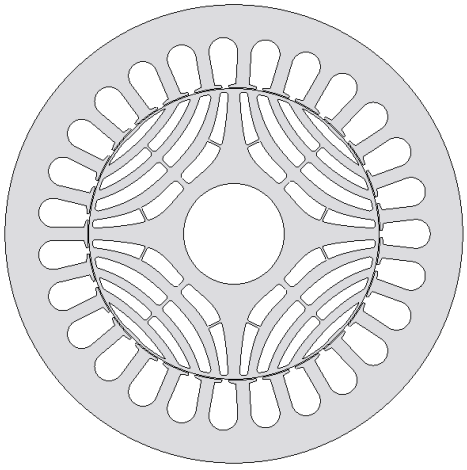

Fig. 4.2 Cross section of machine's final topology

TABLE 4.6 Main dimensions of the machine

Active axial length	145 mm
Air gap	0.45 mm
Stator outer diameter	205 mm
Stator inner diameter	130.9 mm
Rotor diameter	130 mm
Shaft diameter	45 mm

4.2.1. Electromagnetic Analysis

The electromagnetic analysis of the machine is done considering the 2D, 3D, 2D-skewed and 3D-skewed topologies. Parameters of the machine such as torque, torque ripple, voltage and phase current are presented in the graphs. Differences in electromagnetic behavior between skewed and non-skewed topology are discussed.

4.2.1.1. Non-Skewed Topology

Using 2D FEM model of the machine, magnetic field distribution in the machine can be obtained. Fig. 4.3 shows the results of 2D FEM simulations in two cases of zero torque: for d-axis MMF and q-axis MMF. When the maximum of stator's magneto-motive force is aligned with d-axis of the rotor, the magnetic field in the machine is the greatest since the reluctance of magnetic circuit is the lowest. One can see that in this case the machine is very saturated (orange and red color, Fig. 4.3a). Magnetic flux follows the flux paths and seems to completely avoid flux barriers in the rotor (Fig. 4.3b). If the maximum of the stator's magnetic field axis is aligned with the q-axis of the rotor, magnetic reluctance of the machine's magnetic circuit is the greatest. This causes the magnetic field to drop (Fig. 4.3c). Magnetic flux in this case crosses all the flux barriers in the rotor (Fig. 4.3c).

When the machine generates the torque at current angles closer to 90 electrical^0, the magnetic field in the machine drops. This so called flux weakening is used at high speeds due to high values of back electromotive force (EMF).

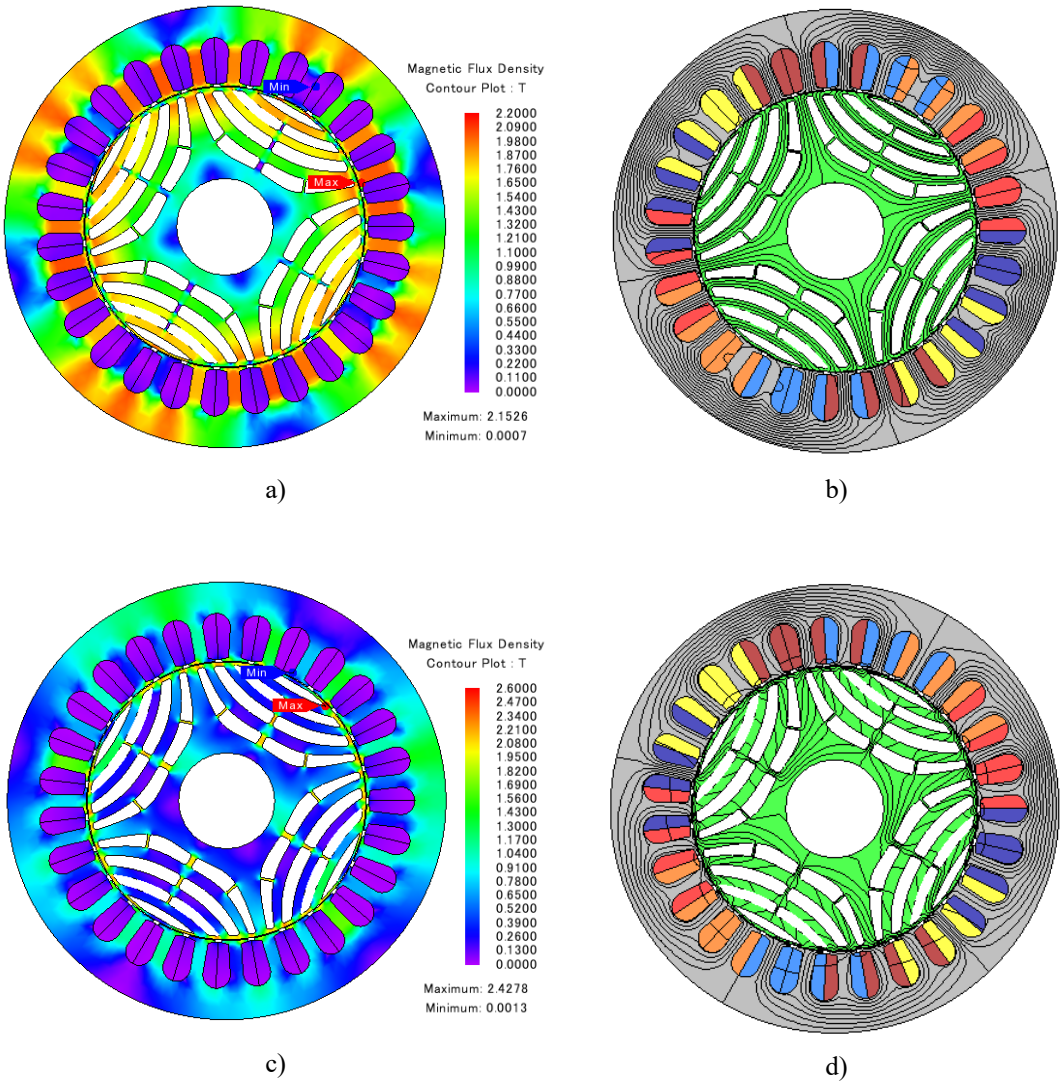

Fig. 4.3 Magnetic field in machine: a) magnetic flux density map for d-axis MMF, b) flux lines for d-axis MMF, c) magnetic flux density map for q-axis MMF, d) flux lines for q-axis MMF

Fig. 4.4 and Fig. 4.5 show magnetic flux density in the air gap of the machine in these two described cases. When the stator MMF is applied in d axis, the air gap magnetic field is almost sinusoidal. Any distortion present in the magnetic field distribution is due to stator slots and rotor flux barriers. In case of q-axis MMF, the magnetic field in the air gap, is distorted.

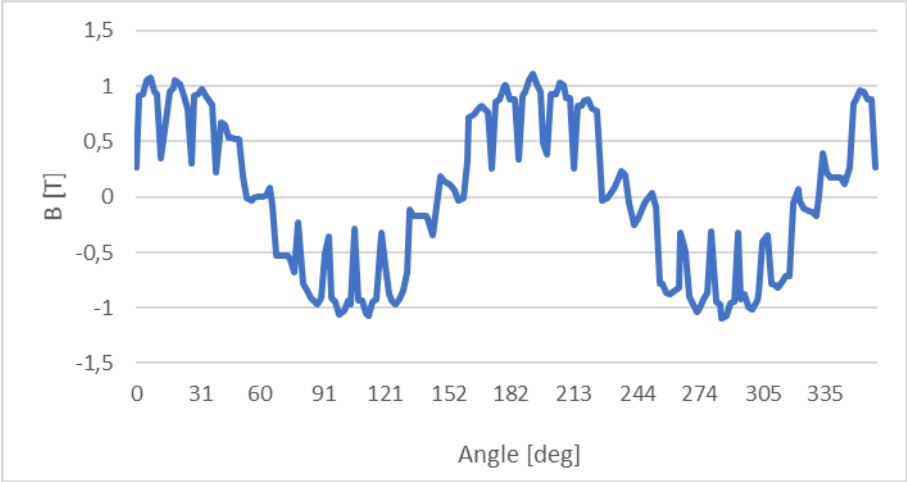

Fig. 4.4 Air gap magnetic field: d-axis MMF

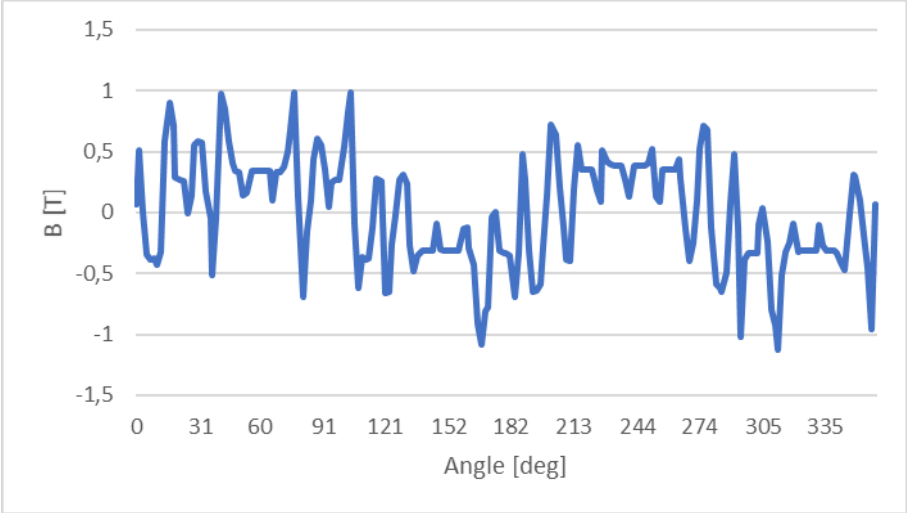

Fig. 4.5 Air gap magnetic field: q-axis MMF

Torque generated by the machine changes with phase current and the angle between the axis of stator magnetic field and d-axis of the rotor. Below, several torque characteristics are shown for current angle from 0 to 90 electrical^0. The torque vs. current angle curves are calculated for four different values of stator phase current. The machine does not generate torque for two current angle values: 0^0 which corresponds to the situation when d-axis of the rotor is aligned with stator magnetic field axis and 90^0 which corresponds to the situation when q-axis of the rotor is aligned with the axis of stator magnetic field. The torque vs. current angle is not sinusoidal though, the maximum of the torque is not at 45^0 but varies from 60 to 70^0. It is caused by the nonlinearity of the magnetic circuit of the machine and cross saturation which occurs in the machine. Increase in phase current causes the torque to increase as well.

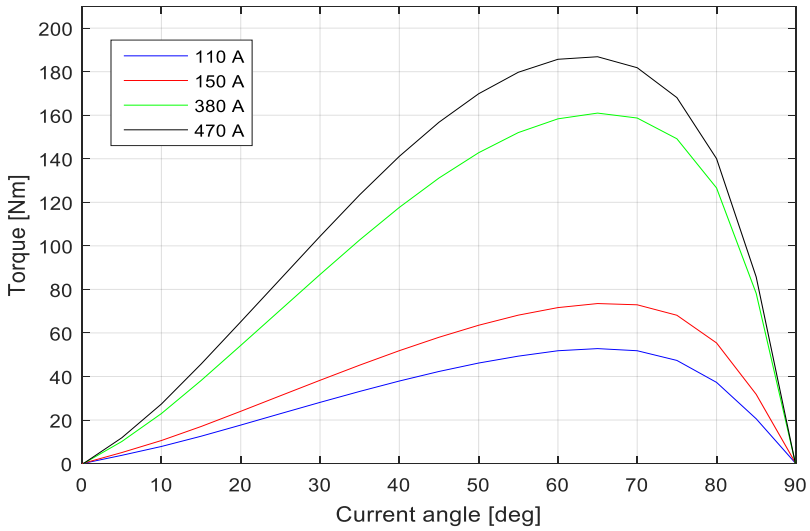

Fig. 4.6 Torque vs. current angle at 4500 rpm

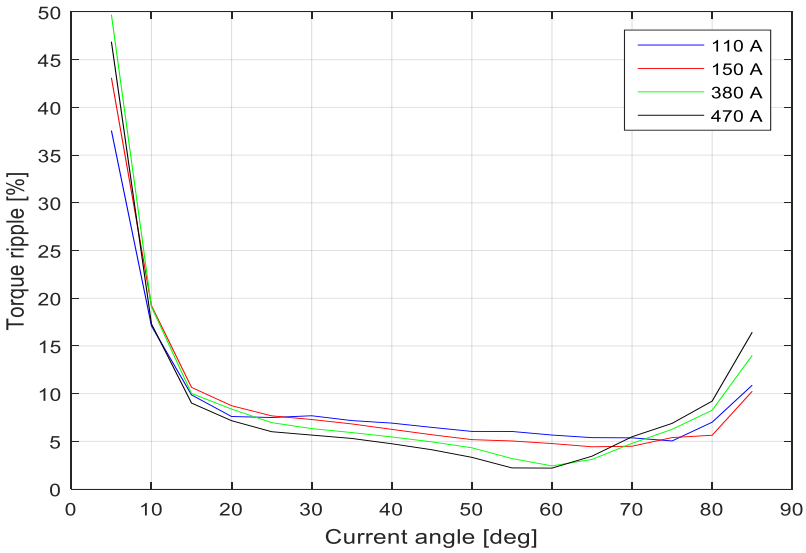

Fig. 4.7 Torque ripple vs. current angle

Torque ripple content is defined as [20]:

$$\Delta T = \frac{T_{max} - T_{min}}{T_{avg}} \qquad (4.2.1.1.1)$$

The variation of the torque ripple content vs the current angle is shown in Fig. 4.7. Torque ripple reaches the highest values at current angles close to 0 and 90 electrical^0 since the average torque generated at these two current angles is zero. For clearance of the figure, values of torque ripple for current angle 0 and 90^0 is not shown. Phase voltage is shown in Fig. 4.8. As one can see, higher phase current requires higher phase voltage. Value of Phase voltage changes with rotational speed and current angle. RMS value of phase voltage drops as the current angle approaches 90 electrical^0 (q-axis). It is because the machine is demagnetized (magnetic flux is low) as it is shown in Fig. 4.3.

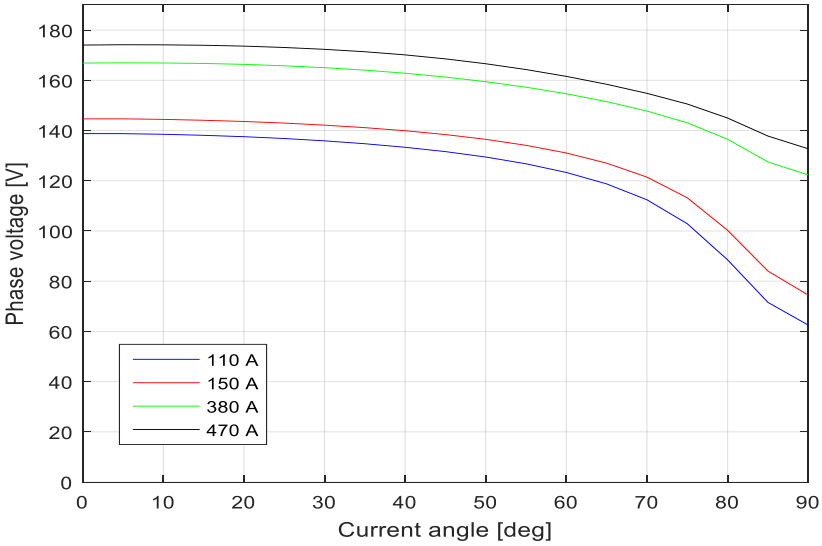

Fig. 4.8 Phase voltage at 4500 rpm for different current angles and phase currents

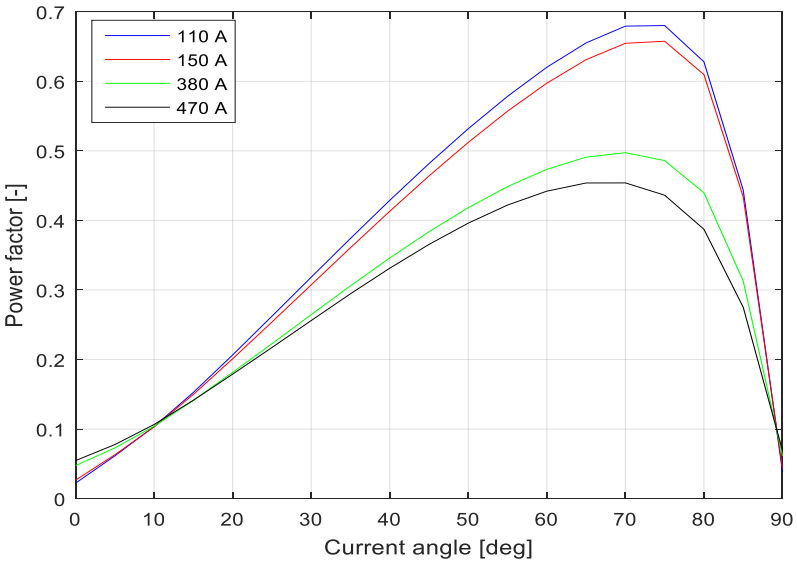

Fig. 4.9 Power factor at 4500 rpm for different current angles and phase currents

Fig. 4.9 shows power factor defined as:

$$\lambda = \frac{P}{S} = \frac{\frac{1}{T}\int_0^T i(t)u(t)dt}{\left(\sqrt{\frac{1}{T}\int_0^T u^2(t)dt}\right) * \left(\sqrt{\frac{1}{T}\int_0^T i^2(t)dt}\right)} \qquad (4.2.1.1.2)$$

When given the saliency ratio of the machine, power factor can be calculated as:

$$\lambda = \frac{\xi - 1}{\xi + 1} \qquad (4.2.1.1.3)$$

The power factor vs. current angle curve follows the shape of torque vs. current angle curve. Equation (4.2.1.1.3) shows that the higher the saliency ratio of the machine, the higher the power factor. Power factor achieves lower values for high phase currents. This is caused by saturation of the magnetic circuit of the machine. In this state, high increase in current results in small increase of torque since the magnetic flux rises very slowly when the magnetic circuit is saturated.

At maximum speed of 12000 rpm, phase voltage is much higher even at much lower phase current. This is because induced voltage is equal to a time derivative of magnetic flux which at high rotational speeds is very high. The highest induced voltage occurs for current angle equal to zero^0 (d-axis MMF) and the lowest voltage occurs for current angle of ninety^0 (q-axis MMF). This situation is presented in Fig. 4.11. Fig. 4.10. shows torque vs. current angle curves at 12000 rpm.

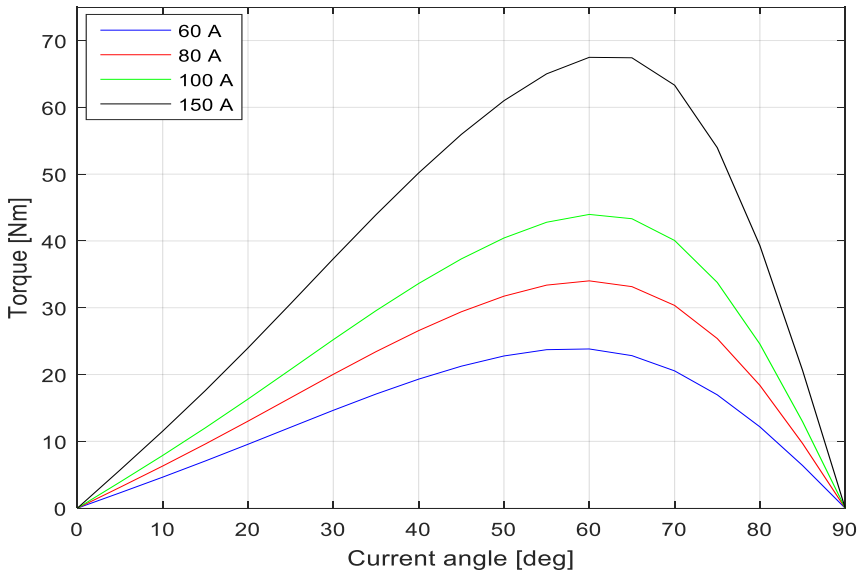

Fig. 4.10 Torque vs. current angle at 12000 rpm

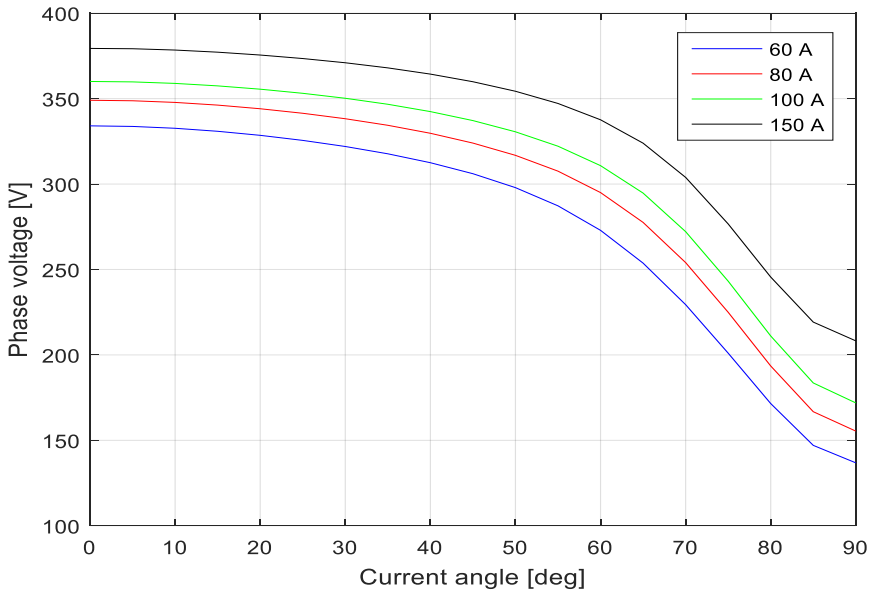

Fig. 4.11 Phase voltage at 12000 rpm for different current angles and phase currents

Inductances of the machine were calculated by means of finite element method. Since SynRM has a strong anisotropy of the magnetic circuit, the inductances were calculated in orthogonal axes - d and q. First the machine flux linkage in d and q-axis was calculated.

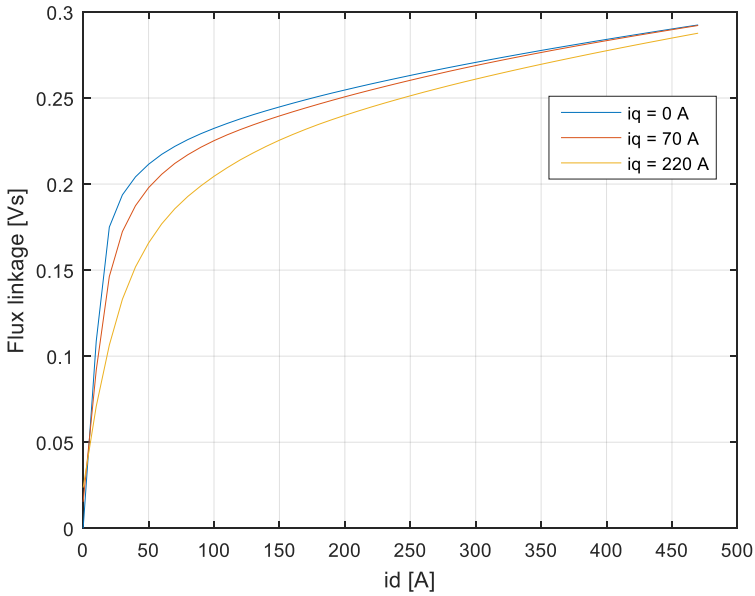

Fig. 4.12 d-axis flux linkage

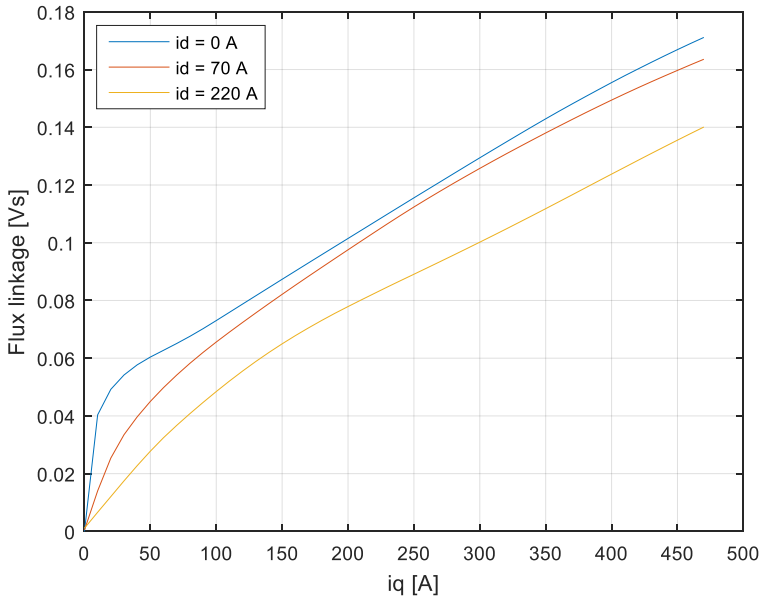

Fig. 4.13 q-axis flux linkage

As one can see in Fig. 4.12 d-axis flux linkage increases very quickly with i_d current and saturates eventually. This is due to the fact that the flux path in d-axis of the rotor mostly consists of iron flux paths. The magnetic field in d-axis flows through iron flux paths avoiding air flux barriers in the rotor. When i_q component is present in stator phase current, the flux linkage in d-axis decreases.

Fig. 4.13 presents flux linkage in q-axis. In this case the flux linkage rises in almost linear manner with i_q current. This is due to the presence of flux barriers in the rotor which are penetrated by magnetic field. The presence of the air in the path of magnetic flux increases the reluctance of q-axis magnetic circuit. In this case, when i_d component of phase current is present, the q-axis flux linkage decreases similarly as in case of d-axis flux linkage. This phenomenon is known as cross saturation. This means that two equivalent circuits of the machine in orthogonal axes in fact depend on each other.

$$\Psi_d = \Psi_d(i_d, i_q)$$
$$\Psi_q = \Psi_q(i_d, i_q) \qquad (4.2.1.1.4)$$

Flux linkage in both axes should be considered as function of two currents - i_d and i_q as shown in equation (4.2.1.1.4). 3D plots of flux linkages in d and q-axis are presented below. In Fig. 4.14. flux linkage in d-axis increases as d-axis current grows. At very high values of d-axis current, flux linkage saturates. Changes in q-axis current introduce some flux linkage distortions in d-axis Fig. 4.15. shows q-axis flux linkage. In this case, the flux linkage grows almost linearly with q-axis current due to high magnetic reluctance of q-axis magnetic circuit. Cross saturation effect is more visible in q-axis flux linkage. In Fig. 4.15. one can see that changes in d-axis current cause quite significant distortion in q-axis flux linkage.

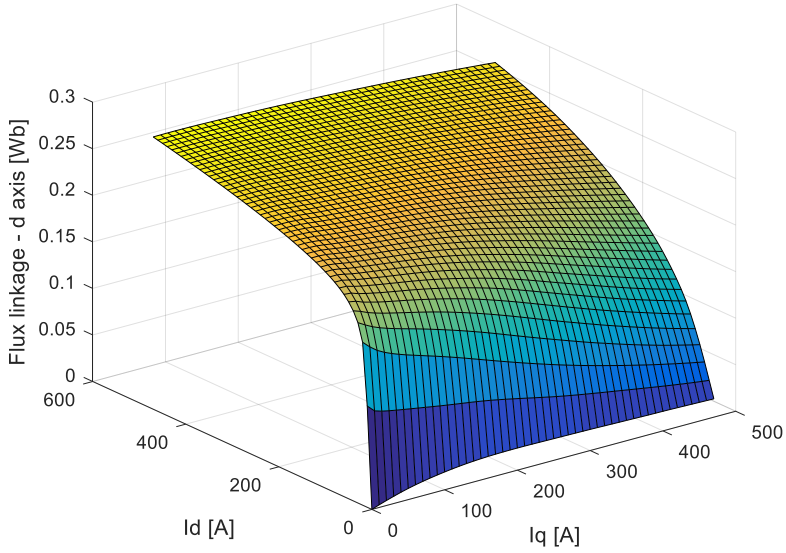

Fig. 4.14 Flux linkage in d-axis

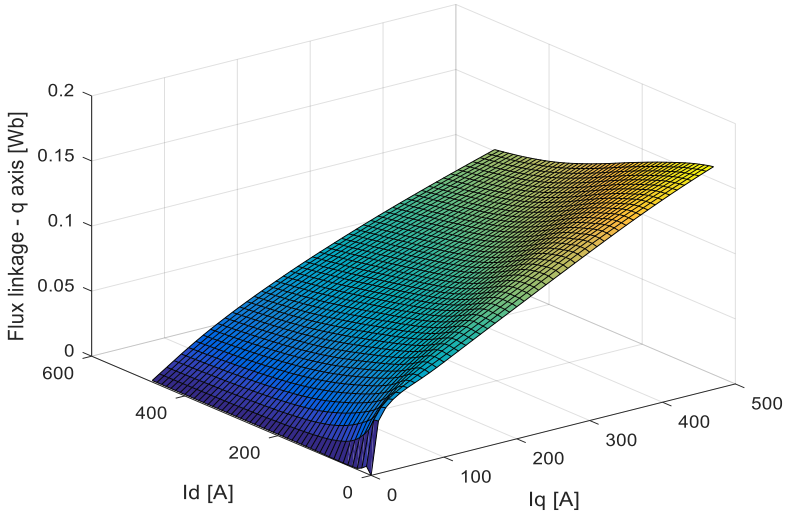

Fig. 4.15 Flux linkage in q-axis

In theory, d and q-axis fluxes are independent on from each other. In theory, current in d-axis produces only d-axis flux and q-axis current produces q-axis flux. This however does not happen practically. Magnetic circuits of the machine for d and q-axis flux are always linked together. Depending on machine's construction, cross saturation might be varying but it cannot be eliminated. Applying d-axis MMF causes some q-axis flux to appear and when stator MMF is applied in q axis, some d-axis flux appears as well. Fig. 4.16. shows the impact of cross saturation on d-axis flux linkage. If there was no cross saturation, the flux linkage in d-axis would depend on d-axis current only and it would remain constant regardless the variations of q-axis current. However, increasing q-axis current causes the flux linkage in d-axis to decrease. This phenomenon is greater for low d-axis current and lowers when the current in d-axis increases. Similarly, q-axis flux decreases when the current in d-axis grows. Variations of q-axis flux linkage are greater than those of d-axis flux. This situation is presented in Fig. 4.17.

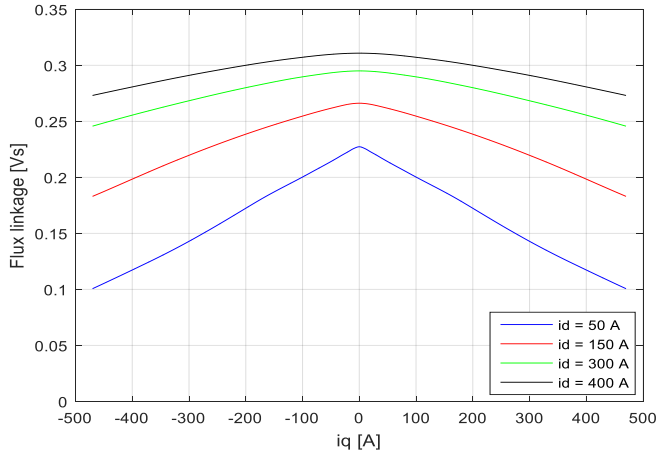

Fig. 4.16 Flux linkage in d axis as function of q-axis current

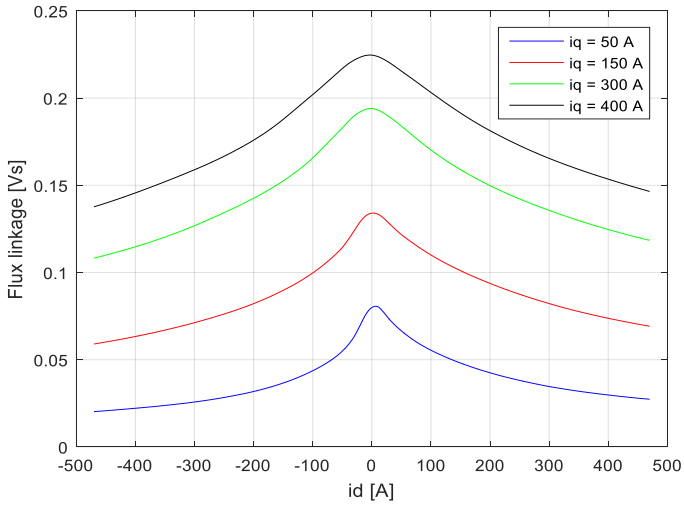

Fig. 4.17 Flux linkage in q axis as function of d-axis current

Presence of cross saturation means that inductances in d and q axes are also functions of two currents and there is a mutual inductance between d and q-axis equivalent circuits.

$$L_d(i_d, i_q) = \frac{\partial \Psi_d(i_d, i_q)}{\partial i_d}$$

$$L_q(i_d, i_q) = \frac{\partial \Psi_q(i_d, i_q)}{\partial i_q} \tag{4.2.1.1.5}$$

$$L_{dq}(i_d, i_q) = \frac{\partial \Psi_d(i_d, i_q)}{\partial i_q} = \frac{\partial \Psi_q(i_d, i_q)}{\partial i_d} = L_{qd}(i_d, i_q)$$

Machine's d and q inductances are shown below. As one can see, values of inductances decrease as the currents grow. This is due to motor's magnetic circuit saturation. Machine' s d and q axis inductances are presented below as functions of two currents - i_d and i_q.

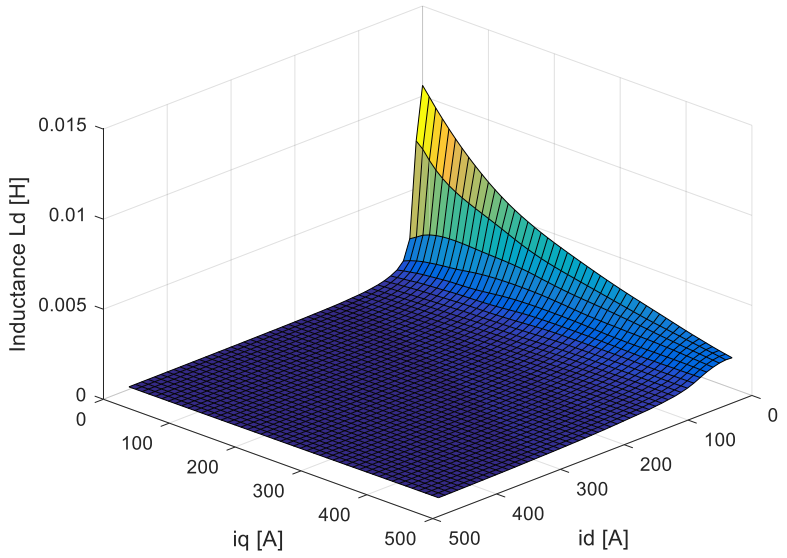

Fig. 4.18 Inductance in d-axis

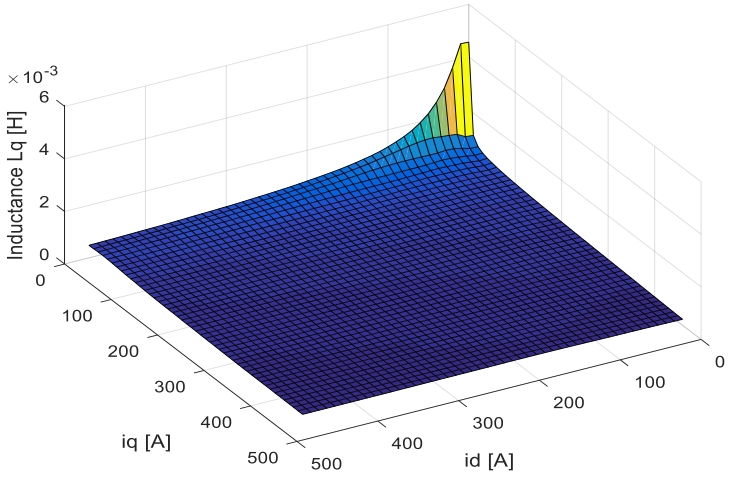

Fig. 4.19 Inductance in q-axis

In Fig. 4.18. one can see d-axis inductance. Its value decreases as the currents grow due to the saturation of magnetic circuit. It reaches higher values than q-axis inductance presented in Fig. 4.19. It is easy to observe that synchronous inductances depend on both orthogonal currents i_d and i_q simultaneously hence to create more accurate model of SynRM, one needs to take into account cross saturation. Fig. 4.20. shows mutual inductance between d and q-axis equivalent circuits of the machine.

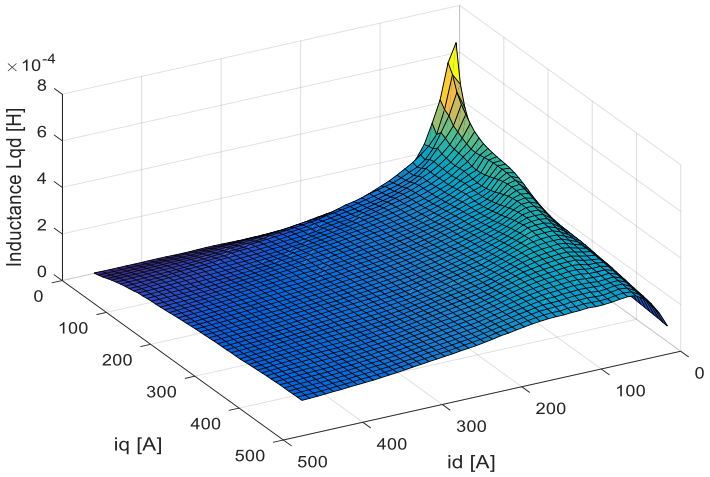

Fig. 4.20 Mutual d-q inductance

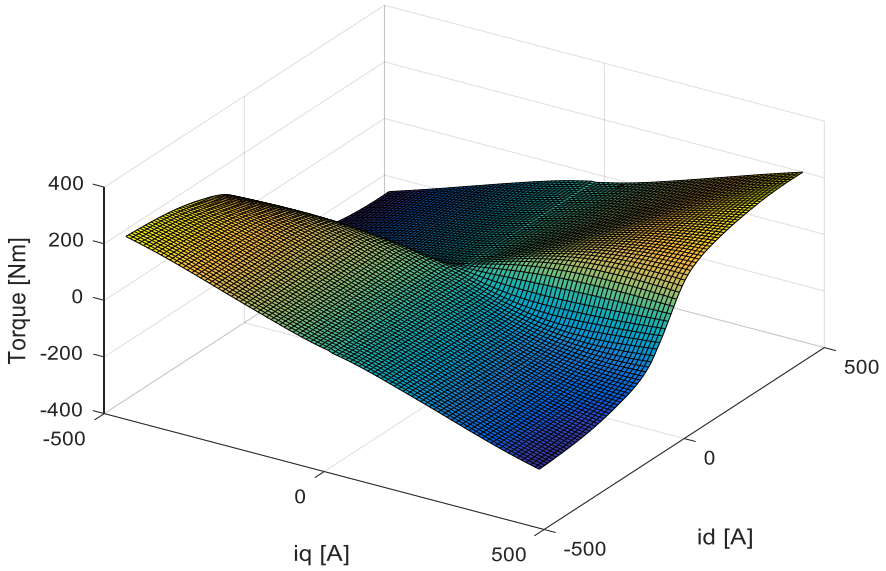

Fig. 4.21 Electromagnetic torque

Using flux linkage in d and q axes and orthogonal currents, one can use Park's equation (3.2.19) to calculate electromagnetic torque of the machine. Torque generated by the machine in four quadrants is presented in Fig. 4.21. By setting different values of d and q currents one can change the direction of the torque generated by the machine thus change operation point of the SynRM.

4.2.1.2. Skewed Topology

Torque ripple of the machine can be limited by skewing the rotor or stator. Rotor (stator) skewing reduces however machine's inductances which causes the torque to decrease. Using finite element method, machine with a skew can be modeled in two ways:

- 3D model
- 2D model with multi-slice

3D model can include the skew very accurately however the computational cost is very high. When using 2D model with multi-slice, the model of the machine is sliced in axial direction in several pieces (in JMAG it is 3, 5 or 7). The more the slices, the more accurate the results but the computational cost also grows.

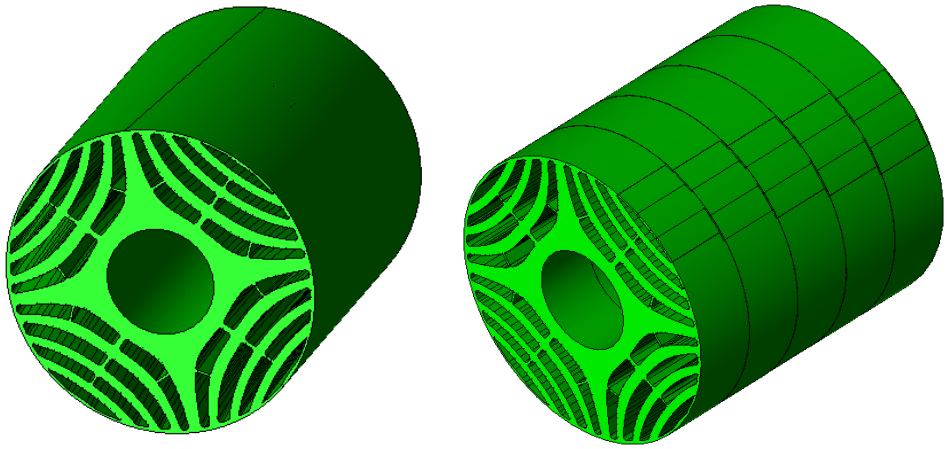

Fig. 4.22 Modeling of rotor skew: a) 3D model, b) the idea of multi-slice in 2D model

Fig. 4.22 shows the difference in modeling the skew of the rotor. When using 2D model with multi-slice, the rotor is divided into slices along its axial length. All the slices are rotated by a certain angle relative to each other. The more slices are used the more accurate results can be obtained.

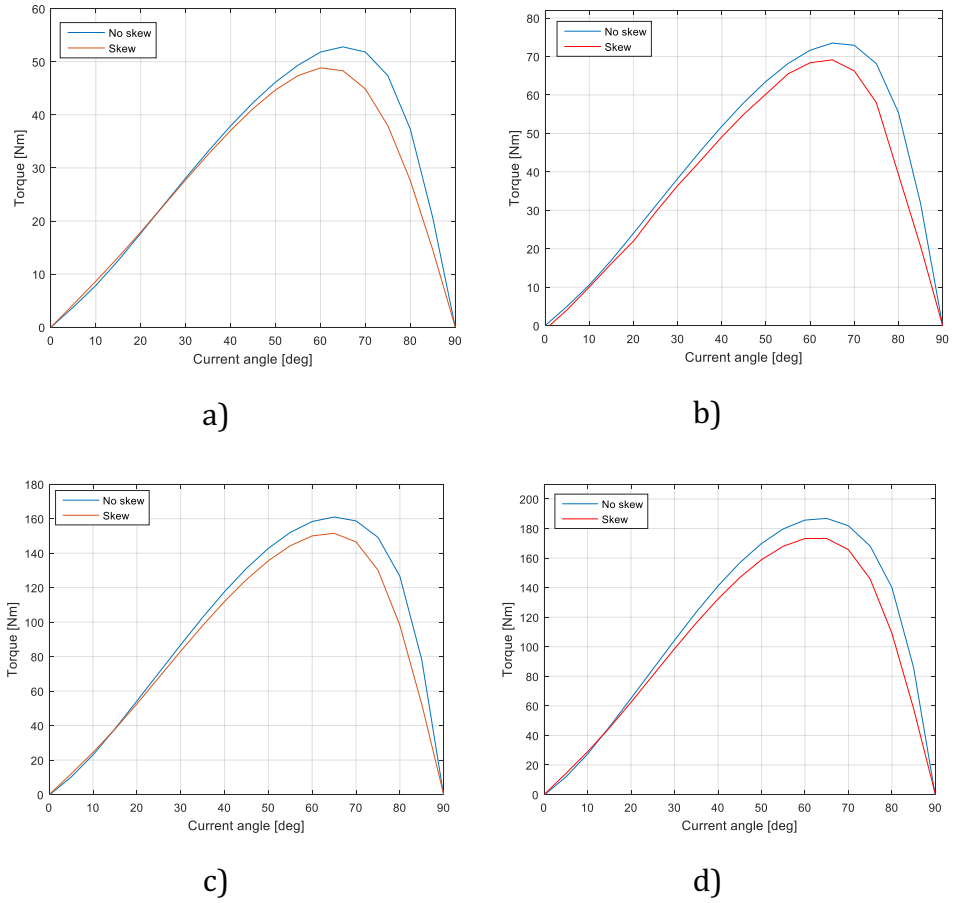

Fig. 4.23 Torque comparison at 4500 rpm: a) 110 ARMS, b) 150 ARMS, c) 380 ARMS, d) 470 ARMS

Fig. 4.23 shows comparison of electromagnetic torque of the SynRM under study with skewed and non-skewed rotor. One can see that skewing the rotor results in lower torque generated by the machine. Machine with skewed rotor also experiences a lower torque ripple as one can see in Fig. 4.24. In both cases, the value of torque ripple changes with the current and current angle value. The highest torque ripple occurs at current angles equal to 0^0 and 90^0 since in those cases the generated torque is zero. Torque ripple seems to be to lowest around 60^0 current angle.

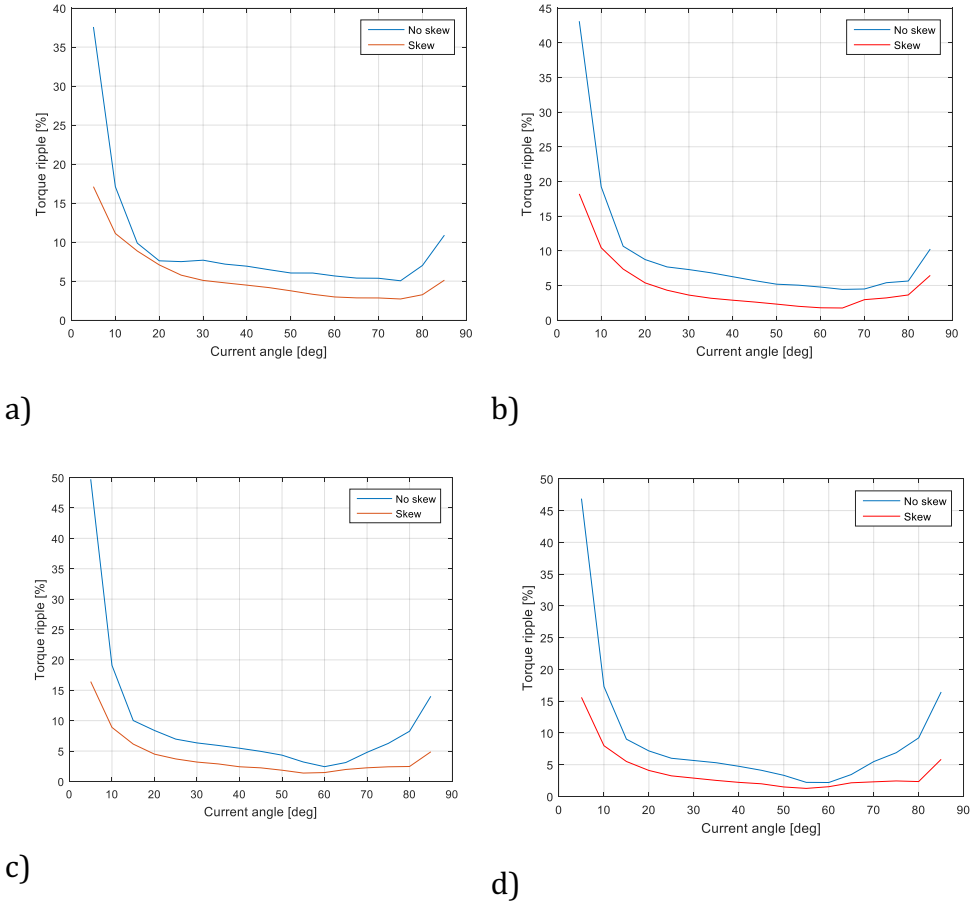

Fig. 4.24 Torque ripple comparison at 4500 rpm: a) 110 ARMS, b) 150 ARMS, c) 380 ARMS, d) 470 ARMS

Fig. 4.25. shows comparison of induced voltage at 4500 rpm for SynRM with skewed and non-skewed rotor. As one can see, the induced voltage changes with current angle. The highest value of induced voltage occurs at 0^0. This corresponds to d-axis stator MMF. In this case, the magnetic field in the machine achieves the highest value. This causes the induced voltage to achieve the highest value. At 90^0 of current angle, the voltage is the lowest since the magnetic flux in the machine is the lowest. The induced voltage in machine with skewed rotor is lower since skewing the rotor results in lower inductance. Generated voltage also depends on the phase current. As one can see, the higher the phase current, the higher the generated voltage.

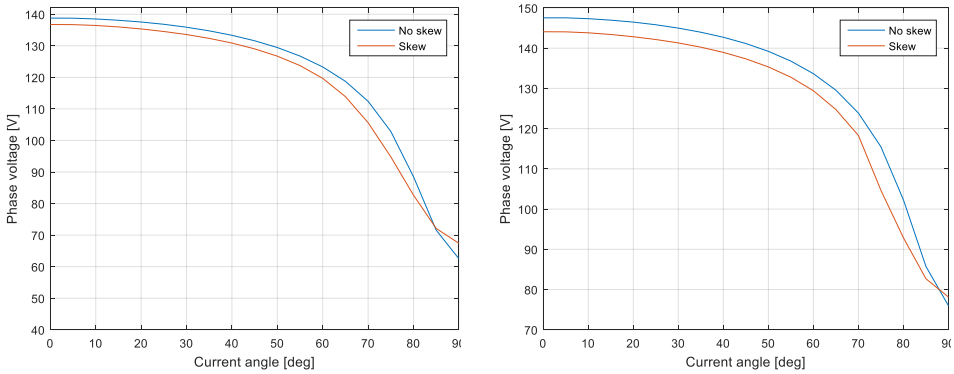

a)

b)

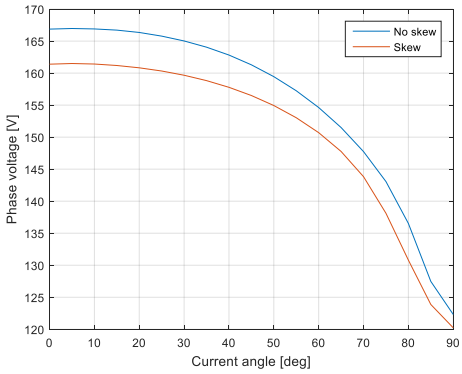

c)

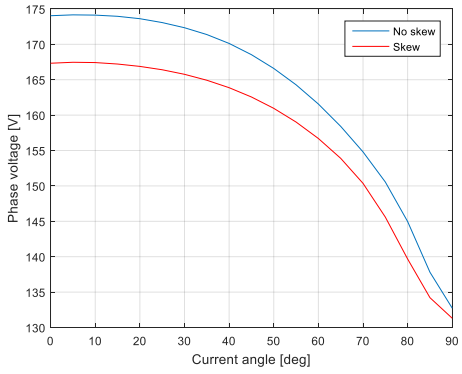

d)

Fig. 4.25 Voltage comparison at 4500 rpm: a) 110 ARMS, b) 150 ARMS, c) 380 ARMS, d) 470 ARMS

Fig. 4.26 and Fig. 4.27 show flux linkage graph in d and q axis respectively. The flux linkage graph looks similar to flux linkage of the machine with non-skewed rotor. The major difference is in its values. Flux linkage of machine with skewed rotor achieves lower values that in case of machine with non-skewed rotor.

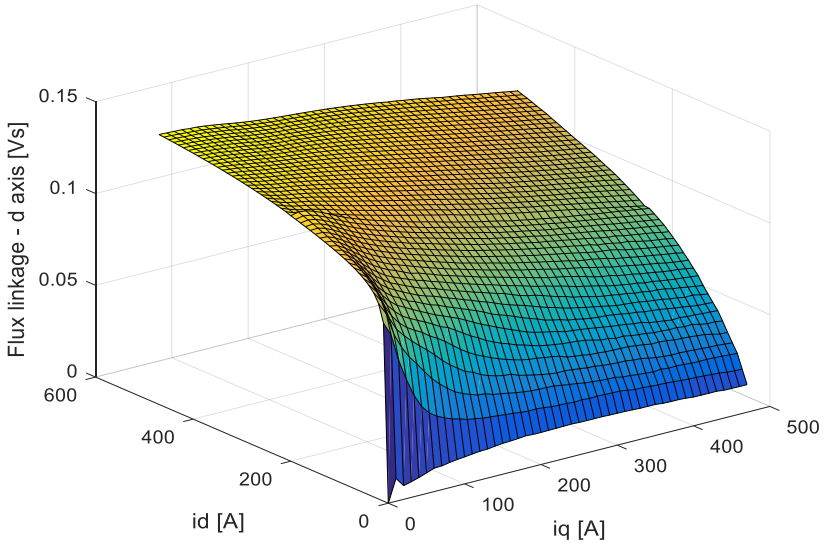

Fig. 4.26 Flux linkage in d-axis - machine with skewed rotor

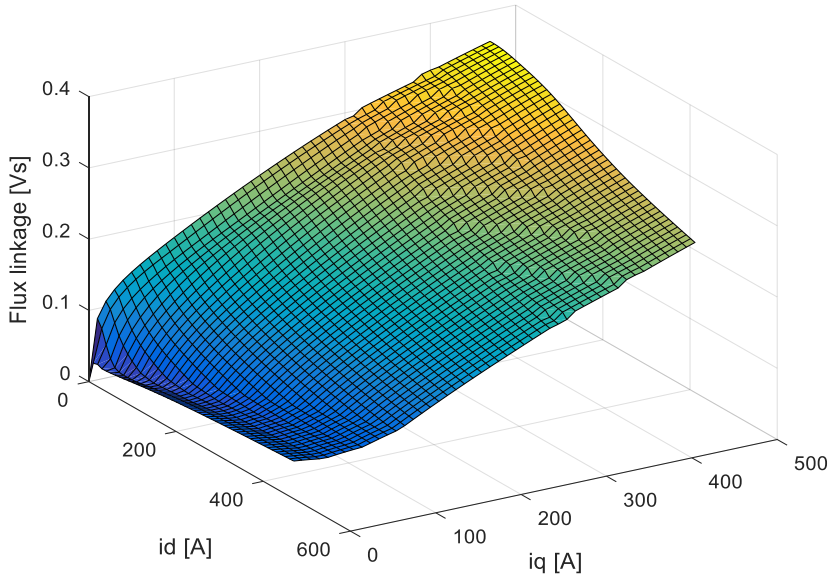

Fig. 4.27 Flux linkage in q-axis - machine with skewed rotor

Rotor skew has a significant impact on machine's flux linkage. In case of d-axis MMF, skewing the rotor results in lower flux linkage. The orthogonal axes (d and q) of a skewed rotor cannot be aligned with orthogonal axes of the stator. Rotor in d-axis provides a magnetic path of the smallest reluctance. Flux linkage in d-axis achieves the maximum value at a given current hence any deviation from this position increases the reluctance of d-axis magnetic circuit. Exact opposite situation occurs in for q-axis MMF. Since the magnetic circuit in q-axis has the highest magnetic reluctance, any deviation from q-axis results in increased magnetic flux flowing between the stator and the rotor. For that reason, one can see that flux linkage in q-axis is sometimes higher than flux linkage in d-axis for machine with skewed rotor. However, the cross saturation is also higher in machine with skewed rotor especially for q-axis flux linkage.

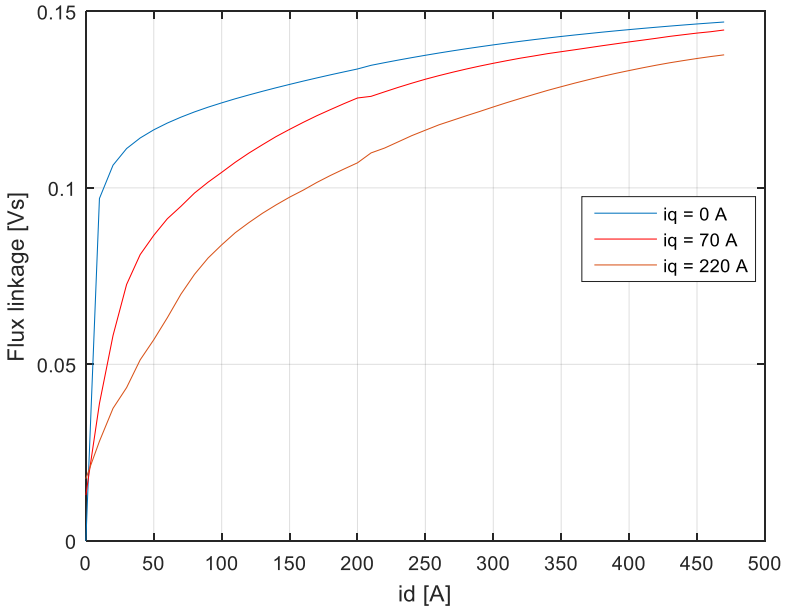

Fig. 4.28 Flux linkage in d-axis - machine with skewed rotor

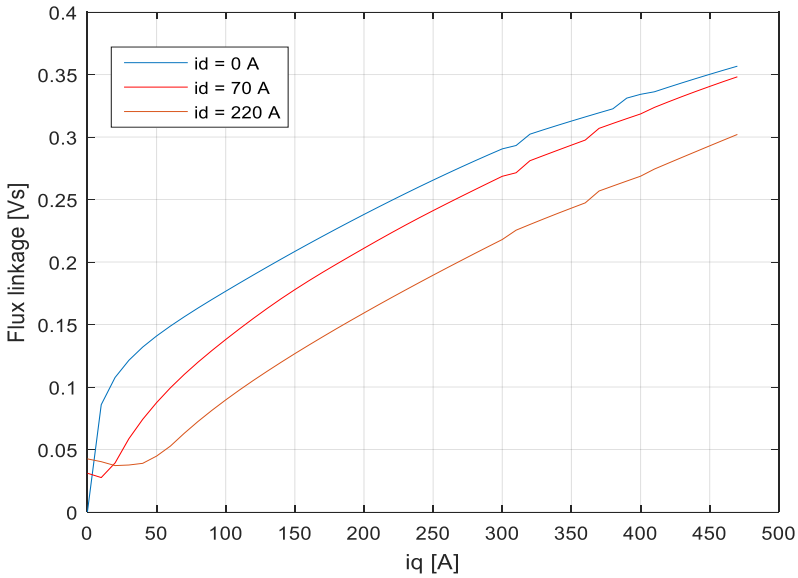

Fig. 4.29 Flux linkage in q-axis - machine with skewed rotor

Fig. 4.28 shows d-axis flux linkage for three values of q-axis current for the machine with skewed rotor. One can observe that the q-axis current has an impact on d-axis flux linkage. In Fig. 4.29 one can see q-axis flux linkage for three values of d-axis current in the machine with skewed rotor. Similarly, in this case one can see the influence of d-axis current on flux linkage in q axis. The values of flux linkage in d and q-axis changed. Flux linkage in d-axis is lower for machine with skewed rotor but also here one can observe a saturation of magnetic circuit. In case of q-axis flux linkage, the flux still increases linearly as it was for machine with non-skewed rotor but the values of the flux increased.

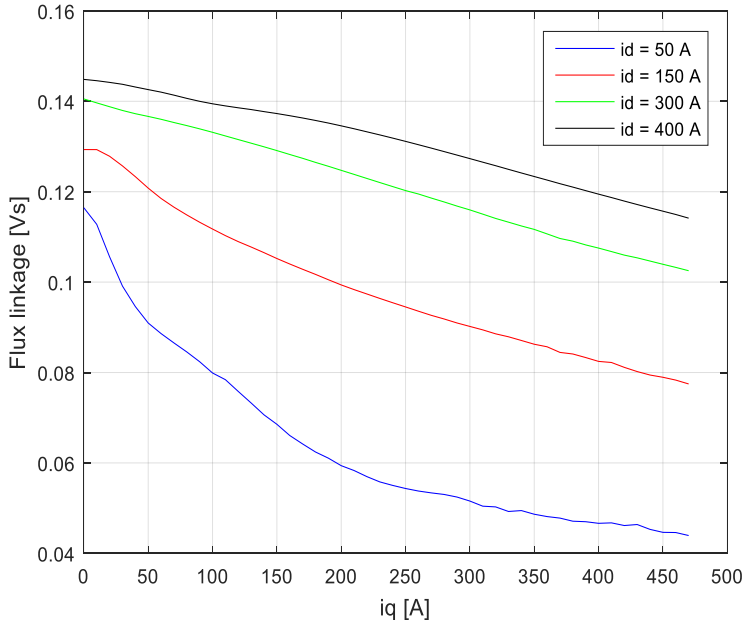

Fig. 4.30 Cross saturation in d-axis - machine with skewed rotor

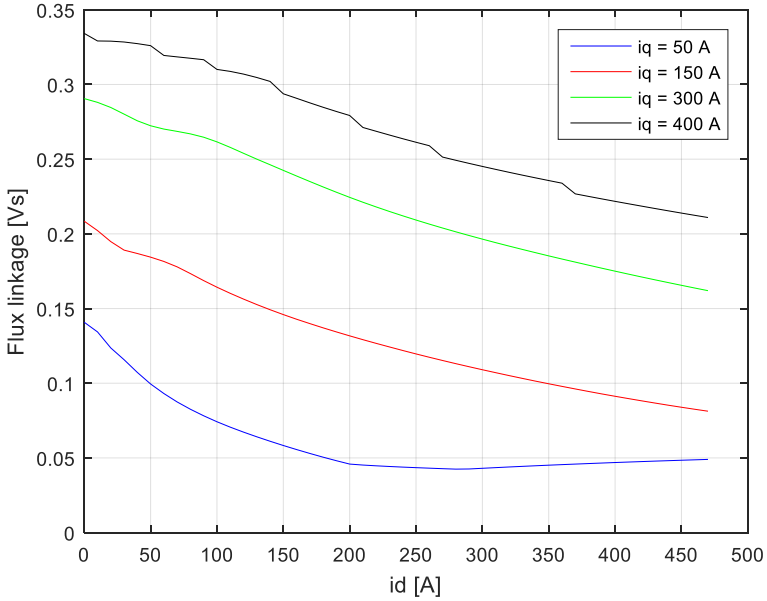

Fig. 4.31 Cross saturation in q-axis - machine with skewed rotor

Fig. 4.30 and Fig. 4.31 show the cross saturation occurring in the machine. One can see that magnetic circuits of the machine are in fact dependent on each other. Any variation of d-axis current results in changes of d-axis flux and also q-axis flux. Similarly, any variations of q-axis current affects not only q-axis flux but also d-axis flux. Hence for more accurate performance analysis of SynRM, flux linkages in d and q-axis should be represented as functions of two current - in d and q-axis.

Results obtained from a 3D model of SynRM with skewed rotor are presented in Fig. 4.32 and Fig. 4.33. In Fig. 4.32 one can see a 3D map of magnetic flux density of the machine. Using 3D model allows to see the distribution of the magnetic field in axial direction of the machine. Fig. 4.33 contains a comparison of instantaneous torque of SynRM with skewed rotor, obtained from 3D model and a 2D model with multi-slice modeling of the skew. Obtained results are similar. In case of skew 2D modeling, the torque waveform contains some sharp peaks and is less smooth than the torque waveform obtained from 3D model. This might be caused by the discontinuity of rotor modeling using slices. The phase shift between 2D and 3D model torque waveform is caused by the difference in initial positions of the rotor in the models.

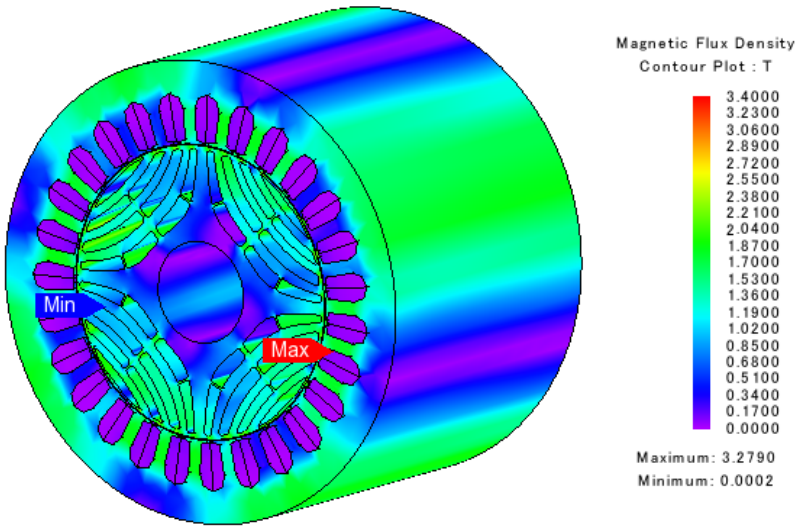

Fig. 4.32 Distribution of magnetic flux density - 3D model of SynRM

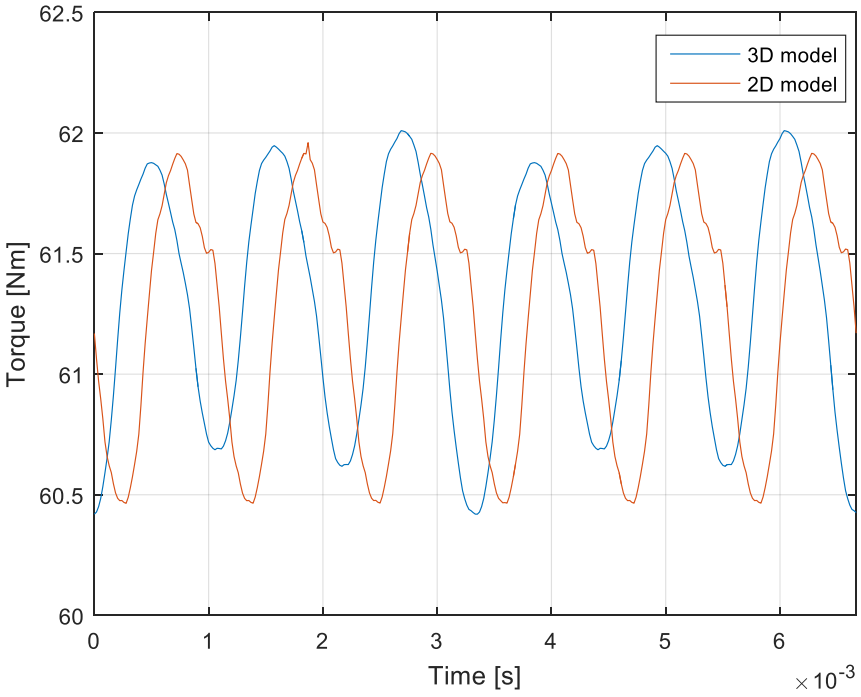

Fig. 4.33 Comparison of torque waveforms

Obtained results prove that rotor skew results in lower torque ripple for all current angles, lower phase voltage and unfortunately lower electromagnetic torque. The highest torque ripple occurs at current angles close to 0 and 90^0 where the generated torque is the lowest. Lower torque is a result of lower inductance which decreases in machines with skewed rotor.

4.2.2. Structural Analysis and SynRM NVH Behavior

The final topology of the SynRM's rotor is presented in Fig. 4.34 d). The rotor has four flux barriers without any cutoff. This makes the air-gap smooth (when neglecting stator slotting). This eliminates windage losses of the machine and reduces torque ripple. The procedure of finding the final topology of the rotor is the same as the one described in Chapter 3.4.

4.2.2.1. Structural Analysis

Structural analysis of electric machines is a crucial part of multiphysics analysis of the machine since it is responsible for the robustness of the structure. From the mechanical point of view, the most endangered part is the rotor as it has to withstand high centrifugal forces due to high rotational speeds.

Structural analyses were run for several rotor topologies in order to find the topology that can operate at 12000 rpm. Comparison of four selected topologies is presented in Fig. 4.34. Basic geometry (Fig. 4.34a), which is the best in terms of electromagnetic behavior, cannot operate at maximum speed due to high von Mises stress. When ribs are introduced, the maximum stress significantly decreases but is still too high for the rotor to operate at maximum speed without any damage. Introducing two additional ribs to the rotor in the firs flux barrier was necessary for the rotor to operate at maximum speed.

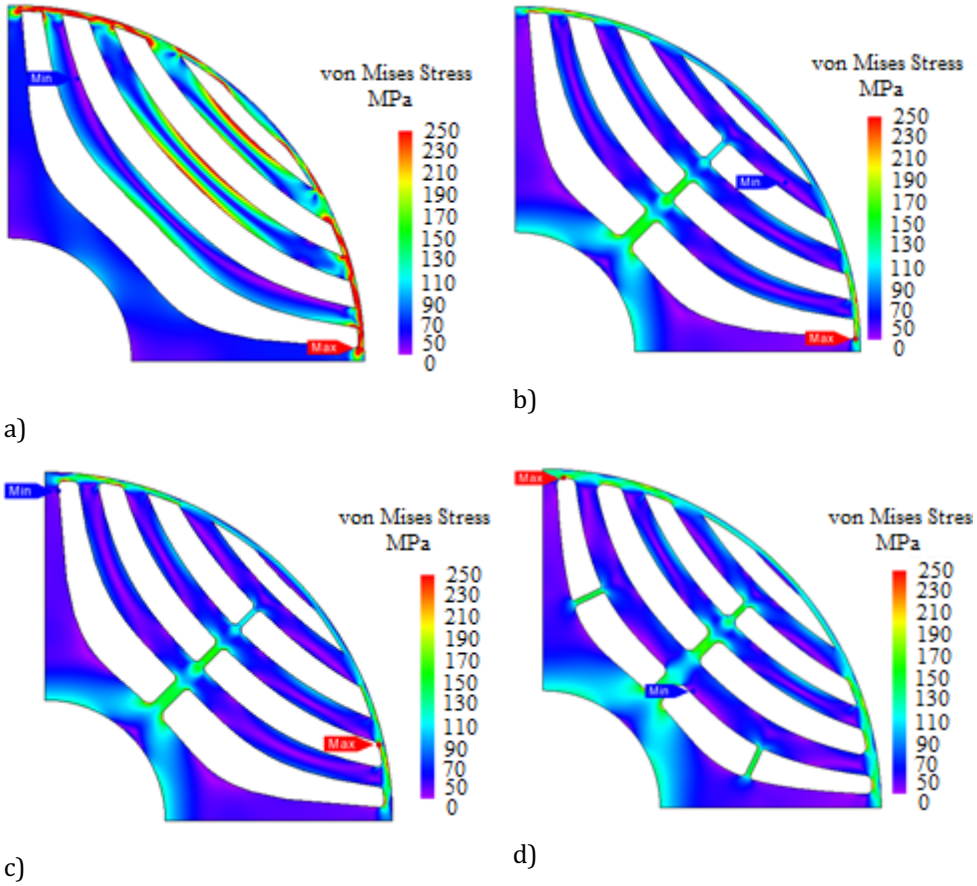

Fig. 4.34 Distribution of von Mises stress in the rotor: a) initial topology, b) topology with ribs, c) topology with ribs and rounded corners, d) final topology

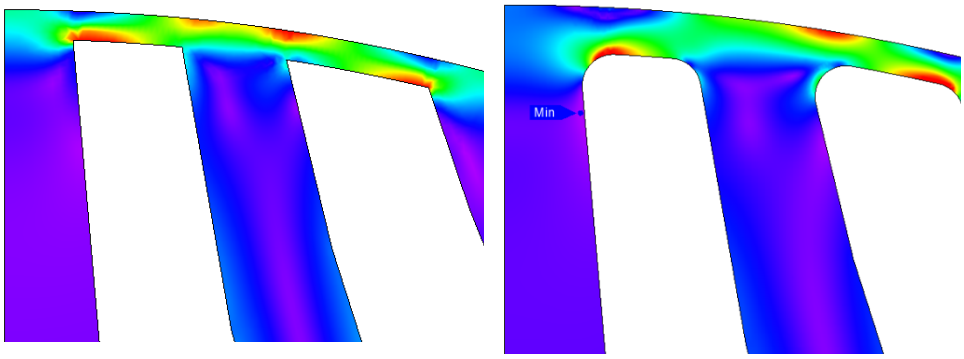

Fig. 4.35 von Mises stress distribution in rotor bridges: sharp corners (left) and rounded corners (right)

Fig. 4.34. shows von Mises stress distribution in four different rotor topologies with four flux barriers. In this case, rotor without a cutout was selected in order to reduce torque ripple. The von Mises stress graph was scaled from 0 to 250 MPa. Places on the rotor where von Mises stress is equal to or greater than 250 MPa are marked with red color. One can notice that the highest stress occurs in first rotor topology (Fig. 4.34a) since this rotor does not have any ribs. The highest stress appears in rotor bridges. Adding ribs (Fig. 4.34 b and c) reduces von Mises stress but its value is still too high. Topologies shown in Fig. 4.34 b) and c) are similar but the differences can be observed in Fig. 4.35.

Topology in Fig. 4.34c) has rounded corners of flux barriers whereas the corners of flux barriers of topology from Fig. 4.34 b) are sharp. This increases the local concentration of von Mises stress (Fig. 4.35 left).

TABLE 4.7 Von Mises stress values for different rotor topologies

Rotor type	Part name	Width	Maximum stress at 12000 rpm
Rotor without ribs	First bridge	1 mm	1497 MPa
	Second bridge	1 mm	
	Third bride	1 mm	
	Fourth bridge	1 mm	
Rotor with three ribs – Fig. 4.34b	First bridge	1 mm	357 MPa
	Second bridge	1 mm	
	Third bridge	1 mm	
	Fourth bridge	1 mm	
	First rib	2.5 mm	
	Second rib	1.5 mm	
	Third rib	1 mm	
Rotor with three ribs – Fig. 4.34c	First bridge	1.5 mm	347 MPa
	Second bridge	1 mm	
	Third bridge	1 mm	
	Fourth bridge	1 mm	
	First rib	2.5 mm	
	Second rib	1.5 mm	
	Third rib	1 mm	
Rotor with five ribs – Fig. 4.34d	First bridge	1.6 mm	165 MPa
	Second bridge	1.8 mm	
	Third bridge	1.5 mm	
	Fourth bridge	1 mm	
	First rib (middle)	3 mm	
	Side ribs (first flux barrier)	1 mm	
	Second rib	2 mm	
	Third rib	1 mm	

Flux barriers introduce discontinuities in the rotor's structure affecting stress distribution. One needs to remember about local stress concentrations in vicinity of the discontinuity when calculating von Mises stress since there the stress is higher than in other parts of the structure where the stress distribution is not distorted. For that reason, it is necessary to use a fine mesh in areas where the stress concentration is high. The finer the mesh the more accurate stress distribution can be obtained but the computational cost is also higher. Size of mesh element should be a trade-off between accuracy and simulation time.

Stress concentration are caused by geometric discontinuities. Typical discontinuities are fillets or holes. The elementary formulas for stress calculation used in the design of structural members are based on the members having a constant section. However, such conditions are hardly attained practically. The presence of fillets, holes, shoulders and so on, results in modification of a simple stress distribution so that local high stresses occur.

Centrifugal forces are not the only forces acting on the rotor during machine's operation. Magnetic field in the machine causes magnetic radial forces to act on both stator and rotor. Whereas the tangential component is responsible for torque generation, the normal component is responsible for deformation of stator and rotor. Centrifugal and radial magnetic forces combined, contribute to rotor's deformation and thus the influence of magnetic forces should also be examined. Since the rotor of the machine of interest is skewed, the radial magnetic forces were analyzed using machine's 3D model. With skewed rotor the distribution of magnetic forces in axial direction of the rotor is not uniform as one can see in Fig. 4.36.

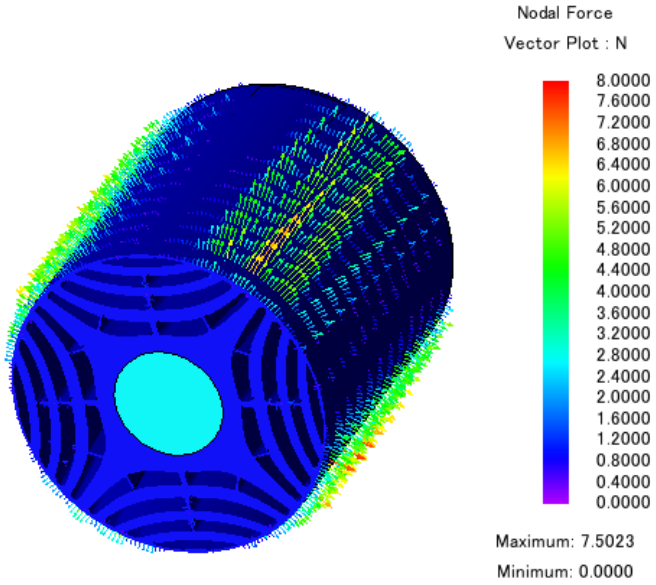

Fig. 4.36 Radial magnetic forces acting on the rotor at 12000 rpm

Presence of magnetic radial forces leads to deformation of rotor's structure. This effect is combined with deformation of the structure caused by centrifugal forces.

Fig. 4.37. shows rotor's structure deformation and distribution of von Mises stress. As one can see, the contribution of magnetic radial forces to overall deformation of the rotor and von Mises stress distribution is negligible hence it might be omitted when performing structural test of the rotor. At high rotational speeds, the centrifugal forces become the major factor that leads to mechanical failure of the material. Magnetic forces might become more relevant at lower rotational speeds and high currents especially for less robust rotor structures.

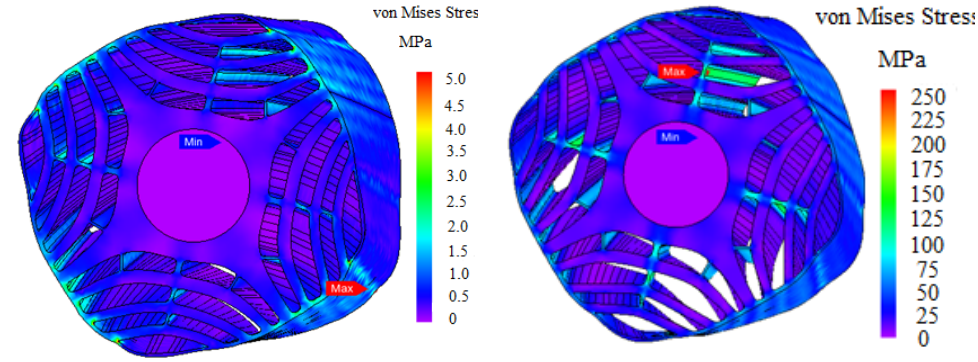

Fig. 4.37 Deformation of rotor's structure: a) deformation due to magnetic forces (scaling factor 10000),
b) deformation due to magnetic and centrifugal forces (scaling factor 300)

Radial forces acting on the inner surface of the stator are shown in figures below. In case of machine with skewed rotor, the forces are shown for each slice. One can see the difference in forces amplitude and distribution for each slice. There is also a significant difference in radial forces' amplitude when the machine operates at different current angles, expecially when the machine operates at d or q-axis stator MMF. At d-axis MMF, the radial forces achieve the greatest amplitudes sine the magnetic field in the machine is the greatest. When operating at q-axis MMF, the machine is demagnetized hence the radial forces achieve the lowest values. The parameters of the machine are shown in Table 4.8.

TABLE 4.8 Parameters of the machine

Parameter	Value
Power	30 kW
Number of poles	4
Number of slots	27
Rated speed	4500 rpm
Maximum speed	12000 rpm
Rotor diameter	130 mm
Shaft diameter	45 mm
Air gap length	0.45 mm
Stator outer diameter	205 mm

In order to perform NHV analysis of the analyzed SynRM, normal modes of stator's structure must be found. Modal analysis was performed in VirtualLAB. Several normal modes of the stator are shown in figure below. Resonance frequencies of the stator are contained in Table 4.9.

TABLE 4.9 Natural frequencies of the stator

Mode number	Undamped frequency (Hz)
1	928.40
	1474.75
2	2485.10
	3331.46
3	4433.87
	5333.00
4	5658.62
	6470.15

Example normal modes of stator's structure are presented in Fig. 4.38. One can see that each mode has its own resonance frequency and a corresponding mode shape.

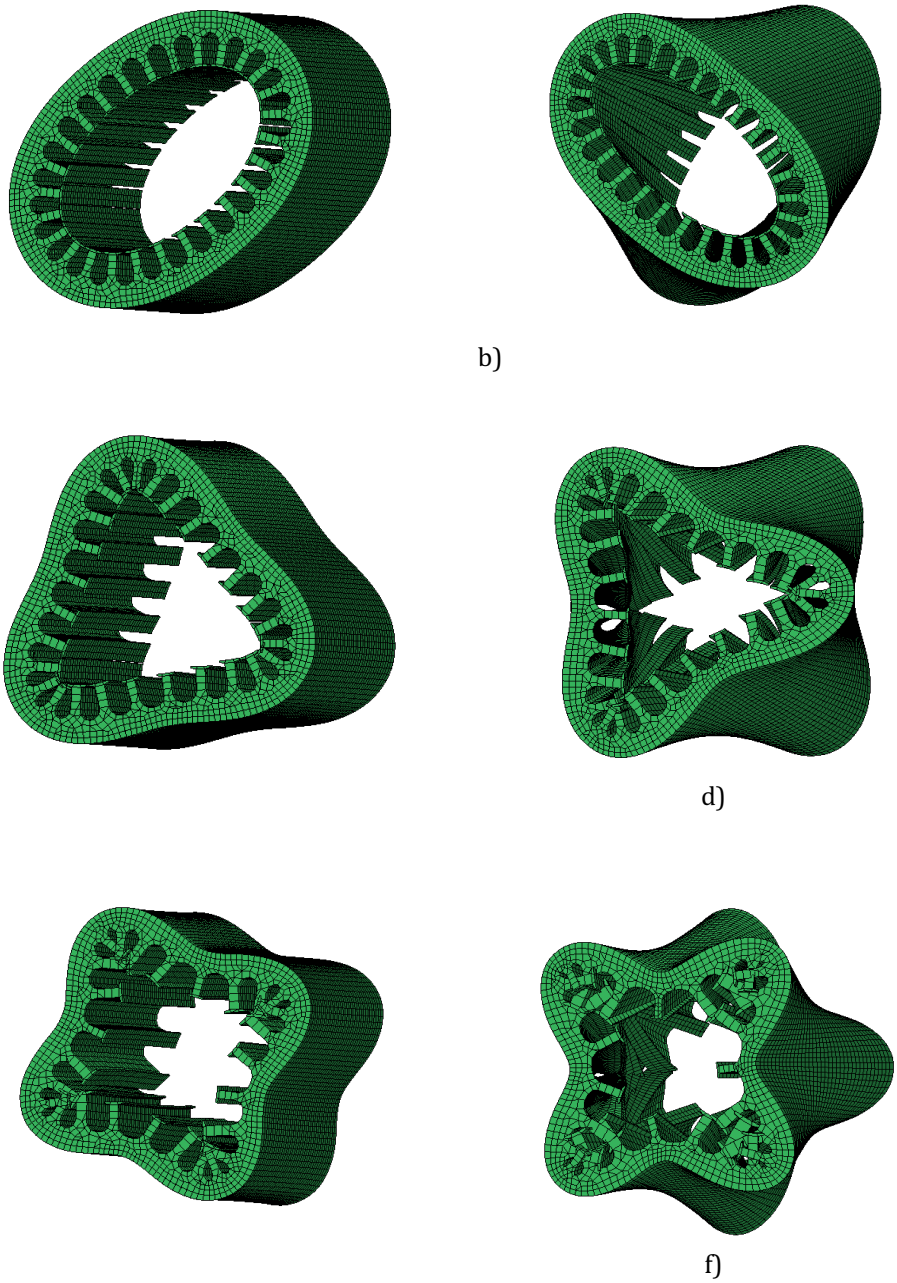

Fig. 4.38 Normal modes of stator's structure: a), b) first mode, c), d) second mode, e), f) fourth mode

Radial forces acting on the inner surface of the stator are presented in Fig. 4.39. In this figure one can see a comparison of radial forces of machine with skewed and non-skewed rotor.

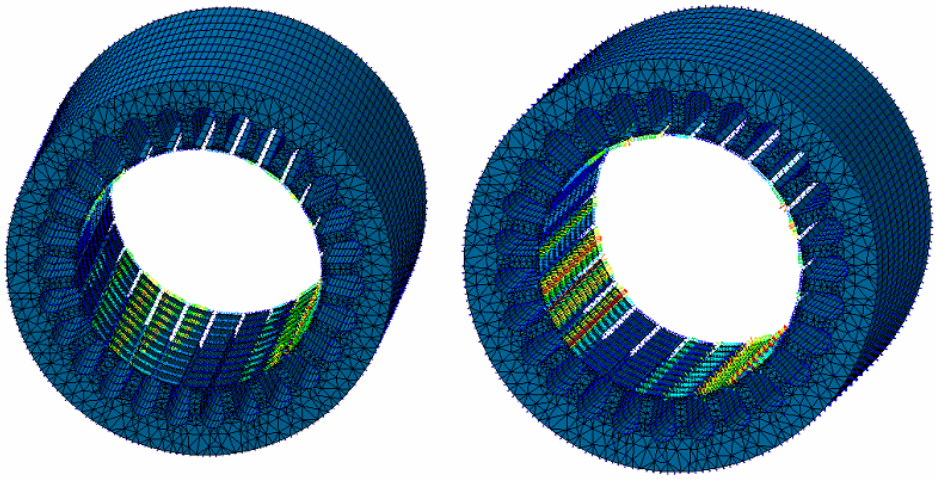

Fig. 4.39 Radial forces acting on the inner surface of the stator: machine with skew (left) and machine without skew (right)

In case of machine with skewed rotor, the analysis was performed using a 2D model with five slices along the axial length and a 3D model. Machine with non-skewed rotor was analyzed using 2D model which is sufficient since the radial forces are distributed uniformly along machine's axial length. In Fig. 4.40 a) one can see radial forces acting on different parts of the stator in SynRM with skewed rotor. The figure shows radial forces on both ends and in the middle of the stator. Fig. 4.40 b) shows the radial forces along the entire axial length of the machine. In Fig. 4.40 c) one can see radial forces of the machine with non-skewed rotor. As one can notice, the amplitudes of the radial forces are greater than those of SynRM with skewed rotor. Since the forces are unifrom along the axial length of the machine, they were not shown on a 3D plot.

Fig. 4.40 d) shows the comparison of radial forces for machine with skewed and non-skewed rotor.

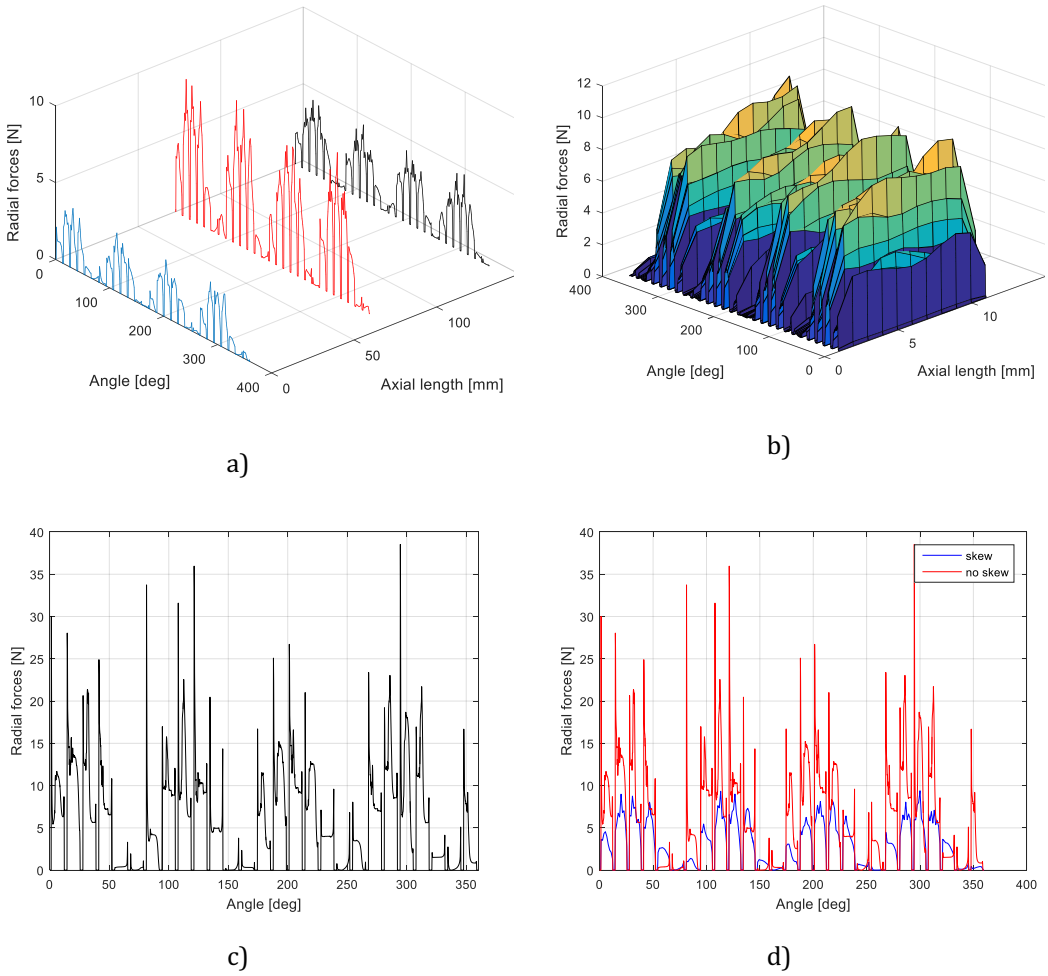

Fig. 4.40 Radial forces acting on the stator: a) radial forces on stator with skewed rotor (three slices), b) radial forces on stator with skewed rotor (3D plot), c) radial forces on stator without skewed rotor,
d) comparison of radial forces of machine with skewed and non-skewed rotor

In case of machine with skewed rotor, 3D analysis was also run. In this way, continuous distribution of radial forces was obtained in axial direction. This improves the accuracy of NVH analysis. In Fig. 4.41 one can see how the torque and radial forces vary with current angle.

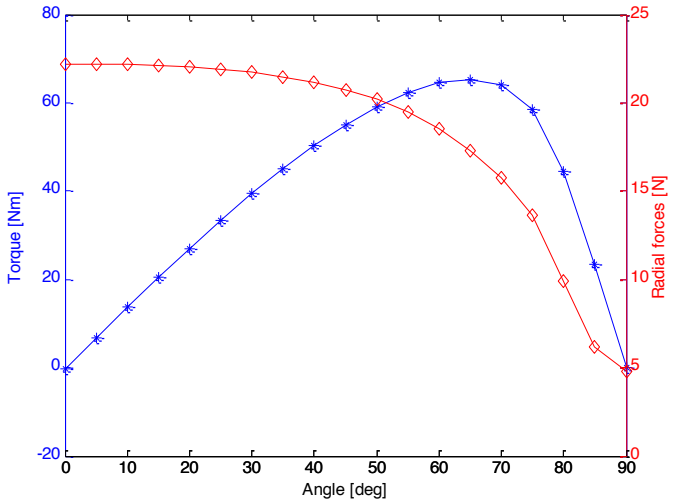

Fig. 4.41 Torque vs. current angle (blue) and radial forces vs. current angle (red)

4.2.2.2. SynRM NVH Behavior

Results of numerical analyses presented so far proved that skewing the rotor affects machine's NVH behavior. Also the radial forces change their amplitudes as the current angle changes. For the final topology of the machine, similar numerical tests were run. Although the final topology of the machine has a skewed rotor, the numerical simulations were also run for a machine without skew. The results are compared below. One can see that rotor skewing affects the axial distribution of radial forces. They have different amplitudes on both ends of the machine. The forces are higher on one end of the machine. This causes higher vibrations on one side of the machine. Also current angle affects vibrations of the structure since it has an influence on the amplitudes of radial forces. Below one can see the comparison of stator's vibration at two different current angles. The values of current angle were chosen to provide the same torque generated by the machine.

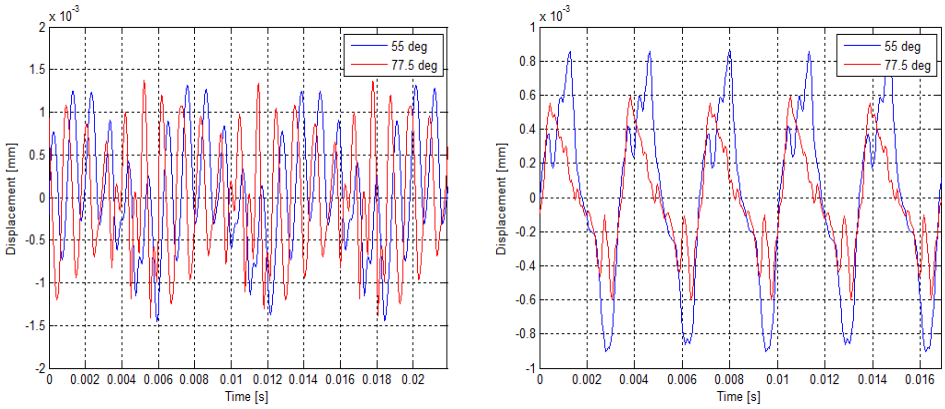

Fig. 4.42 Vibration of the stator at specific point for two different current angles at two rotational speeds: 600 rpm (left) and 4500 rpm (right)

The amplitude of vibration depends of the amplitudes of radial forces acting on the stator and also on the rotational speed of the rotor. The supply frequency varies with rotor's rotational speed. Stator as a structure has its natural frequencies and normal modes. Depending on the frequency of magnetic forces, some normal modes are excited more than the others which has also a big influence on vibrations amplitudes. Fig. 4.42. shows comparison of vibrations of the stator at different current angles at which the machine generates the same torque. At angle closer to 90 electrical^0 (q-axis stator MMF) the radial forces are lower which should cause lower vibration. This happens at 4500 rpm rotational speed (Fig. 4.42. right) however at 600 rpm rotational speed, the vibrations that occur at both current angles are comparable and there is no clear difference in their amplitudes. This shows that the vibration of the structure depends not only on the amplitude of the force but also on the frequency of the applied force. Depending on the frequency of the applied force, various normal modes of the structure respond which causes the vibrations to increase at certain frequencies.

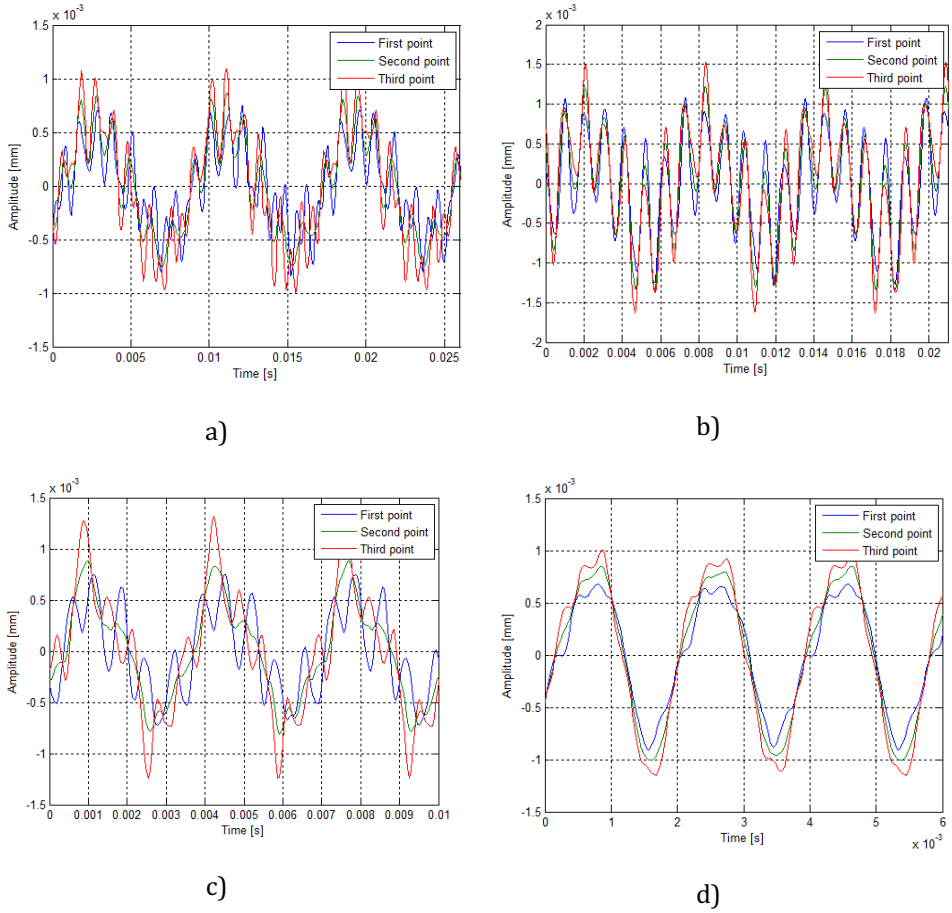

Fig. 4.43 Vibrations of stator's structure measured in three points for machine with skewed rotor: a) 1800 rpm, b) 2400 rpm, c) 4500 rpm and d) 8000 rpm

When the machine has a skewed rotor, the radial forces acting on the stator are not distributed evenly along its axial length. This uneven distribution of radial forces results in different vibration amplitudes on both ends of the machine. Fig. 4.43 shows comparison of vibrations measured at three points on stator's surface along machine's axial length. Two points were placed on both ends of the stator and one point was placed in the middle. It can be observed that the vibrations on one end of the machine obtain higher amplitudes than the vibrations measured in the other points. Especially, the greatest difference occurs between vibrations measured on both ends of the stator. Depending on the rotational speed, the difference between vibrations' amplitudes might

vary. This is caused by normal modes of the stator which are excited at different rotational speeds.

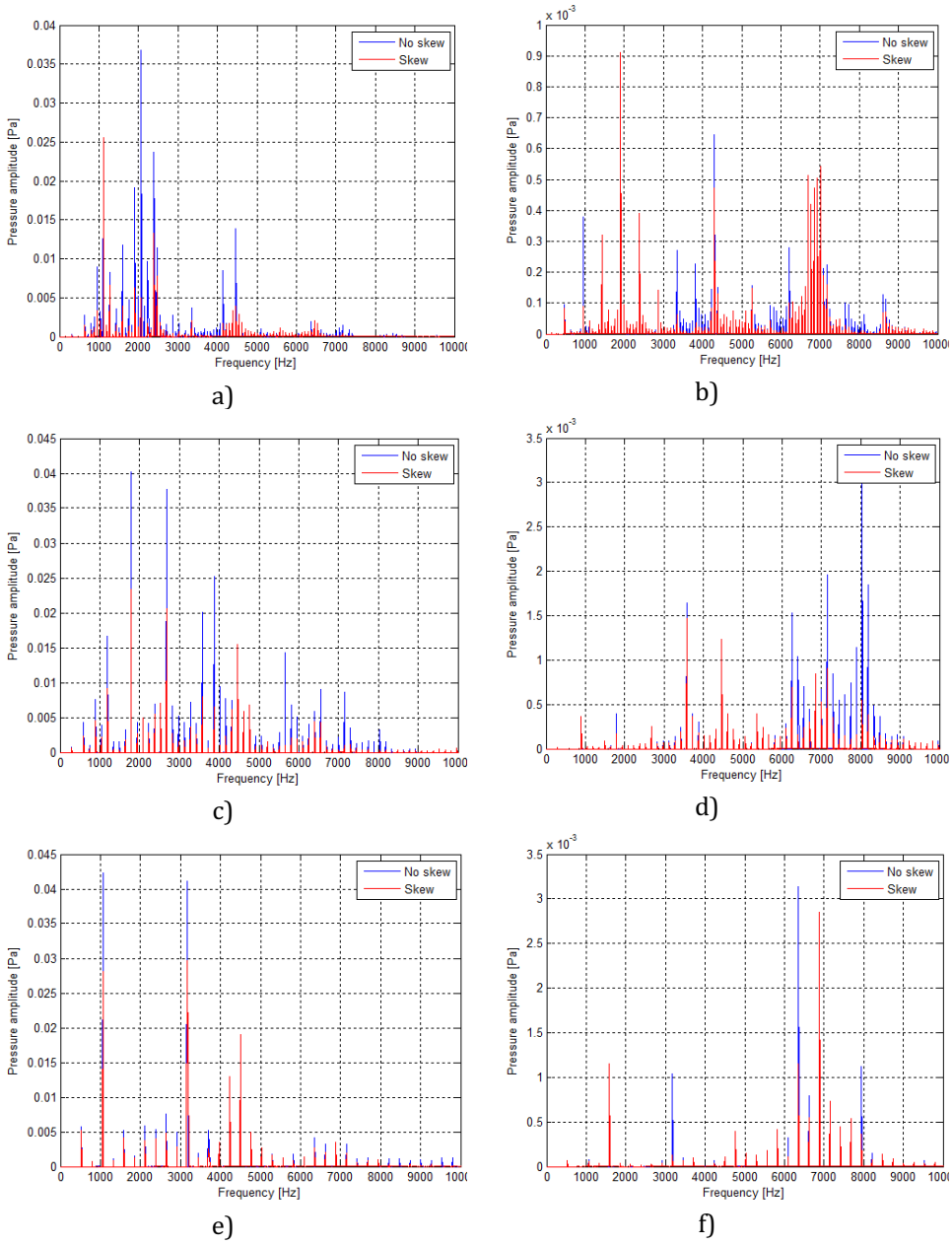

Fig. 4.44 Noise harmonics measured at first point (left column) and fourth point (right column): a), b) 2400 rpm, c), d) 4500 rpm and e), f) 8000 rpm

In Fig. 4.44 one can observe frequency spectra of noise generated by the machine, measured at the first and last point. The amplitudes of the harmonics are in general lower for machine with skewed rotor. In order to have a better understanding of the difference in noise generation by machine with skewed and non-skewed rotor, band power of the noise was calculated. The higher the rotational speed the higher the frequencies of noise harmonics generated by the machine. The biggest difference can be observed at lower speeds. At 8000 rpm, the harmonics are quite similar for both skewed and non-skewed machine. Fig. 4.45 shows the points in which the noise was calculated. The distances of the points from the center of the machine are given in Table 4.10.

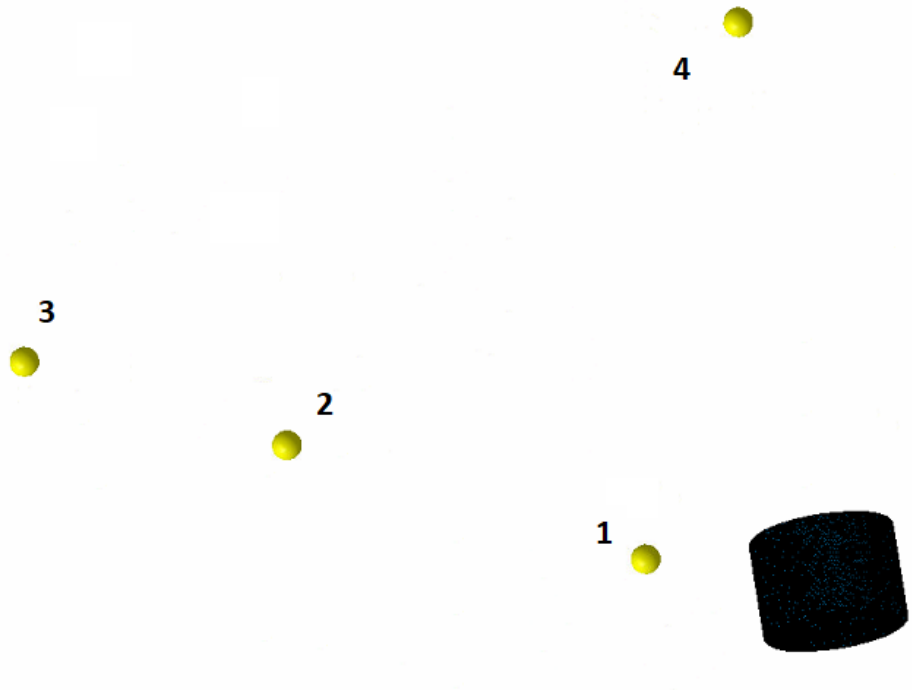

Fig. 4.45 Points for noise measurement

TABLE 4.10 Comparison of noise band power at different points and rotational speeds

Speed [rpm]		**Band power dB(RMS)**			
		Point 1 [500 mm]	**Point 2** [1500 mm]	**Point 3** [2100 mm]	**Point 4** [1100 mm]
1800	No skew	81.921	72.587	69.163	31.857
	Skew	79.381	70.012	66.575	30.464
2400	No skew	76.217	66.864	63.430	32.365
	Skew	70.765	61.433	58.018	35.505
4500	No skew	77.683	68.548	65.131	45.875
	Skew	72.933	63.454	60.018	40.008
8000	No skew	76.279	67.003	63.572	42.418
	Skew	76.012	64.762	61.041	42,066
12000	No skew	87.287	78.819	75.421	39.959
	Skew	81.748	67.480	64.076	38.023

Table 4.10 shows comparison of band power in dB measured in four different points. The simulations were run for several rotational speeds for machine with skewed and non-skewed rotor. Obtained results show that the band power of generated noise changes with rotational speed and distance. In general, the higher the rotational speed the greater band power of generated noise. There are some exceptions e.g. at 1800 rpm the noise has greater power than at 2400 rpm. This is because at specific rotational speeds, some normal modes are excited more than the others leading to higher noise level. The noise level also changes with rotor's skew. Machine with skewed rotor generates noise of lower band power than the machine without skewed rotor.

4.2.3. Thermal Behavior

Thermal analysis of synchronous reluctance machine was performed in MotorCAD and JMAG. While MotorCAD is a dedicated software for thermal analysis of electric motors and its simulations are based on lumped parameters model, JMAG uses finite element method to calculate machine's temperature and requires a 3D model. Final topology of the machine was under investigation. Power losses of the machine for different rotational speeds are shown in picture below. In constant torque region (speed range from 0 to 4500 rpm), copper losses are dominant as they are proportional to square of phase current. At low rotational speed iron losses are low since the frequency of phase current

is low. Machine's power losses at different rotational speeds are shown in Fig. 4.46. This figure also shows comparison of iron losses calculated in JMAG and MotorCAD.

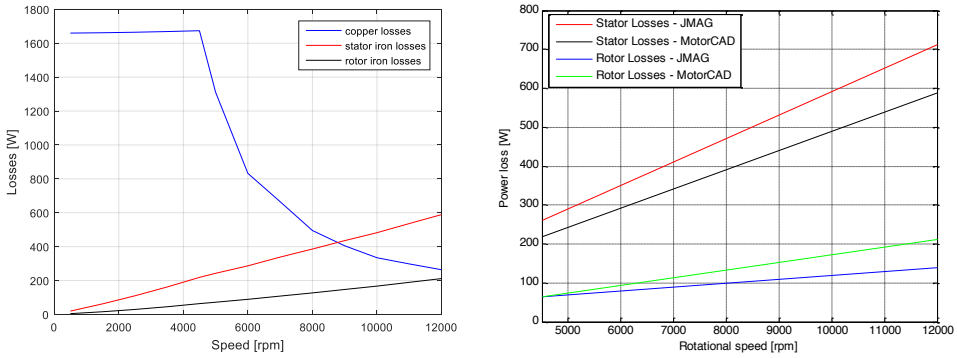

Fig. 4.46 Power losses a) MotorCAD, b) comparison of iron losses

Machine's power losses were calculated in JMAG using 3D model. Operating points at 4500 rpm and 12000 rpm were analyzed both at continuous and maximum power. Iron loss distribution in rotor and stator is presented in figures below.

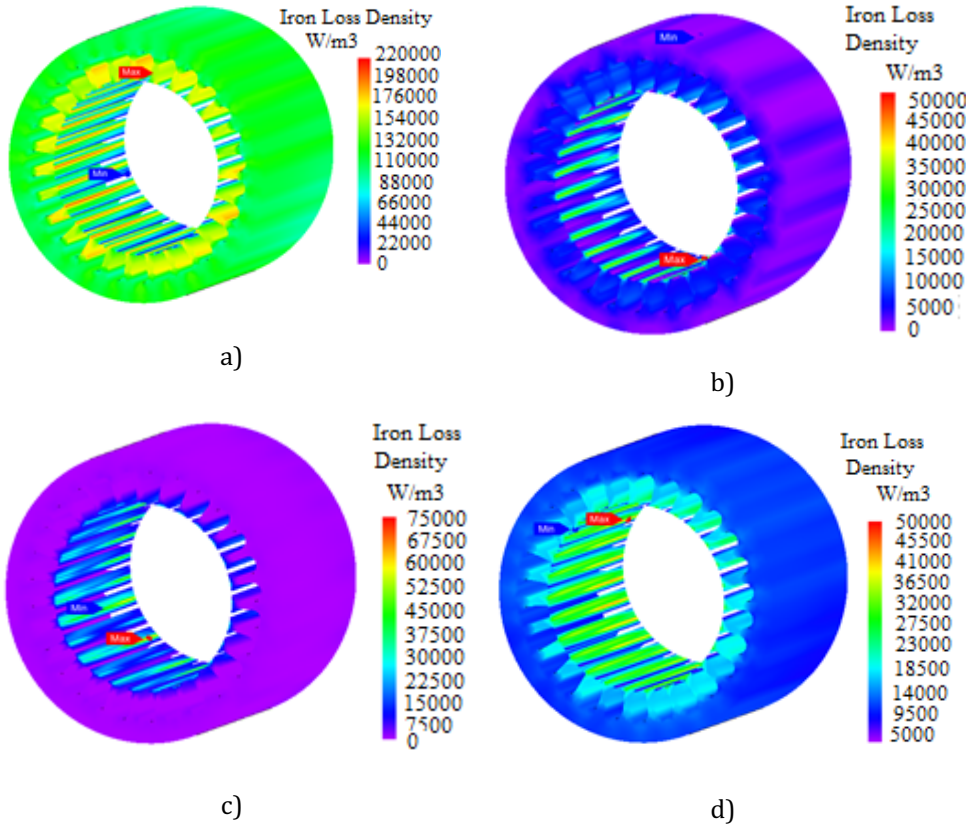

Fig. 4.47 Iron loss density at 4500 rpm: a) 150 Hz, b) 1050 Hz, c) 1950 Hz d) total iron loss

Fig. 4.47. shows iron loss density in stator core for basic harmonic, two higher order harmonics and total iron loss density for all harmonics. The highest iron losses in stator core occur for the supply frequency. Higher frequency components have much lower amplitudes in stator magnetic field. As one can see, the highest loss density is in stator teeth and inner surface. Iron loss density in rotor core is presented below. The highest power loss density is on the surface of the rotor.

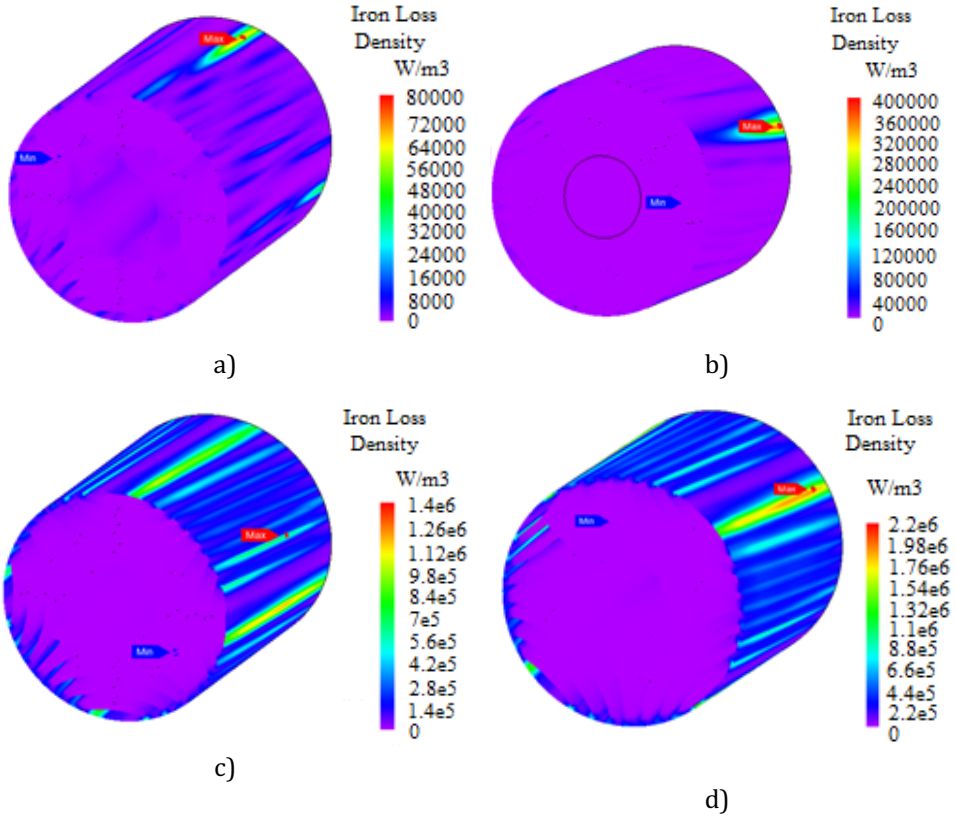

Fig. 4.48 Iron loss density at 4500 rpm: a) 150 Hz, b) 1050 Hz, c) 1950 Hz d) total iron loss

Fig. 4.47 shows that the base harmonic is the biggest contributor to iron loses in stator core. Higher harmonic generates more losses in stator's teeth and inner surface. In case of rotor core, higher harmonics play more significant role in generation of iron losses (Fig. 4.48). Fig. 4.49. shows power loss density in stator core at 12000 rpm rotational speed. Also in this case, supply frequency component of the magnetic field generates the highest iron loss in stator core. Moreover, iron loss distribution seems not to be uniform along machines axial length. It is caused by rotor skewing which changes the magnetic reluctance along machine's axial length. Magnetic density is not uniform in axial direction of the machine which has an impact on iron loss generation. The scale of this effect depends on working condition of the machine, especially on the angle between rotor's d-axis and stator magnetic field-axis.

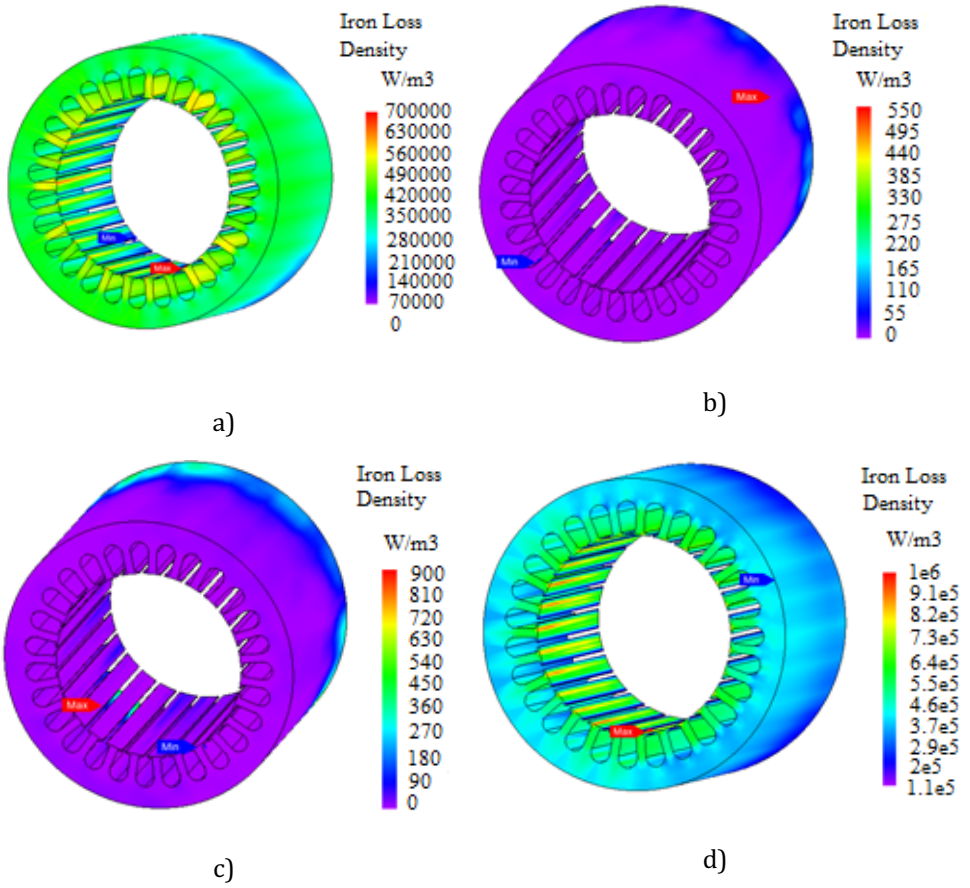

Fig. 4.49 Iron loss density at 12000 rpm: a) 400 Hz, b) 8000 Hz, c) 16000 Hz, d) total iron loss

As in the previous case, iron loss distribution in the rotor is the highest on rotor's surface. The higher the frequency, the more iron losses occur on the surface of the rotor.

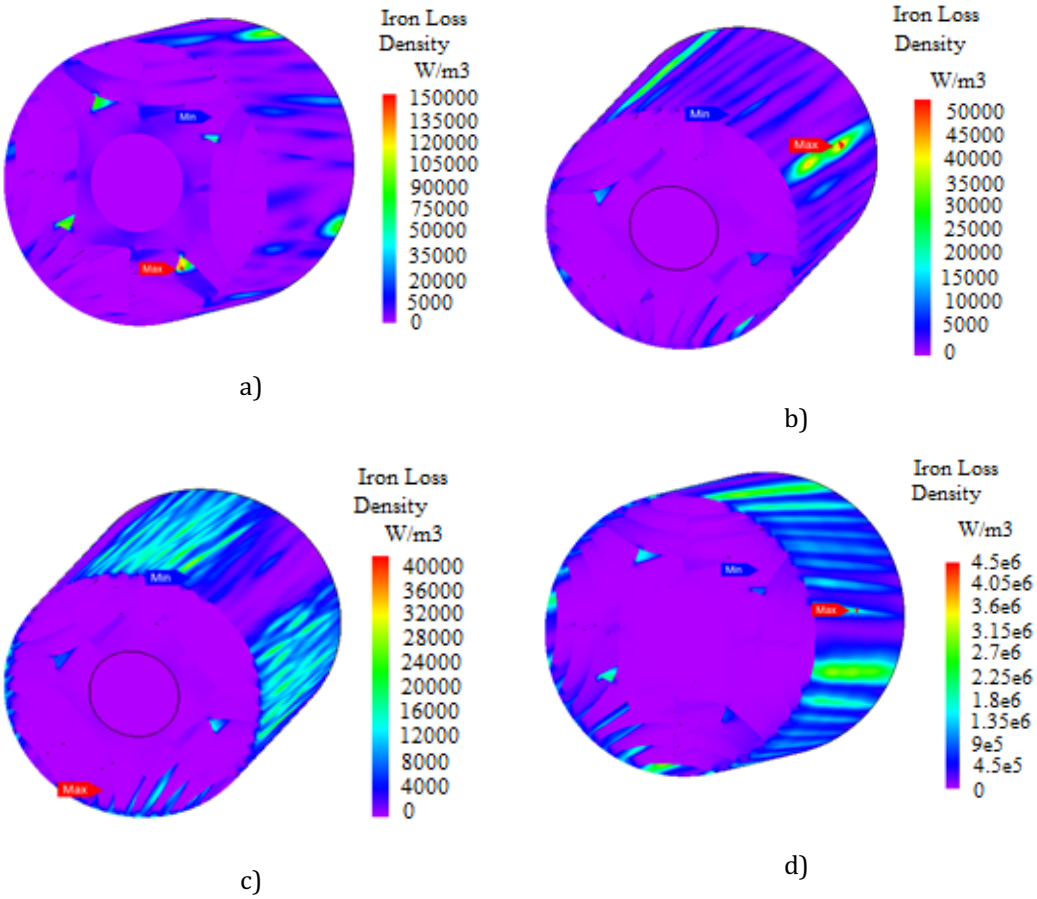

Fig. 4.50 Iron loss density at 12000 rpm: a) 400 Hz, b) 8000 Hz, c) 16000 Hz, d) total iron loss

Iron loss for particular harmonics is shown in figures below. For the stator, one can see that the base harmonic generates the highest power losses. Higher order harmonics' influence on stator iron loss is practically negligible. For the rotor is exactly opposite. High frequency components are dominant and they are the major contributors to iron losses. Figures show that iron losses in the rotor are smaller than those in the stator.

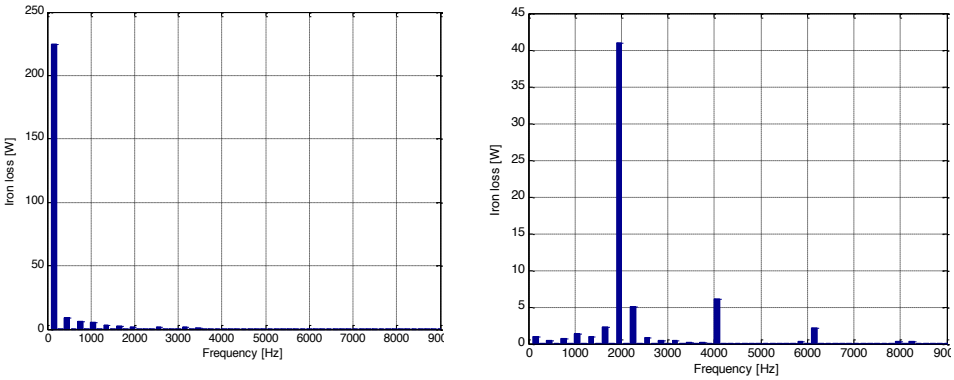

Fig. 4.51 Iron loss for particular harmonics at 4500 rpm: iron loss in stator core (left) and iron loss in rotor core (right)

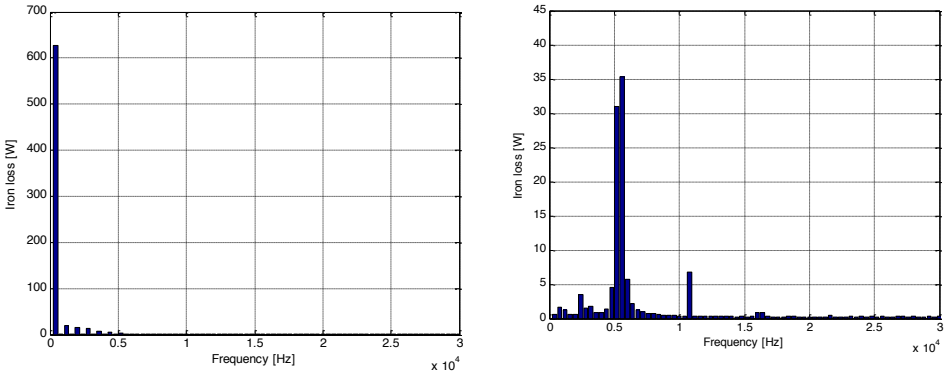

Fig. 4.52 Iron loss for particular harmonics at 12000 rpm: iron loss in stator core (left) and iron loss in rotor core (right)

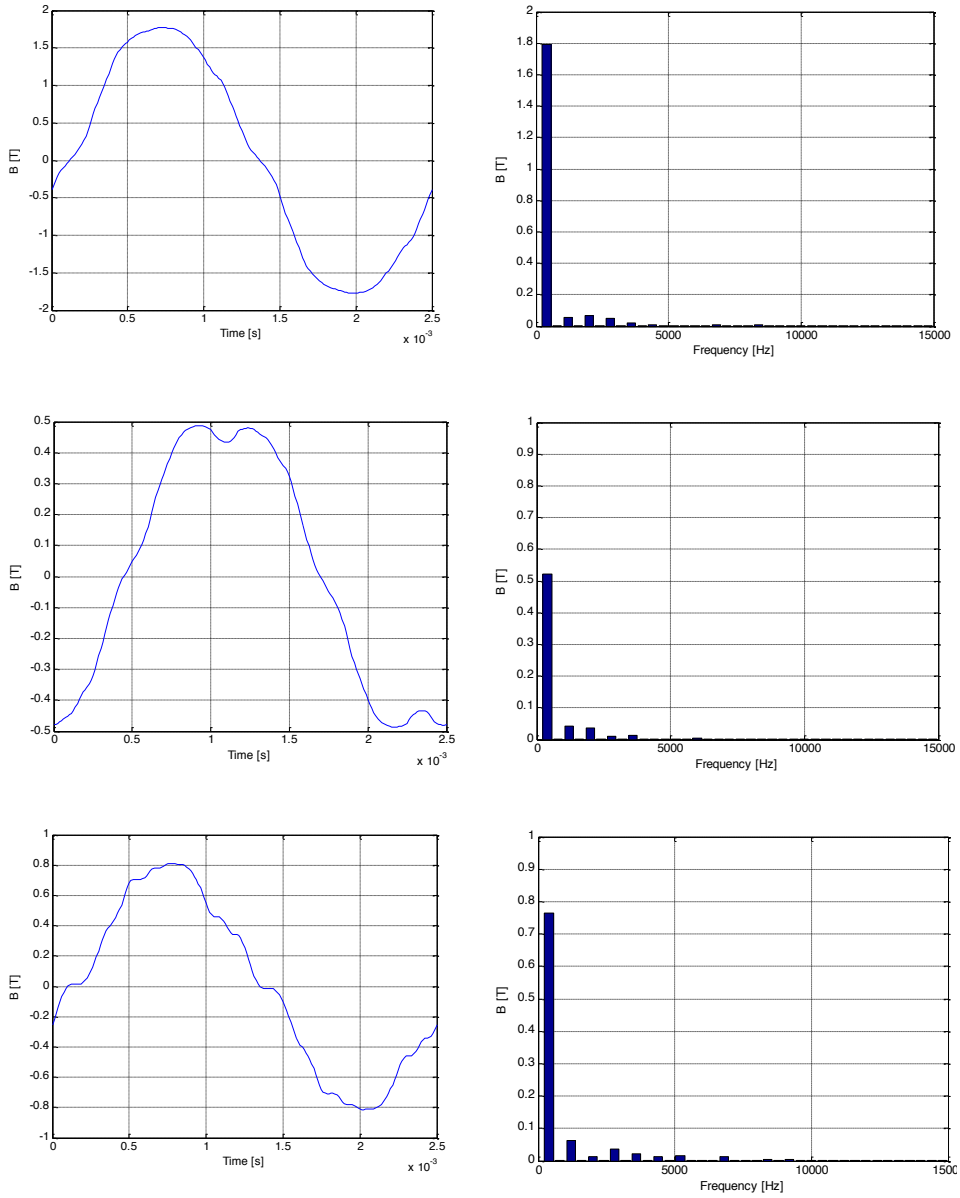

Fig. 4.53 Stator magnetic flux density radial component measured in: point 1 (top), point 2 (middle) and point 3 (bottom)

Iron losses at 12000 rpm rotational speed in the stator and rotor core are shown in Fig. 4.52. The basic harmonic is dominant in generating iron loss in stator core. By comparing Fig. 4.51 and Fig. 4.52 one can notice that iron loss significantly grows as the rotational speeds increases. Higher harmonics also generate some iron loss in stator core, however they are negligible compared to the losses at the base frequency. Iron losses in rotor core are smaller compared to the losses in stator core. They are generated by higher frequency components of the magnetic field. In figures below on can see the variation of magnetic field in different machine parts. In stator core, the magnetic field changes with the frequency of motor's current. Higher harmonics are also present due to machine's reluctance variation caused by the slotting and interaction with the rotor. Points in which the magnetic field was measured are shown in Fig. 4.55. One can notice that in stator core, the magnetic field does not have a 0 Hz component. Such a component though appears in magnetic field of the rotor. It is because the rotor is in synchronism with stator's rotating magnetic field.

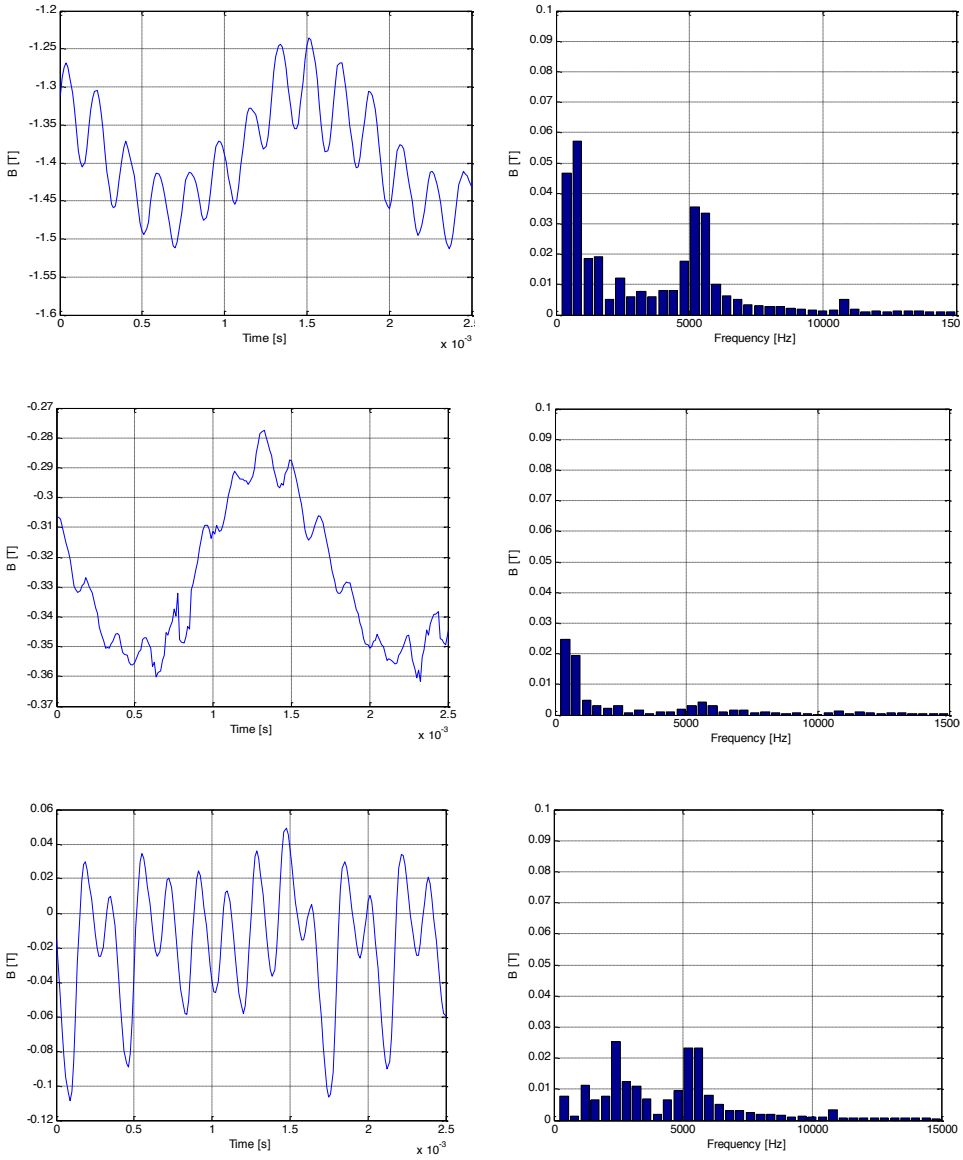

Fig. 4.54 Rotor magnetic flux density radial component measured in: point 1 (top), point 2 (middle) and point 3 (bottom)

Fig. 4.53 and Fig. 4.54 show time waveforms of magnetic flux density and their corresponding FFTs in different parts of the stator and rotor respectively. Magnetic field in the stator has base harmonic component which is dominant regardless the point in which it was measured although its amplitude varies. Magnetic field in the rotor also has basic

harmonic component, however its amplitude is quite small. High frequency components are dominant in rotor's magnetic field. One can see that the highest amplitudes of high frequency components occur on the surface of the rotor. High frequency components of magnetic field send to decrease closer to the shaft. For this reason, the highest iron loss density is on the surface of the rotor.

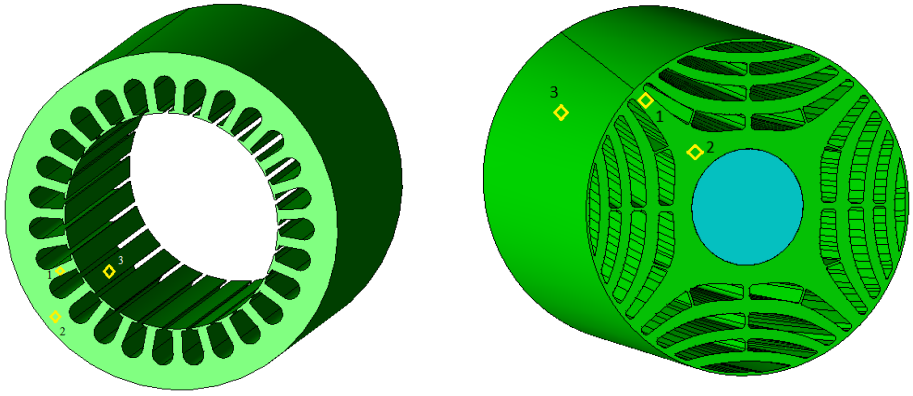

Fig. 4.55 Points for magnetic field measurement on stator (left) and rotor (right)

One can see that in stator's magnetic field, base harmonic of the field is dominant and thus contributes the most to iron losses. Higher order harmonics of magnetic field are also present in stator's field but they are relatively small compared to the base harmonic. In case of rotor's magnetic field, the base harmonic is either absent or has a very small amplitude. Higher order harmonics become more dominant in the rotor. Zero frequency component of magnetic field is also present in rotor's magnetic field since the rotor is synchronized with rotating field of the stator. Since this component does not contribute to iron loss and its amplitude is quite high compared to the amplitudes of other components, in Fig. 4.54 this component was omitted for clarity of the figure.

After calculation of machine's power losses, the next step is to perform thermal analysis. The thermal model of the machine is shown below. Different heat transfer coefficients have to be specified for the materials.

Thermal parameters of water used in water jacket are given in Table 4.11.

TABLE 4.11 Thermal specific capacitance and thermal conductivity of water

Temperature [℃]	$C_\rho \left[\frac{J}{kg\ ℃}\right]$	$\lambda_s \left[\frac{W}{m\ ℃}\right]$
0	4217	0.569
6.85	4198	0.582
11.85	4189	0.59
21.85	4181	0.606
31.85	4178	0.62
41.85	4179	0.634
51.85	4182	0.645
61.85	4186	0.656
71.85	4191	0.668
81.85	4199	0.671
91.85	4209	0.677
100	4217	0.68

Design of water jacket includes determining the flow rate of coolant based on the total heat to be dissipated. This can be done using equation below [105]:

$$Q = c_p \Delta T \rho V \tag{4.2.3.1}$$

In the equation above Q is the heat to be dissipated, c_p is the specific heat of the coolant, ΔT is the temperature rise from inlet to outlet of the channel, ρ is the density of the coolant and V is the volume flow rate. In order to calculate convection heat transfer of water jacket, different equations have to be used depending on the channel shapes. For laminar flow the equations are given below [105].

$$Nu = 3.66 + \frac{0.065 * \left(\frac{D}{L}\right) * Re * Pr}{1 + 0.04 * \left(\left(\frac{D}{L}\right) * Re * Pr\right)^{2/3}} \tag{4.2.3.2}$$

$$Nu = 7.49 - 17.02 * \frac{H}{W} + 22.43 * \left(\frac{H}{W}\right)^2 - 9.94 * \left(\frac{H}{W}\right)^3 + \frac{0.065 * \left(\frac{D}{L}\right) * Re * Pr}{1 + 0.04 * \left(\left(\frac{D}{L}\right) * Re * Pr\right)^{2/3}} \tag{4.2.3.3}$$

$$Nu = 7.54 + \frac{0.03 * \left(\frac{D}{L}\right) * Re * Pr}{1 + 0.016 * \left(\left(\frac{D}{L}\right) * Re * Pr\right)^{2/3}} \quad (4.2.3.4)$$

The equations above can be applied to round channels (eq. 4.2.3.2), rectangular channels (eq. 4.2.3.3) and concentric cylinders (eq. 4.2.3.4). In these equations $\frac{H}{W}$ is the channel height-to-width ratio, D is channel hydraulic diameter, L is the length of the channel and finally Nu, Re, and Pr and Nusselt number, Reynolds number and Prandtl number respectively. They can be calculated using formulas shown in Chapter 3.

When the flow is turbulent, Nusselt number can be calculated using the formula below [105]:

$$Nu = \frac{f}{8} + \frac{(Re - 1000) * Pr}{1 + 12.7 * \left(\frac{f}{8}\right)^{0.5} * (Pr^{2/3} - 1)} \quad (4.2.3.5)$$

where f is the friction factor and it can be estimated for a smooth wall with the equation presented below [105].

$$f = (0.79 * \ln(Re) - 1.64)^{-2} \quad (4.2.3.6)$$

Temperature in machine without water jacket cooling exceeds the maximum allowed temperature as shown in figure below.

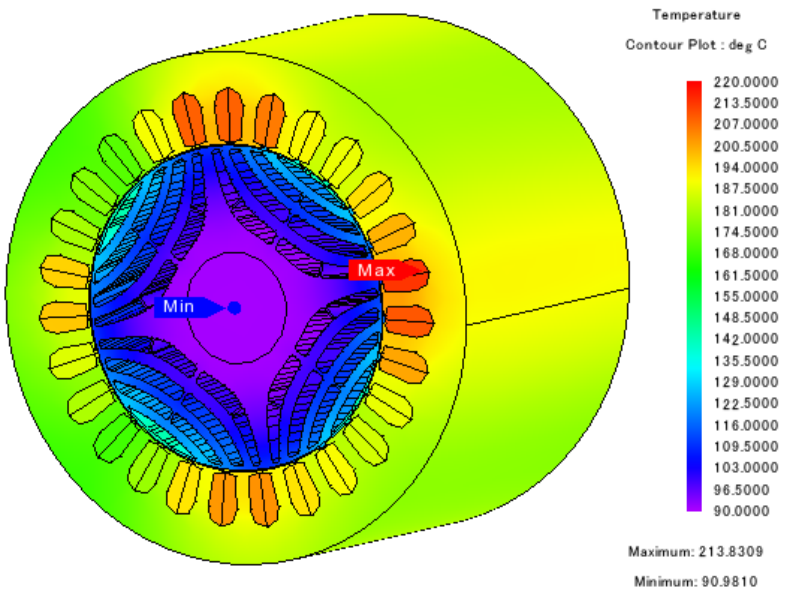

Fig. 4.56 Temperature distribution in machine without cooling

In Fig. 4.56 one can see temperature distribution in SynRM without any cooling. One can see that such a situation is no allowed as the maximum temperature exceeds 200°C. Using cooling method is thus necessary. Due to space and assembly limitations the machine needed to be mounted in enclosed housing. For this reason, there could not be any fan installed and it was necessary to use other cooling method than forced air convection. In order to be able to operate at nominal load, the machine needs water jacket cooling. The water jacket cooling was designed using MotorCAD, which has embedded functions allowing to choose different cooling methods. MotorCAD performs the calculations using lumped parameter network hence machine power losses were calculated in JMAG using finite element method and then transferred to MotorCAD. This allowed to calculate temperature rise of the machine for different cooling methods. The heat transfer coefficients calculated by MotorCAD are next transferred to JMAG which allows to run 3D finite element thermal analysis.

Water jacket placement is shown in figure below.

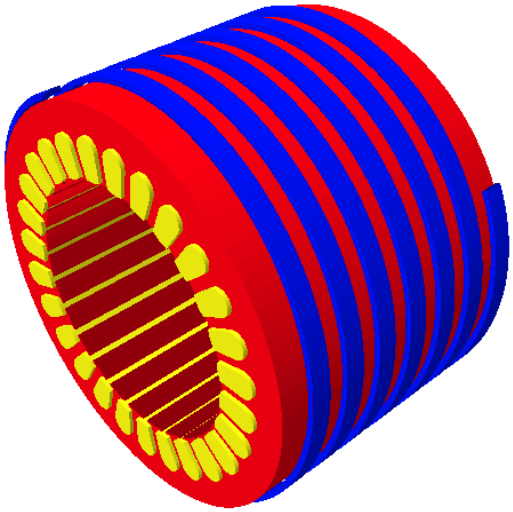

Fig. 4.57 Stator with water jacket model in MotorCAD

The water jacket was modeled in JMAG. For simplicity, instead of using the spiral ducts geometry presented in figure above, the water jacket was modeled in JMAG as hollow cylinder. Between every part of the machine with water jacket, heat coefficient had to be specified.

The amount of heat that the water jacket can dissipate depends on the flow rate. The flow rate defines whether the flow is laminar or turbulent which has an impact on heat transfer coefficient.

Every boundary layer had a heat transfer coefficient specified. The water cooling was modeled as a connection to a fixed temperature in thermal circuit. The cooling system is designed to keep the water temperature below 30^0 Celsius. The heat transfer was considered only in radial direction.

Thermal circuit in JMAG is different from a thermal circuit based on lumped parameters. Since thermal analysis performed in JMAG was run using finite element method, thermal coefficients between adjacent surfaces were defined. Heat capacitances and thermal heat transfer coefficients of particular parts of the machine were defined by the geometry. Thermal circuit is shown in Fig. 4.58.

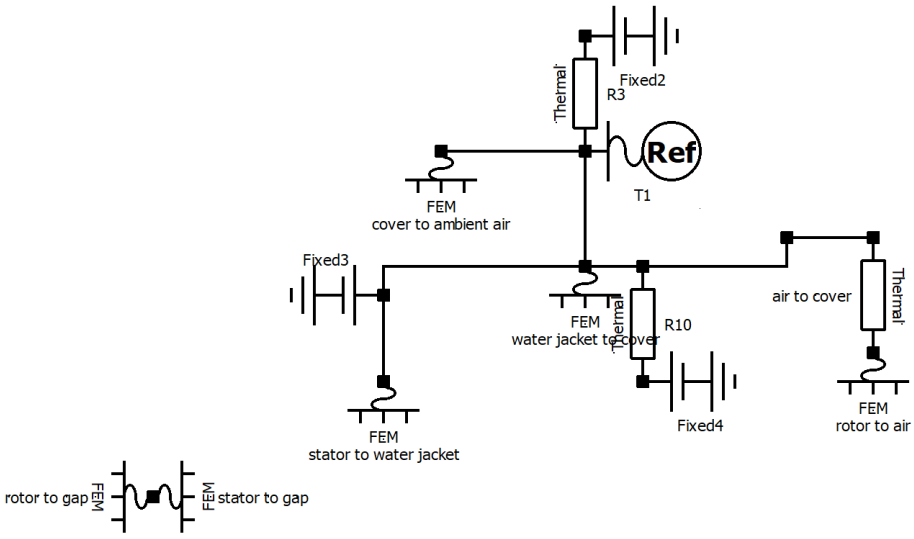

Fig. 4.58 Thermal circuit in JMAG

JMAG does not support cooling system modeling hence, cooling of the water was modeled by connecting water jacket to a fixed temperature in thermal circuit.

For heat transfer boundaries presented in Fig. 4.59, heat transfer coefficients were calculated using formulas shown below. Winding impregnation was modeled as a contact resistance between the winding and stator core as one can see in Fig. 4.59 a) and b). Heat transfer coefficients between parts were calculated using equation (4.2.3.8) where λ is thermal conductivity and d is the distance between them (insulation thickness). In the analysis, the thermal conductivity between parts was chosen to be the conductivity of the air $\lambda = 0.027\ \frac{W}{m\ ℃}$ to model the contact of rough surfaces. For the heat transfer between the rotor and the air gap and between the stator and the air gap, heat transfer coefficient defined by equation (4.2.3.7) was used. This equation takes into account the rotational speed of the rotor.

$$h = \frac{6.6}{10^5}\frac{v^{0.67}}{d^{0.33}}10^4 \tag{4.2.3.7}$$

$$h = \frac{\lambda}{d} \tag{4.2.3.8}$$

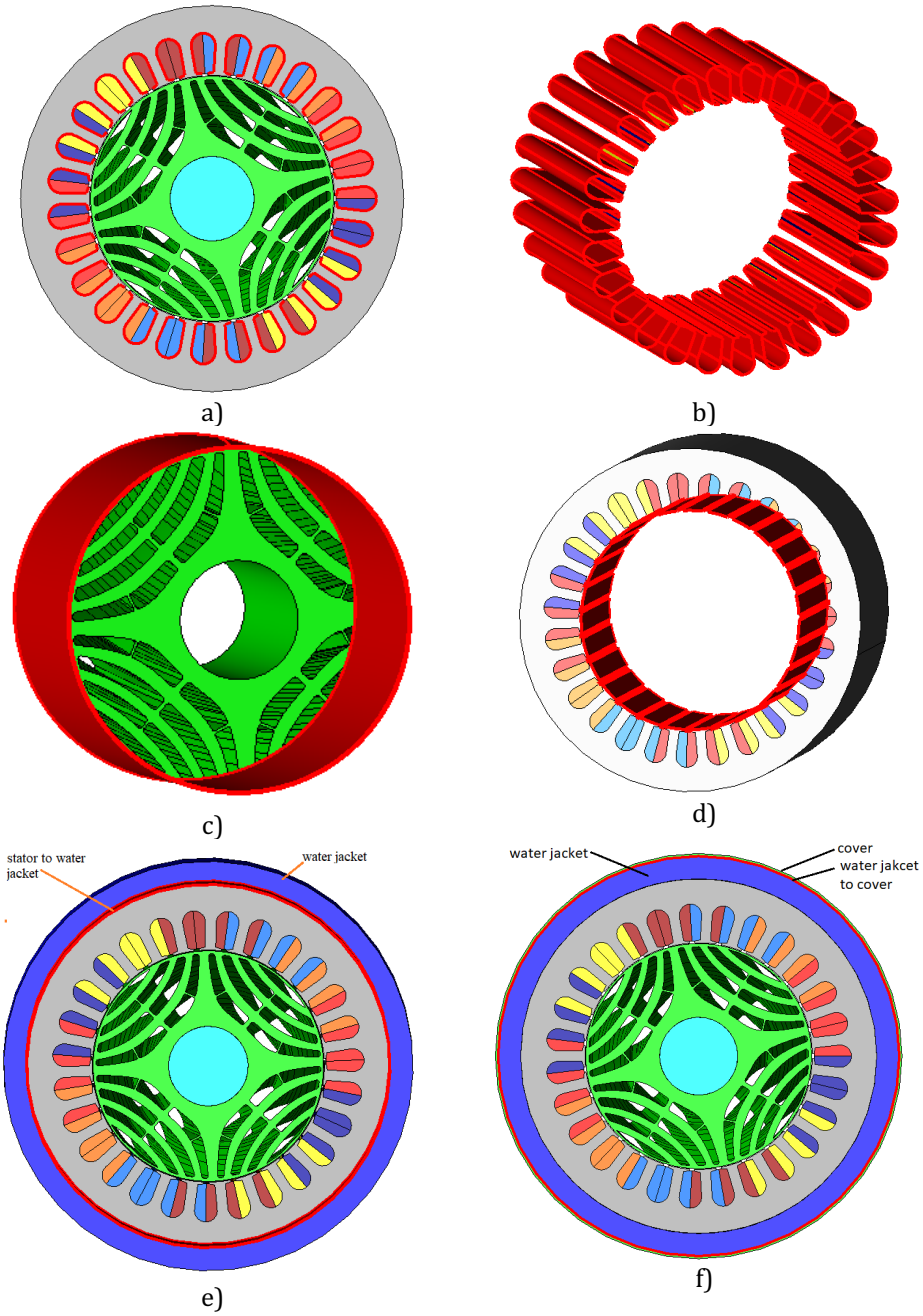

Fig. 4.59 Boundaries for heat transfer: a), b) between winding and stator core, c) between rotor and air gap, d) between stator and air gap, e) between stator and water jacket, f) between water jacket and cover

The machine uses water jacket for cooling with enclosed housing on both ends. This means that no air flow in the air-gap is taken into account when estimating the temperature of the machine during operation. Water jacket cooling capability depends on water flow rate and it can be estimated using computational fluid dynamics method. This, however might be very time consuming. Water flow rate in water jacket affects heat capacity of the water jacket and its heat transfer coefficient. In performed simulations, only conductive heat transfer was considered since radiation effect is negligible compared to conduction. Presence of stator water jacket creates a temperature gradient in radial direction. When combined with the lack of fan on the shaft and enclosed housing on both ends, the heat transfer in radial direction is dominant and heat flux in axial direction might be neglected for simplification.

Heat flux in stator and rotor is shown in Fig. 4.60. One might observe that heat generation is much greater in stator than in the rotor. The only heat source in the rotor are power losses in rotor iron core. They are smaller than those in the stator. Major part of stator heat flux flows to water jacket. Some part flows through air-gap to the rotor. Heat flux in the rotor flows along the iron flux paths and almost completely avoids air flux barriers. This means that heat conduction through the air in the rotor can be neglected.

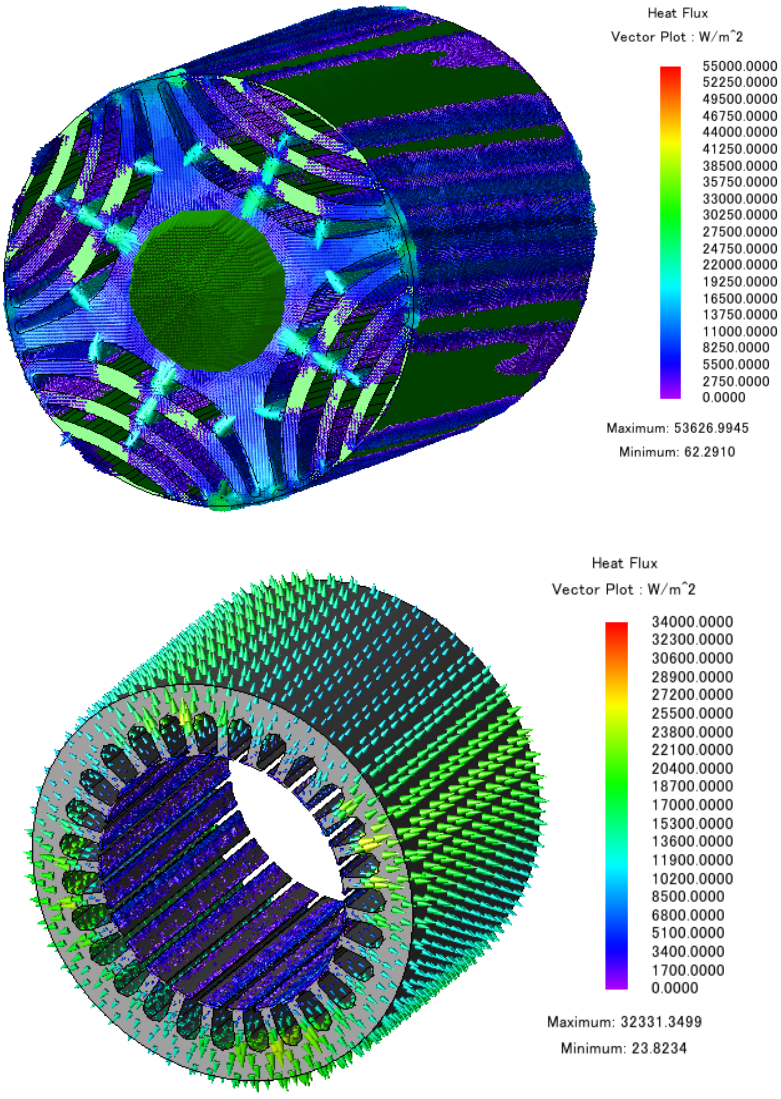

Fig. 4.60 Heat flux generated by rotor (top) and stator (bottom)

Temperature distribution at 4500 rpm and 12000 rpm rotational speeds and continuous power is presented in Fig. 4.61 and Fig. 4.62.

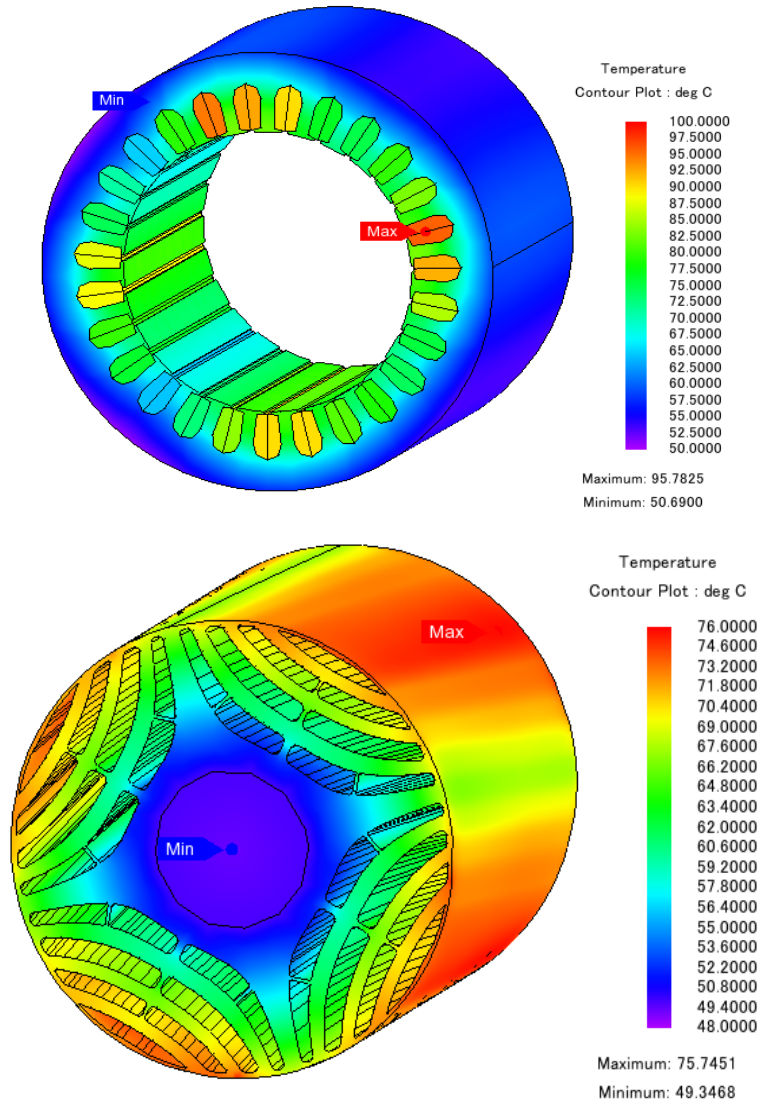

Fig. 4.61 Temperature distribution at 4500 rpm: stator (top) and rotor (bottom)

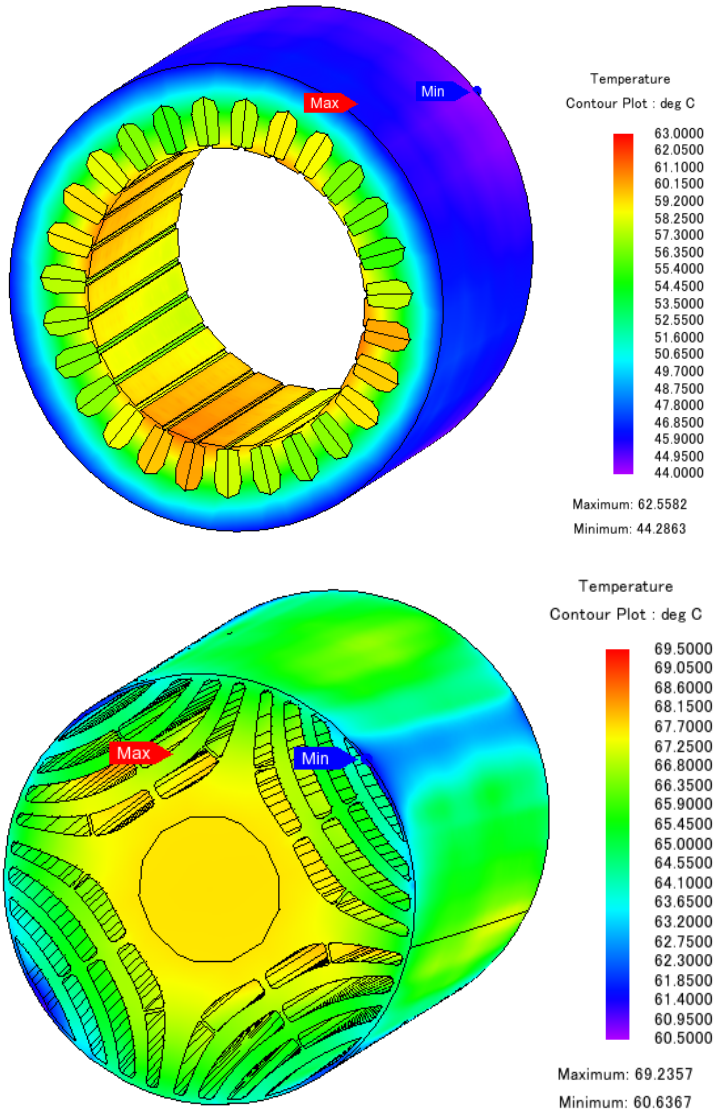

Fig. 4.62 Temperature distribution at 12000 rpm: stator (top) and rotor (bottom)

Results obtained from JMAG show that both stator and rotor achieve similar temperatures, however in case of the rotor, the highest temperature seems to be on the surface. The temperature in other parts of the rotor eventually achieves higher values however it takes more time for the rotor to achieve steady state temperature than for the stator. Although the higher iron losses occur in the stator, the heat dissipation

from the stator is better due to presence of water jacket. Heat dissipation from the rotor is more difficult hence this part also achieves quite high temperature though the iron losses are smaller.

Result of thermal finite analysis of a slot with winding is presented below. The analysis was run in MotorCAD which gives the possibility to model wires distribution in a slot. It can be observed that the highest temperature occurs in the middle of the slot where there is no contact with stator core. Temperature distribution in the slot is more detailed that in case of results obtained from JMAG. Winding in the slot in JMAG was modeled as a uniform surface. Obtained results are similar for both software. Winding temperature calculated by JMAG is several^0 higher than that calculated by MotorCAD. It is caused by different values of stator iron losses and model of water jacket. Magnetic field analysis and iron losses performed by JMAG are more accurate than those in MotorCAD, moreover JMAG does not support modeling of cooling systems hence the water jacket cooling capability was not accurately enough modeled.

MotorCAD uses thermal network to analyze the thermal behavior of the machine. All the heat transfer coefficients and lumped parameters of the thermal circuit are calculated based on machine's geometry and materials. Using thermal network makes it possible to quickly estimate the average temperature in different parts of the machine. For temperature distribution, FEM module of MotorCAD needs to be used.

In case of synchronous reluctance machine, the FEM module is limited to standard predefined flux barriers in the rotor hence temperature distribution in the entire machine is not possible with optimized flux barriers.

Temperature distribution was not available in MotorCAD for the entire geometry of the machine, since the software does not support flux barriers geometry used in this machine. Instead, only temperature distribution around the slot was available. The thermal steady state analysis was run in MotorCAD for three different fluid flow rates in water jacket. Below one can see how fluid flow rate affects cooling capability of water jacket.

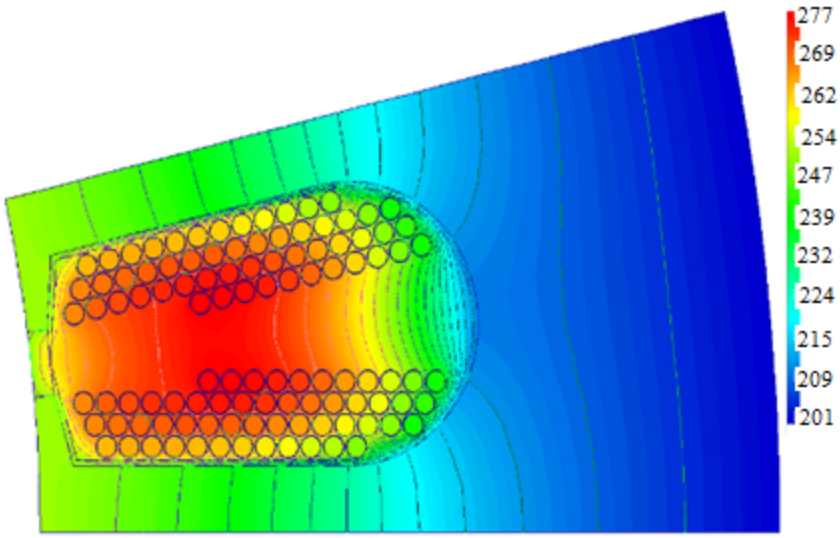

Fig. 4.63 Temperature distribution in a slot at fluid velocity 0.08667 m/s (laminar flow)

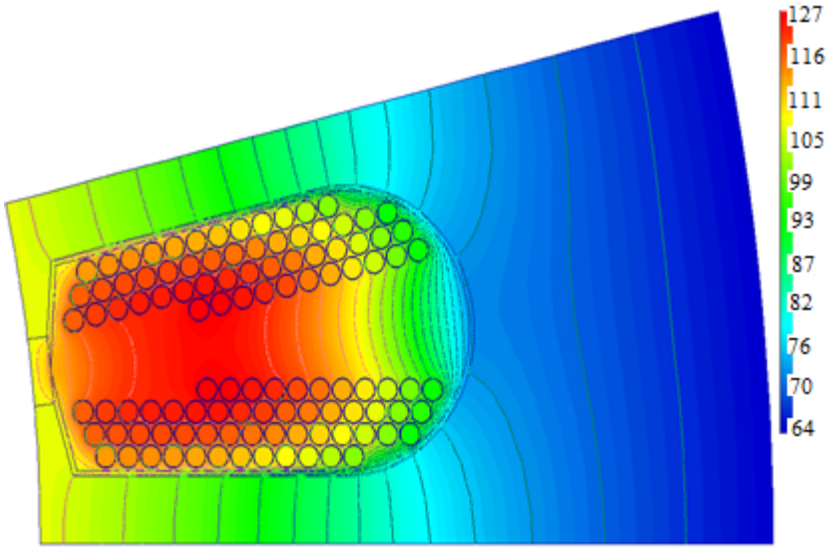

Fig. 4.64 Temperature distribution in a slot at fluid velocity 0.533 m/s (transition flow)

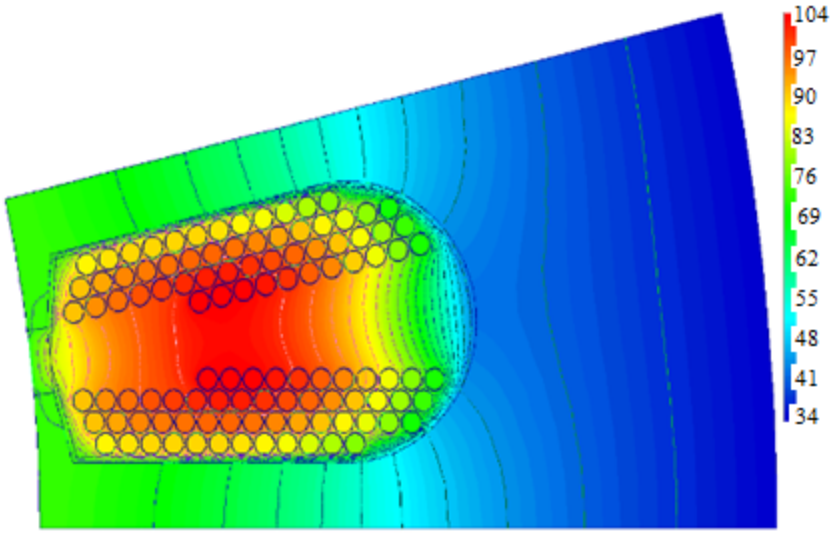

Fig. 4.65 Temperature distribution in a slot at fluid velocity 7.533 m/s (turbulent flow)

As one can see low fluid velocity results in low cooling capability of the water jacket. In Fig. 4.63. the maximum temperature exceeds 270°C. Increasing the fluid flow rate and thus fluid velocity results in lower temperature of the machine. In Fig. 4.64. the maximum temperature exceeds 120°C. The lowest temperature of the machine occurs at turbulent flow of the fluid (Fig. 4.65.). The maximum temperature is around 100°C.

Simulation tests show that in case of synchronous reluctance machine, the rotor is of the least concern. The only heat generation source in the rotor are power losses in the iron core. In case of synchronous motor, iron losses are mainly caused by higher order harmonics since the rotor is synchronized with stator magnetic field. The highest density of iron loss is in the surface of the rotor and this part of the rotor reaches the highest temperature. From thermal point of view, the most vulnerable part of the machine is the winding since the highest power losses occur there especially at high currents. Moreover, heat transfer from the winding to the stator is affected by the contact resistance between the winding and the stator core. Stator also generates some heat due to power losses in the core. In this case, the losses are greater than in the

rotor since they are caused by the base harmonic component whose amplitude is dominant. Lack of permanent magnets in the rotor makes this machine less affected by the temperature rise than a PM machine. For this reason, coupled thermal and magnetic analysis was not run since it increases computational cost.

4.3. Conclusions and Contributions

This chapter presents electromagnetic, structural, vibro-acoustic and thermal analysis of a SynRM for EV propulsion.

Electromagnetic analysis was the first type of analysis to run in order to estimate machine's main parameters. Due to complex geometry of the final SynRM topology, electromagnetic analysis was performed using FEM model of the machine. Two FEM models of SynRM were tested – 2D and 3D and the results obtained from both were similar. In case of 2D model with skewed rotor, the skew was modeled by slicing the rotor. The higher the number of slices the more accurate results were obtained but the computational cost increased. Machine's flux linkage was calculated for d and q axis of stator MMF. It was proven that flux linkage and inductances in orthogonal (d and q) axes are related to each other due to cross saturation. Machine with skewed rotor generates lower torque compared to the same machine with non-skewed rotor. On the other hand, machine with skewed rotor experiences lower torque ripple.

Structural analysis of electric machines is a crucial part of multiphysics analysis of the machine since it is responsible for the robustness of the structure. From the mechanical point of view, the most endangered part is the rotor as it has to withstand high centrifugal forces due to high rotational speeds. It was shown that the rotor with regular flux barriers cannot withstand maximum rotational speed. Additional ribs had to be introduced in rotor's structure in order to make the rotor withstand high rotational speeds. Moreover, the first flux barrier has two additional ribs since it this part of the rotor is exposed to the highest stress. Additionally, the edges of the bridges needed to be rounded to decrease the stress in that area as the stress concentration factor achieves the highest values in the vicinity of discontinuities of the material. The mesh must be fine around sharp edges or curves in since these are the places where the highest stress might occur. For checking the structure's robustness against failure, von Mises theory was applied as this is a very popular

method used in industry. Influence of magnetic forces acting on the rotor was also investigated. At maximum rotational speed, the stress caused by the centrifugal forces is much higher than the stress caused by the magnetic forces. The magnetic forces are higher at nominal speed and nominal torque but on the other hand the mechanical stress due to centrifugal forces is low. In this way, the magnetic forces do not play a significant role in structural analysis of the machine of interest.

Vibrations of the stator's structure were analyzed using VirtualLAB which is a dedicated software for NVH analysis. Vibrations caused by time varying radial forces were investigated. Magnetic radial forces were calculated in electromagnetic simulation using JMAG software. In order to calculate stator's vibrations, modal analysis of the structure needed to be run. Vibrations vary with rotational speed and current angle. Rotational speed affects the vibrations as the rotational speed depends on supply frequency. At some rotational speeds the vibrations might achieve much higher values due to resonance. Amplitude of magnetic radial forces depends on the magnetic field in the stator. The lower the magnetic field the lower the forces. It was proved that changing current angle influences the vibrations since the magnetic field in the stator decreases as the current angle approaches 90 electrical^0. For a machine with skewed rotor, the stator vibrates differently as the magnetic field and thus radial forces are not distributed evenly along machine's length. Vibrations on both ends of the machine achieve different amplitudes as the magnitudes of radial forces are different.

Estimating the noise generated by the machine is the next step of NVH analysis after calculating structure's vibrations. By running modal and ATV analyses of the structure, noise generated by the structure can be estimated. NVH analysis of a machine with four different rotor structures was run in order to investigate how the topology of the rotor influences the noise generated by the machine. Each topology experienced different torque ripple. Simulations proved that the there is no direct relation between torque ripple and noise level of the machine. Torque ripple is caused by variation of tangential component of magnetic forces. Noise however is generated by stator's vibrations which are caused by radial components of the magnetic forces. Rotor skewing has also an impact on the noise generated by the machine. In general, machine with skewed rotor generates noise of lower radiated power than the one with non-skewed rotor. At certain rotational speeds, the difference in noise

generation between machine with skewed and non-skewed rotor is smaller.

Thermal analysis was performed using finite element method in JMAG and also using thermal network in MotorCAD. Results from JMAG obtained by finite element method allow to see temperature distribution in the machine. Before performing thermal analysis in JMAG, one needs to specify heat transfer coefficients between adjacent parts of the machine and thermal properties of the materials. When using simplified geometry, one can represent machine parts by using thermal capacitance and thermal resistance. It is possible to model heat transfer between the machine and the other parts which were not included in the analyzed geometry by using thermal resistances in the circuit. However, the analyzed machine has a stator water jacket which causes the heat flux to flow in radial direction. Axial heat flux can be therefore neglected since the heat conduction in air is smaller than heat conduction between the stator and water jacket. MotorCAD operation is based on lumped thermal network. Thermal resistances and capacitances are calculated by the software based on the geometry of the machine. Moreover, MotorCAD does not support flux barriers shapes which were used in analyzed motor hence temperature distribution is only possible around stator slot. MotorCAD also has simplified algorithms of iron loss calculation and operates on a 2D model of the machine when performing magnetic analysis. In JMAG it is possible to use 3D geometry of the machine which increases the accuracy of the analysis but is more time consuming. The aim of this chapter was to assess the cooling capability of the water jacket and examine thermal behavior of synchronous reluctance machine. The lack of field winding in the rotor results in iron losses being the only heat source. Moreover, since there are no permanent magnets, the torque generation capability of the machine is less affected by the temperature. Performed numerical analyses proved that iron losses in the rotor are much smaller than those in the stator. The greatest density of iron losses occurs on the rotor surface. Since there is no fan installed on the shaft and the housing is enclosed, the heat dissipation from the rotor is less efficient than heat dissipation from the stator, which has a direct contact with water jacket. The higher the frequency the higher heat transfer coefficient from the rotor through the air gap since the velocity of the air is higher. However higher rotational speed results in higher iron losses. Thermal study showed that the winding is the most vulnerable part of the machine in terms of the temperature. The highest power losses occur

in the winding especially at high load. Therefore, proper design and distribution of copper wires in the slot is very important. The wires should have a good contact with the stator core in order to provide a good heat dissipation.

Personal contribution of the author is:

- Analysis of rotor skewing on electromagnetic behavior of the machine
- Analysis of flux linkage in d and q axis of the machine and the influence of magnetic saturation on machine's inductances
- Investigation of cross saturation in SynRM
- Modeling of rotor skewing: 3D and 2D with multi slices
- Analysis of rotor skewing impact on magnetic forces distribution in the machine
- Analysis of the relation between magnetic forces distribution in the stator and vibration of the structure
- Investigation on flux barriers shape on mechanical stress concentration
- Development of thermal model of the machine in JMAG
- Analysis of iron loss distribution in the machine
- Analysis of heat generation in the machine
- Analysis of cooling capability of water jacket at various flow rates

5. Experimental Work

This chapter presents the results of laboratory tests of SynRM. Electromagnetic, vibroacoustic and thermal behavior of the machine was evaluated. In order to validate the numerical models of the machine, the measurement results are compared with simulation results. In case of NVH measurements, the general vibroacoustic behavior of the machine obtained from simulations and measurements are compared.

5.1. Test Bench Description

The test bench is located in the laboratory of Technical University of Cluj-Napoca. It consists of tested SynRM and an induction machine which operates as load. Mechanical coupling of the SynRM with induction machine is shown in Fig. 5.2. Both machines are supplied from four quadrant inverters.

Test bench specifications are given below.

1. Types of the machines that can be tested:
    - Max 3-5-phase PMSM, IM, SynRM, PMSynRM
    - Max 2-4-phase SRM

2. Range of voltage: 0-400 VAC/0-600 VDC

3. Maximum current: 200 A (for 2-phase SRM and 3-phase AC machines)/100 A (for 4-phase SRM and 5-phase AC machines)

4. Load characteristics:
    - rated power/max power: 29 kW/89 kW
    - rated speed/max speed: 4000rpm/12000 rpm
    - Max torque: 320 Nm

5. Facilities for data acquisition and processing
    - Currents
    - Voltages
    - Torque
    - Speed

- Noise
- Vibration
- Temperature

6. Control equipment - MicroLabBox:
    - Compact all-in-one development system for the laboratory
    - More than 100 high-performance I/O channels with easy access
    - Comprehensive support for electric motor control

7. Tests that be performed on the test bench:
    - No-load test
    - Different level of loads
    - Different speed/torque profiles

Cross section of tested machine's topology is presented in Fig. 5.1. Main dimensions of the machine are contained in Table 5.1.

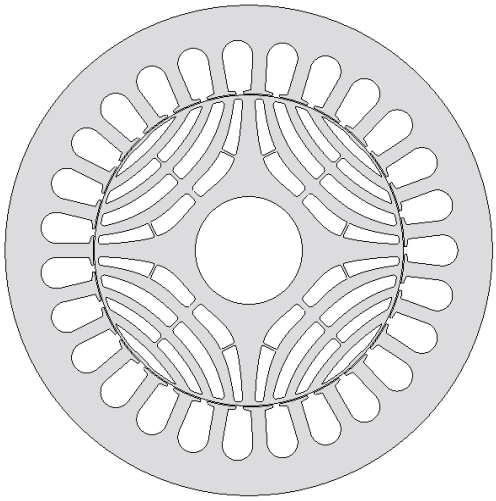

Fig. 5.1 Cross section of machine's final topology

TABLE 5.1 Machine's main dimensions

Active axial length	145 mm
Air gap	0.45 mm
Stator outer diameter	205 mm
Stator inner diameter	130.9 mm
Rotor diameter	130 mm
Shaft diameter	45 mm

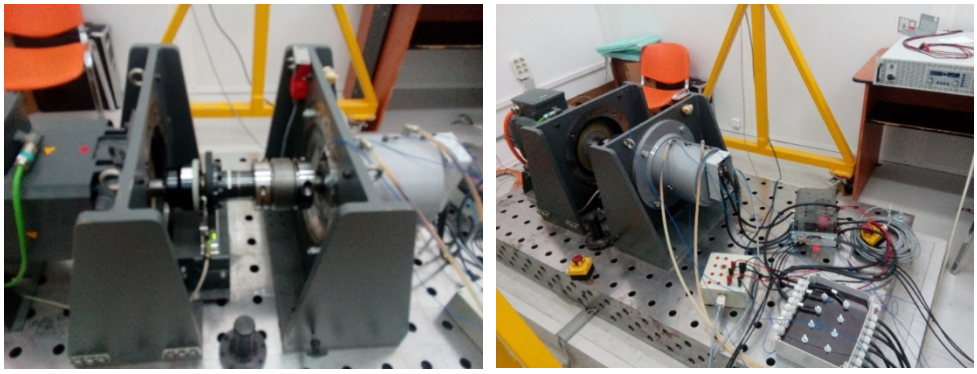

Fig. 5.2 Mechanical coupling of SynRM with induction machine (left), SynRM in a test bench (right)

Vibration sensors' placement and water cooling connection is shown in Fig. 5.3.

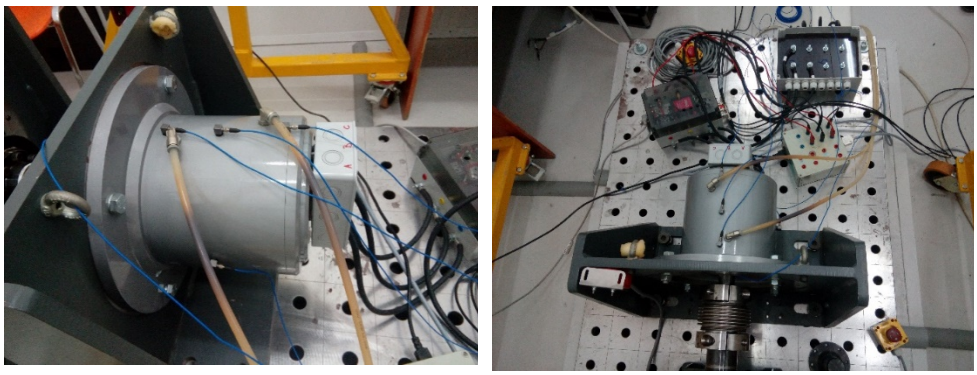

Fig. 5.3 Vibration sensors' placement and water cooling connection

The vibration sensors were placed in x, y and z direction on machine's housing. Moreover, as one can see in Fig. 5.3, on the top of the machine

there were placed three sensors along machine's axial length. The system was controlled using dSPACE hardware with dedicated software. Control model of the drive was built in Matlab/Simulink. The system could measure the following signals:

- Three phase currents
- Three phase voltages
- Rotational speed
- Torque
- SynRM stator's vibrations in x,y and z axis

Fig. 5.4 Two inverters

The two inverters which were used to supply the voltage to the machines are presented in Fig. 5.4. Fig. 5.5 shows the vibration sensor and the microphone which were used to measure the vibration of the machine and acoustic noise.

Fig. 5.5 Vibration sensor (left) and microphone (right)

Diagram of the test bench is presented in Fig. 5.6.

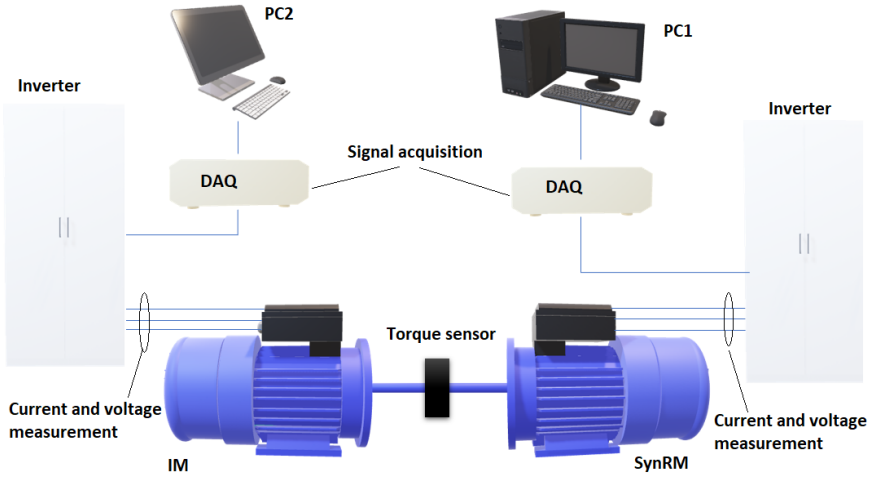

Fig. 5.6 Test bench system diagram

5.2. Experimental Results

Laboratory tests were performed to validate machine modeling and simulation results. Three types of laboratory tests were performed: electromagnetic, NVH and thermal. The goals of each test are as follows:

1) Electromagnetic
    a) Validation of electromagnetic torque
    b) Validation of power factor

c) Validation of d and q axis flux linkage

2) NVH
   a) Level of noise and vibration
   b) Influence of current angle and load on noise and vibration
   c) Influence of switching frequency on noise
   d) Identification of normal modes and natural frequencies
3) Thermal
   a) Investigation of machine's heating
   b) Validation of cooling method

The tests were run in no-load and load state of the machine. The machine was supplied from an inverter and only steady state tests were taken (no dynamic state tests were carried out). No-load state was used to investigate the influence of switching frequency on noise and vibration level of the machine. Validation of electromagnetic torque, power factor or flux linkage was performed in load state of the machine. Also in load state, the influence of current angle and load torque on noise and vibration was investigated together with thermal behavior of the machine and cooling method.

5.2.1. No-load State Tests

The machine was run from 0 to 1500 rpm in order to measure SynRM's vibration and obtain the information about SynRM's normal mode frequencies.

In Fig. 5.7 one can see vibration of the SynRM measured in three points along its axial length. Similar to numerical simulations, the vibration varies along machine's axial length due to non-uniform radial forces distribution caused by skewing the stator core. Moreover, this effect is amplified by the assembly of the machine.

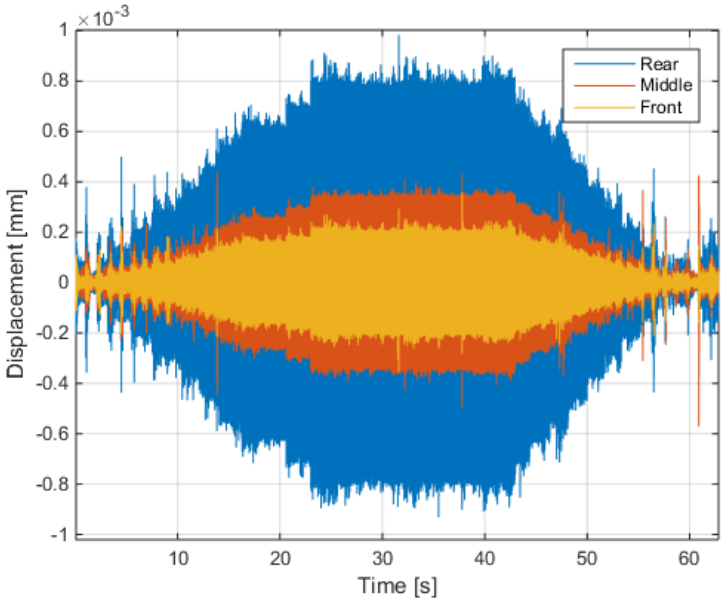

Fig. 5.7 Vibration in three points on the machine

The vibration signal was measured at three switching frequencies of the inverter: 8 kHz, 10 kHz and 12 kHz.

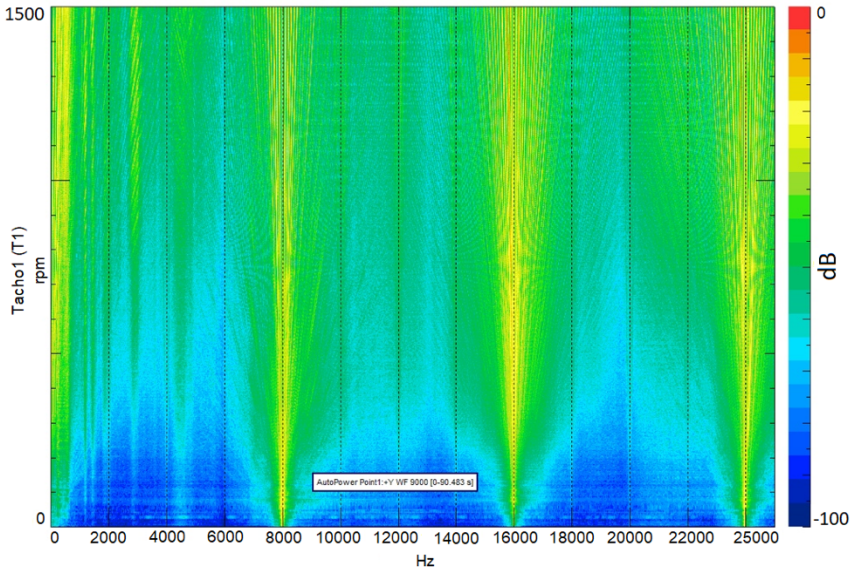

Fig. 5.8 Vibration measured at 8 kHz switching frequency

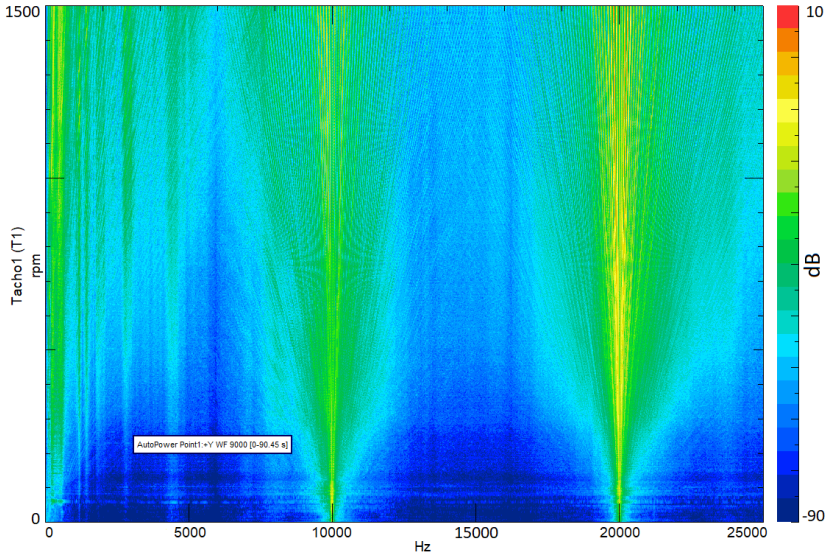

Fig. 5.9 Vibration measured at 10 kHz switching frequency

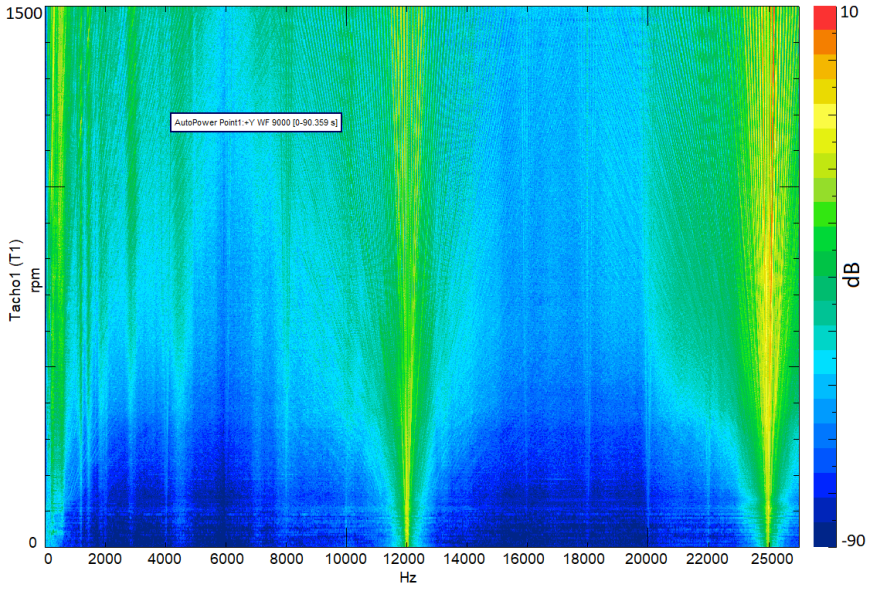

Fig. 5.10 Vibration measured at 12 kHz switching frequency

It can be noticed that the vibration signal in the colormap has higher amplitudes at switching frequency. This is caused by PWM signal whose

harmonics appear in the spectrum of vibration signal. For 8 kHz switching frequency, in the colormap one will observe the vibrations at 8kHz, 16 kHz and 24 kHz (Fig. 5.8) as these are the first, second and third harmonics of the switching frequency. In case of 10 kHz and 12 kHz switching frequency, the situation is similar. In case of 10 kHz switching frequency, the vibration occurs at 10 kHz and 20 kHz (Fig. 5.9) and for 12 kHz switching frequency the vibration occurs at 12 kHz and 24 kHz (Fig. 5.10). The switching frequency signal and its harmonics contribute to vibration and noise signal.

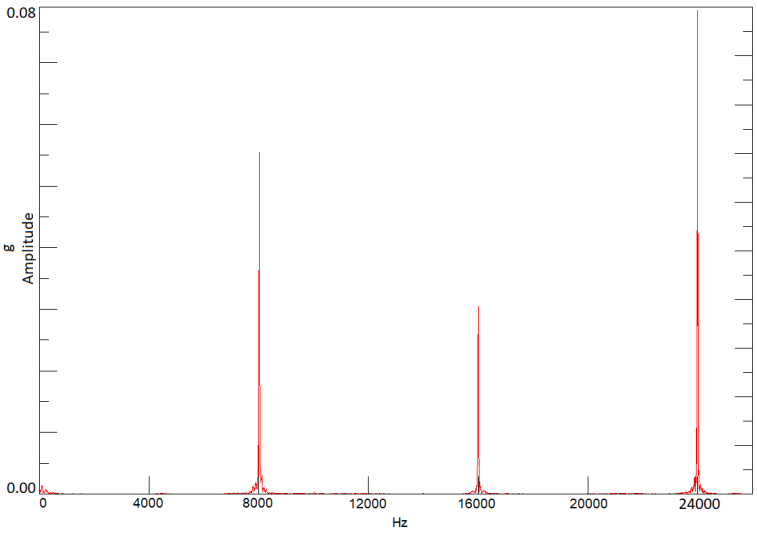

Fig. 5.11 FFT of vibration signal at 8 kHz switching frequency – linear scale

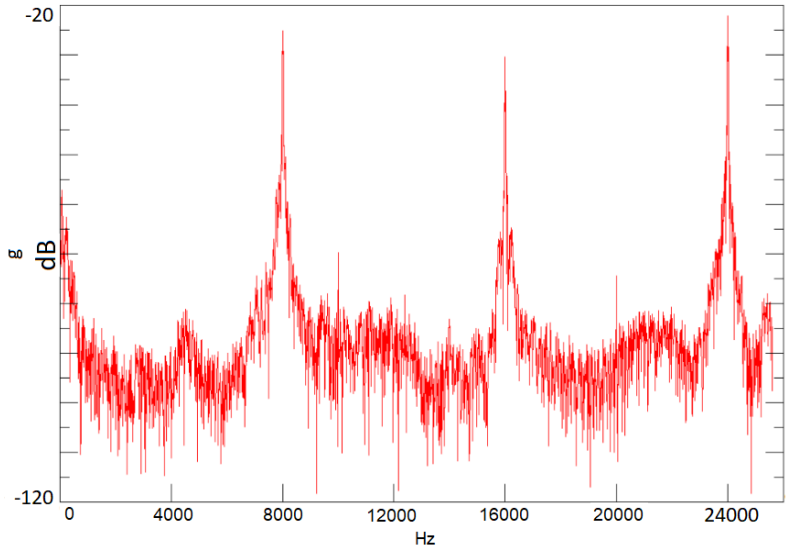

Fig. 5.12 FFT of vibration signal at 8 kHz switching frequency – dB scale

Fig. 5.11 and 5.12 show example FFT of machine's vibration signal generated at 8 kHz switching frequency I linear and dB scale respectively. In these figures one can observe amplitude peaks at 8, 16 and 24 kHz.

In Fig. 5.13 the oblique lines are machine's harmonics also known as orders. As one can see in the figure, they are rotational speed dependent.

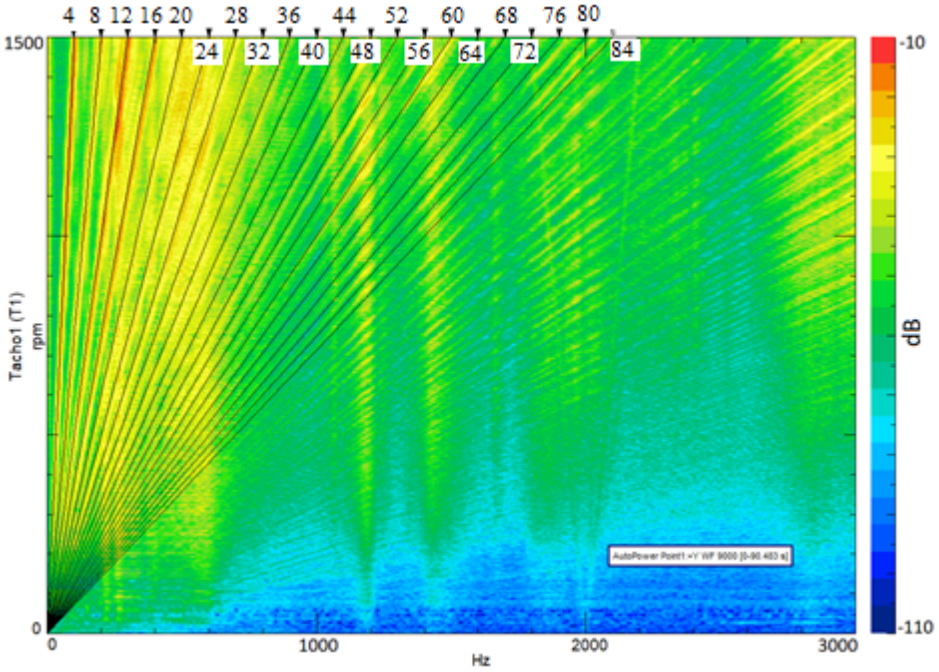

Fig. 5.13 Frequency spectrum of vibration signal with machine orders

Stator's natural frequencies can be identified by analyzing vibration colormap. The resonance frequencies appear on the colormap as vertical line of higher amplitude. This is shown in Fig. 5.14. One can see three typical modes of the stator: ovalization, triangular and square mode. These modes have their natural frequencies. As shown in Chapter 4, modes of the stator can occur with phase shifting which means the deformation is different in longitudinal direction.

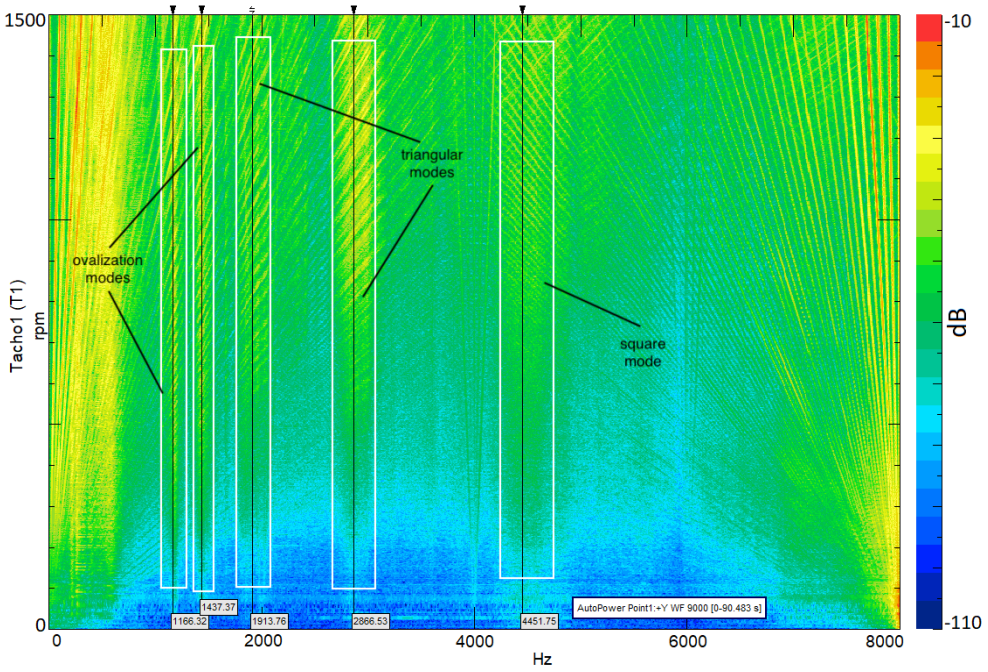

Fig. 5.14 Frequency spectrum of vibration signal with natural mode frequencies marked

The noise generated by the machine is also presented in the form of a colormap. Figures 5.15, 5.16 and 5.17 show colormaps of acoustic signal generated by the machine at 8 kHz, 10 kHz and 12 kHz switching frequency respectively.

One can see that noise of switching frequency and its harmonics are present in the acoustic signal of the machine. Comparison of acoustic noise FFTs is shown in Fig. 5.18.

Just like in case of vibration signal, switching frequency harmonics are rotational speed independent. The higher switching frequency the more noise the machine generates.

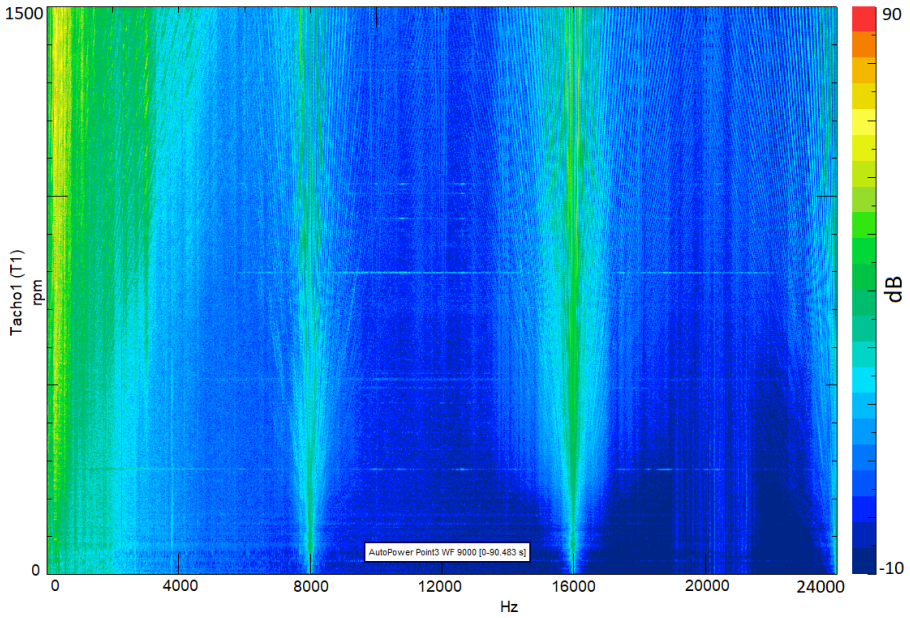

Fig. 5.15 Frequency spectrum of acoustic signal at 8 kHz switching frequency

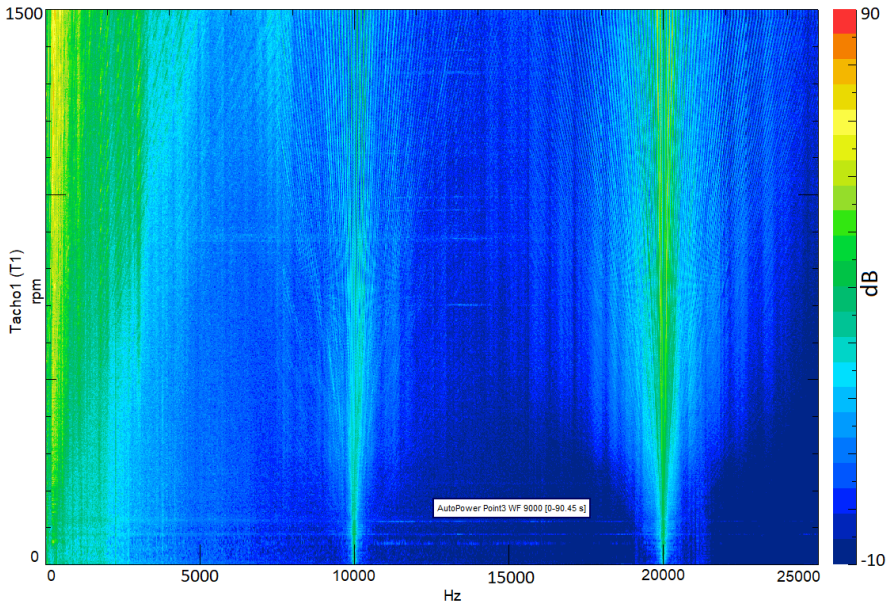

Fig. 5.16 Frequency spectrum of acoustic signal at 10 kHz switching frequency

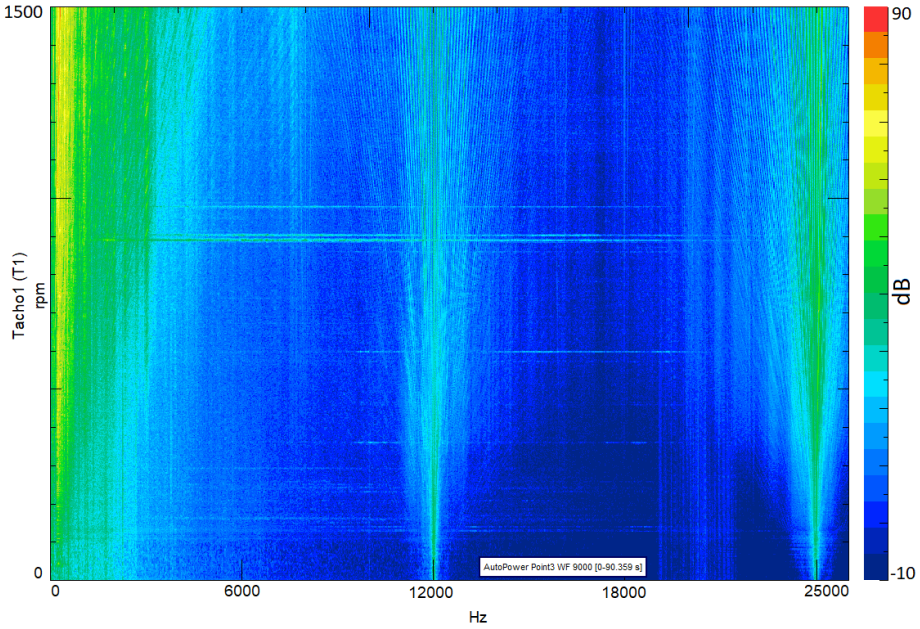

Fig. 5.17 Frequency spectrum of acoustic signal at 12 kHz switching frequency

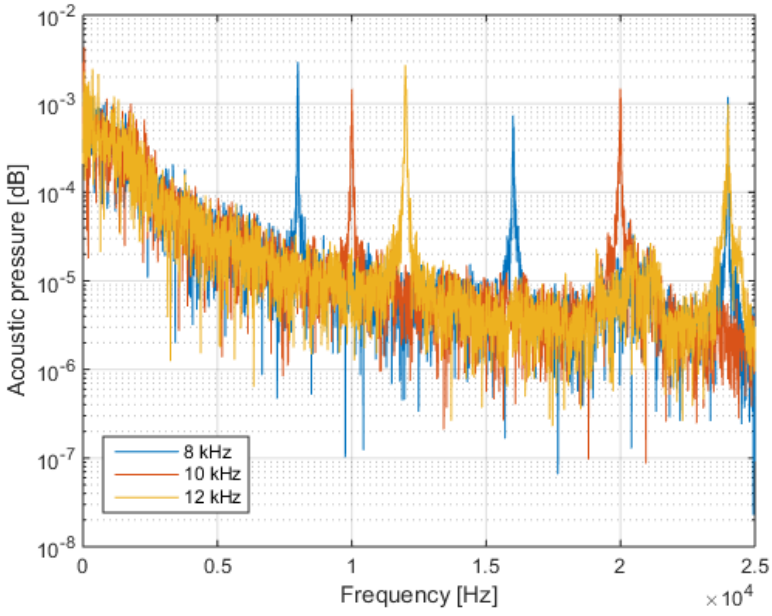

Fig. 5.18 Comparison of frequency spectrum of acoustic signal

5.2.2. Load State Tests

Tests in no load state were carried out for three different switching frequency values. This allowed to investigate how the switching frequency affects the spectrum of vibration and acoustic signal generated by the machine. In order to test how the load affects the NVH behavior of the machine, the measurements were taken in load state at different rotational speeds.

5.2.2.1. Electromagnetic Tests

The tests were carried out at different values of electromagnetic torque generated at various current angle values and at different rotational speeds. These tests allowed also to investigate electromagnetic properties of the machine. Line voltage of the motor was measured in load condition at different torque values at various rotational speeds. In Fig. 5.20 one can see how the voltage changes with the load and rotational speed. The voltage was measured for different values of current angle. One can see that increasing the torque causes the voltage to rise as the phase current also increases. This increase is not as big as in case of rotational speed increase. Higher rotational speed involves higher supply voltage in order to compensate for the EMF generated in stator windings. Current angle has also an effect on voltage amplitude.

As the current angle increases (closer to 90^0) the voltage drops since the flux in the machine is weakened. Higher current angle results in higher *iq* current component and higher reluctance of the magnetic circuit of the machine. Analogically, lower current angle causes the flux in the motor to increase, causing the voltage amplitude to rise.

In Fig. 5.19 one can see example phase and line voltage waveforms measured at 1500 rpm.

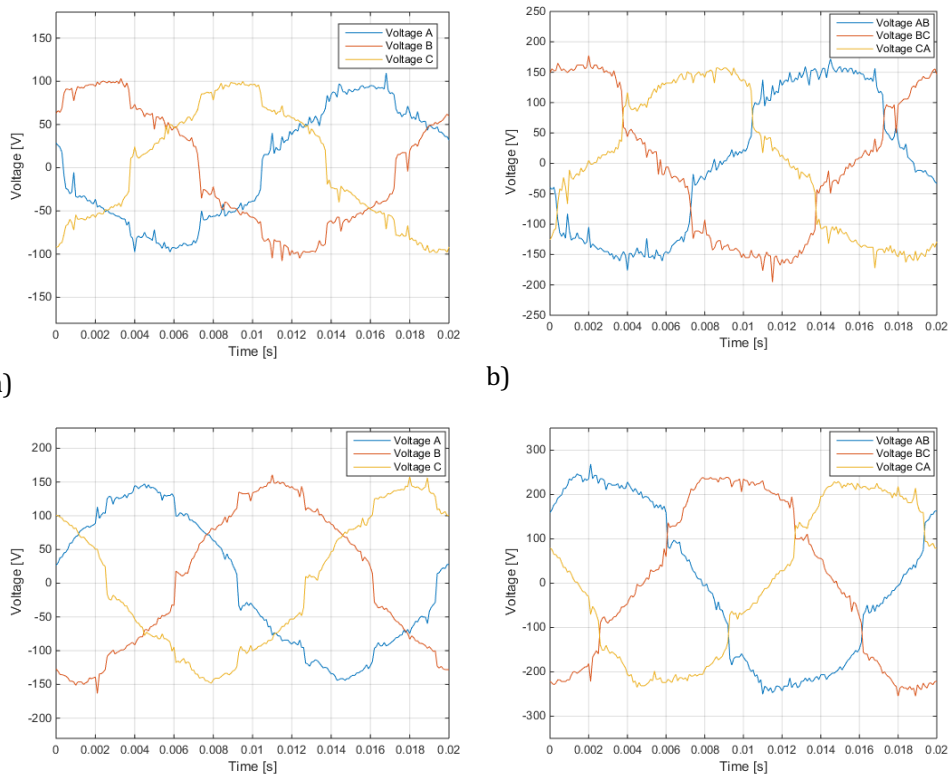

a) b)

c) d)

Fig. 5.19 Line and phase voltage waveforms at 40deg current angle: a) phase voltage at 20Nm load, b) line voltage at 20Nm load, c) phase voltage 40Nm load, d) line voltage at 40Nm load

Fig. 5.20 presents the comparison of line voltage values at different current angles. One can notice that rotational speed has the greatest impact on the line voltage values. Higher load also causes the voltage to increase but the effect is smaller compared to that in case of speed.

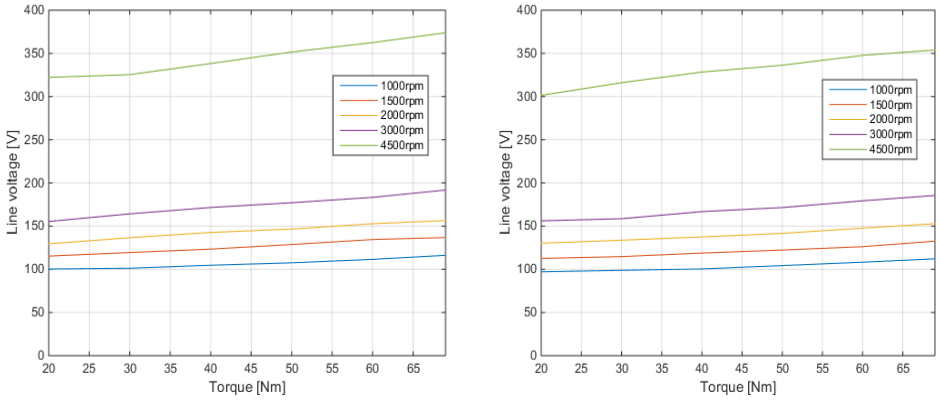

a) b)

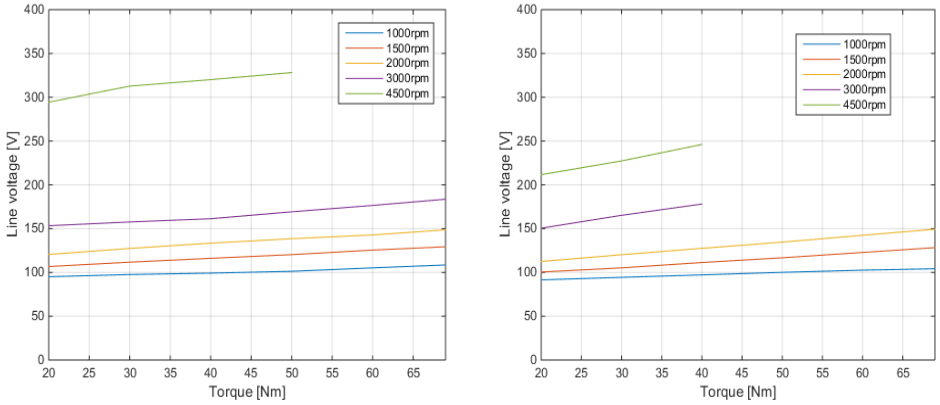

c) d)

Fig. 5.20 Comparison of line voltages at different current angles: a) 40deg, b) 45 deg, c) 50deg and d) 60deg

TABLE 5.2 RMS line voltage comparison

Current angle	Rotational speed	Torque					
		20 Nm	30 Nm	40 Nm	50 Nm	60 Nm	70 Nm
40 deg	1000 rpm	100 V	101 V	104 V	107 V	111 V	116 V
	1500 rpm	115 V	119 V	123 V	128 V	134 V	136 V
	2000 rpm	129.5 V	136.6 V	142 V	146 V	152 V	156 V
	3000 rpm	154 V	164 V	171 V	177 V	183 V	191 V
	4500 rpm	322 V	325 V	338 V	351 V	362 V	373 V
45 deg	1000 rpm	97 V	98 V	100 V	104 V	108 V	112 V
	1500 rpm	112 V	114 V	118 V	122 V	126 V	132 V
	2000 rpm	130 V	133 V	137 V	141 V	147 V	152 V
	3000 rpm	156 V	157 V	166 V	171 V	179 V	185.5 V
	4500 rpm	301 V	316 V	328 V	336 V	347 V	353 V
50 deg	1000 rpm	95 V	97 V	99 V	101 V	105 V	108 V
	1500 rpm	106.7 V	111.7 V	116 V	120 V	125 V	129 V
	2000 rpm	120 V	127.4 V	133 V	138 V	142.8 V	148 V
	3000 rpm	158 V	153 V	161 V	169 V	176 V	183 V
	4500 rpm	294 V	312 V	320 V	328 V		
60 deg	1000 rpm	91 V	94 V	97 V	100 V	102.6 V	104 V
	1500 rpm	100 V	105 V	111 V	116 V	122 V	128 V
	2000 rpm	112 V	120 V	127 V	134.6 V	142 V	149 V
	3000 rpm	150 V	165 V	178 V			
	4500 rpm	211 V	227 V	246 V			

The RMS values of the line voltage for all the investigated cases are contained in Table 5.2. Due to limitations in the laboratory, not all the cases could be measured because of current protection of the inverter. This, however, does not affect the validation of simulation results as the main principles shown in Chapter 4 were confirmed. Fig. 5.21 shows example phase current waveforms.

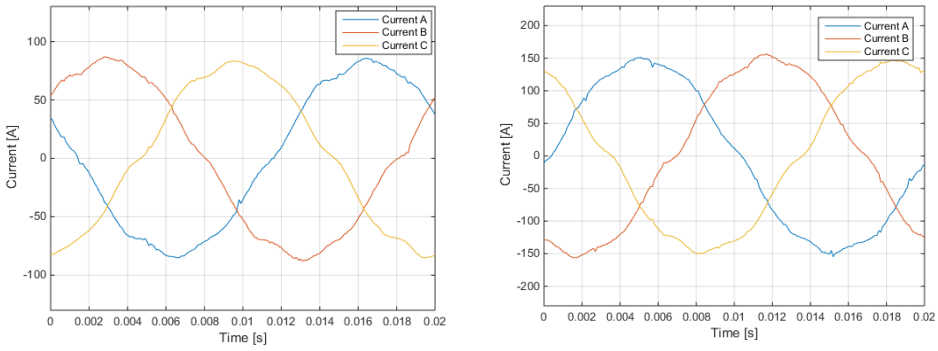

Fig. 5.21 Phase current waveforms at 1500 rpm: 20 Nm (left) and 40 Nm (right)

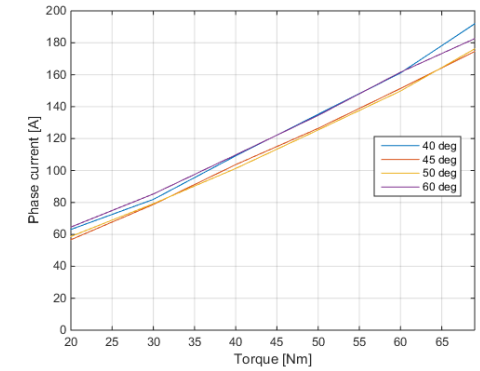

a)

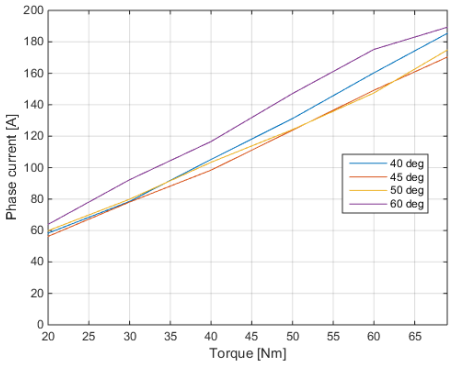

b)

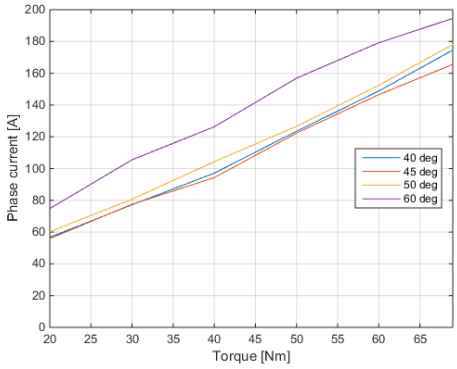

c)

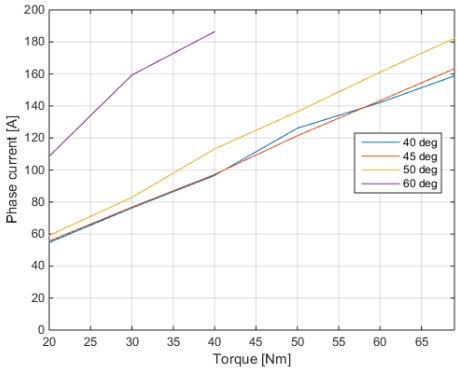

d)

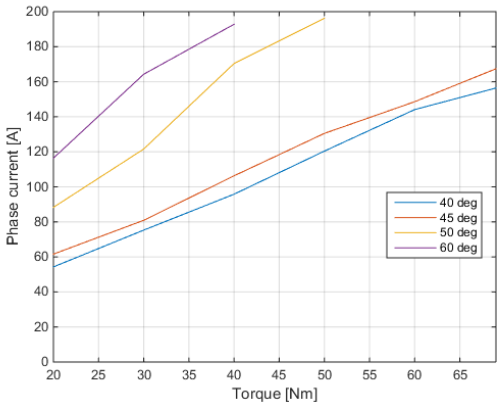

e)

Fig. 5.22 RMS of phase current at different rotational speeds: a) 1000rpm, b) 1500rpm, c) 2000rpm, d) 3000rpm and e) 4500 rpm

Fig. 5.22 shows the RMS value of phase current for different load torque values, rotational speeds and current angles. It can be noticed that the current increases as the torque rises which is natural behavior since the generated torque depends directly on the phase current. One can see that for high values of current angle the phase current is higher at the same load torque. This is cause by the fact that torque generation depends on the interaction of flux angle current. When the current angle increases, the flux in the machine decreases hence in order to keep the same value of the torque, phase current must achieve a higher value. The highest values of phase current are at 60^0 of current angle. The higher the rotational speed, the clearer this effect is visible. At low rotational speed, the difference between current RMS values at different current angles are not very high.

5.2.2.2. NVH

The vibration of the structure was measured for all the cases using the accelerometers mounted on the machine as shown in Fig. 5.3. The comparison of vibration signals from three accelerometers mounted on the machine in Y direction is shown below. Similarly, as it was in no load state, the vibration of the machine along its axial length is not uniform. This is because the machine has a skewed rotor which makes the radial forces distribution non-uniform along the axial length of the machine and also the mounting of the machine significantly limits the vibration level close to the mounting plate.

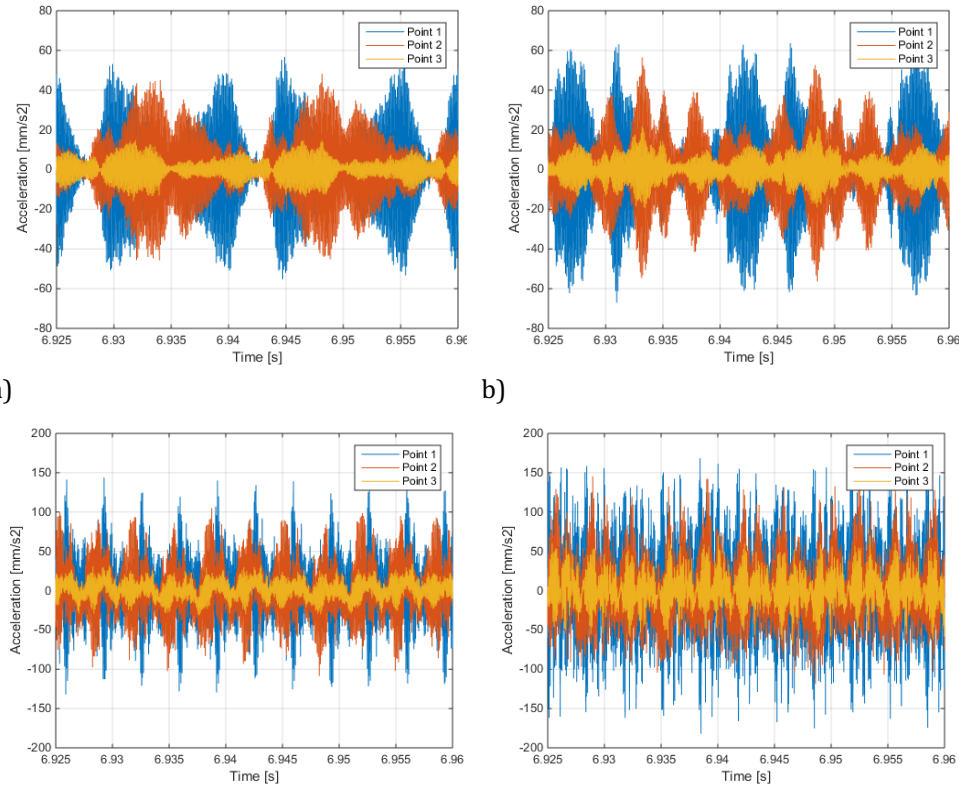

Fig. 5.23 Vibration of the structure: a) 1000rpm and 20Nm, b) 1000rpm and 60Nm, c) 4500rpm and 20Nm, d) 4500rpm and 60Nm

The rotational speed affects the vibration of the machine since at different frequencies the normal modes of the machine are excited in different manner. Comparison of vibration for different rotational speeds is shown below.

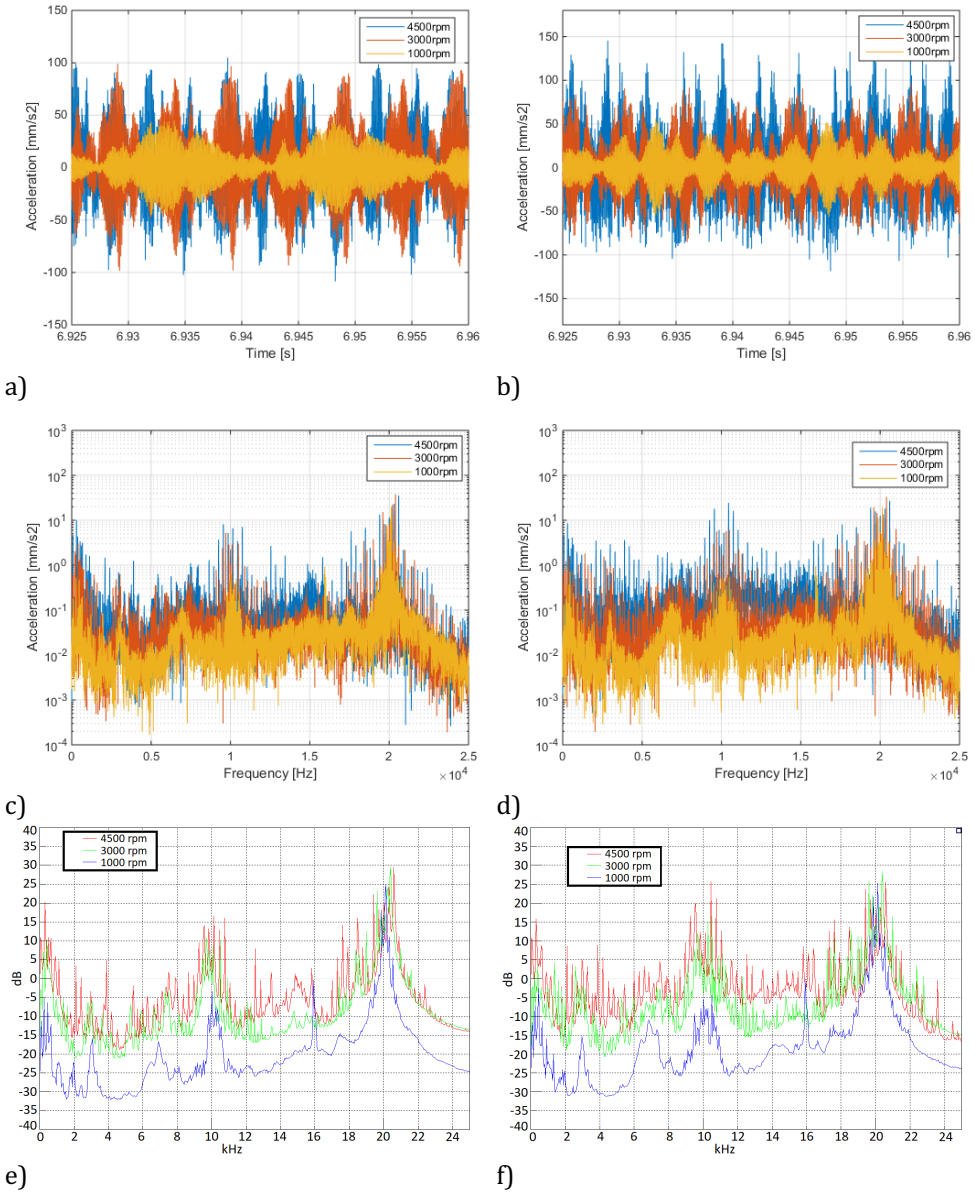

Fig. 5.24 Vibration of the structure at different rotational speeds: a) 20Nm – time waveform, b) 60Nm – time waveform, c) 20Nm - FFT, d) 60Nm – FFT, e) 20Nm – power spectrum, f) 60Nm – power spectrum

Fig. 5.24, shows example results of vibration measurement for three different values of rotational speed and two different values of load torque. Fig. 5.24 a) and Fig. 5.24 b) show time waveform of vibration signal for 20 Nm and 60 Nm load respectively. It can be noticed that the higher the speed the higher the amplitude of vibration signal. Comparison of the FFT of vibration signal as shown in Fig. 5.24 c) and d) gives a better image of how the speed influences the vibration of the structure. Power spectrum of the vibration signal is shown in Fig. 5.24 e) and f). One can see clearly that the vibration strongly depends on the rotational speed. The highest amplitude of both the signal's FFT and the power spectrum occurs at 20 kHz which is the double of switching frequency.

The load has also an impact on the vibration of the structure. One can see in Fig. 5.25 that the vibration changes along with the load. Higher torque requires higher phase current which in turn increases the magnetic field in the machine and causes the radial magnetic forces to rise.

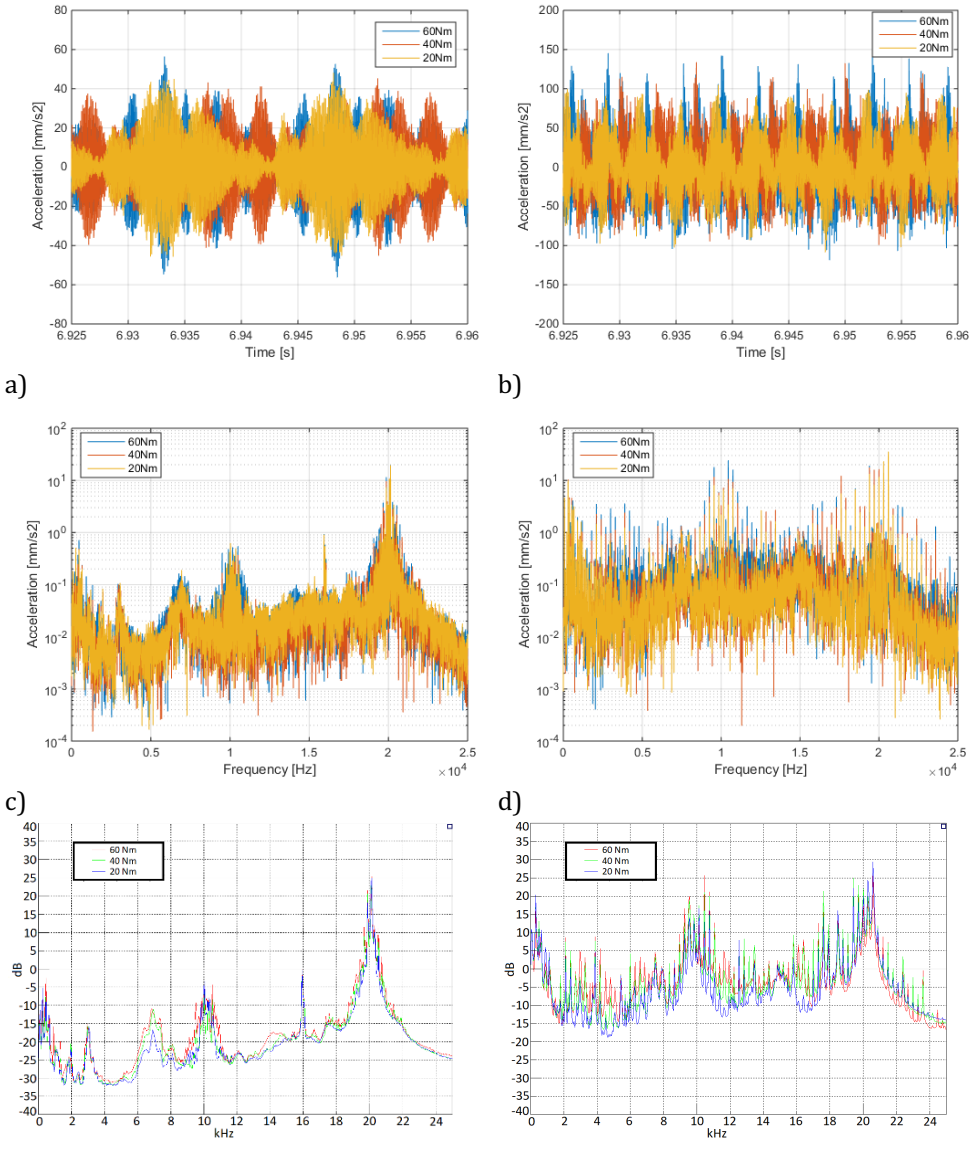

a) b) c) d) e) f)

Fig. 5.25 Vibration of the structure at different loads: a) 1000rpm – time waveform, b) 4500rpm – time waveform, c) 1000rpm - FFT, d) 4500rpm – FFT, e) 1000rpm – power spectrum, f) 4500rpm – power spectrum

The influence of the load on vibration however is not as the influence of rotational speed. In Fig. 5.25 a) and b) one can see the time waveforms of vibration signals for different load values at 1000rpm and 4500rpm respectively. As one can notice, the amplitude of vibration is affected by the load, higher load increases the vibration amplitude. This effect is more visible at 4500rpm rather than at 1000rpm. The FFT of the vibration signals is shown in Fig. 5.25 c) and d). One can see, that the amplitudes are quite similar, at some frequencies the higher amplitudes of vibration occur for the highest load.

Comparison of the power spectrum provides more clear information on how the load affects the vibration. One can notice, that in general for the highest load (60 Nm), the amplitudes of power spectrum achieve the highest values, however at some frequencies the amplitudes of power spectrum are the highest for 20 Nm load.

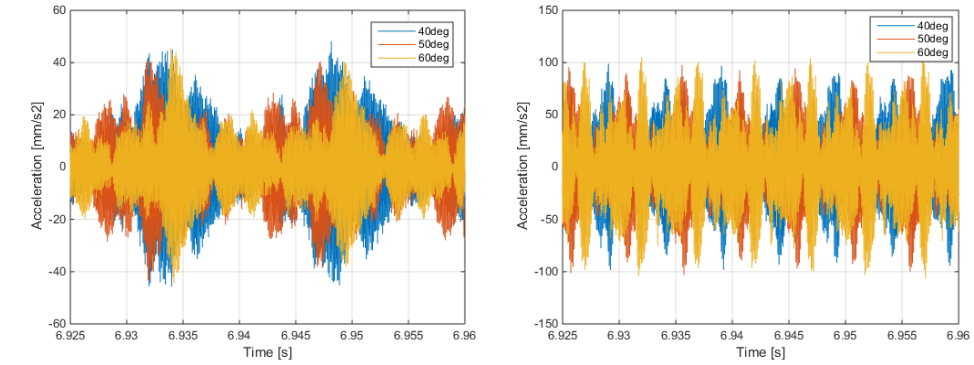

a) b)

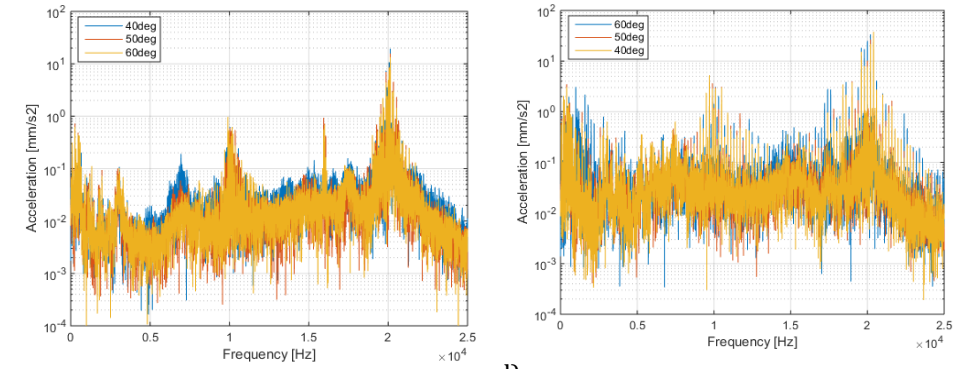

c) d)

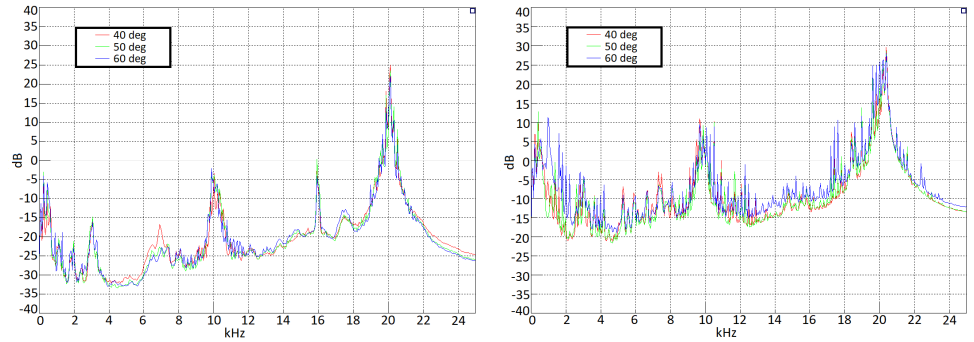

e) f)

Fig. 5.26 Vibration of the structure at current angles: a) 1000rpm – time waveform, b) 3000rpm – time waveform, c) 1000rpm - FFT, d) 3000rpm – FFT, e) 1000rpm – power spectrum, f) 3000rpm – power spectrum

Although the current angle affects the radial forces acting on the stator, its influence on the vibration of the structure is not that clear. In Fig. 5.26 one can see the comparison of the vibration measured at two different rotational speeds at the same load. It can be observed that the amplitudes of the vibration signals are similar for various current angles. In case of 1000 rpm, the difference of amplitudes at different current angles is clearer than in case of 3000 rpm. When comparing the power spectrum of the vibration signal, one can notice that for 1000 rpm at some frequencies the vibration is higher for the lowest current angle (higher radial forces) but around 10 kHz and 20 kHz, which are switching frequency and its double, the vibrations for all measured current angles are quite similar. In case of machine running at 3000 rpm, the power spectrum of vibration signal achieves the highest values for 60^0 current angle, which is quite strange since at this current angle, the flux and thus the radial forces are the lowest. This proves that the vibration of the stator is affected not only by the amplitude of the radial force but also, for the most part, by the frequency of the radial forces since it causes particular normal modes of the structure to excite.

The acoustic signal was measured using two microphones: one placed next to the motor and another hung 1.5 meter above the machine. Below one can see a comparison of noise power spectrum measured in two different points at different rotational speeds.

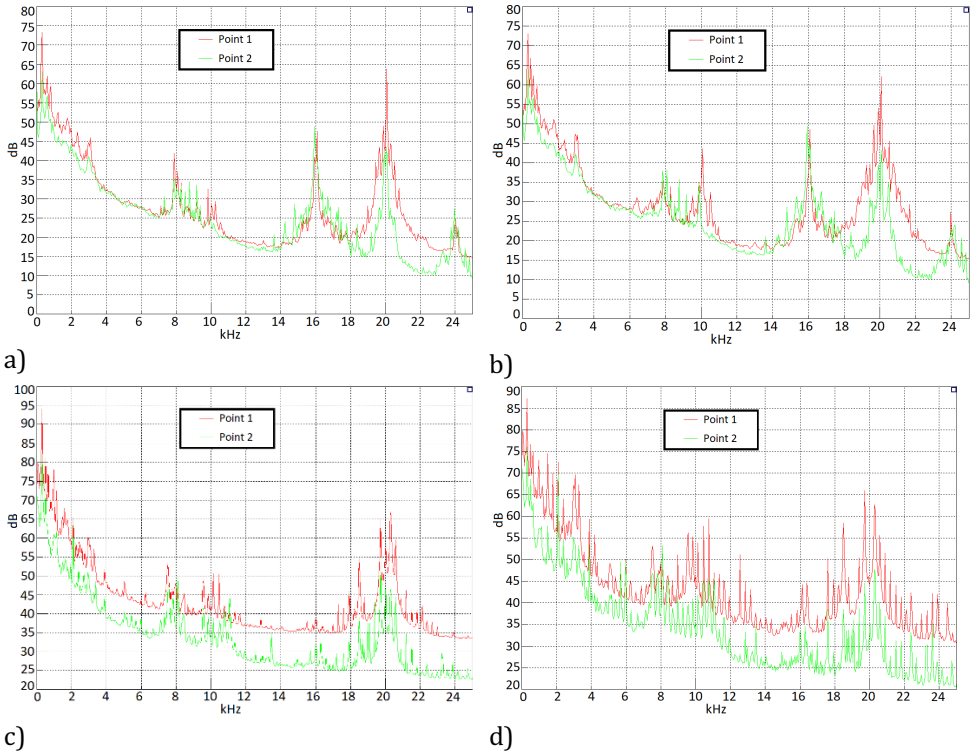

Fig. 5.27 Power spectrum of noise signal measured by two different microphones– next to the machine (red) and 1.5 meter above the machine (green): a) 1000rpm 20Nm,
b) 1000rpm 60Nm, c) 4500rpm 20Nm and d) 4500rpm 60Nm

In Fig. 5.27 one can see the comparison of noise power spectrum, obtained from two microphones. As one could expect, the power spectrum achieves higher values for the signal measured by the microphone closer to the machine. The difference is more visible for higher rotational speeds. Fig. 5.27 a) and b) show the power spectrum of noise measured at 1000 rpm at 20 Nm and 60 Nm respectively. Power spectrum of noise measured at 3000 rpm for the same load is shown in Fig. 5.27 c) and d). The difference in power spectrum for two different microphones is greater for higher speeds. One can see peaks at 8 kHz and 16 kHz which are the switching frequency and its double of the supply system of the induction machine.

Comparison of noise power spectrum measured at different rotational speeds is shown in Fig. 5.28.

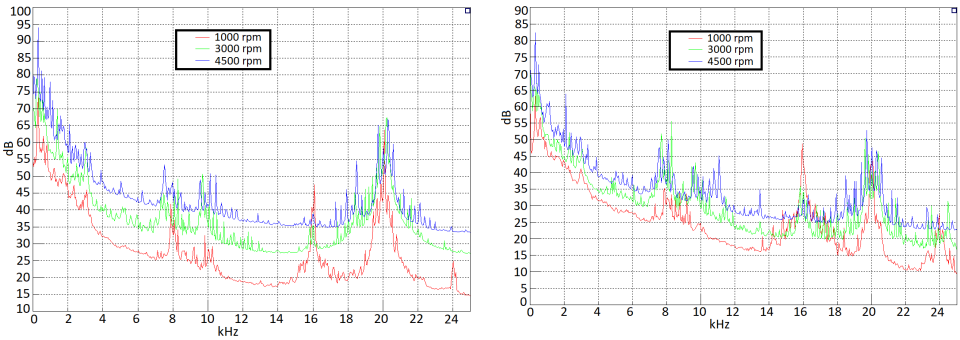

Fig. 5.28 Noise at different rotational speeds at 20 Nm load: microphone next to the machine (left) and hung 1.5 meter above (right)

Noise power achieves higher values as the rotational speed increases. One can see that the noise has the greatest power at 4500 rpm and is the lowest at 1000 rpm. One can see that the noise power spectrum achieves higher values for the noise signal measured by the microphone closer to the machine.

Fig. 5.29 presents the comparison of noise power spectrum for different load values in order to show the influence of the load on the noise emitted by the machine.

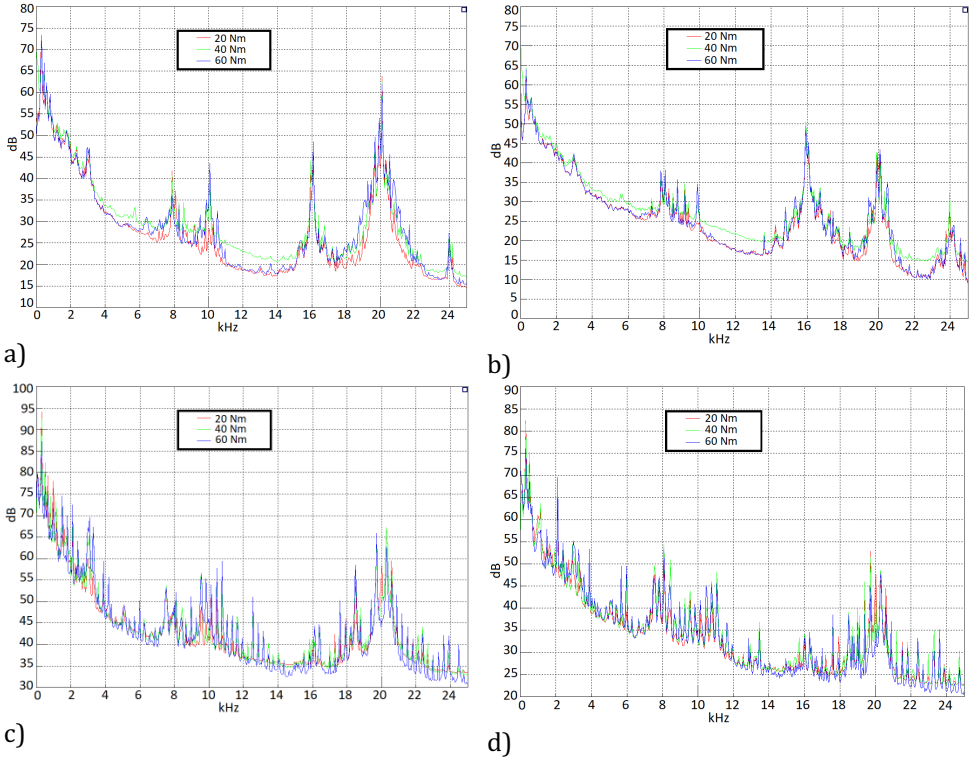

Fig. 5.29 Noise at different rotational speeds: a) 1000rpm microphone next to the machine, b) 1000rpm microphone 1.5 meter above the machine, c) 4500rpm microphone next to the machine, d) 4500rpm microphone 1.5 meter above the machine

It can be observed that the load has also some effect on the noise generated by the machine. Around the switching frequency (10 kHz) and its double, the power spectrum of the noise behaves as one might expect, the higher the load the higher the noise power spectrum. However, in some frequency range, this rule is not followed. This is caused by the fact that in the laboratory during the tests, there were two machines, both contributing to the overall noise measured by the microphones. At higher speed, the effect of the load on the noise is less visible.

The impact of current angle on the noise is shown below.

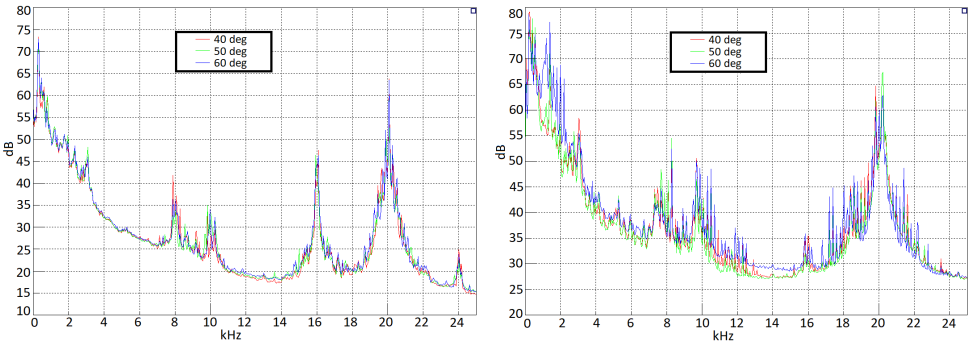

Fig. 5.30 Noise power spectrum at different current anglesat 1000 rpm (left) and 3000 rpm (right)

Similarly, to the vibration signal, the impact of the current angle on the noise is not very clear. Although the radial forces are the weakest for the highest current angle, the noise does not seem to be very affected. Just like in case of the vibration, the rotational speed and thus the radial forces frequency is the dominant factor in vibration and noise generation.

The described above tests were performed at constant rotational speed. Next a run-up test was performed and the results are shown in colormaps. Similarly, as it was done for no load state, the machine was accelerated while operating with a certain load and the vibration and noise signals were measured.

In Fig. 5.31, Fig. 5.32, Fig. 5.33 and Fig. 5.34 one can see example colormap for the run-up test taken at 20 Nm and 60 Nm torque. In the colormap, the orders of the motor are visible. Switching frequency and its double value are visible in the colormaps. As the torque increases, the signals of switching frequency are more visible in the colormap.

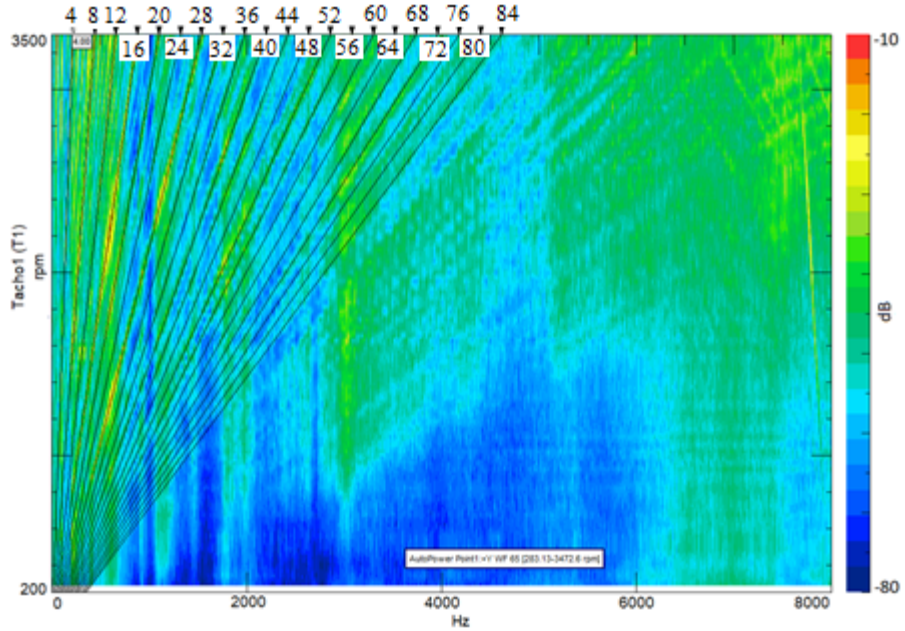

Fig. 5.31 Colormap of vibration signal at 20 Nm load

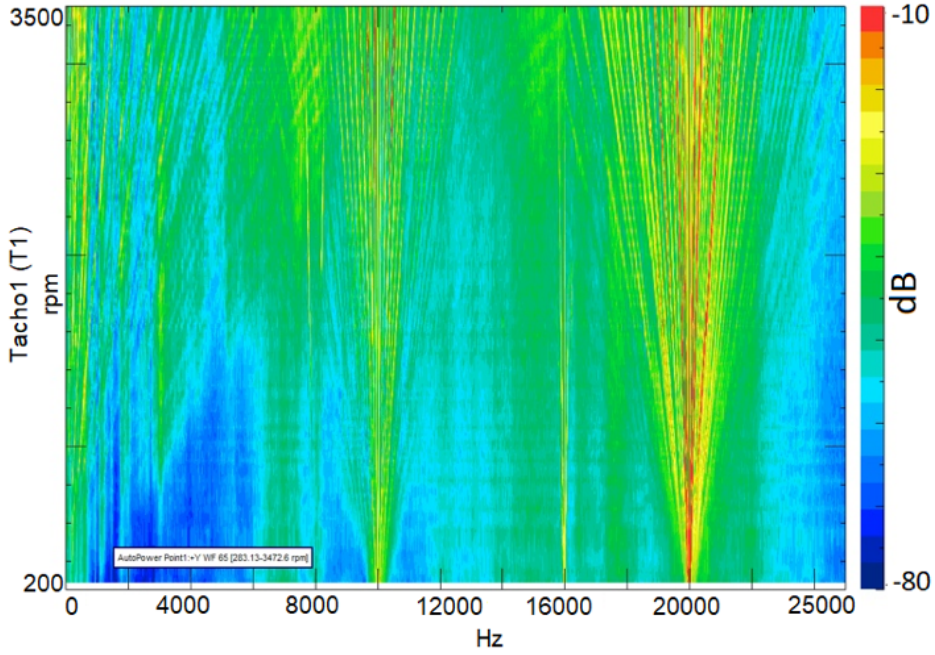

Fig. 5.32 Colormap of vibration signal at 20 Nm load

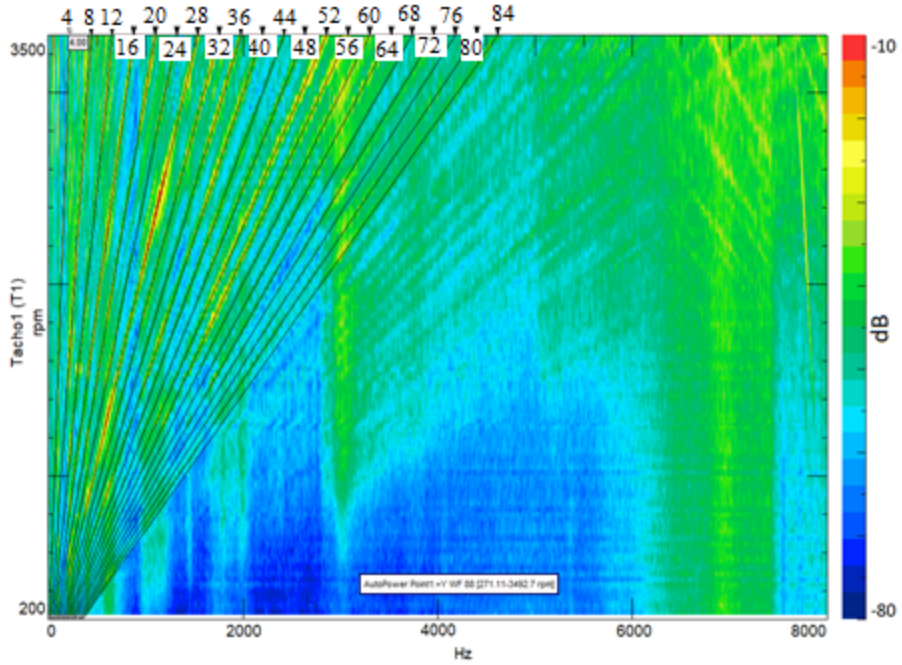

Fig. 5.33 Colormap of vibration signal at 60 Nm load

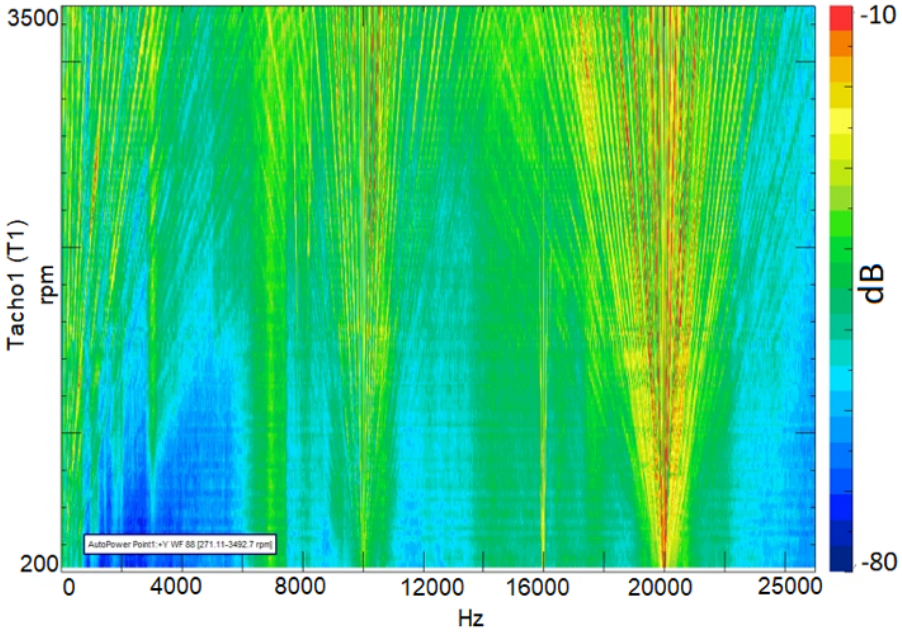

Fig. 5.34 Colormap of vibration signal at 60 Nm load

Characteristic harmonics such as machine orders or stator natural frequencies are also visible in the colormap. In load condition as the load increases these characteristic frequency components might be less visible due to increased amplitudes of other frequency components such as switching frequency.

The noise signal was also registered during the runup test. It is presented in Fig. 5.35 and Fig. 5.36 in form of a colormap. In this figure, one can see two characteristic frequency components: 8 kHz and 10 kHz and their double values. This is caused by the fact that during the test, there were two machines supplied from separate inverters with PWM at different switching frequency. These frequencies with their doubled values are marked in the colormap.

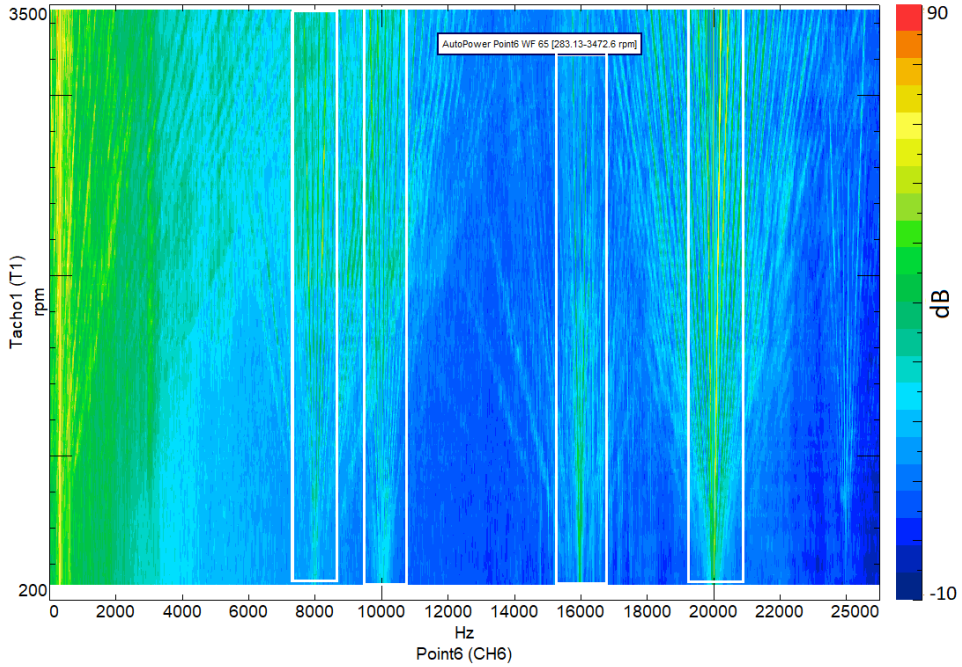

Fig. 5.35 Colormap of noise signal at 20 Nm load

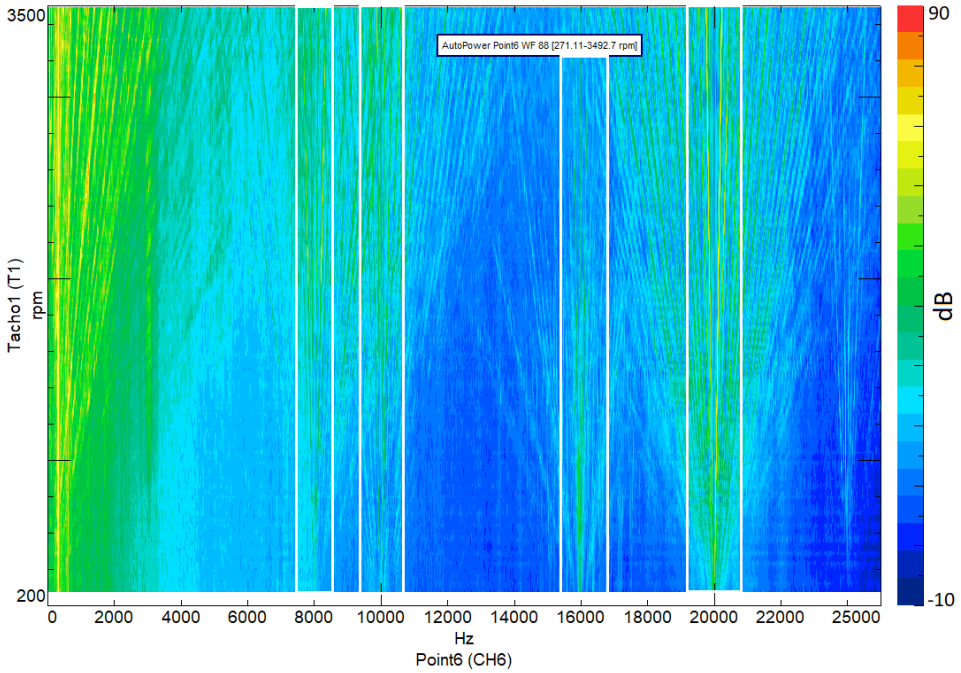

Fig. 5.36 Colormap of noise signal at 60 Nm load

5.2.2.3. Thermal Measurements

During the entire test, the machine was cooled with water of temperature equal to 20°C. The temperature of the coolant had to be kept at this level in order not to damage the windings of the machine. At nominal torque, the temperature oscillated around 115°C. Simulation tests showed similar values of winding temperature. The temperature of course varies with the flow rate and the temperature of the coolant. However, as during the simulations it was possible to check how the temperature changes with different values of flow rate and coolant temperatures, during the laboratory measurements such a test was impossible as the winding could be damaged. Simulations in MotorCAD and JMAG were performed in order to check if the cooling method allows to maintain the winding temperature in allowable range. As one might expect, the temperature was rising as the phase current was increasing. Winding temperature was measured using a temperature sensor mounted inside the motor.

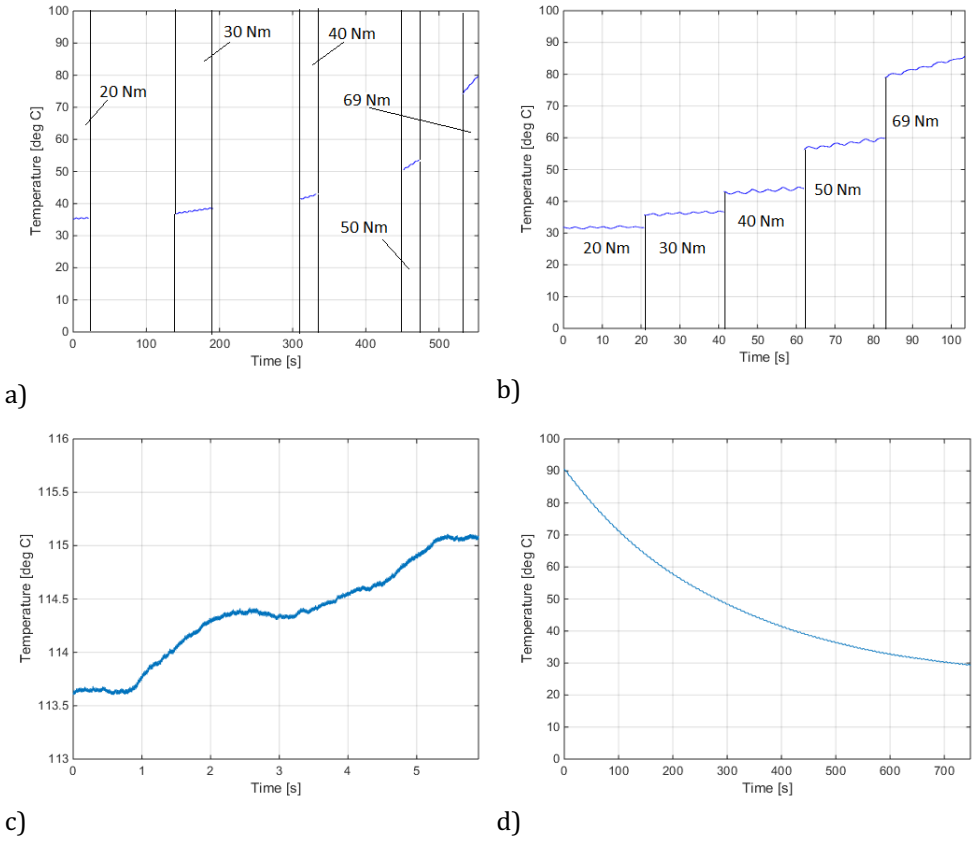

Fig. 5.37 Temperature of the winding: during tests a) and b), reaching maximum temperature c) and temperature drop d)

Fig. 5.37 a) shows the temperature of the winding during tests at different values of load. The temperature was measured during steady state vibration measurements. The gaps in the figure between the next measurements are caused by preparing the equipment to the next measurement. One can see that for higher load which involves higher phase current, the temperature rises at higher rate. For the clearance, the same case is presented in Fig. 5.37 b), without time gaps between the measurement.
In Fig. 5.37 c) one can see the temperature reaching its maximum value during the laboratory tests. Fig. 5.37 d) shows the winding temperature drop at zero current and water jacket cooling running.

The carried out laboratory tests proved that prepared models of the machine are valid. The purpose of electromagnetic modeling of the

machine was to estimate the parameters of the designed machine. The electromagnetic model of the machine allowed to estimate the phase current of the machine in various load conditions and also investigate the impact of current angle on phase voltage and current in load conditions. The impact of load, rotational speed and current angle on radial forces of the machine and thus the vibration of the structure was simulated and verified experimentally. More accurate information o about machine's vibration and noise generation was obtained using NVH calculations of machine's model. The effect of working conditions of the machine on its NVH behavior was validated during laboratory tests. Knowing the phase current and machine's geometry, it is possible to estimate the temperature of the winding. The purpose of thermal modeling of the machine was to find the proper cooling method of the machine, so the temperature of the winding does not exceed allowable value. The laboratory tests proved that the machine is able to operate at nominal torque with the winding temperature at allowable level.

5.2.3. Numerical Model Validation

In order to validate machine's numerical models presented in Chapter 4, measurement results were compared with simulation results.

5.2.3.1. Electromagnetic Model Validation

SynRM's torque, phase currents and voltages and flux linkage was measured in order to validate the electromagnetic model.

Comparison of torque vs. current curves is presented in figures below.

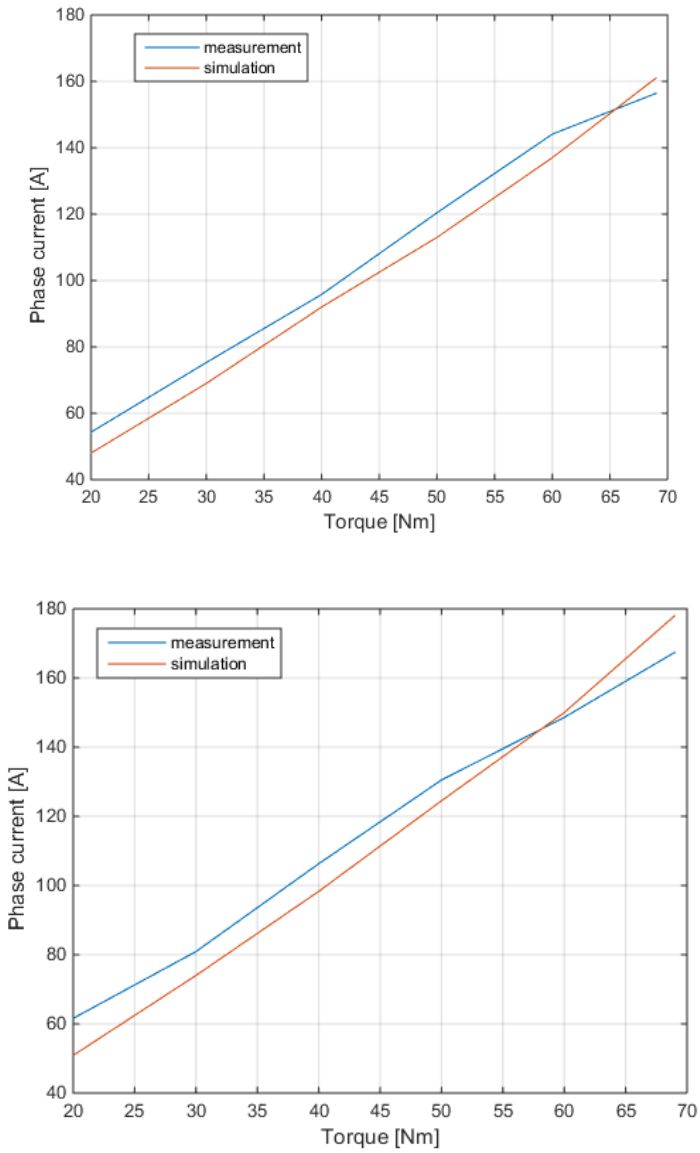

Fig. 5.38 Comparison of calculated and measured phase currents at 4500 rpm: 40^0 - top, 45^0 - bottom

One can see that calculated and measured values of phase current for a given torque are quite similar. In most cases, the phase current values obtained from simulation are lower than the measured ones since the simulations did not include all the effects in the machine such as eddy

currents or hysteresis loss. Moreover, the B-H curve of the steel sheet used in simulations might differ from the one of steel sheet used to manufacture the machine. The manufacturing process of the machine (cutting or punching the steel sheet) affects the B-H curve of the steel sheet. For this reason, the saturation of the magnetic circuit of the machine can occur at phase current values different from the calculated ones.

Machine's flux linkages were calculated by integrating measured stator EMF. The EMF was obtained by subtracting voltage drop on stator winding from supply voltage. Example flux linkage is presented in Fig. 5.39.

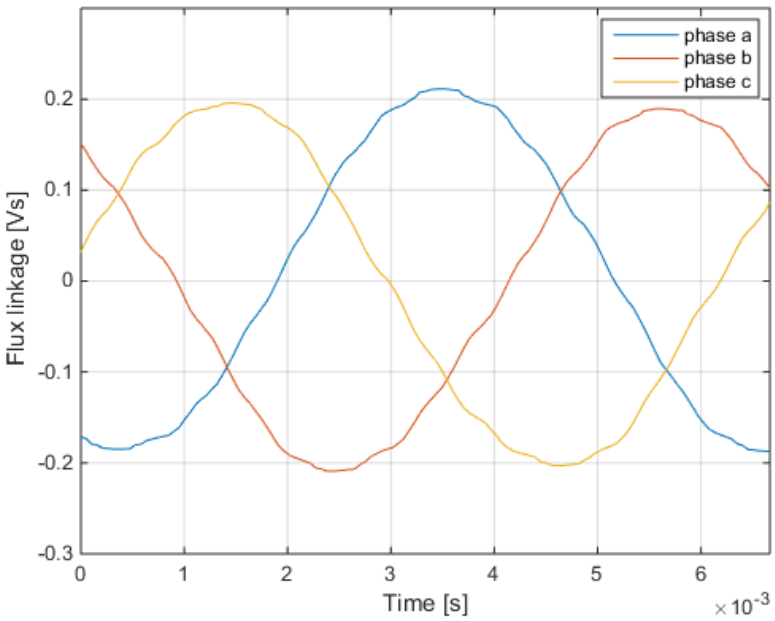

Fig. 5.39 Machine's flux linkage

Applying Park transformation to machine's flux linkage allowed to obtain flux linkage in d and q axes. By imposing different values of i_d and i_q currents using control system, it was possible to obtain flux linkage curves. Fig. 5.40 presents comparison of flux linkages values obtained

from measurements and simulations. One can see that simulated and measured values of flux linkage are quite similar. The shape of the curve that the measured values follow is sometimes different than the simulated one. This is caused by the limited accuracy of the SynRM model with skewed rotor. Also the B-H curve of the steel sheet might significantly differ from the one used in simulations due to manufacturing processes.

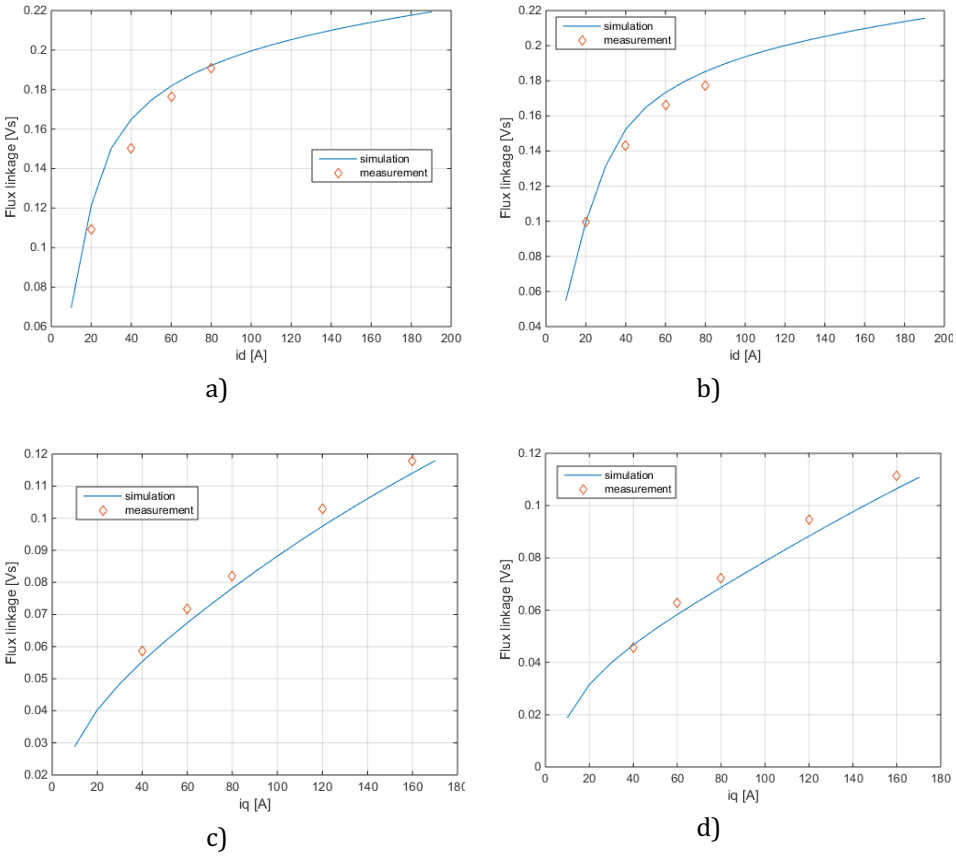

Fig. 5.40 Comparison of measured and simulated d and q axis flux linkage:
a) d axis flux linkage at iq = 40A,
b) d axis flux linkage at iq = 60A, c) d axis flux linkage at iq = 20A,
d) q axis flux linkage at id = 40A,

Comparison of measured and calculated torque and power factor values is presented in Fig. 5.41 and Fig. 5.42. Measured torque achieves similar

values as the calculated. Torque values obtained from simulation in usual are higher than the measured ones. This is caused by limited accuracy of the model. Moreover, during the simulation, the machine was supplied from ideal sinusoidal current source and iron losses were omitted. One can see greater differences between measured and calculated values of power factor. In this case, shape of voltage and current waveform plays important role in machine's power factor. Presence of higher order harmonics in current and voltage do not contribute to active power thus decrease the power factor.

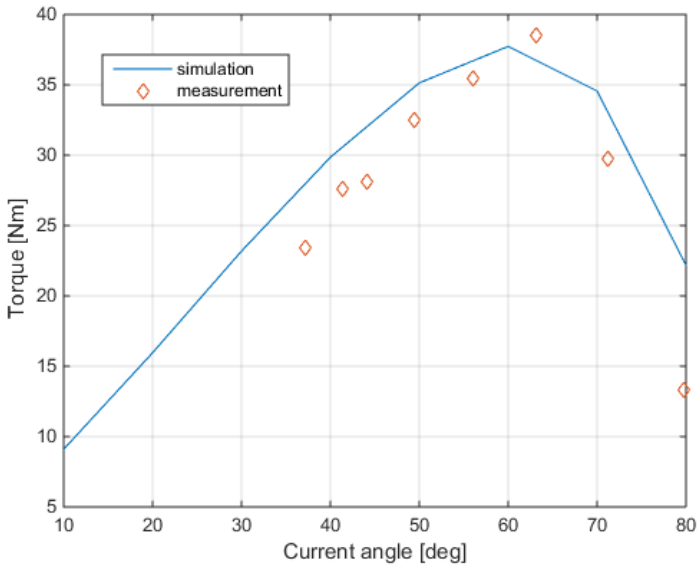

Fig. 5.41 Comparison of torque values at 110A

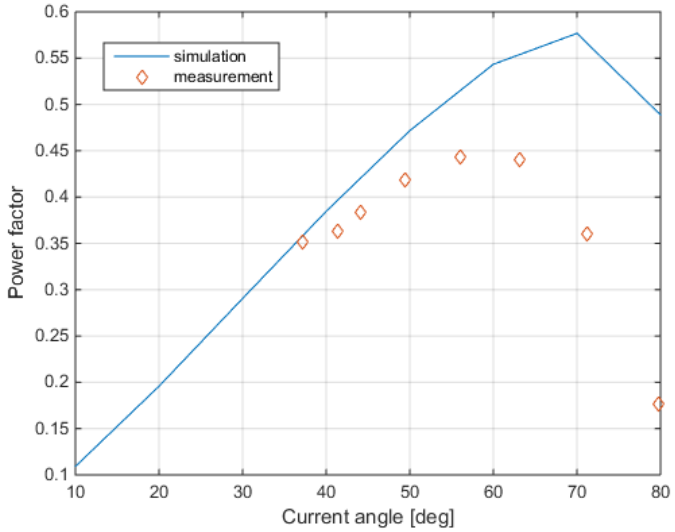

Fig. 5.42 Comparison of power factor values at 110A

5.2.3.2. NVH Model Validation

Machine's calculated natural frequencies and vibrational signal were compared with the measured ones in order to verify the correctness of the model.

Comparison of measured and calculated resonance frequency of machine's normal modes is presented in Table 5.3.

TABLE 5.3 Machine's normal modes frequencies comparison

	Ovalization	**Triangular**	**Square**
Simulation	928 Hz	2485 Hz	4433 Hz
Measurement	1166 Hz	2866 Hz	4451 Hz

As one can see, there is a difference between the calculated and measured natural frequencies. The measured frequencies are higher than the calculated frequency values. The difference is caused by the fact that, during the simulation, only the stator core was considered. The windings, the housing and the water jacket were not modeled. However,

the presence of the windings and housing increases the natural frequencies of the entire machine.

Fig. 5.43 shows comparison of vibration signal obtained from measurements and simulation.

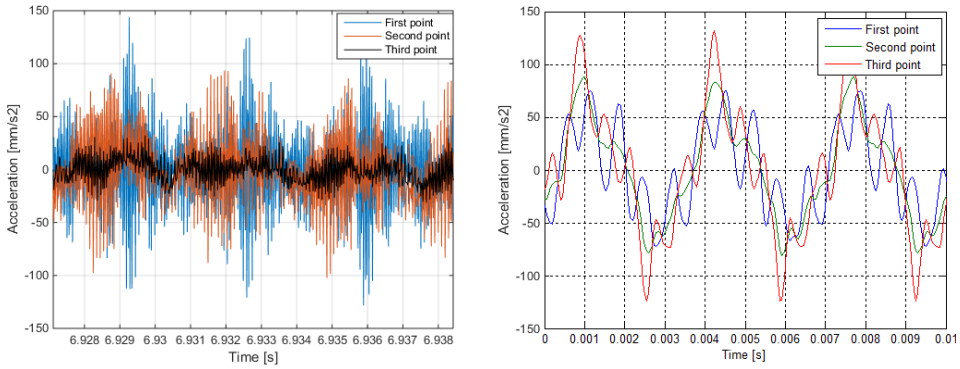

Fig. 5.43 Comparison of measured (left) and calculated (right) vibration signal

One can see that vibration signal along axial length of the stator changes both in measurements and in simulation. The amplitude of the signal is greater on one end of the stator. There is a difference in vibration signal waveform. In case of simulation, the machine was supplied from sinusoidal current source, however during measurements the machine was supplied from an inverter with PWM. The amplitudes and harmonics present in vibration signal are different in measured and simulated signal. However, it was possible to predict the behavior of the structure by running NVH simulations.

5.2.3.3. Thermal Model Validation

The purpose of thermal analysis of the machine was to estimate the temperature of the machine and adjust the cooling system. In order to validate the thermal model, the measured temperature inside the machine was compared with the simulated one.

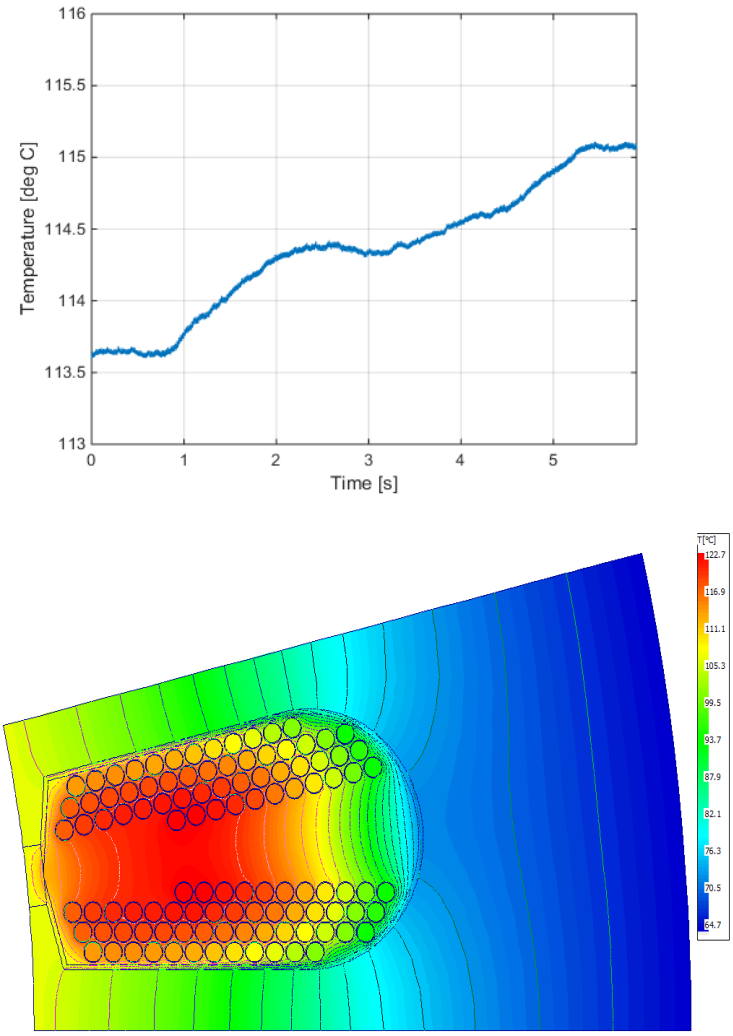

Fig. 5.44 Comparison of measured (top) and calculated (bottom) temperature of the winding

The measured temperature of the winding was 115 °C and calculated maximum temperature of the winding was 127 °C. One can see that thermal simulation allows to estimate the temperature of the winding with a good accuracy.

5.3. Conclusions and Personal Contributions

This chapter presents results of laboratory tests. The tests were carried out in no-load and load state at constant rotational speed. Measurements performed in no-load state allowed to investigate the natural frequencies of the machine. Difference between calculated and measured values of natural frequencies is caused the presence of stator housing and winding. In simulation for simplicity only the stator core was taken into account for natural frequency calculation. However, the presence of the stator winding, stator housing and water jacket affects the values of natural frequencies.

In load state it was possible to investigate the influence of load and current angle on machine's NVH behavior. It was proven that although the radial forces increase with stator current, the amplitude of vibration signal is not directly affected. Apart from the amplitude of the radial forces, the frequency is a crucial factor which decides about the level of vibration.

Electromagnetic tests allowed to validate machine's generated torque and how it is affected by current angle. Measured and calculated values of torque are similar. Differences in their values are caused by limited accuracy of machine's FEM model which does not take into account all the physical phenomena. Measured flux linkage in d and q axis is similar to the calculated one. The difference comes from definition of magnetizing curve of steel sheet used in simulation.

Temperature measurement proved the capability of machine's cooling system. Using water jacket allowed the machine to operate at nominal load in enclosed housing without exceeding allowable winding's temperature. Due to technical limitations, it was not possible to test the machine at peak stator current.

6. Conclusions and Contributions

Synchronous reluctance machine proves to be a serious candidate for EV applications and industrial applications. Its simple construction makes the machine robust and lack of permanent magnets significantly lowers the price and makes the machine less vulnerable to temperature changes. In many industrial applications, SynRM successfully replace induction machines.

Due to the construction, SynRM often operates with saturated magnetic circuit. This makes the machine highly non-linear. Using winding function method for SynRM has very low accuracy. The lowest accuracy was in case of q axis MMF since the flux fringing is very hard to model using analytical functions and Fourier series. Magnetic equivalent circuit method provided a better accuracy compared to winding function method since this method can include saturation of the magnetic circuit of the machine. Also in this case, for d axis MMF the results were quite good since the flux flow is quite simple and easy to model. For q axis MMF however, the results are also of low accuracy. It is very hard to model flux fringing using reluctance network. For simplicity, the SynRM was modeled as two separate circuits: for d and q axis MMF. Flux distribution in the air-gap of SynRM is very hard to model using winding function or magnetic equivalent circuit method. FEM provides the best accuracy of the results but its drawback is the fact that it requires a dedicated software. Moreover, depending on the geometry complexity, the computational cost might be very high.

Simulation tests proved that the construction of the rotor must be adjusted for high speed applications. Additional ribs must be introduced in flux barriers in order for the machine to be able to operate at high rotational speeds.

Electromagnetic and NVH analyses proved to be no relation between machine's torque ripple and the noise generated by the machine. To investigate this, four topologies of SynRM were simulated. Each of the topology had the same stator but different rotor and each of the topology experienced a different level of torque ripple. NVH simulations proved that the noise generated by the machine is not directly related to machine's torque ripple. It is because torque ripple is caused by fluctuations of the tangential component of magnetic forces. The noise of the machine on the other hand is caused by deformation of

the stator. The deformations are caused by the radial component of magnetic forces.

The final topology of the SynRM has 27 slots since the fractional winding reduces torque ripple of the machine. Moreover, in order to minimize the torque ripple, the rotor is skewed. Since the stator has 27 slots, the entire geometry of the machine had to be simulated as there is no symmetry axis. For electromagnetic analysis, 2D model of the machine was used. The rotor skewing was modeled by slicing the machine in axial direction. For validation, the results were compared to the ones obtained from 3D model. The obtained results were similar, hence for further simulations, 2D model was used. Electromagnetic analysis proved that the rotor skewing reduces torque ripple but at the same time causes the electromagnetic torque to drop. Simulations showed that machine's flux linkages in d and q axes are related because of the cross saturation. Flux linkage in d axis quickly saturates and the curve resembles the B-H curve of steel sheet. In q axis, the flux linkage increases almost linearly due to the presence of flux barriers.

The construction of the rotor used in the final topology of SynRM was adjusted to operate at high rotational speeds. Additional ribs were introduced in flux barriers to allow the rotor to withstand high centrifugal forces. Moreover, no sharp edges or corners or any discontinuities should be present in the rotor geometry since they increase the concentration of mechanical stress. Simulations proved that the centrifugal forces have higher impact on mechanical stress than the magnetic forces. Deformation of the rotor is greater due to centrifugal forces.

Rotor skewing also influences the distribution of magnetic forces in the stator. Due to the rotor skewing, the magnetic forces in the stator are distributed unevenly in machine's axial direction. This influences the vibration of the structure. The amplitude of vibration signal is different on both ends of the machine.

The amplitudes of magnetic forces are affected by the current angle of the machine. The higher the current angle, the lower the amplitudes of magnetic forces. It is caused by the fact that at high current angle values, the magnetic field in the machine decreases, which affects the magnetic forces. Also, the voltage is lower when the current angle is high. Operating at high current angle values can be used to weaken the flux in the machine.

Analysis of machine's iron losses shows that the stator and especially the winding are the main sources of heat. Iron losses in the rotor are caused by higher order harmonics of magnetic field since the rotor rotates synchronously with the magnetic field.

Thermal analysis of the machine was performed using 3D FEM model in JMAG and in MotorCAD which is a dedicated software for thermal analysis of electric machines. The goal of the thermal analysis was to choose the right cooling method so the machine could operate without overheating.

Experimental tests were carried out in no-load and load state of the machine. In no-load state, the influence of switching frequency on machine's vibration and noise was investigated. Switching frequency was present in the spectrum of vibration and noise signal. Analysis of vibration signal spectrum allowed to obtain the information on machine's orders and natural frequencies.

Machine's currents, voltages, torque and temperature were measured in load state. Experimental tests proved machine's electromagnetic behavior when operating at various current angles. Increasing current angle lowers the voltage but increases the current in order to maintain the same power. Due to technical limitations of the test bench, maximum power test could not be performed. Measurements of machine's noise and vibration proved that the major factor deciding about the noise of the machine is the rotational speed. Although the load increases machine's phase current and thus magnetic forces, the effect of load or current angle on noise and vibration is not as strong as the effect of rotational speed. It is because the speed is directly related to voltage and current frequency. At certain frequencies, specific normal modes of the machine structure are excited, increasing the level of noise and vibration.

Comparison of machine's calculated and measured torque vs. current angle curve show that there are some differences. The maximum values of torque are similar, however the shape of the curve differs. The higher difference occurs when comparing calculated and measured machine's power factor. The differences might be caused by many factors. In simulation, only B-H curve of the steel sheet was taken into account, not the hysteresis loop. Moreover, the steel sheet model might not have been accurate. Additionally, during machine assembly, the magnetic properties of steel sheet might deteriorate. Finally, eddy currents and hysteresis losses were not considered during simulations in order to limit the computational time.

Calculated natural frequencies differ from the measured ones. During simulation only the stator core was considered completely neglecting the effect of the winding, housing or water jacket. For this reason, the measured values of natural frequencies are higher than the calculated ones.

Chosen cooling method proved to be sufficient for the machine. During the experimental tests, the temperature of the winding did not exceed the maximum allowed value.

Personal contribution:

- Investigation of SynRM rotor topology impact on torque ripple and noise generation
- Investigation of SynRM flux barriers geometry on machine's electromagnetic behavior
- Application of mathematical equations to automatize rotor geometry creation with optimized flux barriers
- Application of parametric equations in calculating rotor's optimized flux barriers reluctances.
- Development of magnetic equivalent circuit of SynRM for d and q axis MMF
- Analysis of rotor's magnetic reluctance calculation for optimized flux barriers
- Comparison of winding function, magnetic equivalent circuit and finite element method for SynRM modeling
- Calculation of air gap magnetic field distribution using winding function and magnetic equivalent circuit
- Investigation of rotor geometry for high speed application
- Analysis of flux barriers topology on mechanical stress distribution in the rotor
- Investigation of stator slots and rotor topology combination for maximizing electromagnetic torque and minimizing torque ripple
- Analysis of flux linkage in the machine
- Calculation of Ld and Lq inductances of synchronous reluctance machine with cross saturation
- NVH simulations of SynRM
- Investigation of rotor skew on machine's parameters and radial magnetic forces distribution

- Comparison of finite element and thermal network models of SynRM
- Modeling of water jacket using finite element method
- Calculation of machine's parameters for control model of the machine
- Estimation of machine's flux linkage based on measured signals
- Validation of machine's NVH behavior
- Investigration of load, speed and current angle impact on noise and vibration of the machine
- Analysis of flux weakening possibility in SynRM by changing current angle

Future work:

- Improvement of MEC model of SynRM for including cross saturation of the machine
- Application of conformal mapping and winding function in inductance calculation of the machine
- Analysis of control strategy impact on NVH behavior of the machine
- Investigation of eddy currents and hysteresis impact on calculated torque and power factor
- Applicaton of optimization algorithm in finding the optimal rotor topology of the machine
- Analysis of SynRM with various number of poles
- Development of thermal network of the machine with optimized flux barriers

7. REFERENCES

[1] S. Amjad, S. Neelakrishnan and R. Rudramoorthy, "Review of design considerations and technological challenges for successful development and deployment of plug-in hybrid electric vehicles," *Renewable and Sustainable Energy Reviews,* vol. 14, no. 3, pp. 1104-1110, April 2010.

[2] M. Dijk, R. J. Orsato and R. Kemp, "The emergence of an electric mobility trajectory," *Energy Policy ,* vol. 52, pp. 135-145, January 2013.

[3] R. Xiong, J. Cao, Q. Yu, H. He and F. Sun, "Critical Review on the Battery State of Charge Estimation Methods for Electric Vehicles," *IEEE Access,* December 2017.

[4] L. T. Lam and R. Louey, "Development of ultra-battery for hybrid-electric vehicle applications," *Journal of Power Sources,* vol. 158, no. 2, pp. 1140-1148, August 2006.

[5] M. Etezadi-Amoli, K. Choma and J. Stefani, "Rapid-Charge Electric-Vehicle Stations," *IEEE Transactions on Power Delivery,* pp. 1883-1887, July 2010.

[6] I. Frade, A. Ribeiro, G. Gonçalves and A. P. Antunes, "Optimal Location of Charging Stations for Electric Vehicles in a Neighborhood in Lisbon, Portugal," *SAGE Journals,* January 2011.

[7] C. C. Chan, "The State of the Art of Electric, Hybrid, and Fuel Cell Vehicles," *IEEE,* April 2007.

[8] O. F. Vynakov, E. Savolova and A. Skrynnyk, "Modern Electric Cars of Tesla Motors Company," *Automation of technological and business-processes,* 2016.

[9] D. Staton and J. Goss, "Open Soure Elecric Motor Models for Commercial EV & Hybrid Traction Motors," in *CWIEME*, Berlin, 2017.

[10] F. Un-Noor, S. Padmanaban, L. Mihet-Popa, M. N. Mollah and E. Hossain, "A Comprehensive Study of Key Electric Vehicle (EV) Components, Technologies, Challenges, Impacts, and Future Direction of Development," *Energies,* 2017.

[11] A. T. D. Almeida, F. J. T. E. Ferreira and A. Quintino, "Technical and economical considerations on super high-efficiency three-phase motors," in *48th IEEE Industrial & Commercial Power Systems Conference*, 2012.

[12] ABB, *Synchronous reluctance motor-drive package for machine builders. High performance for ultimate machine design.,* 2014.

[13] M. Meza, "Industrial LV Motors & Drives: A Global Market Update," 2014.

[14] ABB, *Low voltage IE4 synchronous reluctance motors. Catalog August 2016,* 2016.

[15] R. -. A. K. Company, *REEL SuPremE - The IE5 magnet-free synchronous reluctance motor,* 2017.

[16] S. Tahi, R. Ibtiouen and M. Bounekhla, "Design Optimization of Two Synchronous Reluctance Machine Structures with Maximized Torque and Power Factor," *Progress in Electromagnetics Research,* 2011.

[17] Z. E and G. Zhongqi, "Magnetic Circuit Analysis and parametric Calculation of the New Type of Reluctance Motors," *Scientia Sinica,* 1983.

[18] T. Lipo, "Synchronous Reluctance Machines - A Viable Alternative for AC Drives," Wisconsin Electric Machines and Power Electronics Consortium, 1991.

[19] T. Matsuo and T. A. Lipo, "Rotor Design Optimization of Synchronous Reluctance Machine," *IEEE Transactions on Energy Conversion,* 1994.

[20] J. Kolehmainen, "Synchronous Reluctance Motor With Form Blocked Rotor," *IEEE Transactions on Energy Conversion,* vol. 25, p. 450–456, 2010.

[21] J. Rizk, M. H. Nagria and A. Hellany, "Optimum Design Parameters for Synchronous Reluctance Motors," *Proceedings of the 14th International Middle East Power Systems Conference (MEPCON' 10),* 2010.

[22] A. Vagati, A. Canova, M. Chiampi, M. Pastorelli and M. Repetto, "Design Refinement of Synchronous Reluctance Motors Through Finite-Element Analysis," *IEEE Transactions on Industry Applications,* 2000.

[23] A. Vagati, M. Pastorelli, G. Franceschini and S. C. Petrache, "Design of Low-Torque-Ripple Synchronous Reluctance Motors," *IEEE Transactions on Industry Applications,* 1998.

[24] H. Hofmann and S. R. Sanders, "High-Speed Synchronous Reluctance Machine with Minimized Rotor Losses," *IEEE Transactions on Industry Applications,* 2000.

[25] E. Schmidt and W. Brandl, "Comparative Finite Element Analysis of Synchronous Reluctance Machines with Internal Rotor Flux Barriers," *IEEE,* 2001.

[26] J. Keränen, A. Manninen and J. Pippuri, "Multi-physics simulations for electrical machine development," 2015.

[27] H.-M. Ahn, J.-K. Kim, Y.-H. Oh, K.-D. Song and S.-C. Hahn, "Multi-physics Analysis for Temperature Rise Prediction of Power Transformer," *Journal of Electrical Engineering and Technology,* 2014.

[28] F. Li, P.-q. Ye and H. Zhang, "Multi-physics analysis of permanent magnet tubular linear motors under severe volumetric and thermal constraints," *Journal of Central South University,* 2016.

[29] A. Boglietti, S. Member, A. Cavagnino, D. Staton, M. Shanel, M. Mueller and C. Mejuto, "Evolution and Modern Approaches for Thermal Analysis of Electrical Machines," *IEEE TRANSACTIONS ON INDUSTRIAL ELECTRONICS,* 2009.

[30] W. Soong, "Thermal Analysis of Electrical Machines: Lumped-Circuit, FE Analysis and Testing," Power Engineering Briefing Note Series.

[31] N. Nisar, *Structural Optimization and Thermal Modeling of Flux Switching Machine,* 2014.

[32] B. Andersson, *Lumped Parameter Thermal Modelling of Electric Machines,* 2013.

[33] Z. Kolondzovski, A. Belahcen and A. Arkkio, "Multiphysics thermal design of a highspeed permanent-magnet machine.," *Applied Thermal Engineering,* 2009.

[34] O. Craiu, A. Machedon, T. Tudorache, M. Morega and M. Modreanu, "3D Finite Element Thermal Analysis of a Small Power PM DC Motor," in *12th International Conference on Optimization of Electrical and Electronic Equipment, OPTIM*, 2010.

[35] R. J. Kumar and B. Banakara, "Finite Element Modeling and Analysis in estimation of air-gap torque of Induction Machine using Arkkio's method".*Journal of Electrical Engineering.*

[36] Z. Rehman and K. Seong, "Three-D Numerical Thermal Analysis of Electric Motor with Cooling Jacket," *Energies,* 2018.

[37] N. Bracikowski, M. Hecquet, P. Brochet and S. V. Shirinskii, "Multiphysics Modeling of a Permanent Magnet Synchronous Machine by Using Lumped Models," *IEEE Transactions on Industrial Electronics,* 2012.

[38] P. Kukula and C. Ondrušek, "Electric Machine Vibration Analysis," in *Konference diplomových prací 2007*, Brno, 2007.

[39] F. Chauvicourt, C. Faria, A. Dziechciarz and C. Martis, "Influence of Rotor Geometry on NVH Behavior of Synchronous Reluctance Machine," in *2015 Tenth International Conference on Ecological Vehicles and Renewable Energies (EVER 2015)*, Monte Carlo, 2015.

[40] F. L. M. d. Santos, J. Anthonis, F. Naclerio, J. J. C. Gyselinck, H. V. d. Auweraer and L. C. S. Góes, "Multiphysics NVH Modeling: Simulation of a Switched Reluctance Motor for an Electric Vehicle," *IEEE Transactions on Industrial Electronics,* vol. 61, no. 1, January 2014.

[41] J. DUPONT and P. BOUVET, "Multiphysics Modelling to Simulate the Noise of an Automotive Electric Motor," in *7th International Styrian Noise, Vibration & Harshness Congress: The European Automotive Noise Conference* , 2012.

[42] J. K. Kostko, "Polyphase Reaction Synchronous Motors," November 1923.

[43] J. Bárta and Č. Ondrůšek, "Design and Optimization of Synchronous Reluctance Machine".

[44] J. Barta and C. Ondrusek, "Rotor Design and Optimization of Synchronous Reluctance Machine," *Science Journal,* March 2015.

[45] G. Bacco and N. Bianchi, "Choice of Flux-Barriers Position in Synchronous Reluctance Machines," 2017.

[46] M. PALMIERI, M. PERTA, F. CUPERTINO and G. PELLEGRINO, "Effect of the Numbers of Slots and Barriers on the Optimal Design of Synchronous Reluctance Machines".*Journal of Electrical Engineering.*

[47] O. C., D. A. and M. C., "Comparative Analysis of Different Synchronous Reluctance Motor Topologies," in *15th IEEE International Conference on Environment and Electrical Engineering*, Rome, 2015.

[48] M. Muteba, B. Twala and D. V. Nicolae, "Torque Ripple Minimization in Synchronous Reluctance Motor Using a Sinusoidal Rotor Lamination Shape," *IEEE,* 2016.

[49] C. M. Spargo, B. C. Mecrow, J. D. Widmer, C. Morton and N. J. Baker, "Design and Validation of a Synchronous Reluctance Motor With Single Tooth Windings," *IEEE TRANSACTIONS ON ENERGY CONVERSION,* 2015.

[50] C. M. Donaghy-Spargo, B. C. Mecrow and J. D. Widmer, "Electromagnetic Analysis of a Synchronous Reluctance Motor with Single Tooth Windings".

[51] B. Lehner and D. Gerling, "Design and Comparison of Concentrated and Distributed Winding Synchronous Reluctance Machines".

[52] H. S. Rawat and A. Srivastava, "Comparison of Axially and Transversally Laminated Synchronous Reluctance Motors by Using FEM Based Analysis," *International Journal of Electrical Electronics & Computer Science Engineering,* October 2017.

[53] S. Cai, J. Shen, H. Hao and M. Jin, "Design Methods of Transversally Laminated Synchronous Reluctance Machines," *CES TRANSACTIONS ON ELECTRICAL MACHINES AND SYSTEMS,* June 2017.

[54] S. Armentia, G. Ugalde, J. Poza and A. Julia Escalada, "Numerical 2D methodology for synchronous reluctance motor rotor design," in *2015 5th International Electric Drives Production Conference (EDPC)*, 2015.

[55] J.-H. Lee, S.-J. Parka and S.-J. Jeon, "Optimum design criteria for a synchronous reluctance motor with concentrated winding using response surface methodology," *Journal of Applied Physics,* 2006.

[56] A. Dziechciarz, C. Oprea and C. Martis, "Multi-physics design of synchronous reluctance machine for high speed applications," in *IECON 2016-42nd Annual Conference of the IEEE*, 2016.

[57] M. D. Nardo, G. L. Calzo, M. Galea and C. Gerada, "Structural Design Optimization of a High Speed Synchronous Reluctance Machine".

[58] S. Taghavi and P. Pillay, "Design aspects of a 50hp 6-pole synchronous reluctance motor for electrified powertrain applications," in *IECON*, 2017.

[59] R. Vartanian, H. A. Toliyat, B. Akin and R. Poley, "Power factor improvement of synchronous reluctance motors (SynRM) using permanent magnets for drive size reduction," in *2012 Twenty-Seventh Annual IEEE Applied Power Electronics Conference and Exposition (APEC)*, 2012.

[60] M. N. Ibrahim, E. M. Rashad and P. Sergeant, "Steady-State Analysis and Stability of Synchronous Reluctance Motors Considering Saturation Effects," *IEEE,* 2015.

[61] M. N. Ibrahim, P. Sergeant and E. M. Rashad, "Synchronous Reluctance Motor Performance Based on Different Electrical Steel Grades," *IEEE TRANSACTIONS ON MAGNETICS,* November 2015.

[62] J.-K. Lee, D.-H. Jung, J. Lim, Y. J. Oh, K.-D. Lee and J. Lee, "Rotor Open-Rib Design for Power Density Improvement in Synchronous Reluctance Motor," *Journal of Magnetics,* 2018.

[63] C. M. Donaghy-Spargo, B. Mecrow and J. D. Widmer, "On the Influence of Increased Stator Leakage Inductance in Single Tooth Wound Synchronous Reluctance Motors," *IEEE TRANSACTIONS ON INDUSTRIAL ELECTRONICS,* 2017.

[64] A. Dziechciarz and C. Martis, "New Shape of Rotor Flux Barriers in Synchronous Reluctance Machines Based on Zhukovski Curves," in *he 9th International Symposium on ADVANCED TOPICS IN ELECTRICAL ENGINEERING (ATEE)*, Bucharest, 2015.

[65] A. R. Tariq, C. E. Nino-Baron and E. G. Strangas, "Iron and Magnet Losses and Torque Calculation of Interior Permanent Magnet Synchronous

Machines Using Magnetic Equivalent Circuit," *IEEE Transactions on Magnetics,* vol. 46, 2010.

[66] K.-H. Shin, J.-S. Yu, J.-Y. Choi and H.-W. Cho, "Design and Analysis of Interior Permanent Magnet Synchronous Motor Considering Saturated Rotor Bridge using Equivalent Magnetic Circuit," *Journal of Magnetics,* pp. 404-410, 2014.

[67] E. Stig, "Generalized reluctances in eddy current magnetic circuits," *Archiv für Elektrotechnik,* vol. 49, pp. 67-72, 1964.

[68] J. Perho, Reluctance Network for Analysing Induction Machines, Espoo: Acta Polytechnica Scandinavica, 2002.

[69] S.-L. Ho, "FINITE-ELEMENT ANALYSIS OF MACHINES".*ELECTRICAL ENGINEERING.*

[70] K. Ho-Le, "Finite element mesh generation methods: a review and classification," 1988.

[71] T. Sobczyk, Metodyczne Aspekty Modelowania Matematycznego Maszyn Indukcyjnych, Warsaw: Wydawnictwo Naukowo-Techniczne, 2004.

[72] J. Gao, L. Zhang and X. Wang, "AC Machine Systems: Mathematical Model and Parameters, Analysis and System Performance," *Springer-Verlag Berlin Heidelberg,* 2009.

[73] H. A. Toliyat, S. Nandi, S. Choi and H. Meshgin-Kelk, Electric Machines: Modeling, Condition Monitoring and Fault Diagnosis, CRC Press Taylor & Francis Group, 2013.

[74] A. Dziechciarz and C. Martis, "Simplified model of synchronous reluctance machine with optimized flux," *Electrical Engineering, Springer,* pp. 1-10, 2017.

[75] A. Dziechciarz and C. Martis, "Magnetic Equivalent Circuit of Synchronous Reluctance Machine," in *11th International Conference ELEKTRO 2016*, Strbske Pleso, 2016.

[76] J. Gyselinck and R. V. Sabariego, "Airgap Reluctance Identification for the Magnetic Equivalent Circuit Modelling of Induction Machines," in

Conference on the Computation of Electromagnetic Fields (COMPUMAG), Budapest, Hungary, 2013.

[77] J. M. Williams, *Modeling and Analysis of Electric Machines with Asymmetric Rotor Poles Using a Reluctance Based, Magnetic Equivalent Circuit,* University of Missouri-Rolla, 2004.

[78] V. Ostović, Dynamics of Saturated Electric Machines, Springer-Verlag New York Inc..

[79] L. Bin, L. Chao, L. Hongfeng and L. Guidan, "Torque Analysis of Spherical Permanent Magnetic Motor with Magnetic Equivalent Circuit and Maxwell Stress Tensor," *Informatics in Control, Automation and Robotics,* vol. 2, pp. 617-628.

[80] P. G. C. and V. E. J. A., "On the steady-state determination of networks containing magnetic nonlinearities," *Archiv für Elektrotechnik,* vol. 73, pp. 109-114, 1990.

[81] G. Pellegrino, T. M. Jahns, N. Bianchi, W. L. Soong and F. Cupertino, The Rediscovery of Synchronous Reluctance and Ferrite Permanent Magnet Motors - Tutorial Course Notes, SpringerBriefs in Electrical and Computer Engineering.

[82] K. D. Hagen, Introduction to Engineering Analysis, Prentice Hall.

[83] J. A. Collins, Failure of Materials in Mechanical Design: Analysis, Prediction, Prevention.

[84] M. Janda, O. Vitek and V. Hajek, "Noise of Induction Machines".

[85] A. Hubert and G. Friedrich, "Vibrations and acoustic noise reduction in A.C. electrical drives. Use of analytical and experimental modal techniques.," in *ISMA*.

[86] J. R. Hendershot, "Causes & Sources of audible noise in elecric motors".

[87] K. Shiohata, R. Kusama, S. Ohtsu and T. Iwatsubo, "The Study on Electromagnetic Force Induced Vibration and Noise from a Normal and an Eccentric Universal Motors," in *PIERS Proceedings*, Marrakesh, 2011.

[88] P. Witczak, "Analytical Method for Calculation of Eigenfrequencies and Modes of Stator Cores in AC Machines," *Zeszyty Problemowe - Maszyny Elektryczne,* no. 92, 2011.

[89] M. Pirnat, G. Cepon and M. Boltezar, "Introduction of the linear contact model in the dynamic model of laminated structure dynamics: An experimental and numerical identification," in *Mechanism and Machine Theory*, 2013, p. 144–154.

[90] P. Millithaler, Ã. Sadoulet-Reboul, M. Ouisse, J.-B. Dupont and N. Bouhaddi, "Structural dynamics of electric machine stators: Modelling guidelines and identification of three-dimensional equivalent material properties for multi-layered orthotropic laminates," *Journal of Sound and Vibration,* 2015.

[91] M. v. d. Giet, K. Kasper, R. W. D. Doncker and K. Hameyer, "Material parameters for the structural dynamic simulation of electrical machines," in *2012 XXth International Conference on Electrical Machines (ICEM)*, 2012.

[92] Y. Huang and Z. Cui, "ATV and MATV Techniques for BEM Acoustics in LS-DYNA," in *13th International LS-DYNA Users Coference*.

[93] R. Wrobel, P. H. Mellor, M. Popescu and D. A. Staton, "Power Loss Analysis in Thermal Design of Permanent Magnet Machines – A Review," *IEEE Transactions on Industry Applications,* pp. 1359-1368.

[94] J. Pyrhonen, T. Jokinen and V. Hrabovcova, Design of Rotating Electrical Machines, Wiley & Sons, 2013.

[95] M. Mahmoudi, *Thermal Modelling of the Synchronous Reluctance Machine,* Stockholm, 2012.

[96] G. Dajaku and D. Gerling, "An Improved Lumped Parameter Thermal Model for Electrical Machines".

[97] S. Touhami, Y. Bertin, Y. Lefevre1, J. F. Llibre1, C. Henaux1 and M. Fénot, "LUMPED PARAMETER THERMAL MODEL OF PERMANENT MAGNET SYNCHRONOUS MACHINES," *Electrimacs,* July 2017.

[98] C. Holtmann, F. Rinderknecht and H. E. Friedrich, "Thermal Model of Electric Machines with Correction of Critical Parameters," March 2017.

[99] C. Pohlandt and M. Geimer, "Thermal models of electric machines with dynamic workloads," *Landtechnik,* 2015.

[100] M. L. Hosain, R. B. Fdhila and K. Rönnberg, "Air-Gap Flow and Thermal Analysis of Rotating Machines using CFD," in *The 8th International Conference on Applied Energy – ICAE*, 2016.

[101] C. ANIMA and R. KATUKAM, "HEAT TRANSFER IN ELECTRICAL MACHINE: A CASE STUDY," *International Journal of Mechanical And Production Engineering,* April 2015.

[102] P. H. Connor, S. J. Pickering, C. Gerada, C. N. Eastwick, C. Micallef and C. Tighe, "Computational fluid dynamics modelling of an entire synchronous generator for improved thermal management," *IET Electric Power Applications,* May 2013.

[103] S. Nategh, Z. Huang, A. Krings, O. Wallmark and M. Leksell, "Thermal Modeling of Directly Cooled Electric Machines Using Lumped Parameter and Limited CFD Analysis," *IEEE Transactions on Energy Conversion,* December 2013.

[104] B. Tabbache, S. Djebarri, A. Kheloui and M. Benbouzid, "A Power Presizing Methodology for Electric Vehicle Traction Motors," *International Review on Modelling and Simulations,* pp. 29-32, 2013.

[105] D. A. Staton and A. Cavagnino, "Convection Heat Transfer and Flow Calculations Suitable for Electric Machines Thermal Models," *IEEE TRANSACTIONS ON INDUSTRIAL ELECTRONICS,* October 2008.

[106] C. M. Spargo, "Synchronous Reluctance Technology – Part I," *MagNews.,* 2013.

[107] M. Sarrazin, S. Gillinjs, K. Janssens, H. v. d. Auweraer and K. Verhaeghe, "Vibro-acoustic Measurements and Techniques for Electric Automotive Applications," in *Inter-noise*, Melbourne, 2014.

[108] M.Karamuk, "A Survey on Electric Vehicle Powertrain Systems," in *Agean Conference on Electrical Machines and Power Electronics (ACEMP)*, September 2011.

[109] M. Liu, "Cooling design and thermal analysis for dual-stator 6-slot 4-pole flux-switching permanent magnet machine," in *Master of Science*, 2017.

[110] M. Hamada and A. Chiba, "SR Motor Made Small Enough for Hybrid Cars," *Tech and Industry Analysis from Asia,* Dec 17 2009.

[111] David G. Dorrell, Mircea Popescu, David A. Staton, Lyndon Evans and Andrew M. Knight, "Comparison of Different Motor Design Drives for Hybrid Electric Vehicles".

[112] J. L. Besnerais, A. Fasquelle, M. Hecquet, J. Pelle, V. Lanfranchi, S. Harmand, P. Brochet and A. Randria, "Multiphysics modeling: electro-vibro-acoustics and heat transfer of PWM-fed induction machines," *IEEE,* July, 2009.

[113] A. T. d. Almeida, F. J. T. E. Ferreira and G. Baoming, "Beyond Induction Motors — Technology Trends to Move Up Efficiency," *IEEE TRANSACTIONS ON INDUSTRY APPLICATIONS,* May/June 2014.

8. LIST OF FIGURES

9. LIST OF TABLES

10. LIST OF PUBLICATIONS

1. *Comparative analysis of different synchronous reluctance motor topologies* - Claudiu Oprea, **Arkadiusz Dziechciarz**, Claudia Martis, 2015 IEEE 15th International Conference on Environment and Electrical Engineering (EEEIC),
   DOI: 10.1109/EEEIC.2015.7165463

2. *Infuence of rotor geometry on NVH behavior of synchronous reluctance machine* - Fabien Chauvicourt, Cassio Faria, **Arkadiusz Dziechciarz**, Claudia Martis, 2015 Tenth International Conference on Ecological Vehicles and Renewable Energies (EVER), DOI: 10.1109/EVER.2015.7112973

3. *Magnetic equivalent circuit modelling of Reluctance Machines* - Wei Peng, Johan Gyselinck, **Arkadiusz Dziechciarz**, Claudia Martis, 2016 Eleventh International Conference on Ecological Vehicles and Renewable Energies (EVER),
   DOI: 10.1109/EVER.2016.7476429

4. *New shape of rotor flux barriers in synchronous reluctance machines based on Zhukovski curves* - **Arkadiusz Dziechciarz**, Claudia Martis, 2015 9th International Symposium on Advanced Topics in Electrical Engineering (ATEE),
   DOI: 10.1109/ATEE.2015.7133768

5. *Comparative evaluation of DTC strategies for the Synchronous Reluctance machine* - Simon Wiedemann, **Arkadiusz Dziechciarz**, 2015 Tenth International Conference on Ecological Vehicles and Renewable Energies (EVER),
   DOI: 10.1109/EVER.2015.7112972

6. *Review of multidisciplinary homogenization techniques applied to electric machines* - Fabien Chauvicourt, Pietro Romanazzi, David Howey, **Arkadiusz Dziechciarz**, Claudia Martis, Cassio T Faria, 2016 Eleventh International Conference on Ecological Vehicles and Renewable Energies (EVER),
   DOI: 10.1109/EVER.2016.7476431

7. *Simplified model of synchronous reluctance machine with optimized flux barriers* - **Arkadiusz Dziechciarz**, Claudia Martis, Electrical Engineering 2017/12/1, Springer Berlin Heidelberg, DOI: https://doi.org/10.1007/s00202-017-0616-1

8. *Multi-physics design of synchronous reluctance machine for high speed applications* - **Arkadiusz Dziechciarz**, Claudiu Oprea, Claudia Martis, IECON 2016-42nd Annual Conference of the IEEE Industrial Electronics Society,
DOI: 10.1109/IECON.2016.7793986

9. *Magnetic equivalent circuit of synchronous reluctance machine* - **Arkadiusz Dziechciarz**, Claudia Martis, 2016 ELEKTRO,
DOI: 10.1109/ELEKTRO.2016.7512126

10. *Synchronous Reluctance Machine modeling for accurate performances evaluation* - Ioana Nasui-Zah, **Arkadiusz Dziechciarz**, Claudia Steluţa Marţiș, 2018 International Symposium on Fundamentals of Electrical Engineering (ISFEE), DOI: 10.1109/ISFEE.2018.8742438